



The University of
Nottingham

UNITED KINGDOM • CHINA • MALAYSIA

**Investigating Pharmaceutical Formulations Using
Advanced Analytical Techniques**

Amjad A Selo, BSc, MSc

Thesis submitted to the University of Nottingham for the
degree of Doctor of Philosophy

School of Pharmacy

September 2018

Acknowledgements

Firstly, I would like to thank all those at the University of Nottingham who have supported this work. Thank you to Dr Jonathan Aylott who has given me the opportunity to work under his supervision. I gratefully acknowledge his continued encouragement over the past three years. I am particularly grateful to him for the universal support I have received in all my endeavours in my time at Nottingham. I also gratefully acknowledge Dr Jonathan Burley, Dr David Scurr, Dr Ludovic Renou and Dr Ana Kwokal for their valuable contributions to the project.

Special thanks are going to Dr Veeren Chauhan for being a great friend and colleague. Thanks for your help, support and funny jokes. I wish to thank all the members of the Aylott Group for making D38 a great environment to work in. I have also been fortunate to be a part of the AMHT and Central of Doctoral Training in Advanced Therapeutics and Nanomedicine. I owe much gratitude to Dr Claudia Matz for her support and wise words. Additionally, I would like to acknowledge GSK and the EPSRC for funding this project

A special debt of thanks is reserved for Dr Ammar Al Majan for being a great friend and family and being there when I need help and guidance. Thank you to all my friends who have always been there to talk through everything.

Finally, and most importantly, I would like to thank my parents, my family in Syria and my family in the UK whose love and support throughout my entire education has enabled me to reach this point – thank you, I could not have done it without you. Million zillion thanks Lubna for being my soulmate, for loving me and sharing your life with me. Thank you for your encouragement, patient and spending several hours waiting for me to come back home. I surely could not have asked for a better team-mate than you. I love you to the end of the universe and back to infinity and beyond forever and ever!

“Whoever travels a path in search of knowledge, God will make easy for him
a path to Paradise.”

Prophet Muhammad PBUH

Declaration

I hereby declare that the work contained in this thesis titled “Investigating Pharmaceutical Formulations Using Advanced Analytical Techniques” is the result of my own work conducted at the School of Pharmacy, University of Nottingham between October 2015 and September 2018, under the supervision of Dr Jonathan Aylott, Dr Jonathan Burley, Dr David Scurr and Dr Ludovic Renou (GSK).

Abstract

Drug research and development is a costly and lengthy process and involves a high risk of product failure. The consequences of insufficient understanding and poor control of pharmaceutical physicochemical properties and stability during drug development can delay new drug approvals and increase the cost of developing new drugs. Salts, which are estimated to account for >50% of active pharmaceutical ingredient formulations, are susceptible to drug degradation, which can lead to a phase transformation of the drug from a more soluble salt form to the less soluble free form, also known as salt disproportionation. Salt disproportionation has severe implications on final product stability and performance, such as slow dissolution and reduced bioavailability. As a result, determination of salt disproportionation reactions in the later stages of drug development can significantly increase the cost of development due to changes in the final product formulation. Although salt forms are widely utilised in the pharmaceutical industry, salt disproportionation in the presence of relative humidity and excipients is yet to be fully understood.

Therefore, the research detailed in this thesis aims to apply simple, fast and *in-situ* analytical techniques to investigate the effects of relative humidity and formulation excipients on salt disproportionation in multi-component solid dosage forms during storage and dissolution. The application of advanced analytical technologies will provide a fundamental understanding of salt disproportionation in the presence of formulation excipients and thus assist formulators in predicting the instability of the drug salt and identifying formulation strategies to mitigate salt disproportionation at early stages of drug development.

The experimental work in this thesis is split into three sections: 1) exploring the capabilities and limitations of advanced analytical techniques in a model complex system; 2) investigating salt disproportionation in the presence of excipients during storage at high relative humidity using *in-situ*

optical screening techniques and 3) the application of *in-situ* Raman spectroscopy to study salt disproportionation in multicomponent tablets during dissolution.

A wide range of state-of-the-art advanced analytical techniques was explored using nanoparticles in electrospun fibre hybrids as a challenging, complex multi-component system (Chapter 3). The particle-fibre hybrid morphology was found to be influenced by the encapsulated particle size and nanoparticle concentration. Transmission electron microscopy (TEM) was found to be more efficient than scanning electron microscopy (SEM) in investigating the particle-fibre hybrid morphology due to the transmission capability. Energy dispersive X-ray (EDX) analysis, Raman spectroscopy and time-of-flight secondary ion mass spectroscopy (ToF-SIMS) were utilised to provide valuable elemental, chemical and surface information of the particle-fibre hybrids, respectively. The feasibility of using particle-fibre hybrids containing fluorescent nanoparticles as a new tool for super-resolution fluorescence microscopy calibration was examined. The results showed that fluorescent particle-fibre hybrids served as an effective validating and testing tool.

The salt stability of two salt model systems, Pioglitazone HCl and Ibuprofen sodium, was investigated as a function of different formulation excipients during storage and dissolution in Chapters 4 and 5, respectively.

In-situ optical microscopy equipped with a controlled humidity chamber was used to monitor salt disproportionation in drug-excipient binary mixtures (Chapter 4). This was achieved by tracking the changes in the salt crystal morphology due to phase transformation in real-time. Salt disproportionation to the free-form led to a change in the crystal shape from block-like crystals into needle-like crystal structures in both salt model systems. The effect of acidic and alkaline excipients on the microenvironment pH has a significant role in facilitating or preventing salt disproportionation during storage.

Salt disproportionation does not only occur in solid-state as described previously but can also take place in the solution. A bespoke set-up combining Raman confocal microscopy and an ultraviolet-visible (UV-Vis) spectroscopy flow cell was used to understand the effect of excipients on salt stability in tablets during dissolution (Chapter 5). Raman spectroscopy was employed to detect chemical changes associated with the formation of the undesirable free form of the drug in the solid tablet matrix. In-line UV-vis spectroscopy was used to monitor the concentration of the drug in solution during dissolution. The results showed the vital role of pH both in the dissolution media and the microenvironment (controlled by the formulation excipients) in inducing or preventing salt disproportionation. Raman mapping and cross-sectioning, using a microtome, were performed after dissolution for tablets that exhibited salt conversion. The Raman maps of the cross-sectioned tablets revealed the formation of a shell consisting of the free drug around the edge of the tablet. This shell decreased the rate of penetration of the dissolution medium into the tablet, which had significant implications on the release of the API into the surrounding solution as shown by the UV-Vis drug release data.

Overall, the research in this thesis has demonstrated that the properties of the salt (specifically pH_{max}), excipient properties (such as pK_a , solubility, hydrophobicity), as well as the dissolution medium pH, played essential roles in influencing the disproportionation during storage and dissolution. Analytical techniques such as optical screening and Raman spectroscopy, which can be employed in-line and online, were demonstrated to be effective approaches to investigate salt disproportionation. Results were obtained in real-time and did not require large amounts of solid or extensive sample preparation indicating that these analytical techniques can address the challenges of studying a range of pharmaceutical drug delivery systems, which can ultimately lead to the development of more efficient pharmaceutical formulations.

Table of Contents

Acknowledgements	ii
Declaration	iv
Abstract	v
Chapter1 : General Introduction	1
1.1. Pharmaceutical Drug Development	1
1.2. Form and Formulation	2
1.3. Drug Stability in Pharmaceutical Dosage Forms	5
1.4. Advanced Analytical Techniques.....	9
1.5. Thesis Outline and Structure.....	13
Chapter2 : Instrumentation.....	15
2.1. Dynamic Light Scattering (DLS)	15
2.2. Scanning Electron Microscopy (SEM).....	16
2.3. Transmission Electron Microscopy (TEM).....	18
2.4. Energy- Dispersive X-ray Spectroscopy (EDX)	18
2.5. Time of Flight Secondary Ion Mass Spectroscopy (ToF-SIMS)	20
2.6. Fluorescence Spectroscopy.....	21
2.7. Raman Spectroscopy.....	23
2.7.1. Principles of Raman Spectroscopy	23
2.7.2. Raman Microscopy	25
2.7.3. Raman Mapping	27
2.7.4. Data Analysis	27
Chapter3 : Fabrication and Characterisation of Electrospun Particle-Fibre Hybrid Structures	30
3.1. Introduction	30

3.1.1. Electrospinning Process	30
3.1.2. Silica Nanoparticles	32
3.1.3. Fabrication of Nanoparticle–Electrospun Fibre Hybrids.....	35
3.1.4. Super-Resolution Fluorescence Microscopy: Potential Application of Particle-Fibre Hybrid Structure	37
3.2. Motivation and Aim	40
3.3. Materials and Methods.....	42
3.3.1. Materials	42
3.3.2. Plain Silica Particles Preparation: Changing NH ₄ OH and TEOS Concentration	42
3.3.3. Fluorescent Silica Nanoparticle Preparation.....	43
3.3.4. Preparation of Silica-PVC Hybrids	44
3.3.5. Analytical Characterisations.....	45
3.3.5.1. Dynamic Light Scattering (DLS)	45
3.3.5.2. Transmission Electron Microscopy (TEM).....	45
3.3.5.3. Scanning Electron Microscopy (SEM).....	46
3.3.5.4. Transmission Electron Microscopy/ Energy dispersive X-ray (TEM/EDX) Analysis.....	46
3.3.5.5. Raman Spectroscopy.....	46
3.3.5.6. Time of Flight Secondary Ion Mass Spectroscopy (ToF-SIMS)	47
3.3.5.7. Super-Resolution Fluorescence Microscopy.....	48
3.4. Results and Discussion	49
3.4.1. Synthesis and Characterisation of Size-Tuneable Plain Silica Nanoparticles	49
3.4.1.1. Effect of Ammonium Hydroxide (NH ₄ OH) Volume on Nanoparticle Size	50
3.4.1.2. Effect of TEOS Volume and Seed Growth Technique on Nanoparticle Size	53
3.4.2. Synthesis and Characterisation of Fluorescent Silica Nanoparticles	56
3.4.3. Fabrication of Particle-Fibre Hybrid using Colloidal Electrospinning Technique.....	58

3.4.3.1. Optimising PVC Electrospun Fibres	58
3.4.3.2. Incorporation of Silica Nanoparticles into Electrospun PVC Fibres	60
3.4.4. Advanced Characterisation of Particle-Fibre Hybrids	64
3.4.4.1. Transmission Electron Microscopy/Energy Dispersive X-ray Spectroscopy	64
3.4.4.2. Raman Spectroscopy.....	66
3.4.4.3. Time of Flight Secondary Ion Mass Spectroscopy.....	67
3.4.4.4. Super-Resolution Fluorescence Microscopy.....	71
3.4.5. Summary of the Results and Discussion	75
3.5. Conclusion.....	79
Chapter4 : Investigation of Salt Disproportionation using <i>In-Situ</i> Optical Imaging	80
4.1. Introduction	80
4.1.1. Pharmaceutical Salts	80
4.1.2. pH-Solubility Profile and pH_{max}	82
4.1.3. Salt Disproportionation.....	88
4.1.3.1. What is Salt Disproportionation?.....	88
4.1.3.2. Salt Disproportionation during Storage: Role of Excipients.....	92
4.1.4. Solid State Excipient Compatibility Testing.....	94
4.1.5. Advanced Analytical Techniques.....	95
4.2. Motivation and the Aim	98
4.3. Materials and Methods.....	102
4.3.1. Materials	102
4.3.2. Formulation and Binary Mixture Preparation.....	103
4.3.3. APIs and Excipients Characterisations	103
4.3.3.1. Measurement of the Microenvironment pH	103
4.3.3.2. Scanning Electron Microscopy (SEM).....	104

4.3.3.3. Raman Spectroscopy.....	104
4.3.4. Optical Screening Control Humidity System.....	105
4.4. Results and Discussion.....	107
4.4.1. Slurry pH Values of Excipients.....	107
4.4.2. Salt Disproportionation in Solid-State during Storage.....	108
4.4.2.1. Identification of the Salt and Free Form.....	110
4.4.2.2. The Impact of Relative Humidity on Salt Disproportionation in Solid State.....	114
4.4.2.3. The Effect of Excipient on Salt Disproportionation in Solid State.....	117
4.4.2.3.1. Citric Acid Monohydrate.....	118
4.4.2.3.2. Ascorbic Acid.....	121
4.4.2.3.3. Stearic Acid.....	123
4.4.2.3.4. Croscarmellose Sodium (AC-DI-SOL).....	125
4.4.2.3.5. Sodium Starch Glycolate.....	128
4.4.2.3.6. Lactose Monohydrate.....	128
4.4.2.3.7. Hydroxypropyl Methylcellulose (HPMC).....	130
4.4.2.3.8. Microcrystalline Cellulose (MCC).....	133
4.4.2.3.9. Calcium Phosphate Dibasic.....	134
4.4.2.3.10. Magnesium Stearate.....	135
4.4.2.3.11. Sodium Phosphate Dibasic.....	137
4.4.2.3.12. Sodium Stearyl Fumarate.....	139
4.4.3. Results and Discussion Summary.....	141
4.5. Conclusion.....	143
Chapter5 : The Effect of Excipients on Salt Disproportionation during Dissolution: Novel Application of <i>In-Situ</i> Raman Imaging.....	145
5.1. Introduction.....	145

5.1.1. Salt Disproportionation during Dissolution	146
5.1.2. Advanced Analytical Techniques & Mitigation Strategies:	148
5.2. Motivation and the Aim	151
5.3. Materials and Methods.....	154
5.3.1. Materials	154
5.3.2. Formulation and Tablet Preparation.....	155
5.3.3. Buffer Preparation:	157
5.3.4. Raman Spectroscopy.....	157
5.3.5. Raman Ultraviolet-Visible Flow Cell System	158
5.3.6. Post-Dissolution Analysis:	161
5.4. Results and Discussion	163
5.4.1. Pioglitazone HCl: Free Base Case Study	163
5.4.1.1. Dry Pure Material Spectra.....	163
5.4.1.2. Dissolution Experiments	164
5.4.1.2.1. The Effect of the Buffer pH	164
5.4.1.2.2. The Effect of the Excipients.....	173
5.4.1.2.2.1. Formulation A-Pioglitazone HCl: Citric Acid	173
5.4.1.2.2.2. Formulation B-Pioglitazone HCl: Lactose Monohydrate	180
5.4.1.2.2.3. Formulation C-Pioglitazone HCl: Magnesium Stearate.....	184
5.4.1.2.2.4. Dissolution Profile: Ultraviolet-Visible Data.....	193
5.4.2. Ibuprofen Sodium: Free Acid Case Study.....	196
5.4.2.1. Dry Pure Material Spectra.....	196
5.4.2.2. Dissolution Experiments	198
5.4.2.2.1. The Effect of the Buffer pH	198
5.4.2.2.2. The Effect of the Excipients.....	203

5.4.2.2.2.1.	Formulation E-Ibuprofen Sodium: Sodium Phosphate Dibasic.....	204
5.4.2.2.2.2.	Formulation G-Ibuprofen sodium: Microcrystalline Cellulose.....	207
5.4.2.2.2.3.	Formulation H-Ibuprofen Sodium: Stearic Acid	211
5.4.2.2.2.4.	Dissolution Profile: Ultraviolet-Visible Data.....	217
5.4.3.	Results and Discussion Summary.....	220
5.5.	Conclusion:.....	222
Chapter6 :	Conclusions and Future Works.....	224
6.1.	Summary:.....	224
6.2.	Future Work.....	229
References.....		232

List of Tables

Table 1.1: Characterisation techniques commonly used for solid-state analysis of pharmaceuticals. Adapted from the References [28], [35]–[39].....	10
Table 4.1: Classification of acids and bases according to their pKa.....	82
Table 4.3: Summary of the selected excipients role and chemical structures.	100
Table 4.4: Excipients microenvironment pH measured by the slurry pH method.	108
Table 5.1: Summary of excipients used in the binary mixture tablets.	153
Table 5.2: Pioglitazone HCl formulations compositions, excipients role and the mixture weight ratio of each formulation.	156
Table 5.3: Ibuprofen sodium formulations compositions, excipients role and the mixture weight ratio of each formulation.	156

List of Figures

Figure 1.1: Schematic representation of different types of drug form of active pharmaceutical ingredients [15].	3
Figure 1.2: Schematic representation of the process of formulating a drug through proof-of-concept studies (including toxicology evaluation) to the marketed formulation [15].	5
Figure 2.1: Fluctuations in the intensity of scattered light due to the motion of dispersed particles.	16
Figure 2.2: Diagram illustrating the possible interactions of electrons with the sample.	17
Figure 2.3: Diagram showing the principle of EDX. The process through which X-rays are emitted when an electron shell is bombarded by incident electrons.	19
Figure 2.4: Schematic representation of a ToF-SIMS instrument [44].	21
Figure 2.5: The Jablonski energy diagram shows the process of light absorption and emission [57].	22
Figure 2.6: Schematic representation of the energy levels changes in Infrared (IR), near-IR, Rayleigh scattering, Raman scattering and fluorescence [69].	24
Figure 2.7: Standard configuration of a confocal Raman microscopy [71].	26
Figure 2.8: Examples of common constraints used in MCR. (A) non-negativity, (B) unimodality, (C) closure. Bold black profiles on the left plots are unconstrained. Red profiles on the right are profiles that have been constrained [85].	29
Figure 3.1: Experimental set-up of the electrospinning technique.	31
Figure 3.2: Synthesis of silica nanoparticles by the Stöber method.	33
Figure 3.3: Chemical reaction scheme for (A) the conjugation of amino-silane precursor (APTES) to succinimidyl ester derivative of a fluorophore (●) to produce fluorophore-APTES conjugate (B) The synthesis of fluorescent silica nanoparticles.	34
Figure 3.4: Chemical structure of Oregon Green® 488 (OG), 5-(and-6)-carboxyfluorescein (FAM), 5-(and-6)- carboxytetramethylrhodamine (TAMRA) and Alexa 647.	35

Figure 3.5: Representative photo switching mechanisms of fluorescent Alexa 647 molecule [163], [166].
..... 38

Figure 3.6: Experimental set-up for silica particle preparation. 43

Figure 3.7: The effect of ammonium hydroxide volumes on mean particle diameter measured by (A) DLS and (B) TEM; n=3. 51

Figure 3.8: (A) Comparison of mean particle size for silica nanoparticles measured by DLS (Green line) and TEM (Blue line). (B): A picture of nanoparticle suspension vials with different ammonium hydroxide volumes. 51

Figure 3.9: TEM images of size-controllable silica particles produced using different amounts of NH₄OH.
..... 52

Figure 3.10: The effect of increasing TEOS amount on silica mean particle size measured by DLS; n=3... 54

Figure 3.11: Particle size distribution (Left column) and TEM images (Right column) of silica particles prepared by seed growth technique: (A) NH₄OH volume = 2.0 ml (B) NH₄OH volume = 3.0 ml (C) NH₄OH volume = 4.0 ml (D) NH₄OH volume = 5.0 ml. Particle size distribution and median particle diameter obtained from TEM images using ImageJ. White Scale Bar= 1000 nm/ Red Scale Bar= 2000 nm 55

Figure 3.12: (A) The mean particle diameter (error bar= SED) of different fluorophore silica nanoparticles measured by DLS; n=3 (B): A picture of particle suspension vials with different fluorophore dye. (C): Representative TEM image of Alexa 647 silica nanoparticles (Scale bar=1000nm). 57

Figure 3.13: Effect of electrospinning parameters on PVC fibre morphology and diameter. Representative SEM image of PVC fibres electrospun under (A) unoptimised and (B) optimised electrospinning conditions. Scale bar = 10 µm 59

Figure 3.14: The fibre size distribution of PVC scaffolds obtained from SEM images using ImageJ. (100 measurements) 60

Figure 3.15: The influence of < 100 nm silica particle concentration on the morphology of silica-PVC hybrids: Top: (A) TEM (B) SEM images of particle-fibre hybrids at silica particle concentration = 1% w/v- Bottom: (C) TEM (D) SEM images of particle-fibre hybrids at silica particle concentration= 5% w/v 61

Figure 3.16: The influence of ~200 nm silica particle concentration on the morphology of silica-PVC hybrids: Top: (A) TEM (B) SEM images of particle-fibre hybrids at silica particle concentration = 1% w/v- Bottom: (C) TEM (D) SEM images of particle-fibre hybrids at silica particle concentration = 5% w/v- The insets are magnified SEM images..... 62

Figure 3.17: The influence of silica nanoparticle size and concentration on the morphology of silica-PVC hybrids: At silica particle concentration = 1% w/v: TEM and SEM images of particle-fibre hybrids prepared using ~ 400 nm (A&B) and ~700 nm (E&F) silica nanoparticles. At silica particle concentration = 5% w/v: TEM and SEM images of particle-fibre hybrids prepared using ~ 400 nm (C&D) and ~700 nm (G&H). The insets are magnified TEM images..... 63

Figure 3.18: STEM-EDX elemental mapping of particle-fibre hybrid. (A) High-angle annular dark-field imaging (HAADF) STEM image; (B) Silicon map (Blue); (C) Oxygen map (Red), (D) Carbon map (Green); (E) Chlorine map (Purple) 65

Figure 3.19: Raman spectra of pure silica particles, plain PVC fibres and silica-PVC hybrids over the range of 100 cm⁻¹ to 3400 cm⁻¹..... 67

Figure 3.20: (A) Optical image of the particle-fibre hybrids deposited on TEM finder grids. (B-D) ToF-SIMS intensity maps for the surface of particle-fibre hybrids, PVC only fibres and silica nanoparticles. Row (B) shows the results of the total intensity signal. Rows (C) and (D) show negative polarity images of Cl⁻ and SiO₂⁻, respectively. Row (E) shows the negative polarity image of Au⁻ characterising the frame of the TEM gold grid. Scanned area= 150 ×150 μm..... 69

Figure 3.21: (A) Optical image of the particle-fibre hybrids deposited on TEM finder grids. (B-D) ToF-SIMS intensity maps for the surface of particle-fibre hybrids, PVC only fibres and silica nanoparticles. Row (B) shows the results of the total intensity signal. Rows (C) and (D) show negative polarity images of Cl⁻ and

SiO₂⁻, respectively. Row (E) shows the negative polarity image of Au⁻ characterising the frame of the TEM gold grid. Scanned area= 50 × 50 μm. 70

Figure 3.22: (A&D) Bright field image, (B&E) wide field image and (C&F) super-resolution image of the same region of particle-fibre hybrid systems mounted with PVC/glycerol medium. (G) The measured circumferences of a single nanoparticle 73

Figure 3.23: (A&D) Bright field image, (B&E) wide field image and (C&F) super-resolution image of the same region of particle-fibre hybrid systems mounted with water. (G) The measured circumferences of a single nanoparticle 74

Figure 3.24: Size distribution histogram of the resulting silica particles batches (Size range 20-650 nm) 75

Figure 3.25: Morphologies obtained under different particle sizes and concentrations via colloidal electrospinning of particles and polymer solutions. 76

Figure 3.26: Summary (A) diagram and (B) table of the detection capabilities of the advanced analytical techniques used to investigate the particle-fibre hybrid systems. 78

Figure 4.1: Schematic representation of the pH-solubility profile of an acidic drug presenting the pH_{max} point and indicating that the solubility may be expressed by two independent regions[29]. 84

Figure 4.2: Schematic representation of the pH-solubility profile of a basic drug presenting the pH_{max} point and indicating that the solubility may be expressed by two independent regions[29]. 86

Figure 4.3: Effects of (A) pKa, (B) S₀ and (C) K_{sp} on pH_{max} (Adapted from Ref [220]). 87

Figure 4.4: Chemical structure of Pioglitazone HCl salt and Ibuprofen sodium salt..... 100

Figure 4.5: (A) Schematic diagram of the optical screening-controlled humidity system. (B) Front view of the humidity control unit and the stage-top humidity chamber. (C) Humidity chamber..... 106

Figure 4.6: Mechanism of the salt disproportionation reaction of Pioglitazone HCl at pH > pH_{max}. 109

Figure 4.7: Mechanism of the salt disproportionation reaction of Ibuprofen sodium at pH < pH_{max}. 109

Figure 4.8: Microscopic images of Pioglitazone salt and free-form as received material: A & C: optical microscopic image of Pioglitazone HCl and Pioglitazone free base, respectively; B & D: SEM images of Pioglitazone HCl and Pioglitazone free base, respectively..... 111

Figure 4.9: Raman spectra of Pioglitazone HCl salt and Pioglitazone free base as received material over the range 1200 cm^{-1} to 1800 cm^{-1} 112

Figure 4.10: Microscopic images of Ibuprofen salt and free-form as received material: A & C: optical microscopic image of Ibuprofen sodium and Ibuprofen free acid, respectively; B & D: SEM images of Ibuprofen sodium and Ibuprofen free acid, respectively..... 113

Figure 4.11: Raman spectra of Ibuprofen sodium salt and Ibuprofen free acid form over the range 200 cm^{-1} to 1500 cm^{-1} 114

Figure 4.12: *In situ* optical microscopy images of Pioglitazone HCl crystal morphological variation during salt disproportionation stored at 75-90% RH: (A) Start (B) 2.5 min (C) 5.0 min (D) 10 min. Scale bar for images is 100 μm 115

Figure 4.13: Raman spectra (100 to 4000 cm^{-1}) of Pioglitazone HCl (Blue spectra), Pioglitazone free base (red spectra) and Pioglitazone HCl after incubation in 75-90% RH. Y-axis offsets were applied for presentational purposes. 116

Figure 4.14: *In situ* optical microscopy images of Ibuprofen sodium crystal dissolution during the storage at 75-90% RH: (A) Start (B) 0.5 min (C) 1.0 min (D) 1.5 min. Scale bar for images is 100 μm 117

Figure 4.15: *In situ* optical microscopy images of Pioglitazone HCl crystal mixed with citric acid during storage at 75-90% RH: (A) Start (B) 10 min. Scale bar for images is 100 μm 119

Figure 4.16: *In situ* optical microscopy images of Ibuprofen crystals mixed with citric acid during storage at 75-90% RH: (A) Start (B) 2.5 min (C) 5.0 min (D) 10 min. Scale bar for images is 100 μm 120

Figure 4.17: Raman spectra (200 to 1500 cm^{-1}) of Ibuprofen sodium (Blue spectra), Ibuprofen free acid (red spectra) and Ibuprofen sodium after incubation in 75-90% RH with citric acid monohydrate. Y-axis offsets were applied for presentational purposes. 121

Figure 4.18: *In situ* optical microscopy images of Pioglitazone HCl crystal mixed with ascorbic acid during storage at 75-90% RH: (A) Start (B) 2.5 min (C) 3.0 min and (D) 3.5 min. Scale bar for images is 100 μm .
..... 122

Figure 4.19: *In situ* optical microscopy images of Pioglitazone HCl crystal (Orange arrow) mixed with stearic acid during storage at 75-90% RH: (A) Start (B) 5 min. Scale bar for images is 100 μm 123

Figure 4.20: *In situ* optical microscopy images of Ibuprofen crystals mixed with stearic acid during storage at 75-90% RH: (A) Start (B) 1.0 min (C) 2.0 min (D) 3.0 min. Scale bar for images is 100 μm 125

Figure 4.21: *In situ* optical microscopy images of Pioglitazone HCl crystal (Orange arrow) mixed with croscarmellose sodium during storage at 75-90% RH: (A) Start (B) 10 min (C) 20 min (D) 40 min. Scale bar for images is 200 μm 127

Figure 4.22: *In situ* optical microscopy images of Pioglitazone HCl crystals (Orange arrows) mixed with lactose monohydrate during storage at 75-90% RH: (A) Start (B) 2.5 min (C) 5.0 min (D) 7.5 min. Scale bar for images is 100 μm 129

Figure 4.23: *In situ* optical microscopy images of Pioglitazone HCl crystals (Orange arrows) mixed with hydroxypropyl methylcellulose (HPMC) during storage at 75-90% RH: (A) Start (B) 3.5 min (C) 5.0 min (D) 10 min. Scale bar for images is 100 μm 132

Figure 4.24: *In situ* optical microscopy images of Ibuprofen sodium crystals (Orange arrows) mixed with hydroxypropyl methylcellulose (HPMC) during storage at 75-90% RH: (A) Start (B) 2.5 min (C) 5.0 min (D) 10 min. Scale bar for images is 100 μm 133

Figure 4.25: *In situ* optical microscopy images of Ibuprofen sodium crystals (Orange arrows) mixed with microcrystalline cellulose (MCC) during storage at 75-90% RH: (A) Start (B) 3.5 min (C) 5.0 min (D) 10 min. Scale bar for images is 100 μm 134

Figure 4.26: *In situ* optical microscopy images of Pioglitazone HCl crystal (Orange arrow) mixed with magnesium stearate during storage at 75-90% RH: (A) Start (B) 5.0min (C) 10 min (D) 15 min. Scale bar for images is 100 μm 137

Figure 4.27: *In situ* optical microscopy images of Pioglitazone HCl crystal (Orange arrow) mixed with sodium phosphate dibasic during storage at 75-90% RH: (A) Start (B) 1.0min (C) 2.0 min (D) 5.0 min. Scale bar for images is 100 μm 138

Figure 4.28: *In situ* optical microscopy images of Pioglitazone HCl crystal (Orange arrow) mixed with sodium stearyl fumarate during storage at 75-90% RH: (A) Start (B) 5.0min (C) 10 min (D) 15 min. Scale bar for images is 100 μm 140

Figure 5.1: Diffusion layer model for drug dissolution. 147

Figure 5.2: Photographic image of the 100 mg (Left) and 50 mg (Right) tablets..... 157

Figure 5.3: (A) Schematic diagram of the Raman Ultraviolet-Visible Flow Cell System. (B) Front view of the flow-cell under the Raman spectroscopy objective. (C) Top view of the tablet placed inside the flow-cell. 159

Figure 5.4: Raman spectra of Pioglitazone HCl salt, Pioglitazone free base and excipients used in formulations over the range 1200 cm^{-1} to 1800 cm^{-1} 164

Figure 5.5: Averaged Raman spectra (1200 to 1800 cm^{-1}) of the dissolution of the pure Pioglitazone HCl tablet in the acidic buffer. Y-axis offsets were applied for presentational purposes. 165

Figure 5.6: Raman maps of the pure Pioglitazone HCl tablet during dissolution in the acidic buffer as a function of time, generated by (a) MCR analysis (b) CLS analysis..... 167

Figure 5.7: Averaged Raman spectra (1200 to 1800 cm^{-1}) of the dissolution of the pure Pioglitazone HCl tablet in the basic buffer. Y-axis offsets were applied for presentational purposes. 169

Figure 5.8: Raman maps of the pure Pioglitazone HCl tablet during dissolution in the basic buffer as a function of time, generated by (a) MCR analysis (b) CLS analysis..... 171

Figure 5.9: Optical image and Raman maps of the pure Pioglitazone HCl cross-sectioned tablet after dissolution in the basic buffer generated by CLS fittings. 172

Figure 5.10: Averaged Raman spectra (1200 to 1800 cm^{-1}) of the dissolution of formulation A (Pio HCl: Citric Acid) tablet in the acidic buffer. Y-axis offsets were applied for presentational purposes..... 174

Figure 5.11: Raman maps of formulation A tablet (Pio HCl: Citric Acid) during dissolution in the acidic buffer as a function of time, generated by (a) MCR analysis (b) CLS analysis.	175
Figure 5.12: Averaged Raman spectra (1200 to 1800 cm^{-1}) of the dissolution of formulation A (Pio HCl: Citric Acid) tablet in the basic buffer. Y-axis offsets were applied for presentational purposes.....	177
Figure 5.13: Raman maps of formulation A tablet (Pio HCl: Citric Acid) during dissolution in the basic buffer as a function of time, generated by (a) MCR analysis (b) CLS analysis.	178
Figure 5.14: Optical image and Raman maps of the formulation A (Pio HCl: Citric Acid) cross-sectioned tablet after dissolution in the basic buffer generated by CLS fittings.....	179
Figure 5.15: Averaged Raman spectra (1200 to 1800 cm^{-1}) of the dissolution of formulation B (Pio HCl: LM) tablet in the acidic buffer. Y-axis offsets were applied for presentational purposes.	181
Figure 5.16: Raman maps of formulation B tablet (Pio HCl: LM) during dissolution in the acidic buffer as a function of time, generated by MCR analysis.	182
Figure 5.17: Raman maps of formulation B tablet (Pio HCl: LM) during dissolution in the acidic buffer as a function of time, generated by CLS analysis.	183
Figure 5.18: Averaged Raman spectra (1200 to 1800 cm^{-1}) of the dissolution of formulation C (Pio HCl: MgSt) tablet in the acidic buffer. Y-axis offsets were applied for presentational purposes.....	186
Figure 5.19: Raman maps of formulation C tablet (Pio HCl: MgSt) during dissolution in the acidic buffer as a function of time, generated by MCR analysis.	187
Figure 5.20: Raman maps of formulation C tablet (Pio HCl: MgSt) during dissolution in the acidic buffer as a function of time, generated by CLS analysis.	188
Figure 5.21: Optical image and Raman maps of the formulation C (Pio HCl: MgSt) cross-sectioned tablet after dissolution in the acidic buffer generated by CLS fittings.	189
Figure 5.22: Averaged Raman spectra (1200 to 1800 cm^{-1}) of the dissolution of formulation C (Pio HCl: MgSt) tablet in the basic buffer. Y-axis offsets were applied for presentational purposes.....	190

Figure 5.23: Raman maps of formulation C tablet (Pio HCl: MgSt) during dissolution in the basic buffer as a function of time, generated by MCR analysis. 191

Figure 5.24: Optical image and Raman maps of the formulation C (Pio HCl: MgSt) cross-sectioned tablet after dissolution in the basic buffer generated by CLS fittings. 192

Figure 5.25:(A) Dissolution profiles obtained using UV-Vis detection that presents the percentage of Pioglitazone HCl released from the tablet as a function of time for the pure drug and different formulation tablets studied in the acidic medium. (B) The maximum drug release percentage. 194

Figure 5.26: (A) Dissolution profiles obtained using UV-Vis detection that presents the percentage of Pioglitazone HCl released from the tablet as a function of time for the pure drug and different formulation tablets studied in the basic medium. (B) The maximum drug release percentage. 195

Figure 5.27: Raman spectra of Ibuprofen sodium salt and Ibuprofen free acid form over the range 200 cm^{-1} to 1500 cm^{-1} 197

Figure 5.28: Raman spectra of Ibuprofen sodium salt, Ibuprofen free acid and excipients used in formulations over the range 700 cm^{-1} to 1500 cm^{-1} 198

Figure 5.29: Averaged Raman spectra (900 to 1600 cm^{-1}) of the dissolution of the pure Ibuprofen sodium tablet in the acidic buffer. Y-axis offsets were applied for presentational purposes. 199

Figure 5.30: Raman maps of the pure Ibuprofen sodium tablet during dissolution in the acidic buffer as a function of time, generated by (a) MCR analysis (b) CLS analysis..... 201

Figure 5.31: Averaged Raman spectra (900 to 1600 cm^{-1}) of the dissolution of the pure Ibuprofen sodium tablet in the basic buffer. Y-axis offsets were applied for presentational purposes. 202

Figure 5.32: Raman maps of the pure Ibuprofen sodium tablet during dissolution in the basic buffer as a function of time, generated by (a) MCR analysis (b) CLS analysis..... 203

Figure 5.33: Averaged Raman spectra (800 to 1500 cm^{-1}) of the dissolution of formulation E (Ibu Na: NPD) tablet in the acidic buffer. Y-axis offsets were applied for presentational purposes. 205

Figure 5.34: Raman maps of formulation E (Ibu Na: NPD) tablet during dissolution in the acidic buffer as a function of time, generated by MCR analysis. 206

Figure 5.35: Raman maps of formulation E (Ibu Na: NPD) tablet during dissolution in the acidic buffer as a function of time, generated by CLS analysis. 207

Figure 5.36: Averaged Raman spectra (400 to 1100 cm^{-1}) of the dissolution of the formulation G (Ibu Na: MCC) tablet in the acidic buffer. Y-axis offsets were applied for presentational purposes. 208

Figure 5.37: Raman maps of the formulation G (Ibu Na: MCC) tablet during dissolution in the acidic buffer as a function of time, generated by MCR analysis. 210

Figure 5.38: Averaged Raman spectra (900 to 1600 cm^{-1}) of the dissolution of formulation H (Ibu Na: SA) tablet in the acidic buffer. Y-axis offsets were applied for presentational purposes. 212

Figure 5.39: Raman maps of the formulation H (Ibu Na: SA) tablet during dissolution in the acidic buffer as a function of time, generated by MCR analysis. 213

Figure 5.40: Averaged Raman spectra (900 to 1600 cm^{-1}) of the dissolution of formulation H (Ibu Na: SA) tablet in the basic buffer. Y-axis offsets were applied for presentational purposes. 215

Figure 5.41: Raman maps of the formulation H (Ibu Na: SA) tablet during dissolution in the basic buffer as a function of time, generated by (a) MCR analysis and (b) CLS. 216

Figure 5.42: (A) Dissolution profiles obtained using UV-Vis detection that presents the percentage of Ibuprofen released from the tablet as a function of time for the pure drug and different formulation tablets studied in the acidic medium. (B) The maximum drug release percentage. 218

Figure 5.43: (A) Dissolution profiles obtained using UV-Vis detection that presents the percentage of Ibuprofen released from the tablet as a function of time for the pure drug and different formulation tablets studied in the basic medium. (B) The maximum drug release percentage. 219

List of Abbreviations

AIDS	Acquired Immune Deficiency Syndrome
API	Active Pharmaceutical Ingredient
APTES	3-aminopropyltriethoxysilane
CCD	Charge-Coupled Device
CCNa	Croscarmellose Sodium
CLS	Classical Least Square
C_{max}	Maximum Drug Concentration
CPD	Calcium Phosphate Dibasic
DLS	Dynamic Light Scattering
DMF	Dimethylformamide
DSC	Differential Scanning Calorimetry
EDS	Energy-Dispersive X-ray Spectroscopy
EDX	Energy-Dispersive X-ray
EM	Electron Microscopy
FDA	Food and Drug Administration
GI	Gastrointestinal
GSK	GlaxoSmithKline
HAADF	High Angle Annular Dark Field
HCl	Hydrochloride
HIV	Human Immunodeficiency Virus
HPLC	High-Performance Liquid Chromatography
hr	Hour
Ibu Na	Ibuprofen Sodium
IR	Infrared
K_a	Dissociation Constant
Kv	Kilovolt
LM	Lactose Monohydrate
M	Molar Concentration
m/z	Mass /Charge
mA	Milliampere
MCC	Microcrystalline Cellulose
MCR-ALS	Multivariate Curve Resolution-Alternating Least Squares

MgSt	Magnesium Stearate
min	Minute
MS	Mass Spectroscopy
mW	Milliwatt
Mw	Molecular Weight
Na	Sodium
NH₄OH	Ammonium Hydroxide
NHS	N-Hydroxysuccinimide
nm	Nanometre
NPD	Sodium Phosphate Dibasic
PCL	Polycaprolactone
PDI	PolyDispersity Index
pH_{max}	pH of maximum solubility
Pio HCl	Pioglitazone Hydrochloride
PLA	Polylactic Acid
PLGA	Poly lactide-co-Glycolide
PLM	Polarised Light Microscopy
PPI	Proton Pump Inhibitor
PSF	Point Spread Function
PVC	Polyvinyl Chloride
PVM	Particle Vision and Measurement
R&D	Research and Development
RH	Relative Humidity
rpm	Round per Minute
SA	Stearic Acid
SED	Standard Error Deviation
SEM	Scanning Electron Microscopy
SMPT	Solution-Mediated Phase Transformation
SNPs	Silica Nanoparticles
SSF	Sodium Stearyl Fumarate
SSG	Sodium Starch Glycolate
SS-NMR	Solid-State Nuclear Magnetic Resonance
STEM	Scanning Transmission Electron Microscopy
STORM	Stochastic Optical Reconstruction Microscopy
TEM	Transmission Electron Microscopy

TEOS	Tetraethyl Orthosilicate
TGA	Thermal Gravimetric Analysis
THF	Tetrahydrofuran
ToF-SIMS	Time of Flight Secondary Ion Mass Spectroscopy
TSPd	Tribasic Sodium Phosphate dodecahydrate
UV-Vis	Ultraviolet-Visible Spectroscopy
XRPD	X-ray Powder Diffractometer
°C	Celsius Degree
μm	Micrometre

Chapter1: General Introduction

1.1. Pharmaceutical Drug Development

The pharmaceutical drug development is a several steps process that involves taking a new drug from concept to the clinic and eventually to commercialisation [1]. The average cost of the drug development process from drug discovery to the market through preclinical testing, formulation and manufacturing evaluations, and the extensive clinical programme is estimated to exceed £1.2 billion per one compound [2]. The average time span for this process is 10-15 years, and the success rate is one in five thousand compounds reaching the market [3]. Given these alarming statistics, the pharmaceutical industry is actively seeking to streamline the drug development process [4], [5]. Without efficient strategies to screen, identify and optimise new compounds for development, the pharmaceutical industry cannot sustain innovation and drug development especially with the recent spate of successful drug patent expirations and subsequent generic competition for blockbuster drugs [6]–[10]. The key to tackle this problem is to significantly increase the number and quality of cost-effective, innovative new medicines in development and managing them through the high-risk drug development process while controlling the research and development (R&D) costs [11].

In order to reduce the risk of the drug development process, pharmaceutical companies set strict criteria for progressing drugs through the development process with a clear 'go' or 'stop' decision point for each drug as it completes each development milestone. A stop decision on progressing drugs can be based on a few reasons such as discouraging results from preclinical studies, an intolerable clinical safety profile, low bioavailability and manufacturing and

formulation problems [12]–[14]. According to Jean-Paul Garnier, CEO of GlaxoSmithKline (GSK), more than 50% of the compounds that enter clinical trials fizzle due to efficacy and safety concerns; the other 40% fail due to patent concerns and physicochemical characteristic issues such as solubility and drug interactions [15]. In fact, the consequences of poor physical and chemical properties on drug discovery are merely the tip of the iceberg. Inadequate understanding and poor control over pharmaceutical properties are at the root of dropping pharmaceutical industry productivity that delays new drug approvals by regulatory agencies and thus, increasing the cost of developing new drugs [15], [16]. These issues support the claim that the pharmaceutical industry is years behind other industries in developing novel technologies in its manufacturing sites [17], [18].

1.2. Form and Formulation

The efficacy of an active pharmaceutical ingredient (API) is determined by its chemical structure and how it interacts with its targets such as receptors or enzymes. However, the physicochemical properties of the compound in the solid state largely controls the ability to deliver the drug to the patient in a safe, efficacious and cost-effective manner. The API can exist in different solid forms depending on the functional groups in its chemical structure and the three-dimensional structure of the molecule. The API can be produced in different crystalline states, some of which are polymorphic forms of the parent moiety. Other drugs are multicomponent crystalline forms of complexes of the drug and ions or molecules such as salts, hydrates, solvates or co-crystals [19]. Some drugs are difficult to crystallise and thus invariably exist as amorphous solids such as peptides and proteins [19]. A summary of the different types of form of API is illustrated in Figure 1.1.

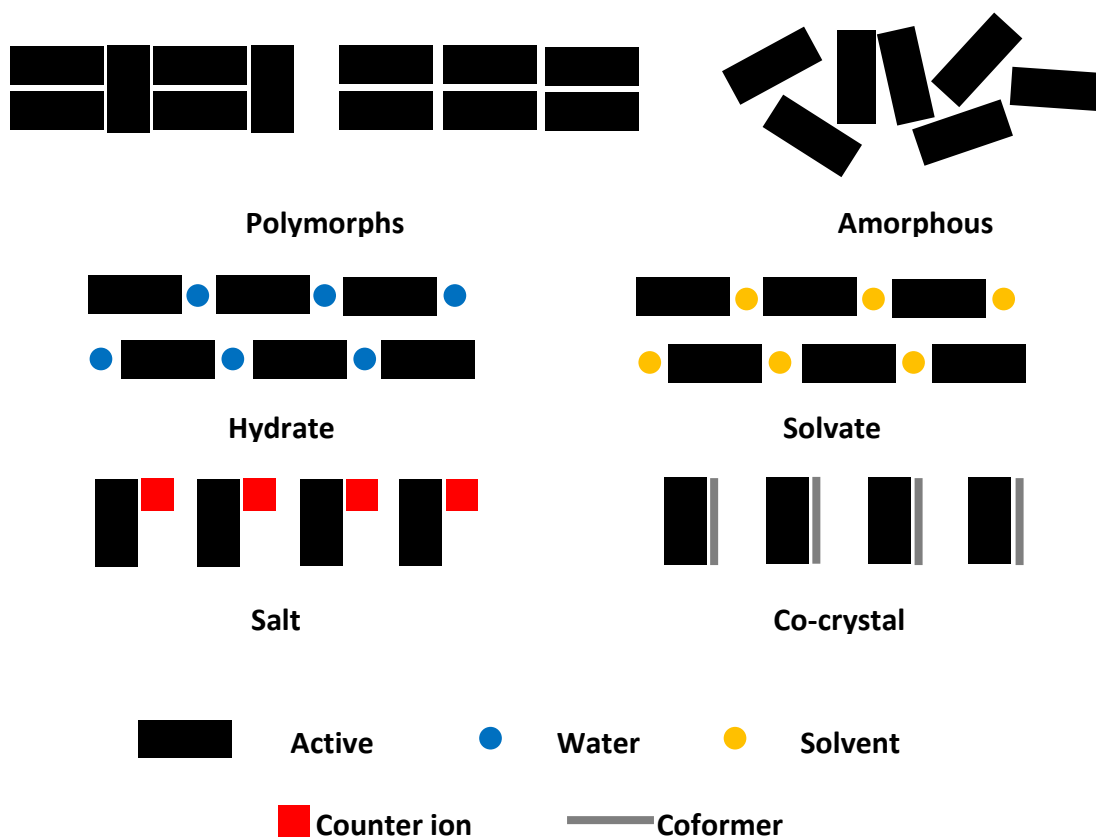


Figure 1.1: Schematic representation of different types of drug form of active pharmaceutical ingredients [15].

These various forms of API can have different physical and chemical properties that result in a different performance regarding chemical and physical stability, as well as solubility and dissolution rate. These critical characteristics can significantly influence how a drug molecule should be stored, formulated and delivered to the patient. Some well-known case studies can demonstrate the influence of the pharmaceutical form on final drug product stability and performance. The oral statin drug, Atorvastatin, developed by Pfizer (Lipitor™) was formulated as an amorphous drug during the development stage. During Phase III clinical studies, it was reported that the amorphous drug re-crystallised and some properties have changed. Additional studies were conducted to show that the performance and stability of the new form were relative to that used in the development phase. Conversion of the amorphous form to the crystalline form results typically in decreased solubility that negatively impacts the dissolution performance of the

drug [15]. In another case study, the crystalline free base form of indinavir, HIV protease inhibitor, was initially studied in human. The drug showed good performance with patients exhibiting normal gastric acidity, however, due to the pH-dependent solubility of the drug, poor oral bioavailability was noticed in patients with “Achlorhydria” or lack of hydrochloric acid in the stomach, a condition widely seen in HIV/AIDS patients. The preparation of stable sulphate salt/ethanolate allowed the progress of product development, which is now marketed by Merck as Crixivan™ [20]. Lastly, another HIV protease inhibitor was developed and launched by Abbott in 1996 with only one crystalline form of the API known to exist. After two years, the drug failed the food and drug administration (FDA) approved dissolution specification [21]. Abbott investigations demonstrated that the drug crystallised into two polymorphs, one of which is more stable however less soluble. Abbott decided to re-develop and re-launch the drug product in a new formulation of the more thermodynamically stable polymorph [21]. The previous cases demonstrated the consequences of incomplete physical form evaluation and the importance of that information to develop more stable and effective pharmaceutical products.

Formulation of a drug candidate is another crucial aspect of drug discovery. The current process of formulation, illustrated in Figure 1.2, aims to deliver the API in a formulation that has to meet specific criteria according to the stage at which the drug is evaluated. For example, in the early stages, it is essential to ensure drug exposure in preclinical studies and toxicology evaluation. Therefore, the drug bioavailability at this stage outweighs long-term stability properties. If the drug advances to a later stage, like phase III clinical trials, the processability and stability become more important.

At present, pharmaceutical companies invested insufficient efforts in assessing physicochemical properties of the drug and its formulation possibilities and limitations in early

stages of drug development. This could lead to fatal flaws in the drug candidate discovered at a later stage.

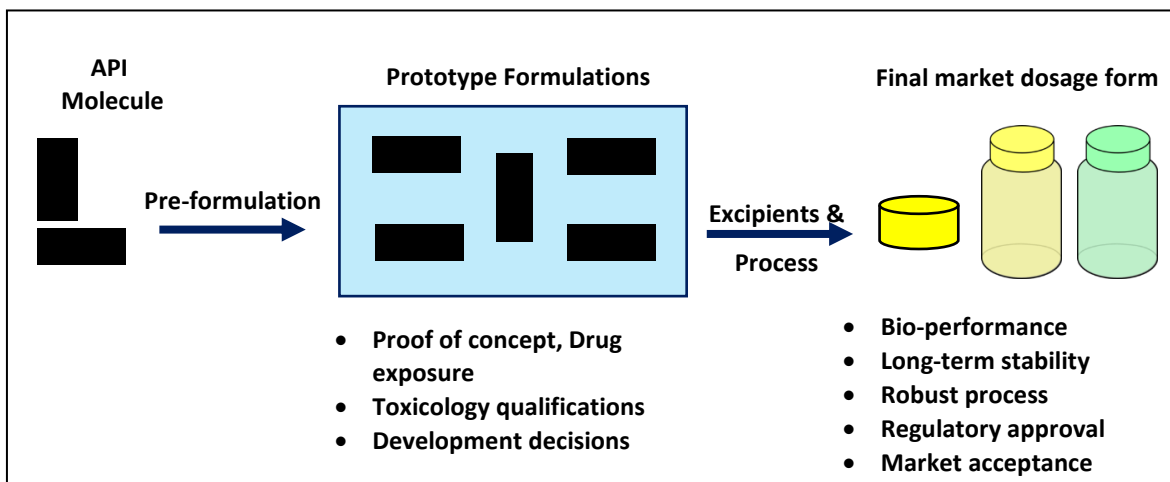


Figure 1.2: Schematic representation of the process of formulating a drug through proof-of-concept studies (including toxicology evaluation) to the marketed formulation [15].

The ability to optimise and consider collectively all criteria for developability at an early stage prevents or at least minimises downstream complications such as inadequate stability, low solubility or slow dissolution rate resulting in poor in-vivo performance. Therefore, getting the maximum amount of information about the physicochemical properties of the drug and its stability in the multicomponent formulation in the early discovery stage can help accelerate drug discovery and development processes and accordingly, an increased success rate.

1.3. Drug Stability in Pharmaceutical Dosage Forms

Drug stability is one of the critical quality and performance attributes that needs to be precisely evaluated during pharmaceutical development and controlled during clinical studies and marketing. Stability of pharmaceutical products refers to the capacity of the product or a given API to be maintained within established specifications of identity, performance, and purity during a specified time period under controlled conditions of temperature and relative humidity (RH)

[22]. Therefore, the stability testing investigates the impact of the environmental factors on the quality and performance of the API or a formulated product, predicates the product's shelf life and determines the proper storage conditions [23].

Even though temperature and humidity are the two main factors that usually affect the stability of the pharmaceutical product, other factors can also influence the stability of a pharmaceutical product and therefore increases the complexity of the stability testing. These factors include the stability of the active ingredient(s); interaction between the drugs and excipients, manufacturing process followed and environmental conditions (e.g. light, temperature and moisture) encountered during manufacturing, packaging, shipment, storage and handling [22].

Physical instability refers to changes in the characteristics of a drug product that do not involve chemical bond formation or breakage in the drug molecule's structure such as changes in appearance, taste, odour or polymorphic form; or phenomena such as crystallisation in amorphous systems [24]. Chemical instability, on the other hand, refers to changes in the chemical structure of the drug molecule in the dosage form [24]. Chemical degradation reactions like oxidation, reduction or hydrolysis, can play a critical role in the stability of a pharmaceutical product. These chemical reactions may lead to the formation of toxic degradation products, loss of activity of the API, poor performance of the final product and loss of excipient activity like preservative action and antioxidants [25].

Drug chemical degradation in crystalline solids is mostly mediated by moisture whereby water molecules involve directly in the reaction such as hydrolysis. In addition, the humidity may form a thin layer of solution on the solid crystal surface [26], leading to an increase in molecular mobility and reactivity that consequently enhances drug degradation [27]. Furthermore, drug

degradation complexity increases in multicomponent heterogeneous systems. Some commonly-used excipients are known to interact directly with some drug molecules such as Maillard reaction which is a reaction between a primary or secondary amine and a reducing sugar like lactose. In addition, excipients present in the formulation that possess acidic and basic functionalities may change the microenvironment pH around the solid drug particle and thus, increase the drug degradation. Drug oxidation has been linked to various impurities such as peroxide and metal ions that exist in some excipients [27].

Drug degradation, whether it is chemical or physical, usually leads to a phase transformation of the drug from a less stable state to a more stable state influenced by specific environmental conditions such as temperature, humidity and pH [28]. Solution-mediated phase transformation (SMPT) is a very common phase transformation, which involves the initial dissolution of the highly soluble metastable form creating a supersaturated solution. At this stage, nucleation and growth of the stable form are expected to occur [28]. Common examples of phase transformations include polymorphic conversion, amorphous-crystalline conversion and salt-to-parent form conversion. The solid phase transformation can potentially alter the quality attributes and performance behaviour of a drug product due to the difference in the physical and chemical properties among different solid forms [27].

The salt form of APIs may disproportionate, i.e. revert back to the less soluble unionised free form due to harsh manufacturing process conditions coupled with a possible reaction with formulation excipients [29]. Salt disproportionation can adversely affect the final product stability and performance such as loss of activity, slow dissolution and reduced bioavailability [30]–[32]. Disproportionation reactions are mainly observed during dissolution studies, where the salt endures phase transformation in the dissolution medium and then crystallise back to the less

soluble free form. However, salt disproportionation can also be observed in the solid state where the moisture (i.e. water layer) present at the API excipient interface facilitates the intermolecular interactions and consequently leads to salt disproportionation. Salt conversion to less soluble unionised free drug form has severe implications on final product stability and performance.

The impact of salt disproportionation on final product performance and drug bioavailability can be demonstrated in the following representative example. Prasugrel HCl, a platelet aggregation inhibitor, was approved by the FDA in 2009. The HCl salt was found to disproportionate back to the free base up to the extent of ~ 70% in the final product tablets [33]. FDA raised the following two concerns during the product review process-(i) the techniques used for manufacturing, processing and packaging were insufficient to preserve the drug identity, quality, stability, purity and bioavailability, (ii) the difference in the relative bioavailability of three batches have 5%, 58%, and 70% of conversion to the free base of the 60 mg loading dose, when co-administrated with proton pump inhibitor (PPI; lansoprazole). The co-administration with PPI resulted in a statistically significant reduction in platelet aggregation inhibition activity in the batch containing 70% conversion to the free base compared to the other two, within one hour of administration. The difference in activity was due to the inequivalent maximum drug concentration (C_{max}) in the circulation, which led to the delay in reaching the maximal effects with the batches subjected to more substantial salt conversion to the free form. The consequence of this finding was that the inequivalent C_{max} might require a change of the loading dose. The FDA approved the drug after the manufacturer had implemented a control strategy to keep the free base content below 25% [29], [33].

Detecting salt disproportionation reaction in later stages of drug development can significantly increase the cost of development by requiring the change in final product

formulation. The new formulation will need repeating many of the biological, toxicological and formulation stability tests, which result in significant and undesirable delays in drug launching [29]. Salt disproportionation due to drug-excipients interactions is still not well understood. Therefore, understanding the salt disproportionation mechanistic would be beneficial to predict the instability of the drug salt, which would help in identifying formulation strategies to minimise the salt conversion at early stages of drug development. The development of advanced analytical technologies, which would evaluate the drug and its formulation properties before the selection of development drug candidate can provide a solution to mitigate inadequate stability and poor drug product performance issues.

1.4. Advanced Analytical Techniques

A solid dosage form formulation, such as tablet and capsule, is a complex mixture of multiple solid components consisting of one API or more mixed with various excipients, which have different roles. During formulation development, it is important to aim at achieving predefined product quality attributes. In addition, the influence of selected components on product quality, stability and performance should be fully understood and anticipated. Further, variability in the chosen materials must be effectively monitored and controlled such that formulation can reliably yield desired quality attributes during drug product lifecycle [27].

The analytical investigation of bulk drug materials, intermediates, drug formulations, impurities and degradation products, and biological samples containing the drugs and their metabolites plays a vital role in the field of pharmaceutical research [34]. The primary objective of the pharmaceutical analysis is to ensure the quality, physical and chemical stability and efficacy of the pharmaceutical formulation. In addition, the pharmaceutical analysis investigates the

performance of the final products obtained and ensure that they meet the required specifications. A combination of techniques is generally necessary to gain an in-depth understanding of the properties of the pharmaceutical materials. The most commonly used methods for solid-state characterisation have been X-ray powder diffraction (XRPD), infrared spectroscopy (IR), Raman spectroscopy and solid-state nuclear magnetic resonance (SS-NMR). Some commonly used thermal techniques involve differential scanning calorimetry (DSC) and thermal gravimetric analysis (TGA). The microscopic analysis involves examining the optical and morphological properties of the drug by techniques such as light microscopy (LM) and electron microscopy (EM). The instrumental pharmaceutical analysis includes different state-of-the-art advanced analytical techniques are listed in Table 1.1, categorised based on the investigated properties [35]–[37].

Table 1.1: Characterisation techniques commonly used for solid-state analysis of pharmaceuticals. Adapted from the References [28], [35]–[39].

Characterisation Techniques	Physicochemical Characteristics Analysed
Spectroscopic Techniques	
Infrared (IR) Spectroscopy	Molecular vibrations (Dipole moment changes) Chemical structure and functional group analysis
Raman Spectroscopy	Molecular vibrations (Polarizability changes) Chemical structure and functional group analysis
Solid-State Nuclear Magnetic Resonance (ss-NMR)	Magnetic resonance Nuclei and chemical environment within a molecule Molecular dynamics Interactions: drug-drug or drug-excipients
Mass Spectrometry (MS)	Mass to charge ratio Molecular mass-chemical structure Surface properties (Secondary ion MS)
Energy Dispersive Spectroscopy (EDS)	X-ray emission Elemental analysis
Fluorescence Spectroscopy	The electronic transition from the excited state to the grounded state (Emission) Drug content and localisation In vitro drug targeting
Ultraviolet-Visible Spectroscopy (UV-Vis)	The electronic transition from the ground state to the excited state (Absorption) Quantitative determination of different analytes

X-ray Diffraction	
X-ray powder diffractometer (XRPD)	Structural information Crystal form identification Quantification of the degree of crystallinity
Single Crystal XRD	
Thermal and Gravimetric Analysis	
Differential Scanning Calorimetry (DSC)	Thermal events: glass transition, crystallisation, melting point and heat capacity Interactions: drug-drug, drug-excipient
Thermal Gravimetric Analysis (TGA)	Transitions involving a change in mass (mass vs temperature)
Microscopy	
Optical Microscopy	Size and morphology Crystallinity (Polarized Light Microscopy (PLM))
Electron Microscopy (EM) Scanning Electron Microscopy (SEM) Transmission Electron Microscopy (TEM)	Size and Shape (High resolution) Elemental analysis (with EDS)

The continuous development of advanced analytical techniques and methods are of the highest importance to sustain, innovate and improve the efficiency of drug discovery and development process. However, most of the analytical techniques are offline techniques that required sampling, and in most cases, sample preparation before the final measurement can be taken. The limitation of offline analytical techniques is the sample manipulation, which may have drastic effects on phase transformation analysis, especially with metastable samples transforming to stable forms. Therefore, offline analytical techniques are not suitable to investigate metastable systems that undergo a transition between two different forms [40].

In-situ analytical techniques offer the potential for better and faster understanding of the drug phase transformation in solid dosage forms as compared to traditional offline analysis. The ability to monitor *in-situ* and in real-time can be highly valuable during product development. *In-situ* Raman spectroscopy and *in-situ* optical imaging have great potential in this area.

Raman spectroscopy is widely used in the pharmaceutical industry for characterising complex pharmaceutical formulation [40]. It is based on the detection of changes in the Raman

shift, which is associated with inelastic scattering of incident photons. The different Raman shift is indicative of changes in the intermolecular bonding, which produce differences in electron distribution in the molecular and lattice environment[40]. Therefore, different Raman spectra for the salt and the free form can be detected as they both have different chemical structure [40].

Another *in-situ* tool commonly used for crystal analysis during crystallisation and, more recently, for monitoring phase transitions is *in-situ* optical microscopy also known as particle vision and measurement (PVM) [40], [41]. The *in-situ* optical imaging is a high-resolution video microscope [42], which is typically employed for in-process high-resolution imaging of solid crystals within the crystallisation process or storage environment. *In situ* optical imaging microscopy is a well-established online technique for characterising and tracking changes in material phase transformation, which is associated with the dissolution of the metastable form and the nucleation and subsequent growth of the stable form [43]. This phase transformation is often accompanied by a change in the crystal habit (although not always), which can cause dramatic changes to the shape of the material crystal. Crystal habit changes can be successfully monitored using the *in-situ* optical imaging system and quantified using advanced image analysis software. Conversion of the salt to the free phase can cause a change in the drug crystal shape, which can be tracked in real-time using *in-situ* optical imaging microscopy.

Therefore, *in-situ* Raman spectroscopy and *in-situ* optical imaging microscopy can be utilised to investigate salt stability and *in-vitro* performance in multicomponent solid dosage forms during storage and dissolution. Both techniques can provide an in-depth insight into the fundamentals and mechanistic of salt disproportionation and drug phase transitions.

1.5. Thesis Outline and Structure

As described in this introduction, salt disproportionation is an undesirable process whereby the salt form of a drug is converted into the free form in both solid and solution state. The resultant free form may exhibit undesirable physical properties, which have an effect on the final product stability and performance. The detection of salt disproportionation reaction in later stages of drug development can significantly increase the cost of development. Currently, there is a limited understanding of the mechanisms of the salt disproportionation in solid dosage form due to the application of traditional and offline analytical techniques.

Therefore, the overall aim of this work is to employ fast and *in-situ* advanced analytical techniques to investigate salt disproportionation in multi-component solid dosage forms during storage and dissolution.

In Chapter 3, the capabilities and limitations of selected advanced analytical techniques were explored by investigating challenging, multi-component structures. Nanoparticles in electrospun fibre hybrids were fabricated and characterised using transmission electron microscopy (TEM), scanning electron microscopy (SEM), energy-dispersive X-ray (EDX) spectroscopy, Raman spectroscopy, time-of-flight secondary ion mass spectroscopy (ToF-SIMS) and super-resolution fluorescence microscopy. The principle and theory of these analytical techniques are discussed in **Chapter 2**.

In Chapter 4, salt disproportionation in drug-exipient binary mixtures stored at high relative humidity are investigated using *in-situ* optical imaging. The novelty of this method derived from tracking the change in salt crystal morphology *in-situ* as a result of salt disproportionation during storage using a simple and fast analytical technique that requires a small sample size.

In Chapter 5, Raman spectroscopy was employed to investigate salt disproportionation in binary drug-excipient tablets in real-time during the course of dissolution experiment using a flow-cell system. The dissolution medium pumped through the flow cell had pH conditions to mimic the stomach and small intestine condition. Integrated in-line UV-Vis spectroscopy was employed to directly relate the changes in dissolution performance to the physicochemical changes that occurred to the drug salt during dissolution.

The thesis then concludes in **Chapter 6** with a summary of the research and discussion of possible opportunities for continuation of this work in the future.

Chapter2: Instrumentation

This chapter aims to provide an overview of the analytical techniques employed in this thesis to analyse the particle-fibre hybrids and salt formulations under investigation. In this chapter, the theory behind the techniques as well as the reasons for their use will be briefly discussed.

The full sample preparation and experimental details are presented in the respective "Materials and Methods" sections of Chapters 3, 4 and 5.

2.1. Dynamic Light Scattering (DLS)

DLS is a non-invasive, reliable and rapid characterisation tool used to measure the hydrodynamic diameter, size distribution and detect dispersity of particles within nanosuspensions [44].

Particles in suspension are moving in a random motion known as, Brownian motion. The speed of the particle movements is dependent on the particle shape, hydrodynamic diameter, concentration of the solution, viscosity of the solvent and temperature [45]. The relationship between the translational diffusion coefficient and the particle size can be obtained from the famous Stokes-Einstein equation [46]:

$$r = \frac{kT}{6\pi\eta D} \quad (2.1)$$

Where k is Boltzmann's constant, T is the temperature, η is viscosity; r is the radius of the spherical particle and D is the diffusion coefficient

In dynamic light scattering, the speed at which the particles are diffusing due to Brownian motion is measured. The surface of the particles is illuminated with a laser beam, which induces particle polarisation (dipoles). The polarised particles scatter light at the same frequency of the incident light and spread in all directions (Rayleigh or Mie light scattering). The intensity of the scattered light fluctuates by a small portion that is proportional to the speed of the particle (i.e. particle diameter) as shown in Figure 2.1 [47].

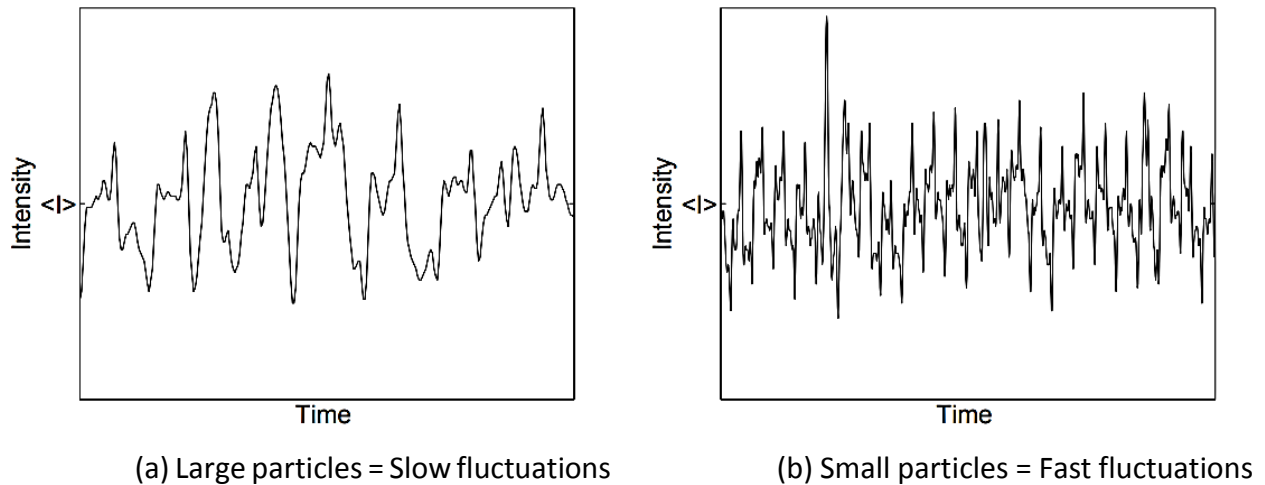


Figure 2.1: Fluctuations in the intensity of scattered light due to the motion of dispersed particles. The brackets $\langle \rangle$ denote an intensity average [44].

The dynamic light scattering was used to measure the mean particle size and the polydispersity index of the size tuneable silica nanoparticles prepared in Chapter 3

2.2. Scanning Electron Microscopy (SEM)

Scanning electron microscopy (SEM) is a morphology analysis method whereby a beam of accelerated electrons, usually emitted from a heated tungsten filament, is scanned over the surface of the sample placed in a vacuum chamber. As the electron beam reaches the surface, a complex set of signals in the form of secondary electrons, backscattered electrons and characteristic X-ray is emitted as shown in Figure 2.2. These signals contain information about the

samples surface topography and composition. Secondary electrons are low energy electrons that originate from the interaction of the beam electrons with the valence shell electrons in the outer shell of the sample atoms. Since the energy of the secondary electrons is very low, they are only emitted from a thin layer of the specimen surface. Therefore, detecting these signals is suitable for investigating the topography and surface variation of the sample. The secondary electron signal is recorded and transferred to a scanner, which converts it into pixels to create the image of the sample surface [48].

SEM was used to image the electrospun fibres and particle-fibre hybrids produced in Chapter 3. In addition, SEM was employed to investigate the crystal shape difference between the salt and the free-form.

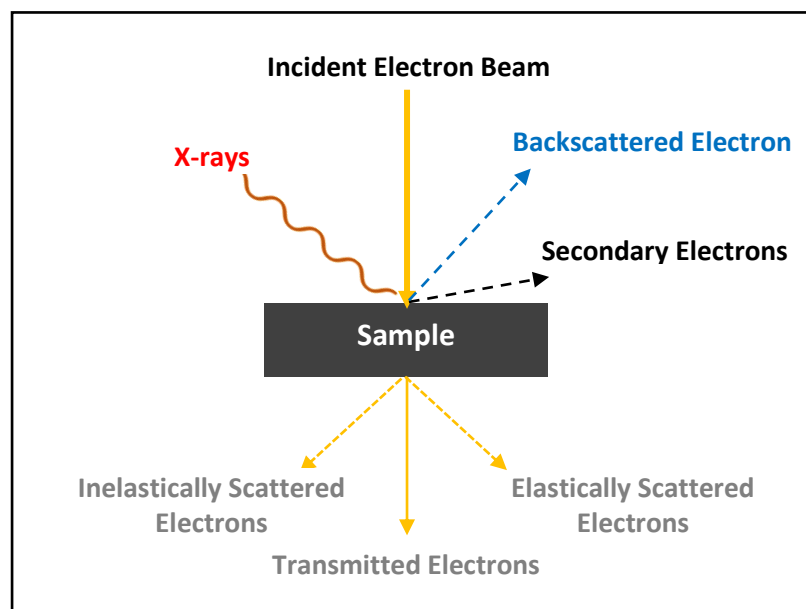


Figure 2.2: Diagram illustrating the possible interactions of electrons with the sample.

2.3. Transmission Electron Microscopy (TEM)

As with SEM, electrons produced at the source in the TEM are accelerated by a high potential, typically from 100 kV to 300 kV. The electron beam is focused on a thin sample film, mounted onto a conductive mesh. The elastically scattered electrons and transmitted electrons provide the contrast in TEM images, known as diffraction contrast (Figure 2.2). The transmitted electrons proceed towards the objective aperture; where electrons that are deviated from the optical axis (i.e. scattered electrons) are effectively blocked out. The transmitted electrons are then used to form bright field images of the sample [49].

Scanning transmission electron microscopy (STEM) is a special type of TEM that can scan the finely focused beam of electrons across the sample in a raster pattern. The transmitted electron beam may be elastically scattered by the core of sample atoms and then detected using a high angle annular dark field (HAADF) detector (Figure 2.2). The scattered electrons are then used to produce black-field images of the sample [50].

TEM was used to image the silica nanoparticles and particle-fibre hybrids produced in Chapter 3. STEM was utilised in combination with energy- dispersive X-ray spectroscopy (Section 2.4) for the elemental analysis of the particle-fibre hybrids prepared in Chapter 3.

2.4. Energy- Dispersive X-ray Spectroscopy (EDX)

Energy- dispersive X-ray spectroscopy (EDX) is an analytical technique that is combined with electron microscopes, such as SEM and STEM, to analyse the elemental composition of a sample. While energy- dispersive X-ray spectroscopy operates similarly to SEM or STEM, it allows observation of the emitted X-ray properties. X-rays are produced when an electron from the beam strikes out an inner shell electron in the sample, creating a hole. An electron from the

valence shell within the respective atoms drops down to fill this hole. As a result of the movement of electrons between energy levels, an X-ray is emitted with energy equal to the difference between those two electron energy levels, in order to conserve energy (Figure 2.3) [51], [52].

The emitted X-rays have distinctive energies, which are all collected and recorded by the solid-state X-ray detector. The energy of the X-rays emitted is unique to each element, which allows the elemental composition of the sample to be measured [51], [52].

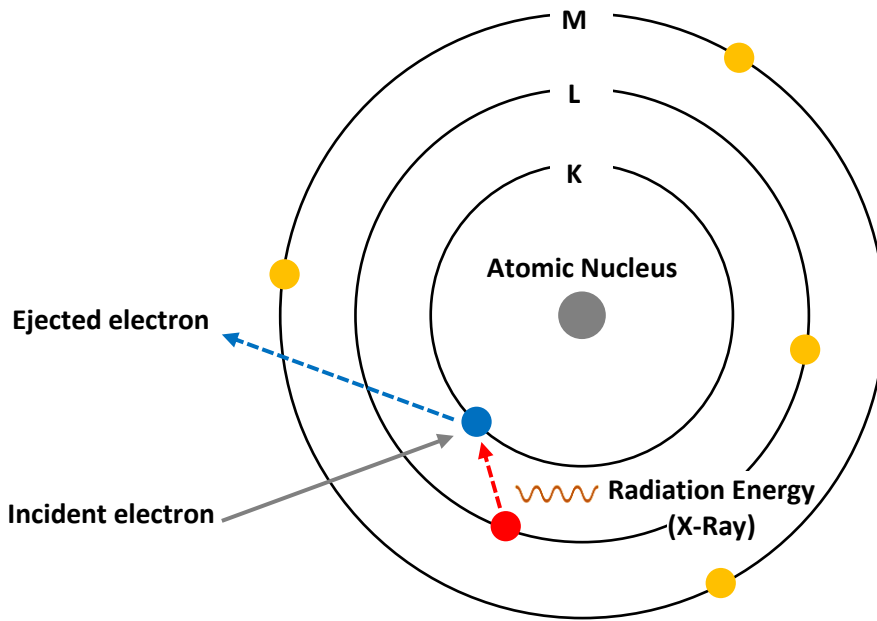


Figure 2.3: Diagram showing the principle of EDX. The process through which X-rays are emitted when an electron shell is bombarded by incident electrons.

STEM combined with EDX was used to investigate the elemental composition of the particle-fibre hybrids prepared in Chapter 3. Images are created for every element present in the particle-fibre hybrid samples examined. The element is shown as the coloured part of the image while the rest of the picture is dark.

2.5. Time of Flight Secondary Ion Mass Spectroscopy (ToF-SIMS)

Time of flight secondary ion mass spectroscopy (ToF-SIMS) is a highly sensitive surface characterisation technique that can be used for investigating the first two nanometres of the material's surfaces. ToF-SIMS allows to assess, qualitatively, the composition of sample surfaces and visualise the distribution of chemical entities on these surfaces. The principle behind the ToF-SIMS operation is represented in Figure 2.4.

ToF-SIMS utilised a variety of primary ions such as Gallium (Ga^+), Cesium (Cs^+), Fullerene (C_{60}) and Bismuth (Bi_3^+) as excitation sources [53]. The primary ions are generated in short pulses, which are then accelerated and focused onto the surface of the sample. The energy of the primary ion beam is transferred to the surface layer of the sample, resulting in binary collisions and ejection (sputtering) of secondary ions and neutral species. Charged secondary ions are drawn into the time-of-flight tube, where they are accelerated via the high potential between the mass analyser and sample surface. The secondary ions enter the tube with velocities according to their masses. Therefore, the secondary ions of different masses arrive at the mass analyser at different times. The arrival times are measured for each secondary ion and used to generate spectra using ToF-SIMS software [54]. The precise control of the primary ion beam enables deriving chemical spectra for each pixel of the sample scanned surface through a raster scanning approach [55], [56]. This can be transformed into a chemical image via ToF-SIMS software.

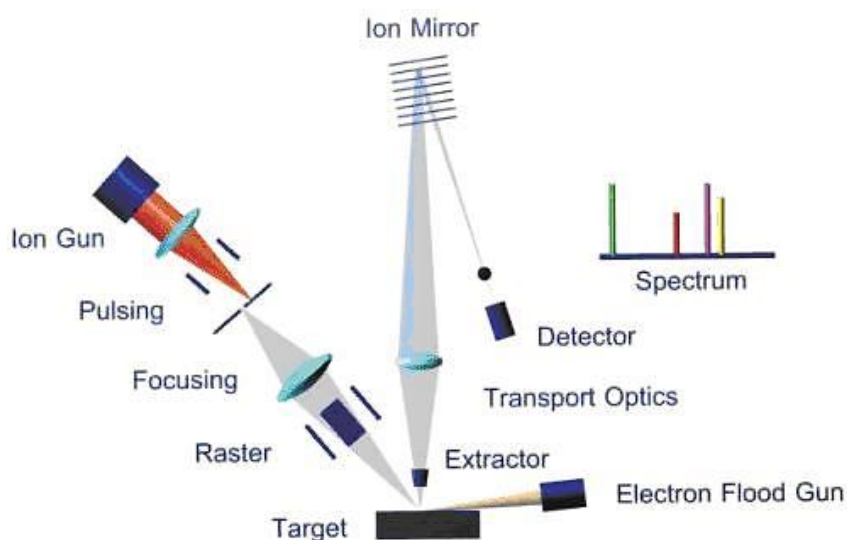


Figure 2.4: Schematic representation of a ToF-SIMS instrument [44].

ToF-SIMS was employed to explore the surface properties of the particle-fibre hybrids prepared in Chapter 3.

2.6. Fluorescence Spectroscopy

Fluorescence spectroscopy deals with excitation and emission in molecules. Molecules can transit from the ground state to an electronically excited state when exposed to the light of a wavelength (energy level) equal to the energy gap between the ground state and excited state. This is known as molecular absorbance of light. The fluorescence process involves a light emission by a fluorescent substance (i.e. Fluorophore) during relaxation from the excited to the ground state [57], [58]. Fluorophores are typically substances with delocalised electrons, as in systems containing aromatic rings and conjugated double bonds [58], [59].

The fluorescence mechanism in the molecule can be illustrated through the Jablonski diagram seen in Figure 2.5 [57]. Depending on the energy of the light, the molecule absorbs photons energy and uses the absorbed energy to excite an electron to different electronic singlet

states S_1 , S_2 ... etc. Molecule relaxation through emission of light will always occur from the lowest energy excited electronic state of a molecule (S_1) (Kashas rule) [60]. Therefore, molecules excited to a higher energy electronic state (S_2 or S_3) will go through internal conversion before emission. As emission almost always occurs at the lowest excited state, thus maximum emission wavelength is constant for each particular substance, independent of the wavelength of the excitation light [57], [61]. Light emission involves loss of energy and thus emitted light is always shifted towards longer wavelength relative to the excitation light [57], [61]. The difference between excitation and emission wavelength is called the Stokes shift, which relates to energy loss.

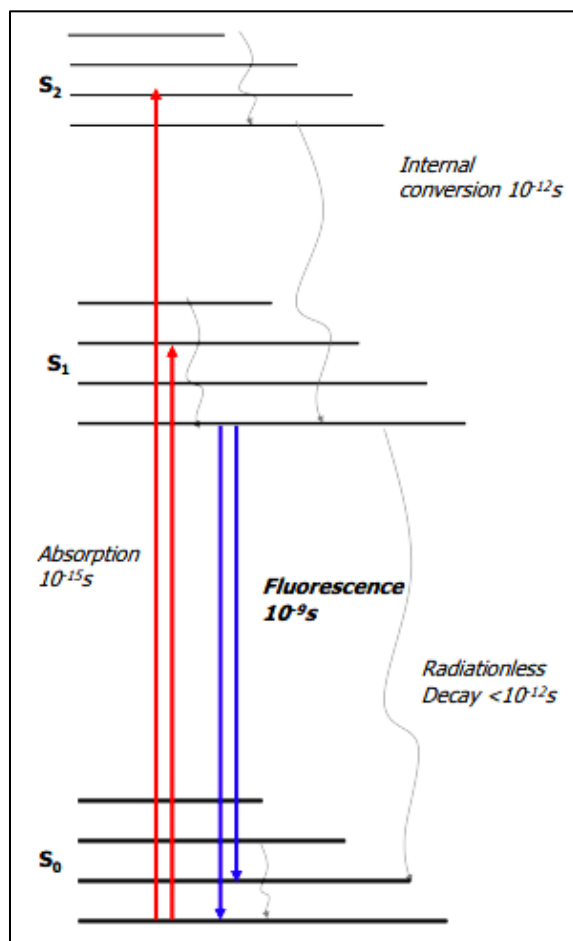


Figure 2.5: The Jablonski energy diagram shows the process of light absorption and emission [57].

Fluorescence spectroscopy consists mainly of four basic units: a light source, monochromator, sample compartment and detector. The light source is usually a laser, a xenon lamp, or LED, which is utilised to excite the fluorescent molecules. The monochromator or filter controls the excitation/emission intensity and the light wavelength range that crosses through the sample to finally strike the detector. The detector converts the collected signals into measurable signals. The data acquired from fluorescence measurement can be represented as fluorescent images.

Fluorescence microscopy has become a vital, non-invasive tool for biological research, particularly in investigating morphological structures and interactions of biological molecules inside living cells, tissues, and whole organisms [62]. However, the spatial resolution of fluorescence microscopy is typically limited to about 200 nm which limits the ability of this technique to resolve too small subcellular structure (< 200 nm). In recent years, super-resolution fluorescence microscopy imaging techniques have been invented, which yield an order of magnitude improvement in the spatial resolution [62]. Stochastic optical reconstruction microscopy (STORM) is one of the most commonly used super-resolution fluorescence microscopy imaging techniques [63], [64].

In Chapter 3, fluorescent particle-fibre hybrids were investigated as possible calibration and performance test kit for super-resolution fluorescence microscopy.

2.7. Raman Spectroscopy

2.7.1. Principles of Raman Spectroscopy

Raman and Krishnan first reported the Raman effect in 1928, which can be described as the inelastic scattering of radiation from a sample [65]. The frequency and energy of photons of

monochromatic light altered upon interaction with a sample in inelastic scattering. When the sample is irradiated with monochromatic light (usually using a laser in the visible (532 nm) or near-infrared (785 nm) regions of the spectrum), molecules are promoted to a virtual state (Figure 2.6) [66]. When molecules relax, they return to the ground state emitting light mostly with the same frequency as the excitation source (Rayleigh scattering) [67]. Only a small proportion of light (10^{-6}) is emitted with a different wavelength (Raman scattering). Raman scattering can be either stokes (i.e. molecules are initially in the ground state) or anti-stokes (i.e. molecules are initially in the excited state) scattering. In stokes scattering, some of the photon energy is transferred to the molecular vibration, leading to a reduction in the resulting frequency of the scattered light. In anti-stokes scattering, the extra energy of the excited molecular vibration is released leading to an increase in the frequency of the scattered light. Since most molecules exist in the ground state at ambient temperature [68], stokes scattering is dominant over the anti-stokes scattering.

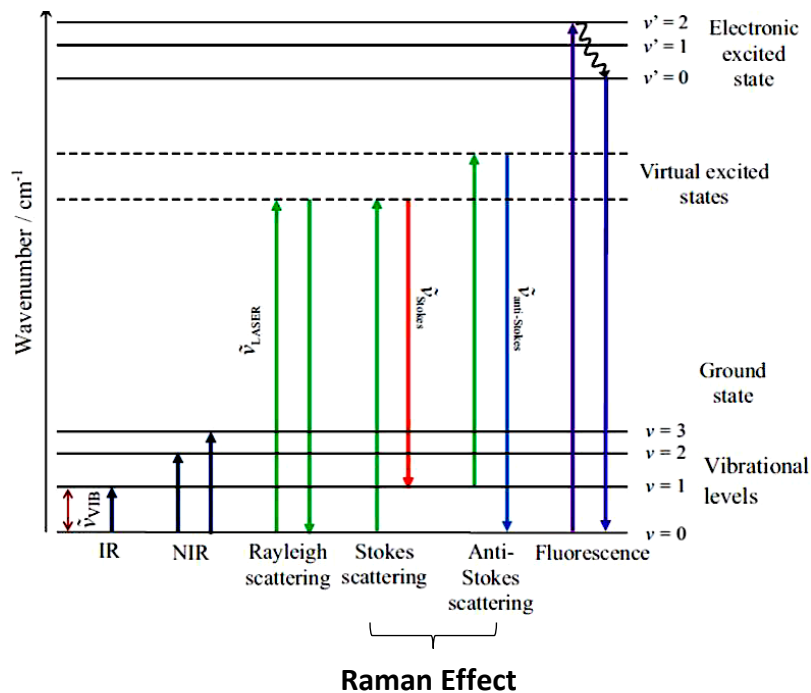


Figure 2.6: Schematic representation of the energy levels changes in Infrared (IR), near-IR, Rayleigh scattering, Raman scattering and fluorescence [69].

The shift in frequency (Stokes and anti-stokes scattering) is directly related to vibration energy levels transition [67]. Therefore, Raman spectroscopy measures the vibrational energies of the molecules in a sample, which are associated with the type of chemical bonds.

Infrared (IR) spectroscopy investigates the same range of energies as Raman. However, it is based on light absorption instead of scattering. The frequencies of the molecular vibrations in vibrational spectra (IR and Raman) rely on the strength of the atom's chemical bonds and their masses. Furthermore, the IR transitions follow different selection rules from Raman. A vibration is Raman active when molecules showed a change in polarisability [66] and is IR active when there is a change in dipole moment. This means that strong IR vibrations could be weak in Raman spectra and vice versa. For instance, water molecules exhibit an intense IR spectrum as it has a strong dipole moment, whereas the electrons are not easily polarised and therefore the Raman scattering is weak. In addition, most drugs contain π electrons, which are easily polarised, and consequently, they exhibit strong Raman scattering. In contrast, excipients show weak Raman scattering as they are mainly σ bonded molecules. This can be highly beneficial when detecting low levels of the drug in multicomponent pharmaceutical products such as tablet [70].

2.7.2.Raman Microscopy

In order to analyse a microscopic area with Raman spectroscopy, Raman spectroscopy is combined with a microscope as shown in Figure 2.7. In Raman microscopy, the laser beam is focused on the sample using the objective lens, and the scattered light is collected using the same objective lens (180° back-scattered configuration). The Raman light is then directed into a spectrograph and diffracted across a charge-coupled device (CCD) detector. The use of pinhole apertures positioned between the objective lens and the CCD detector in confocal microscopy

permits the depth of field to be controlled, by allowing only the scattered light from the confocal plane of the sample to reach the detector.

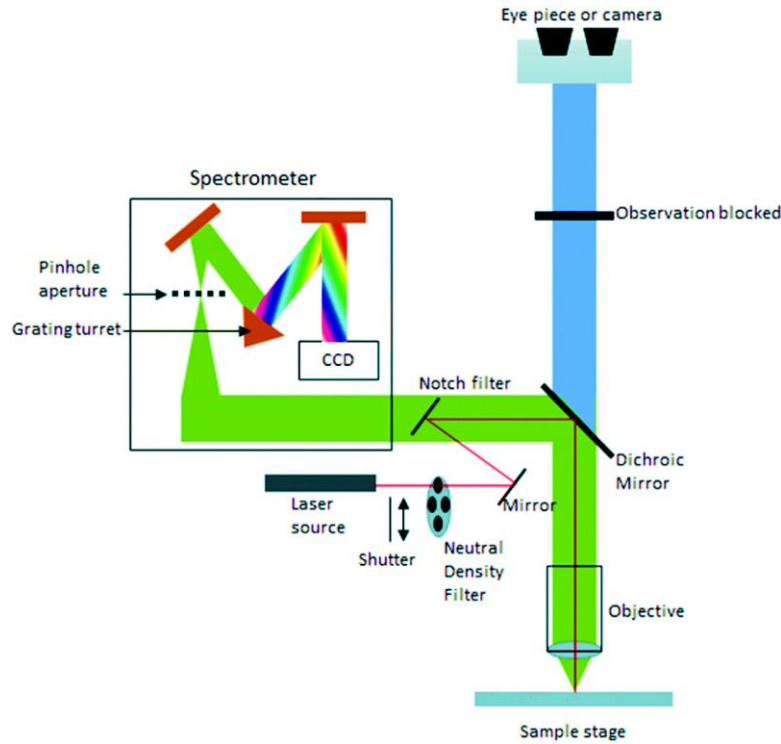


Figure 2.7: Standard configuration of a confocal Raman microscopy [71].

The Raman microscopy spatial resolution is primarily controlled by the laser wavelength and the microscope’s objective lens being used. The following equation can define the diameter of the laser spot:

$$d = \frac{\lambda}{2NA} \quad (2.2)$$

in which d is the laser spot diameter, λ is the laser wavelength, and NA is the objective numerical aperture.

2.7.3.Raman Mapping

Raman mapping involves collecting Raman spectral and spatial information from the sample's surface [72]–[74]. This technique offers the ability to obtain components distribution and their concentration in multi-component samples [73]. Generally, the laser point is focused, and the sample under test is translated using motor-driven x–y stages past the laser focus. This method is called point-by-point mapping.

2.7.4.Data Analysis

Hundreds of thousands of Raman spectra can be generated using Raman spectroscopy/microscopy, which can be rather large. Therefore, in order to extract unambiguous and meaningful outputs, statistical analysis of data is performed. Data analysis can be divided into two main steps: data pre-processing and processing.

Pre-processing: Data pre-processing step is responsible for removing any spectral and spatial artefacts. In multivariate data analysis, it is essential to perform adequate data pre-processing to avoid having models containing variances related to the experimental set-up (such as sample focus) rather than changes in chemical composition. Data variance-scaling is a simple method to minimise the effect of variations in Raman scattering efficiency [75]. In addition, subatomic particles can be detected by the CCD detectors, which can give a higher intensity signal than Raman scattering (cosmic events). Commercial software can be used to remove these very sharp narrow spikes automatically.

Data Processing: Data processing using multivariate analysis can be used to produce the false-colour images, which are based on the entire Raman spectrum and not on one single band like univariate analysis. Classical least square (CLS) [76], [77] and multivariate curve resolution-

alternating least squares (MCR-ALS) [78]–[80] are established multivariate analysis techniques used to deconvolute Raman data from pharmaceutical samples. CLS operates by modelling the spectra found in each pixel as the linear combination (the weighted average) of the pure component spectra. These weight factors can be easily computed when the reference spectra are known [81]. The MCR-ALS method attempts to deconvolute the data into the individual spectral components and their concentration. The number of components contributing to the data matrix resolved by MCR can be estimated based on prior knowledge of the system or by using other multivariate techniques. Subsequently, the iterative optimisation of the spectral and concentration matrices using the ALS algorithm is performed [82]–[84]. Constraints of non-negativity, unimodality and closure are often employed during ALS to help guide solutions to the true value and reduce the complexity of MCR. Commonly used constraints are schematically presented in Figure 2.8 [85]. Non-negativity compels concentration or response profiles to be positive. Unimodality forces profiles to have only one maximum (e.g. chromatographic peaks). Finally, closure or mass balance allows concentration profiles to add up to a specific constant value.

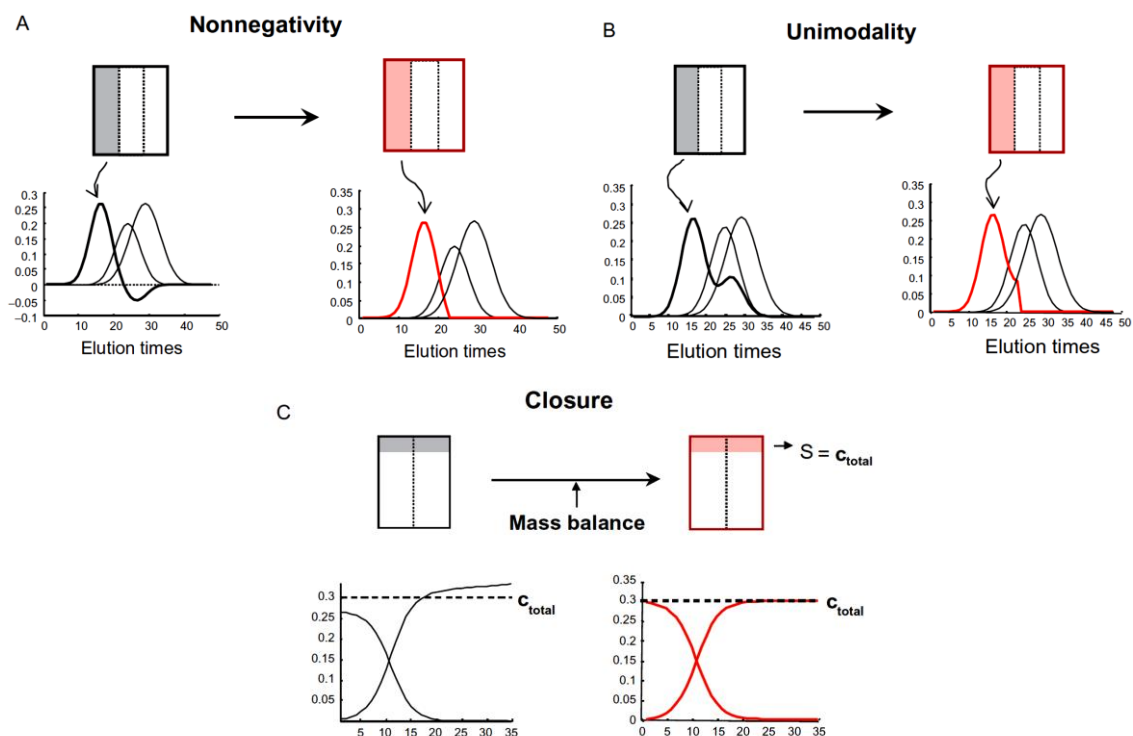


Figure 2.8: Examples of common constraints used in MCR. (A) non-negativity, (B) unimodality, (C) closure. Bold black profiles on the left plots are unconstrained. Red profiles on the right are profiles that have been constrained [85].

Raman Spectroscopy was used to probe the chemical structure of the particle-fibre hybrids in Chapter 3. In addition, Raman spectroscopy was employed to investigate salt disproportionation in multicomponent solid dosage forms during storage and dissolution in Chapter 4 and Chapter 5, respectively. CLS and MCR-ALS are both used in Chapter 5 to analyse Raman data.

Chapter3 : Fabrication and Characterisation of Electrospun Particle-Fibre Hybrid Structures

This chapter of the thesis deals with exploring the capability and limitations of a wide range of in-house advanced analytical techniques. Silica nanoparticle (SNP) and polyvinyl chloride (PVC) nanofibre hybrids fabricated using the colloidal electrospinning process were investigated as a complex, multicomponent model system. In this chapter, particle-fibre hybrid morphologies were altered by varying the particle to fibre size ratio and the concentration of the particle in the electrospinning polymer solution. A combination of advanced analytical techniques was used to characterise the particle-fibre hybrids. A potential application of the particle-fibre hybrids as a calibration device for super-resolution fluorescence microscopy was also investigated at the end of the chapter.

3.1. Introduction

3.1.1. Electrospinning Process

Electrospinning is a unique and simple technique that has received considerable attention in the production of non-woven fibrous structures with fibre diameters ranging from nanometers to microns in width [86]. The electrospinning process was first introduced and patented in 1934 by Formhals [87]. The process involved the production of artificial filaments by applying an electrical field on liquids containing solid material. After four decades (1971), Baumgarten executed systematic experiments to rediscover and employ the electrospinning process to polymeric solutions dissolved in dimethylformamide (DMF) to fabricate fine fibres ranged from 50 to 1000 nm in diameter [88]. Generally, the electrospinning system consists mainly of three

parts; 1) a source of high voltage power, 2) a spinneret and 3) a grounded collector plate as illustrated in Figure 3.1.

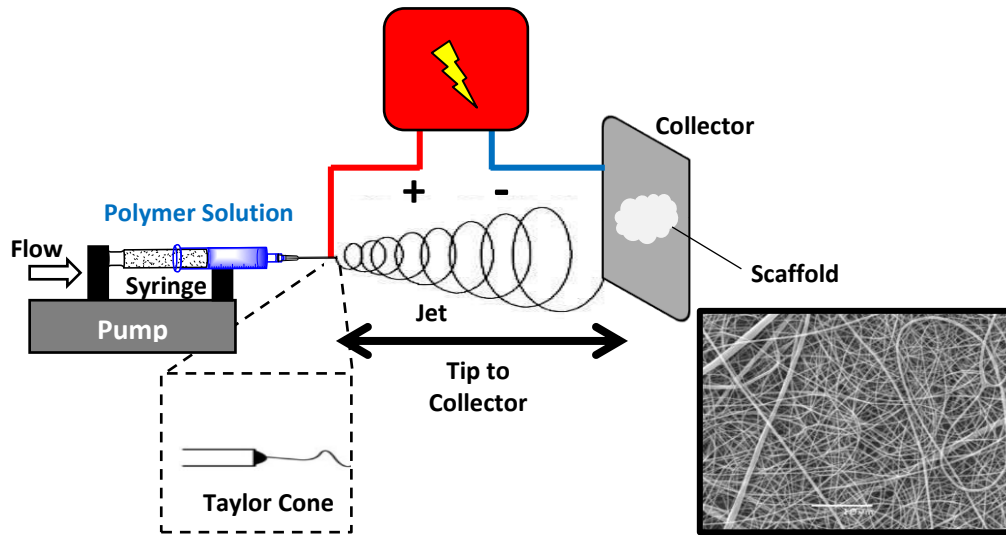


Figure 3.1: Experimental set-up of the electrospinning technique.

The fundamental principle of the electrospinning process is that the polymer solution is pumped through the spinneret forming a droplet at the tip of the needle. A high voltage connected to the tip of the needle is used to electrify the polymer droplet. The electrified droplet deforms as the electrostatic repulsion forces overcome the surface tension forces of the droplet, creating a conical shape known as Taylor cone [89]. As the voltage increases, the Taylor cone continues to stretch towards the grounded plate. Once a critical point is reached, a charged jet will be extruded and collected on the ground collector plate. During the flight time to the plate, the charges in the fibres are being rearranged, which leads to a bending instability [90]. As a result of the bending instability, the fibre undergoes a whipping motion that causes further elongation and thinning of the fibre [91], [92].

The fibre diameter and morphology produced by electrospinning can be changed by controlling specific parameters such as the polymer solution concentration, molecular weight of the polymer, tip-to-collection plate distance, electrostatic field strength applied to the polymer

solution, polymer solution feed rate and the geometry of the grounded collecting plate [86], [88]. For example, larger diameters of fibres are usually associated with a higher concentration of polymer solution while low concentration solutions result in thinner fibres, which have the tendency to form beads [93]–[96].

Numerous polymers have been successfully utilised for electrospinning, which can be roughly divided into natural polymers (e.g. collagen, gelatin, elastin, chitosan, etc.), synthetic polymer (polyesters, polyamides, polysulfones, polycarbonates, etc.) and synthetic biodegradable polymers (Polycaprolactone (PCL), polylactic acid (PLA), polylactide-co-glycolide (PLGA) etc.).

The simplicity, low cost and flexibility of electrospinning technology provide it with wide access to many areas. Major applications have included tissue engineering [97]–[100], wound dressings [101]–[103], drug delivery [104]–[108], chemical and biological sensing [109]–[113] and mechanical engineering applications [114].

3.1.2. Silica Nanoparticles

Silica nanoparticles (SNPs), also known as silicon dioxide nanoparticles, have drawn widespread attention due to their applications in many emerging nanotechnology areas [115]. More specifically, silica nanoparticles are mainly considered for pharmaceutical applications because of their biocompatibility, low toxicity, scalability and tailorable morphology and size [115], [116]. SNPs are produced from a rigid silica matrix that can resist solvent swelling and maintain their structural properties [117]. Furthermore, the surface of silica nanoparticles can be modified with several functional groups that allow precise control of surface chemistry and facilitate attachment of other biomaterial or ligands to the SNP surface [116], [118]–[120].

In 1968, Stöber reported a pioneering and effective method for the preparation of monodisperse silica spheres nanoparticles illustrated in Figure 3.2 [121]. The synthesis of these nanoparticles was performed by the hydrolysis and condensation of tetraethyl orthosilicate (TEOS) as a silica source, in a mixture of absolute ethanol and water as a solvent with the presence of ammonia as a catalyst to initiate the reaction [121]. After this work, there have been many investigations regarding the silica nanoparticles generated from Stöber process in an attempt to precisely control the nanoparticles size and uniformity. Changing reaction parameters such as the amount of TEOS, ammonium hydroxide concentration or the rate of addition of TEOS has generated different sizes of silica nanoparticles ranging from 50 nm to 1.0 μm [122]–[129].

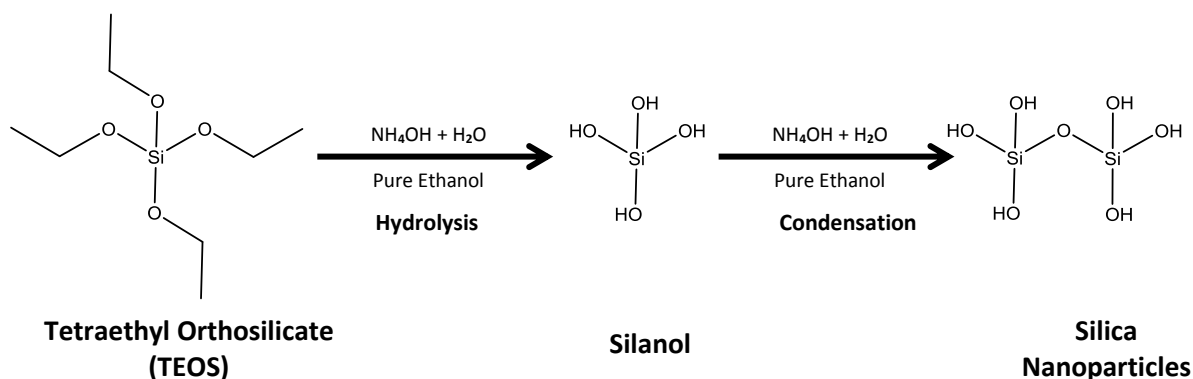


Figure 3.2: Synthesis of silica nanoparticles by the Stöber method.

Fluorescent silica nanoparticles are produced via covalent binding of the fluorophore to the silica particle matrix. The covalent linking is performed via conjugation of a silane coupling agent, such as 3-aminopropyltriethoxysilane (APTES), with the succinimidyl ester derivative of the fluorophore to produce APTES-fluorophore conjugates. The primary amines that existed in the APTES structure have positively charged nucleophilic groups at neutral pH. Therefore, the primary amine groups are readily accessible to conjugation reagents introduced into the medium. The N-hydroxysuccinimide (NHS) ester moiety in the fluorophore structure will react with the primary

amine to form a conjugate linked by a very stable aliphatic amide bond. The reaction is illustrated in Figure 3.3-A. The resulting conjugate is susceptible for hydrolysis and condensation, like the silica precursor (TEOS), leading to the incorporation of the fluorophore into the silica particle matrix forming fluorescent silica nanoparticles (Figure 3.3-B) [130].

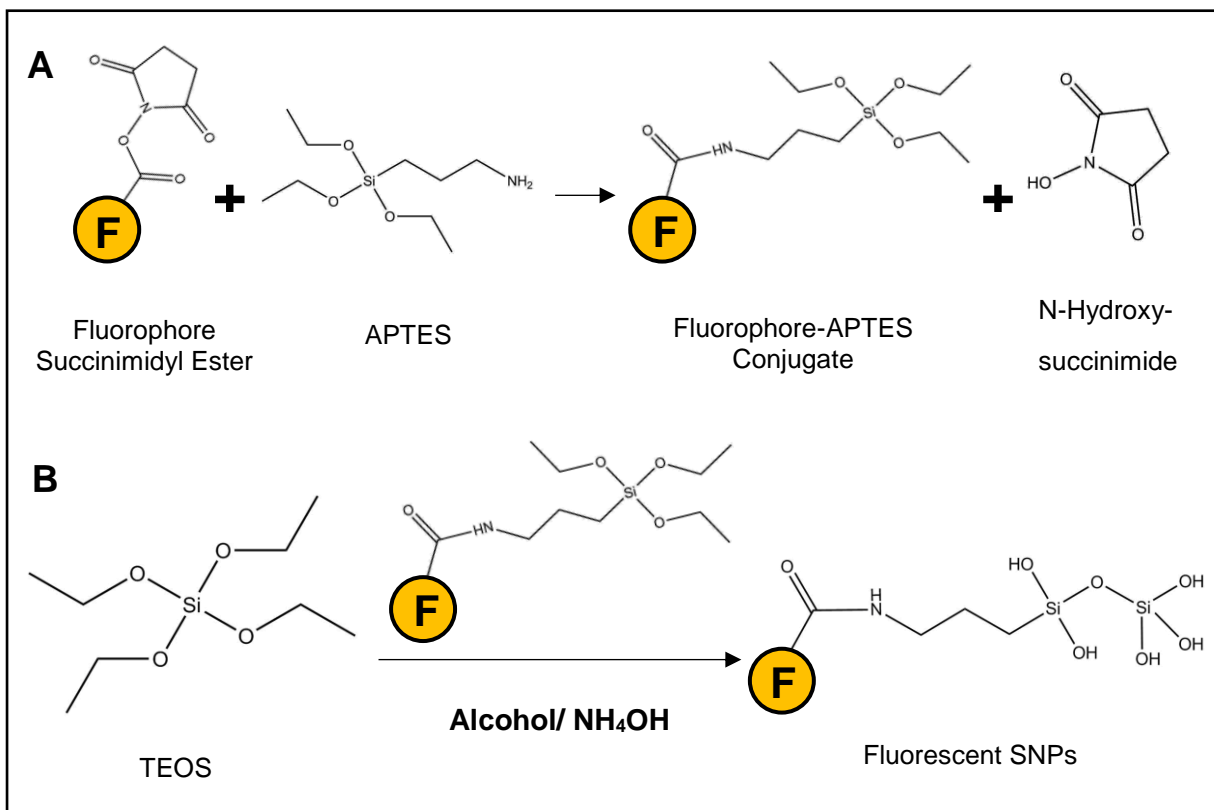


Figure 3.3: Chemical reaction scheme for (A) the conjugation of amino-silane precursor (APTES) to succinimidyl ester derivative of a fluorophore (●) to produce fluorophore-APTES conjugate (B) The synthesis of fluorescent silica nanoparticles.

Silica particle can be functionalised with various fluorophores for different applications. Figure 3.4 shows examples of fluorophores chemical structures including Oregon Green[®] 488 (OG), 5-(and-6)-carboxyfluorescein (FAM), 5-(and-6)-carboxytetramethylrhodamine (TAMRA) and Alexa 647 that will be used in this chapter.

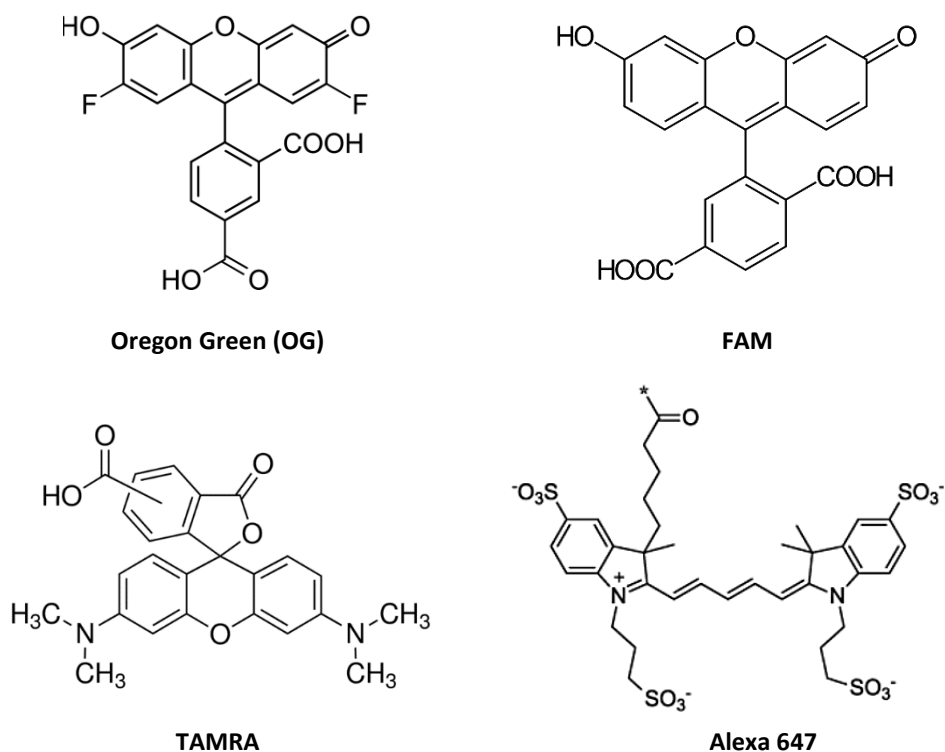


Figure 3.4: Chemical structure of Oregon Green® 488 (OG), 5-(and-6)-carboxyfluorescein (FAM), 5-(and-6)- carboxytetramethylrhodamine (TAMRA) and Alexa 647.

3.1.3. Fabrication of Nanoparticle–Electrospun Fibre Hybrids

In recent years, hybrid nanocomposite systems have attracted the interest of researchers due to their synergistic and hybrid characteristics derived from several components [131]. The incorporation of functional materials such as bioactive materials [132], drug molecules [133], [134] and nano to micro-sized particles [135]–[139] enhance the hybrid nanocomposites with improved performance and broader applications [140].

Colloidal electrospinning technique is a widespread technique to fabricate fibre-nanoparticle hybrid systems. It is implemented by electrospinning the polymer solution, which has been mixed with colloidal particles [141]–[143]. Colloidal electrospinning can provide several advantages including a broad selection of components and high productivity with a simple one-step process at ambient conditions. The hybridisation of nano-to micro-sized particles with

electrospun fibres has attracted attention from the medical research community as a result of many advantages including higher drug loading efficiency [144], enhanced release pattern, controlled drug release and improved drug safety and stability [140], [145].

The nanoparticle- fibre hybrid systems can provide better performance (e.g. high sensing sensitivity) due to the large surface, the capability to imitate complicated structure while maintaining the nanoparticles properties and enhanced physical properties including mechanical, optical and electrical properties [140]. More importantly, the fact that particles can be immobilised and isolated in fibre matrices is of high interest for fundamental science [144]. Pure nanoparticles exhibit high surface area that makes them very difficult to isolate and manipulate. The ability to isolate and immobilise nanoparticles can be highly advantageous for some advanced analytical techniques including super-resolution fluorescence microscopy. This unique application will be discussed in more detail in the next section.

Several studies [146]–[154] have reported attempts of electrospinning polymer and colloidal particles. However, the effect of incorporating particles with different sizes and concentration in the electrospun fibres on the physical properties of the hybrid structure was scarcely reported. Lim and co-workers used electrospun fibres as confining geometries for fabricating silica particle-fibre hybrids [155]. The effect of different polymer solutions and different silica particles size on hybrid configuration were examined. Furthermore, Jin and co-workers investigated how different process parameters, such as the diameter of silica particles or applied voltage, influenced the electrospun fibres morphology [156].

Both attempts successfully reported that particle-fibre hybrid system morphology could be altered when changing several parameters generating some distinct morphology such as pearl-necklace structure. However, there are gaps in the understanding of the mechanism by which the

hybrid systems fabrication process can be controlled. These gaps are a potential cause of failure in the precise control of the hybrid structures.

3.1.4. Super-Resolution Fluorescence Microscopy: Potential Application of Particle-Fibre Hybrid Structure

Fluorescence microscopy is mainly used to image samples with the highest detail possible. However, the optical diffraction limit of conventional light microscope controls the detail that can be resolved. The diffraction limit will blur out any small point of light to a certain minimal size and shape known as the point spread function (PSF) [157]. Therefore, the PSFs of two objects that are closer together than the PSF width will show a large overlap, making it hard to distinguish them from one another. Abbe [158] and Rayleigh [159], estimated the resolution limit in the focal plane as:

$$\textit{Limit of Resolution} = \frac{0.61 \lambda}{NA} \quad (3.1)$$

whereas λ being the wavelength of light and NA the numerical aperture of the microscope's objective lens. Therefore, for an optical microscope using visible light ($\lambda = 550$ nm) and a high-NA objective lens ($NA = 1.4$), the attainable resolution is fundamentally limited to around 200-300 nm.

In recent years, super-resolution fluorescence microscopy imaging methods have emerged to overcome the optical diffraction, thus gaining optical microscopy images with a higher resolution [160]. This innovation was awarded the Nobel Prize for chemistry in 2014 [161]. Super-resolution fluorescence microscopy images methods such as, stochastic optical reconstruction microscopy (STORM) [162], achieve sub-diffraction-limit resolution by

consecutively imaging and localising single fluorophores that are located in the target structure [163]. This involves using fluorescent probes that can switch between a fluorescent and a dark state, which can be activated/deactivated (i.e. blinking) at different time points so they can be individually localised. For example, the STORM technique can be employed to experimentally determine the distance between two photoswitchable fluorescence molecules (Such as Alexa 647). STORM exploits the fact that in the presence of an imaging buffer containing primary thiol compounds such as β -mercaptoethanol or mercaptoethylamine, the fluorescence of Alexa 647, for example, can be reversibly switched off to a dark state by forming a thiol-adduct after excitation by high wavenumber laser (~ 650 nm) as shown in Figure 3.5 [164], [165]. The coordinates of different fluorophores can be mapped, and super-resolution images consequently reconstructed [160], [163].

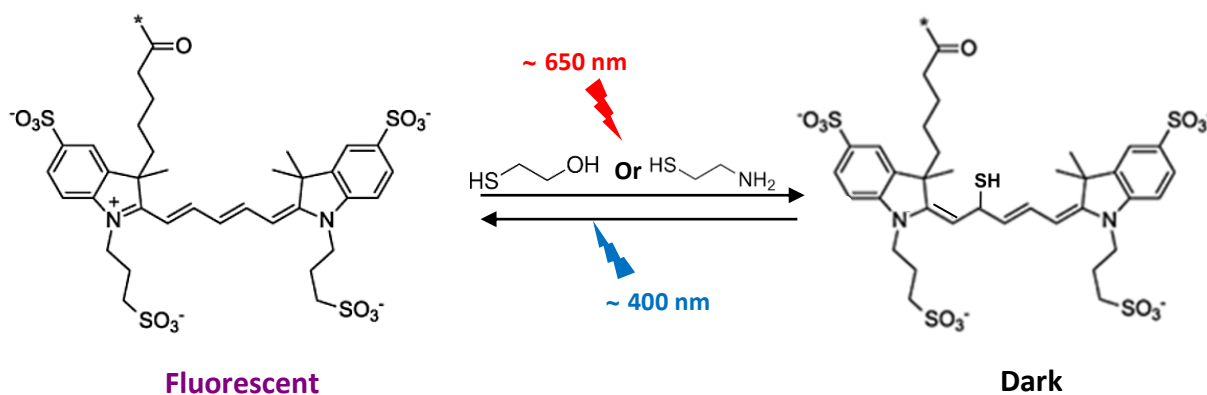


Figure 3.5: Representative photo switching mechanisms of fluorescent Alexa 647 molecule [163], [166].

For many super-resolution microscopy techniques, the resolution requires to be assessed experimentally [167]. The high quality of super-resolution microscopy images can be achieved by running a series of tests to ensure that the microscope is functioning correctly. Currently, microscopists prepare performance test sample slides via different methods including, fluorescent conjugates coating of glass, fluorescent actin filaments on the glass and fluorescent

microsphere mounted on glass coverslips. A common problem when imaging any of these samples is the high labelling density, which may cause the images to overlap and compromise high precision localisation. In addition, the presence of diffusing entities moving within and out of the focal plane can interfere with the image clarity and the calibration process [168].

In order to design a better performance test sample slide, specific properties and specifications are required. Ideally, the specimen would have a simple and well-understood morphology; would be immobilised to a single, defined optical plane; and would have many isolated single fluorophores across the sample. Furthermore, this sample should be easily created, prepared and handled [169]. Electrospinning can fulfil these requirements and can be utilised as a suitable preparative method for the test sample slide. Colloidal electrospinning can be used to prepare fluorescent particle-fibre hybrids. These hybrids have the advantages of immobilising and isolating fluorescence nanoparticles in fibres and can be handled easily to calibrate and test the performance of super-resolution fluorescence microscopes.

3.2. Motivation and Aim

Particle–electrospun fibre hybrids exhibit a huge variety of potential applications. Fabrication process parameters have major roles in controlling the structure of the hybrid systems. Different hybrid structures have been reported, however, there are gaps in the current knowledge of the mechanism by which the hybrid systems fabrication can be controlled. This ambiguity could be arisen from using basic and conventional imaging and characterisation techniques in investigating particle-fibre hybrid systems. Therefore, the first aim of this chapter is to apply a range of advanced analytical techniques to investigate how different fabrication parameters such as particle size and particle concentration, influence the hybrid structure. The geometrical, chemical and surface properties of the fabricated particle-fibre hybrids were characterised using scanning electron microscopy (SEM), transmission electron microscopy (TEM), energy-dispersive X-ray (EDX) spectroscopy, Raman Spectroscopy and time of flight secondary ion mass spectroscopy (ToF-SIMS).

In addition, these particle-fibre hybrid systems have potential applications in various fields due to their unique properties as described previously. Immobilising functional particles into confined geometry nanofibres could be highly beneficial for easier and more efficient nanoparticles characterisation using various analytical techniques. Therefore, the second aim of this chapter is to demonstrate a potential application of immobilised fluorescent silica nanoparticles in electrospun fibres for instrument performance testing and calibration tool for super-resolution fluorescence microscopy.

Size-tunable silica nanoparticles have been selected as a model example of nanoparticles to be incorporated into electrospun fibres due to their robust fabrication method, narrow size distribution and stability under harsh conditions [127], [170], [171]. Electrospun fibres were

prepared from polyvinyl chloride (PVC). PVC is a widely used polymer due to its superior properties such as safety, biocompatibility, chemical stability, transparency and durability [172].

The specific objectives of this chapter are to:

- Produce and characterise size-tuneable silica nanoparticles manufactured by changing ammonium hydroxide volume, TEOS volume and using seed growth technique. In addition, Fluorescent silica particles covalently linked to fluorophore molecules, such as Oregon green (OG), 5-(6)-carboxyfluorescein (FAM), 5-(and-6)-carboxytetramethylrhodamine (TAMRA) and Alexa Fluor 647, were prepared for super-resolution fluorescence microscopy performance test slide application.
- Optimise polyvinyl chloride (PVC) electrospinning process parameters to produce beads-free smooth electrospun fibres.
- Prepare silica nanoparticle-fibre hybrids using a colloidal electrospinning manufacturing process.
- Apply advanced analytical techniques to characterise the different physiochemical properties of the silica-PVC hybrid systems.
- Examine the feasibility of using fluorescent silica particle-PVC fibre hybrid systems as a product to test the performance for super-resolution fluorescence spectroscopy.

3.3. Materials and Methods

3.3.1. Materials

Reagents: Tetraethylorthosilicate (TEOS, $\geq 99\%$), 3-aminopropyl-triethoxysilane (APTES, 98%), ammonium hydroxide solution (NH_4OH , 28-30 %) and polyvinyl chloride (PVC, $M_w \approx 233,000$) were purchased from Sigma-Aldrich, UK. Tetrahydrofuran (THF, HPLC grade) and ethanol absolute (99.5%) were obtained from Fisher Scientific.

Fluorophores: The succinimidyl ester derivatives of Oregon Green 488 (OG), 5-(and-6)-carboxyfluorescein (FAM), 5-(and-6)-carboxytetramethylrhodamine (TAMRA) and Alexa 647 were obtained from Invitrogen, USA.

Instruments used for particles washing and drying: Centrifuge (Hermle Z300), Rotary evaporator (Buchi Rotavapor R-200).

Electrospinning apparatus: 10 ml syringes and 18G blunt needles were obtained from BD Falcon (UK), a syringe pump (Harvard Apparatus PHD 200), voltage supply box (Genvolt model 71320), alligator electrical clips purchased from RS Components (UK), 10x15 cm stainless steel collector plate.

3.3.2. Plain Silica Particles Preparation: Changing NH_4OH and TEOS

Concentration

Plain silica particles were prepared according to the Stöber method [121]. Solutions of absolute ethanol (16.75 ml) and ammonium hydroxide (30% w/v, 0.3-5.0 ml) were mixed under stirring for 15 minutes. The reactions were initiated through the addition of the monomer tetraethyl orthosilicate (TEOS) (0.5-1.5 ml) at a controlled dropwise rate using the syringe pump.

All reactions occurred at room temperature and were left under stirring for 24 hours (48 hours for 0.3, 0.5 ml samples) before being washed and purified in absolute ethanol (30 ml) using centrifugation (3 times, 6000 rpm, 15 minutes). Following the final wash, the particles were re-suspended in 10 ml of absolute ethanol and dried using rotary evaporation. Dried particles were stored at 4°C.

A seeded growth technique described by Bogush et al. [123] was used for the preparation of larger particles. Primary seed suspensions were prepared as described above, using 1.5 ml of tetraethyl orthosilicate (TEOS) with 2.0 ml, 3.0 ml, 4.0 ml and 5.0 ml of 30% ammonium hydroxide solution. After the reaction completion (24 hr after the 1st addition of TEOS), another addition of 1.5 ml TEOS with 0.27 ml water (1:2 molar ratio) was performed, and the suspension was left to stir for another 24 hours. Particle washing, purification and drying were performed as described above. A summary of silica particle preparation methods is presented in Figure 3.6.

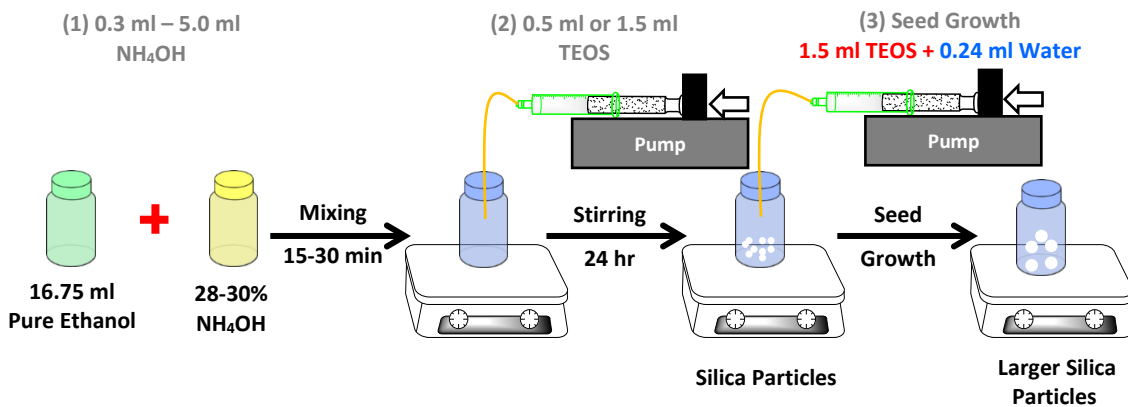


Figure 3.6: Experimental set-up for silica particle preparation.

3.3.3. Fluorescent Silica Nanoparticle Preparation

Fluorescent silica nanoparticles were produced by incorporating APTES-fluorescent conjugates into the silica particle matrix via covalent bonds. Fluorophore conjugation to APTES, a chemically active silane compound, was first performed by separately dissolving 10 mg of the

succinimidyl ester derivatives of OG, FAM, TAMRA and Alexa 647 into 1.0 mL of absolute ethanol. APTES was then added to each dye solution at a dye: APTES molar ratio of 1:2 (Volume= 18 μ l). The mixture was left stirring for 24 hours in the dark [173]. Fluorescence silica nanoparticles were prepared by stirring 16.75ml ethanol with 0.75 ml of ammonium hydroxide (28-30%) for at least 15 -30 minutes. Then, 100 μ l of fluorophore-APTES conjugates were added to the mixture and stirred for 24 hours in the dark. Finally, 0.5 ml of TEOS was added drop-wise to the reaction mixture and stirred for another 24 hours. Particle washing, purification and drying were performed as described previously. Fluorescence silica nanoparticles were kept in the dark at 4°C.

3.3.4. Preparation of Silica-PVC Hybrids

Silica/PVC dispersions were prepared by dispersing 1.0-5.0 % w/v of silica particles in 2.0 ml HPLC grade tetrahydrofuran (THF). Hereafter, PVC was added gradually to the THF silica nanoparticles to form a suspension with a final concentration of 10% w/v PVC. The suspension was then stirred for a minimum of 5.0 hours at room temperature to ensure a homogenous distribution of silica particles and complete dissolution of PVC.

The particle-fibre hybrids were prepared by a colloidal electrospinning method at ambient conditions. The silica/PVC dispersions were loaded in a 10 ml syringe and dispensed through an 18-gauge blunt end needle tip at a flow rate (1.0 ml /hr) using a syringe pump (Harvard Apparatus, PHD 2000) with a voltage of 15 kV. A distance of 15 cm was kept between the needle tip and a grounded stainless-steel collector plate. The scaffolds were air-dried in a fume hood overnight to allow the residual solvent to evaporate.

3.3.5. Analytical Characterisations

3.3.5.1. Dynamic Light Scattering (DLS)

The mean particle diameter and polydispersity index (PDI) were measured by dynamic light scattering (DLS) (Zetasizer Nano ZS, Malvern Instrument Ltd) equipped with a 5mW He-Ne laser source (633nm). A non-invasive backscattering configuration (Detection angle 173° with respect to the incident laser light) was used to collect measurements. Silica particles were suspended to a concentration of 5 mg/ml in deionised water.

3.3.5.2. Transmission Electron Microscopy (TEM)

The morphology and the size of the particles were determined by transmission electron microscopy (TEM) (FEI Technai 12, Biotwin). A drop of sufficiently concentrated re-suspended silica nanoparticles in water (1 mg/ml) was deposited onto Formvar-coated Cu grids (EM Resolutions LTD, United Kingdom). The suspension was allowed to settle on the grid for 10-15 minutes after which excess liquid was removed with filter paper. The median diameter and size distribution of the silica particles were determined using ImageJ (ImageJ 1.5i) software.

The TEM was used to investigate the morphology of the particles-fibres hybrid and to image the encapsulated silica particle. Gold finder TEM grid (EM Resolutions LTD, UK) was placed on the collector plate in order to electrospun directly on the grid. After 5.0 minutes, the grid was removed, and the electrospinning run was continued.

3.3.5.3. Scanning Electron Microscopy (SEM)

Morphology of electrospun fibres with incorporated silica particles was also imaged by scanning electron microscopy (SEM) (JEOL 6060LV, UK). Small samples of scaffolds were placed onto 12 mm carbon adhesive tabs and fixed onto aluminium SEM stubs (Agar Scientific, UK). Samples were gold coated using sputter coater (Leica EM SCD005, Germany) at 25 mA, 10^{-3} Vacuum for 300 seconds. Images were acquired using voltages between 20-30 kV and a working distance of 10 mm. The average fibres diameter was calculated from three different experiments using ImageJ software.

3.3.5.4. Transmission Electron Microscopy/ Energy dispersive X-ray (TEM/EDX) Analysis

Elemental mapping of the particle-fibre was performed using an Oxford Instruments XMax 80 T silicon drift detector with INCA Energy 250 Microanalysis system attached to a high-resolution TEM (JEOL 2100F) operating at 200 kV. STEM images were acquired using the JEOL digital STEM system.

3.3.5.5. Raman Spectroscopy

Raman spectra of pure bulk silica particles, plain PVC fibres and particle-fibre hybrids were acquired using a Horiba LabRAM HR confocal microscopy/spectroscopy. A near-IR laser (785 nm) of 250 mW power was employed. Spectra were acquired using a 50× objective lens and a 300 μm confocal hole. Raman spectra were obtained using a SYNAPSE CCD detector (1024 pixels). The particle-fibre hybrids samples on TEM finder grids were placed on a quartz slide under the

objective of the Raman microscopy. Single point Raman spectrum in the spectral range from 100 to 1500 cm^{-1} was collected for at least 30 seconds and repeated once to remove any high-intensity spikes.

3.3.5.6. Time of Flight Secondary Ion Mass Spectroscopy (ToF-SIMS)

The particle-fibre hybrids electrospun directly on TEM finder grids were mounted on double-sided adhesive tape to produce an immobilised surface suitable for ToF-SIMS analysis. Prior to analysis, Zeta 20 true colour 3D optical profiler (Zeta Instruments, USA) was used to image the sample after being mounted. The optical profiler was employed to select the analysis area containing high-density silica-PVC hybrids. The surface characterisation of the particle-fibre hybrids was acquired using a ToF-SIMS IV instrument (ION-TOF GmbH., Münster, Germany) equipped with a bismuth liquid metal ion gun and a single-stage reflectron analyser. Operating conditions utilised Bi_3^+ cluster ion source with primary ion energy of 25 kV and a pulsed target current of approximately 1.0 pA at a pressure of 10^{-8} mbar. A flood gun producing low energy electrons (20 eV) was used to compensate for surface charging caused by the positively charged primary ion beam on the insulating sample surface. Areas ranging from $50 \times 50 \mu\text{m}$ to $500 \times 500 \mu\text{m}$ were raster scanned at a resolution of 256×256 pixels. The total primary ion beam dose for each analysed area was kept below 1×10^{12} ions cm^{-2} , ensuring static conditions. Silica and PVC were identified using SiO_2^- ($m/z = 59.96$), and Cl^- ($m/z = 34.95$) respectively. Data in the negative secondary ion polarities were collected and analysed using SurfaceLab 6 (IONTOF GmbH) software.

3.3.5.7. Super-Resolution Fluorescence Microscopy

Particle-fibre hybrids were electrospun directly on high precision microscope coverslips with thickness No. 1.5H (Thickness of $170 \mu\text{m} \pm 5 \mu\text{m}$). Polyvinyl alcohol (PVA) and glycerol mounting medium or water was added to the surface of the coverslip and placed on a microscope slide for analysis.

Super-resolution fluorescence spectroscopy STORM imaging has been done on a Zeiss Elyra PS.1 microscope equipped with Zen 2012 acquisition and processing software. Acquisition parameters: microscope objective alpha Plan-Apochromat 100x/1.46 Oil DIC M27 Elyra; excitation lasers were 642 nm at 50.0 %, 405 nm at 0.0700 %, detection filter set LP 655, imaging frequency was 50Hz at camera gain of 200.

Image processing has been done in Zen 2012 Black using the PALM module. The 10000 images were processed where single molecule events were identified with a peak intensity to noise value set to 6. Drift correction was applied using model-based automatic, eight segments settings. To avoid oversampling the same molecule Group filter was set to max on time 5, off gap 10, capture radius 2, equiv. of 20 nm. Other filters applied include localisation precision 2-40 nm, number of photons 350-5000.

3.4. Results and Discussion

Fabrication and characterisation of silica nanoparticles (SNPs) and polyvinyl chloride (PVC) nanofibre hybrids using the colloidal electrospinning process were performed for designing calibration standards for super-resolution fluorescence microscopy. This was done in four stages; firstly, a method for preparation of silica nanoparticles with different sizes was optimised. In addition, fluorescent silica particles covalently linked to different fluorophore molecules were also prepared. Secondly, particle-fibre hybrid systems were fabricated in different morphologies using colloidal electrospinning. Thirdly, a combination of advanced analytical techniques was applied to characterise the hybrid systems obtained. Finally, calibration standard design for super-resolution fluorescence microscopy based on incorporating fluorescent silica nanoparticles into electrospun fibres was evaluated.

3.4.1. Synthesis and Characterisation of Size-Tuneable Plain Silica

Nanoparticles

To determine the amenability to load nanoparticles within electrospun fibres and to identify the limitation towards imaging and spectroscopic analysis, silica nanoparticles were produced in a variety of sizes.

The production of silica nanoparticles via the Stöber method [121] is highly influenced by the volumes of catalyst (ammonium hydroxide), and silica monomer (TEOS) added during synthesis. Therefore, to enhance the understanding of the particle production method and to determine the effect of individual parameters on the resultant particle size, each parameter was modified in turn, while maintaining the volume and concentration of all other parameters at constant values.

3.4.1.1. Effect of Ammonium Hydroxide (NH₄OH) Volume on Nanoparticle Size

Through controlled addition of different volumes of ammonium hydroxide alone, silica nanoparticles with hydrodynamic diameters ranging from 22 ± 1.2 nm to 210 ± 18 nm (mean particle size \pm SED) were produced, such that addition of ammonium hydroxide above 2.0 ml did not cause a significant increase in nanoparticle diameter (Figure 3.7-A). The polydispersity index (PDI) of all batches were <0.1 measured by DLS technique. Generally, polydisperse nanoparticles are considered to have PDI values > 0.7 , while the PDI values obtained for polystyrene latex standards used to calibrate instruments are ~ 0.05 [174]. Therefore, the silica nanoparticles produced by modifying the ammonium hydroxide volume are considered to have a relatively narrow size distribution [44]. The standard error value (error bars) measured from at least three individual batches of silica nanoparticles demonstrated the reliability and reproducibility of the production method. However, there was a tendency toward wide size difference across batches with the higher ammonium hydroxide volumes, which has been reported in other studies [121], [123].

Silica nanoparticle imaging using TEM was performed to confirm the DLS data and study the morphology of the nanoparticles. Silica nanoparticle size, when imaged using TEM showed that particle size increased at a greater degree during the addition of 0.3 – 1.0 ml of ammonium hydroxide, when compared to the addition of ammonium hydroxide > 1.0 ml, which correlated reasonably well with DLS data (Figure 3.7-B).

However, TEM indicated a smaller size than that determined by DLS as illustrated in Figure 3.8-A. The size of nanoparticles measured using DLS is typically larger than that determined using electron microscopy. The difference in the particle size values is attributed to the fact that DLS

and TEM measure totally different aspects of the particulate systems. DLS produces an intensity-based distribution, which is obtained from the intensity of the light scattered by the measured particles. This intensity size distribution is proportional to the particle size to the power six. Therefore, the presence of larger particles may contribute to an increase in light scattering, shifting the average particles size towards larger values. On the other hand, TEM probes the electron rich area of a particle and produces a number-based distribution. In addition, DLS measures hydrodynamic diameters, which are the size of a hypothetical hard sphere that diffuses in the same fashion as that of the particle being measured, whereas TEM measures the actual physical dimensions of the dried particle [129], [170], [175].

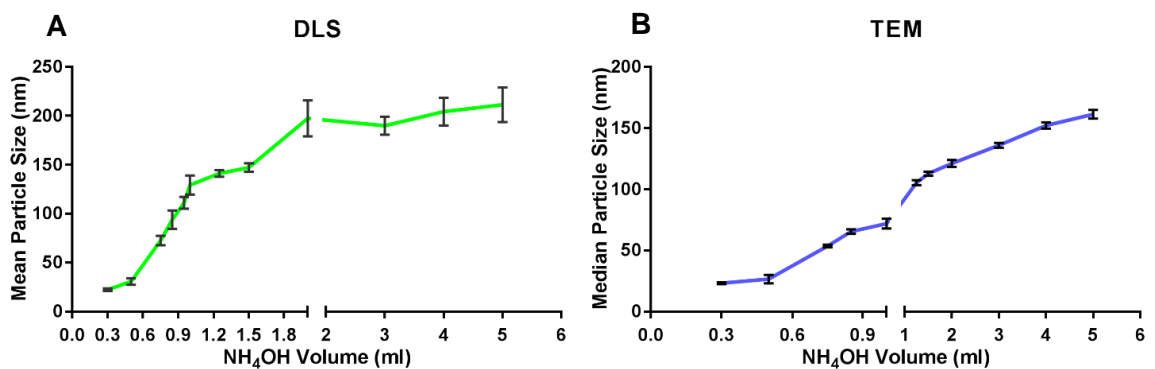


Figure 3.7: The effect of ammonium hydroxide volumes on mean particle diameter measured by (A) DLS and (B) TEM; n=3.

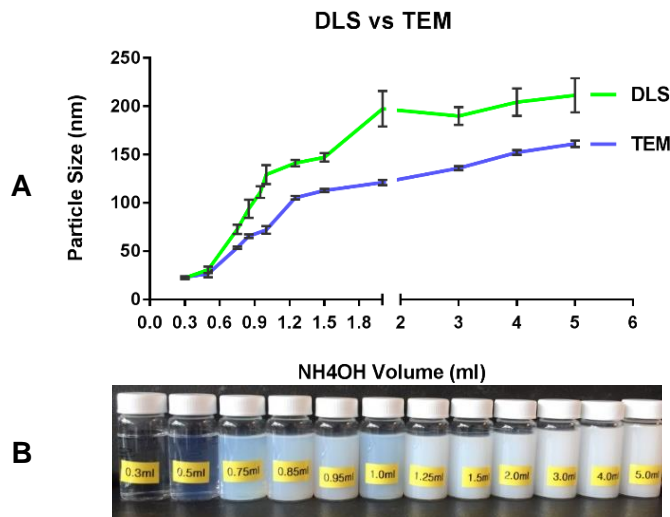


Figure 3.8: (A) Comparison of mean particle size for silica nanoparticles measured by DLS (Green line) and TEM (Blue line). (B): A picture of nanoparticle suspension vials with different ammonium hydroxide volumes.

Furthermore, the particles produced with ammonium hydroxide volumes of less than 0.5 ml were irregularly shaped spheres (Figure 3.9).

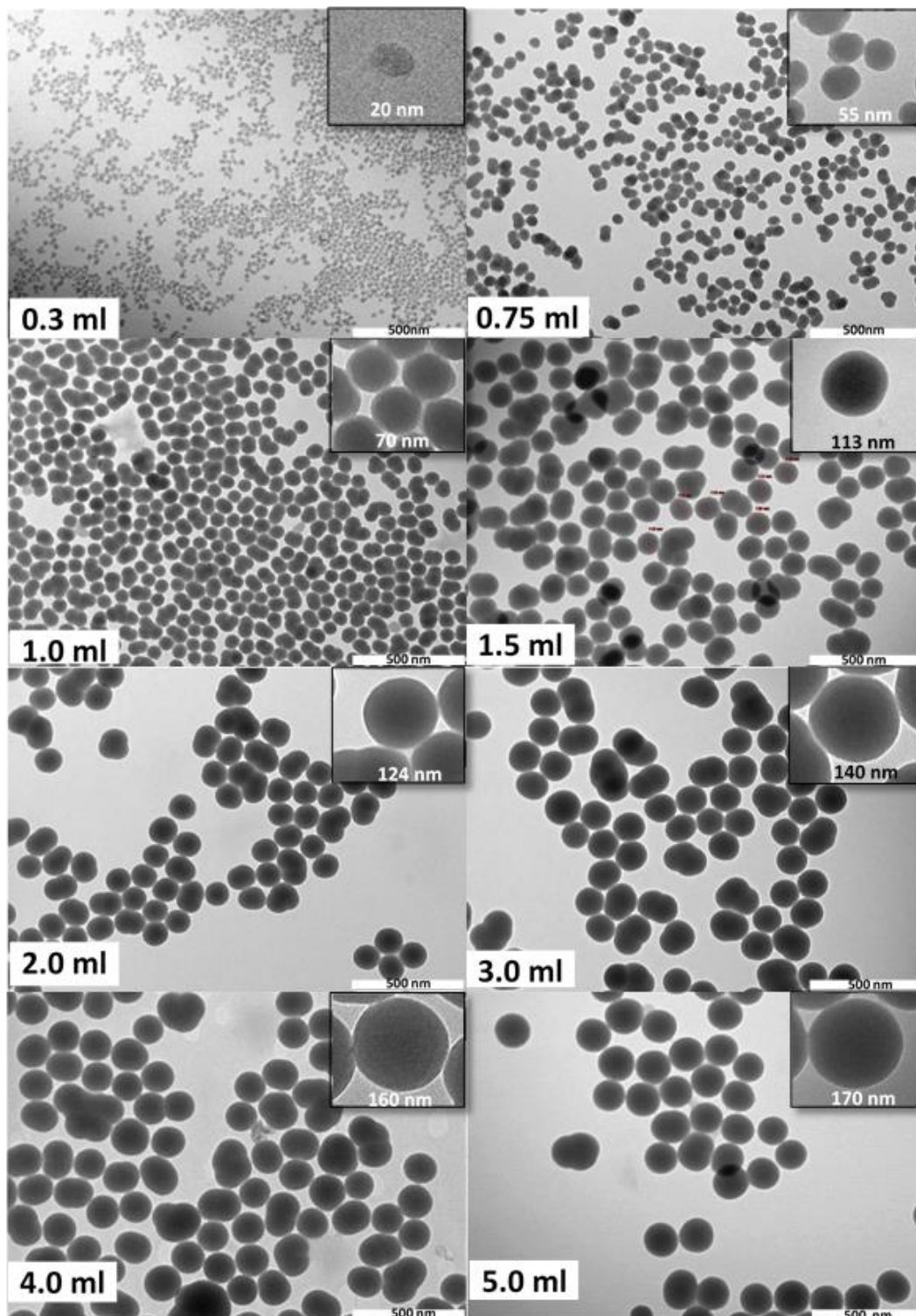


Figure 3.9: TEM images of size-controllable silica particles produced using different amounts of NH₄OH.

The catalytic ability of ammonium hydroxide can explain the steady increase in particle size and irregularly shaped spheres. Ammonium hydroxide accelerates the hydrolysis and condensation rate of TEOS [126], [128]. At low volumes of ammonium hydroxide reaction rates are slow, which produces small particles, whereas, at higher volumes, reaction rates are accelerated and produce large particles [121].

As the experiment proceeds, the available TEOS supply is exhausted, and the particle growth is limited (Figure 3.9). Figure 3.9 also shows the particle size has not maximised, although the degree of particle growth upon addition of ammonium hydroxide >1.0 mL has decreased, such that larger volumes of TEOS would be required to produce nanoparticles greater than 200 nm.

3.4.1.2. Effect of TEOS Volume and Seed Growth Technique on Nanoparticle Size

Another approach that could augment nanoparticle size is by increasing the volume of TEOS in the reaction mixture. This can be achieved by either increasing the initial volume TEOS at the start of the reaction or by adding extra TEOS, after the primary phase of the reaction reaches the point where all the available monomers have been used (Seed growth).

To study the effect of increasing TEOS amount on the silica particle size, 0.5 ml and 1.5 ml of TEOS were used at 2.0ml, 3.0ml, 4.0ml and 5.0ml of NH₄OH volume. Increasing the initial volume of TEOS from 0.5 ml to 1.5 ml increased the particle size from 200 ± 18 nm to 380 ± 12 nm (Figure 3.10). These results were in agreement with previous studies that have shown an increase in particle size upon increasing the initial amount of TEOS [128]. All batches have a low polydispersity index (<0.1), which indicates a relatively narrow size distribution for all samples.

The standard error deviation values in the mean value of particle size (error bars) indicate the reliability and reproducibility of the fabrication method.

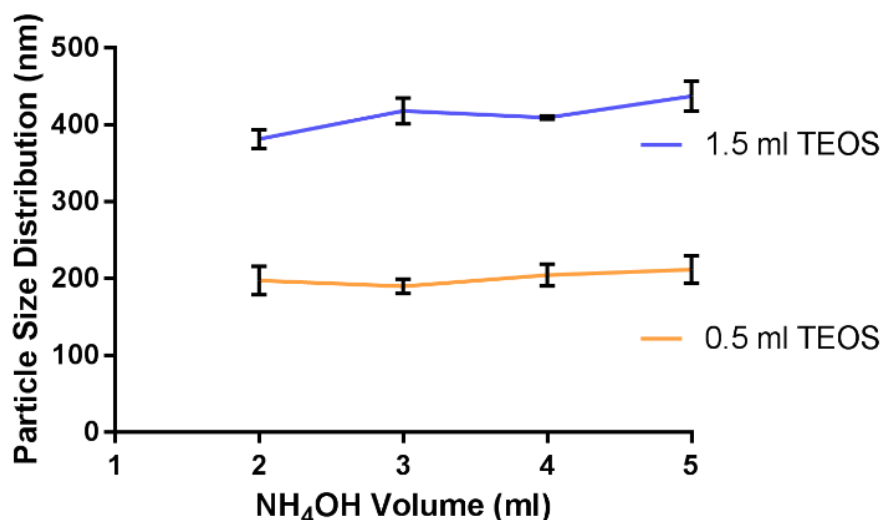


Figure 3.10: The effect of increasing TEOS amount on silica mean particle size measured by DLS; n=3.

The seed growth technique was first described by Bogush and co-workers [123]. Extra TEOS and water were added after 24 hours of the primary seed suspension preparation prepared in the previous section (Section 3.4.1.1). The seed growth technique resulted in increasing the particle size to around 500 nm when 4.0ml of NH₄OH was used. (Figure 3.11-C). The images also show some particle clusters (Orange arrows in Figure 3.11-B&C) that indicate the possibility of aggregation when using larger amounts of ammonium hydroxide and TEOS and explain the high value of PDI in the DLS data (not shown). Further increase in the NH₄OH volume (volume = 5.0ml) resulted in the growth of a second population of silica particles in both the primary seed and the seed growth suspension (Figure 3.11-D). Similar findings have been reported in previous works [123].

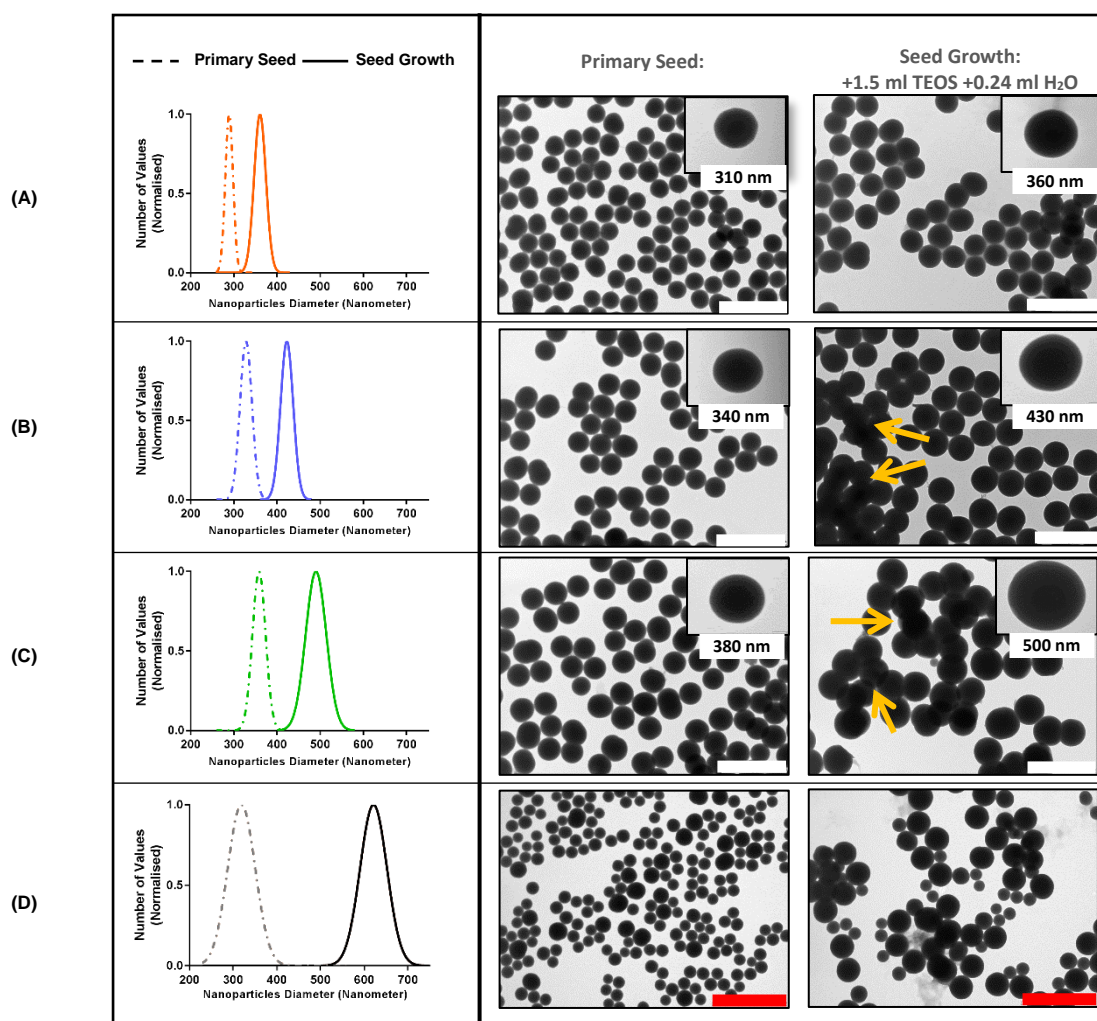


Figure 3.11: Particle size distribution (Left column) and TEM images (Right column) of silica particles prepared by seed growth technique: (A) NH_4OH volume = 2.0 ml (B) NH_4OH volume = 3.0 ml (C) NH_4OH volume = 4.0 ml (D) NH_4OH volume = 5.0 ml. Particle size distribution and median particle diameter obtained from TEM images using ImageJ. White Scale Bar= 1000 nm/ Red Scale Bar= 2000 nm

The previous findings can be explained by understanding how nanoparticles are normally formed and the role of fabrication process parameters in controlling the rate of nucleation (Hydrolysis) and the rate of growth (Condensation). Von Weimarn and Ostwald ripening theories are widely used to elucidate how colloidal stable particles are formed [176], [177]. As stated by Von Weimarn, a supersaturated solution of the monomers/molecules is required to induce nucleation and form primary unstable small nuclei to reach equilibrium [177]. Ostwald ripening theory explained how these nuclei combined to form more thermodynamically stable secondary larger nuclei in order to minimise the surface to area ratio [176]. As a result, the synthesis of size-

tuned silica particles can be controlled by the supersaturation level of silica source (i.e. TEOS) and the nucleation rate, controlled by the amount of NH_4OH [121]. These two parameters will affect the final particle size and the batch monodispersity.

During the synthesis of silica particles, changing the ammonium hydroxide volume with a limited amount of TEOS (Volume=0.5 ml or 1.5 ml), the supersaturation rate generated from the hydrolysis of the TEOS was thoroughly exhausted in the growth of primary particles. Consequently, the primary particles grow proportionately as a function of NH_4OH amount resulting in monodisperse particles. However, further addition of TEOS in the seed growth technique at high NH_4OH concentration led to an increase in the solution monomers supersaturation beyond the critical level. Therefore, the rate of hydrolysis was higher than the rate of consumption for particle growth, resulting in the generation of secondary particles to reach equilibrium and the formation of polydisperse batches.

In summary, silica particles of relatively acceptable size distribution for our application can be reproducibly manufactured over a size range of 20-650 nm diameter.

3.4.2. Synthesis and Characterisation of Fluorescent Silica Nanoparticles

Silica fluorescent nanoparticles were produced to be later incorporated into the electrospun fibre and characterised using super-resolution fluorescence microscopy.

Fluorescent particles were synthesised by incorporating APTES-fluorophore conjugates into a nanoparticle matrix via covalent bonds. This preparation method offers the possibility of incorporating different types of fluorophores into silica particles for different applications. Commercially available fluorophores, such as Oregon Green® (OG), 5(6)carboxyfluorescein (FAM), 5(6) carboxytetramethylrhodamine (TAMRA) and Alexa 647 have been selected to be

incorporated in silica matrix due to their wide analytical and biological applications [178]–[180]. In addition, Alexa 647 fluorophore has photoswitchable or photoactivatable properties that can be highly advantageous for super-resolution imaging methods such as stochastic optical reconstruction microscopy (STORM) [160], [163]. As a result, Alexa647-silica nanoparticles with a diameter below 100 nm (Below the optical diffraction limit) can be individually localised by switching between a fluorescent and a dark state at different time points using STORM method.

In order to obtain particle size below the optical diffraction limit (<100nm), 0.75ml NH₄OH and 0.5 ml TEOS were used to obtain < 100 nm silica nanoparticles based on previous section findings (Section 3.4.1.1). The hydrodynamic diameter of OG, FAM, TAMRA and Alexa 647 silica nanoparticles were 76.5 ± 2.5 nm, 81.3 ± 5.8 nm, 85.2 ± 6.0 nm and 78.7 ± 1.1 nm, respectively (Figure 3.12-A).

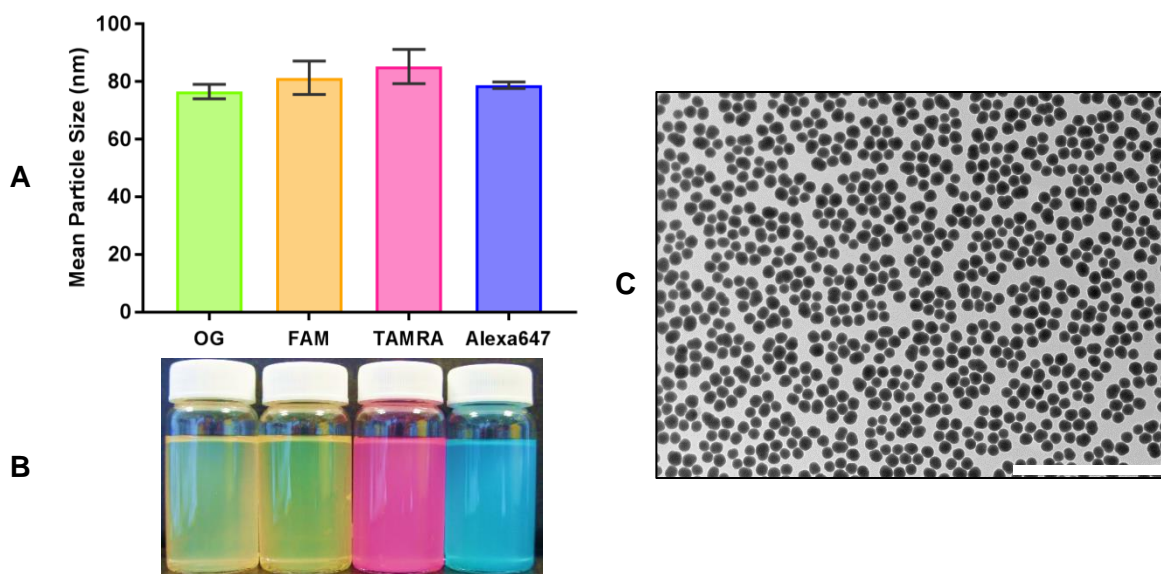


Figure 3.12: (A) The mean particle diameter (error bar= SED) of different fluorophore silica nanoparticles measured by DLS; n=3
(B): A picture of particle suspension vials with different fluorophore dye.
(C): Representative TEM image of Alexa 647 silica nanoparticles (Scale bar=1000nm).

TEM images show monodispersity and well-spherical shape morphology (Figure 3.12-C). The polydispersity index (PDI) of all batches were <0.1. The standard error value (error bars)

measured from at least three individual batches of silica nanoparticles demonstrated the reliability and reproducibility of the production method.

3.4.3. Fabrication of Particle-Fibre Hybrid using Colloidal Electrospinning

Technique

Four different plain silica particle diameters (< 100 nm, 200 nm, 400 nm and 650 nm), as well as fluorescence silica particles (diameter < 100 nm), were taken forward to be incorporated into the electrospun nanofibres to obtain the particle-fibre hybrids amenable to analysis.

3.4.3.1. Optimising PVC Electrospun Fibres

Initially, the optimisation of the electrospinning process was performed by tuning multiple parameters. The electrospinning process optimisation is necessary to obtain smooth and beads free fibres to ensure that the change in fibres morphology is due to particles addition only.

Electrospinning parameters, such as polymer concentration, electrospinning solvent, working distance, voltage and flow rate were optimised to obtain smooth, uniform and nanosized fibres in the scaffolds. The starting parameters for PVC were obtained from the literature where PVC has been electrospun previously [181]–[183]. Then multiple trials were conducted to optimise the process and obtain the desired fibre size and morphology.

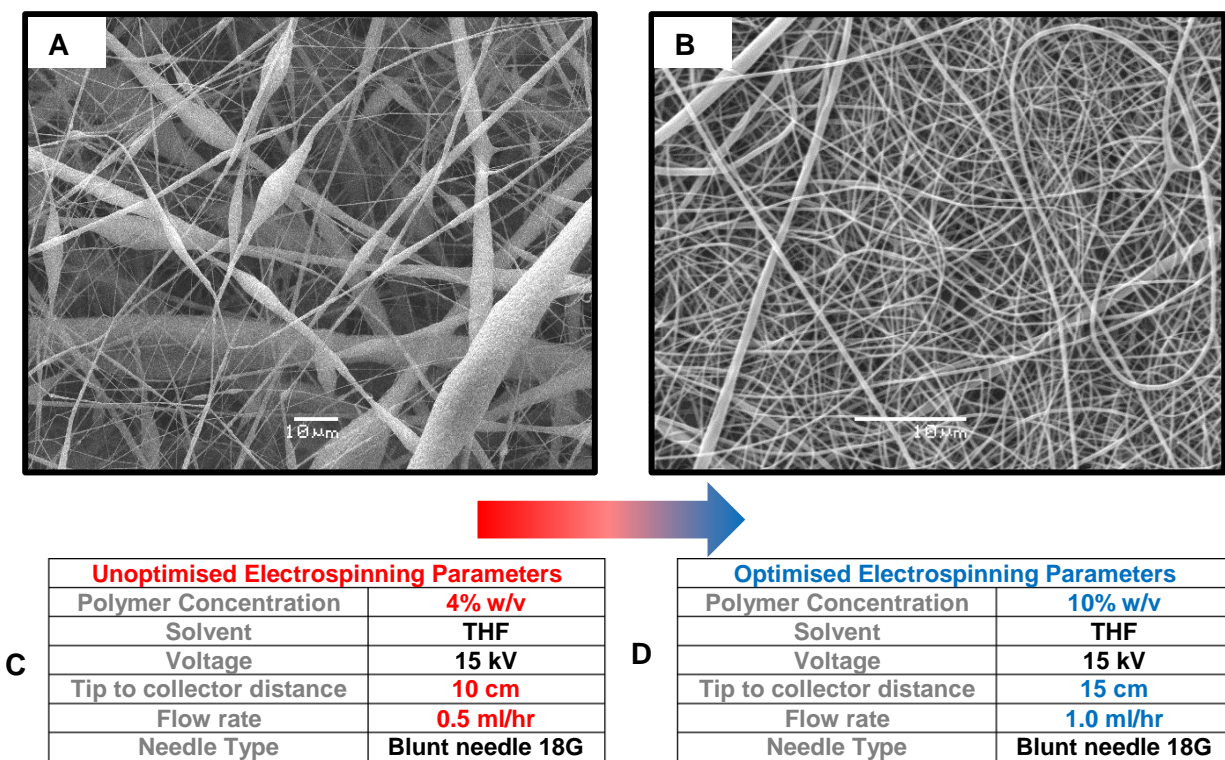


Figure 3.13: Effect of electrospinning parameters on PVC fibre morphology and diameter. Representative SEM image of PVC fibres electrospun under (A) unoptimised and (B) optimised electrospinning conditions. Scale bar = 10 μm

The initial investigation into the electrospinning parameters focussed on the PVC concentration, the distance between the tip and the collector and the flow rate. When attempting to spin PVC fibres at low polymer concentration (4% w/v), 10 cm distance and 0.5 ml/hr flow rate, highly beaded fibres with wide fibre size distribution were produced (Figure 3.13-A). Increasing the polymer concentration to 10% w/v caused a visible morphological improvement of the resultant fibres. Figure 3.13-B shows smooth and beads-free fibres across the scaffold. Doubling the flow rate to 1.0 ml/hr was necessary to prevent the solution from drying and blocking the syringe needle when electrospinning 10% w/v PVC solution.

The optimised electrospinning parameters selected to manufacture uniform, beads-free PVC fibres are listed in Figure 3.13-D. The fibre diameter was 271 ± 12.4 nm (median \pm SED) with a relatively narrow range of 124 nm to 400 nm as shown in Figure 3.14.

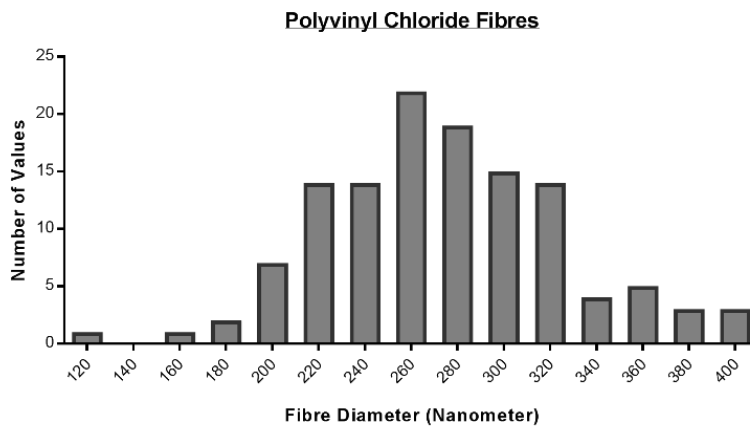


Figure 3.14: The fibre size distribution of PVC scaffolds obtained from SEM images using ImageJ. (100 measurements)

The beads-free fibre morphology and the narrow mean fibre diameter obtained using the optimised electrospinning conditions is suitable for investigating any change in fibre morphology induced by adding different sizes and concentration of silica nanoparticle prepared in section 3.4.1.

3.4.3.2. Incorporation of Silica Nanoparticles into Electrospun PVC Fibres

Four different silica particle diameters (< 100 nm (+fluorescence dye), ~ 200 nm, ~ 400 nm and ~700 nm) were incorporated into the electrospun nanofibres to obtain the particle-fibre hybrids required. The selection of the particle diameter was based on having silica particle sizes of smaller (<100 nm), comparable (200 nm) and larger (400 nm and 700 nm) than the mean fibre diameters. In addition, the effect of the particle concentration on hybrid morphology was investigated where silica particles were loaded at low (1% w/v) and high (5% w/v) concentration. The hybrid structures morphologies were imaged using both SEM and TEM.

Figure 3.15 demonstrated the encapsulation of silica nanoparticles < 100 nm in electrospun PVC fibres. There was no sign of beading or any change in fibre morphology due to the nanoparticle addition found under SEM analysis as seen in Figure 3.15-B. However, TEM

analysis was able to resolve and locate nanoparticles incorporated into electrospun fibres (Figure 3.15 -A). The absence of beading or any change in the fibre morphology due to the relatively small particle size compared to the fibre size reduced the ability of the SEM to characterise the samples (Figure 3.15-B). Inversely, the transmission capability of the TEM combined with the significant difference in electron density between particles and fibres lead to successfully resolve the encapsulated particles inside the fibres. As shown in Figure 3.15-C&D, small particles tended to aggregate into clusters of particles, especially at a high concentration of silica nanoparticles. This close packing of particles was reduced by decreasing the silica particles concentration to 1% w/v, where separated particles can be seen across the samples. Particle aggregation can be explained by the relatively large surface energy of the small particle and the relatively larger diameter of fibres that lead to packing the particles together. These results agree with similar work reported previously by Jin et al. [156].

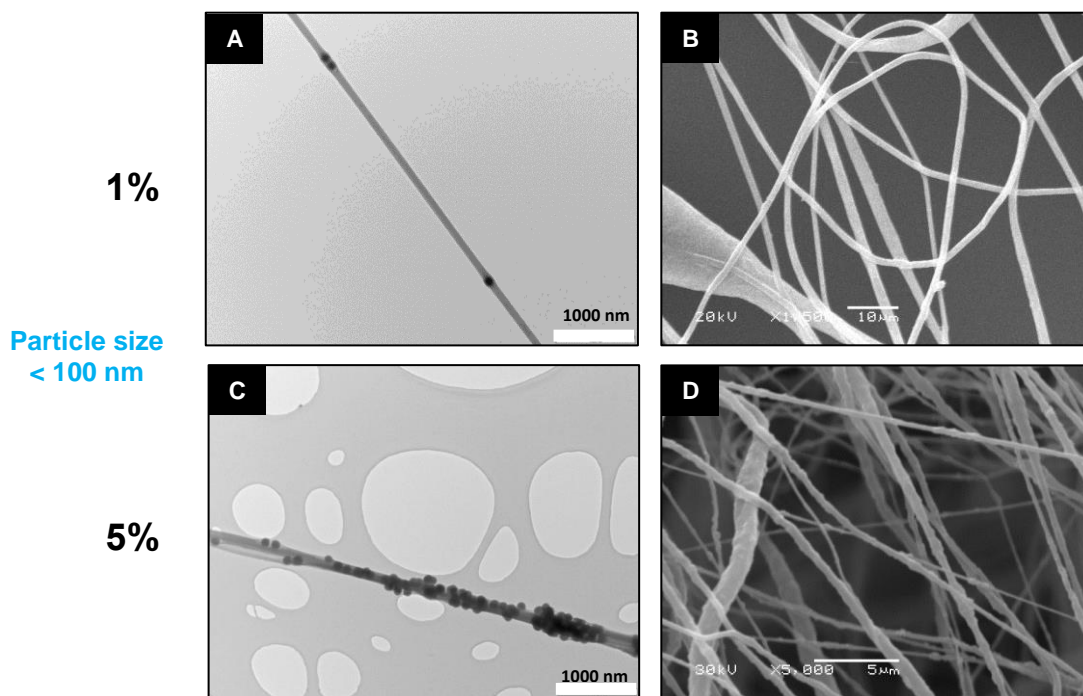


Figure 3.15: The influence of < 100 nm silica particle concentration on the morphology of silica-PVC hybrids: Top: (A) TEM (B) SEM images of particle-fibre hybrids at silica particle concentration = 1% w/v- Bottom: (C) TEM (D) SEM images of particle-fibre hybrids at silica particle concentration= 5% w/v

Increasing the particle diameter, to become comparable to or larger than the diameter of the fibres, led to an altered morphology of fibres. In the SEM images, it was noticed that an area of bulging or swelling of the fibres was formed near the particle's locations, which was not the case in smaller particles (<100 nm).

The 200 nm silica particles at high concentration tended to aggregate to form blackberry-like structures, which can be observed by SEM and TEM (Figure 3.16-C&D). However, after decreasing silica particles concentrations, necklace-like structures were formed with a distinctive separation distance between individual particles (Figure 3.16-A&B).

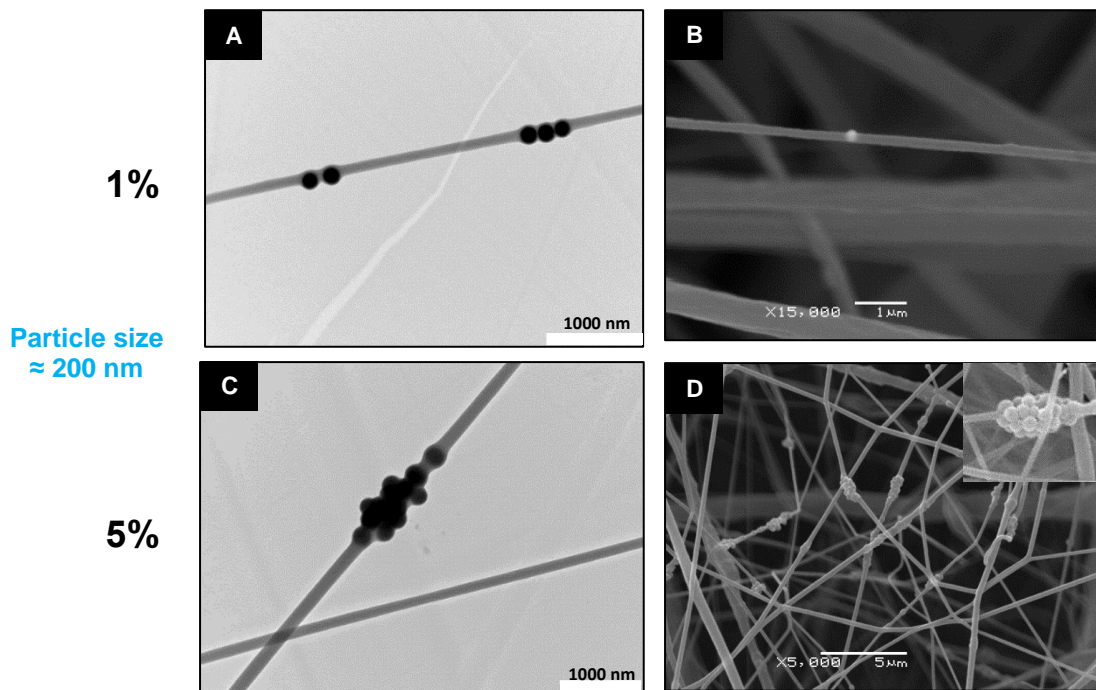


Figure 3.16: The influence of ~200 nm silica particle concentration on the morphology of silica-PVC hybrids: Top: (A) TEM (B) SEM images of particle-fibre hybrids at silica particle concentration = 1% w/v- Bottom: (C) TEM (D) SEM images of particle-fibre hybrids at silica particle concentration = 5% w/v- The insets are magnified SEM images

Similarly, for ~ 400 nm and ~700 nm particles (Figure 3.17), the morphology of fibres and the separation distance between particles were affected by the concentration of silica particles. At low silica concentration, the distance between particles was relatively large (2.0-5.0 μm) and the structure resembled beading (i.e. necklace shape) as shown in Figure 3.17-A & E.

Increasing the silica particles concentration led to a shrinkage in the distance between particles (Figure 3.17-C & G). Few blackberry-like structures were formed using ~ 700 nm particles at high concentration, which could be due to the aggregation formed during the particle preparation via seed growth technique in section 3.4.1.2.

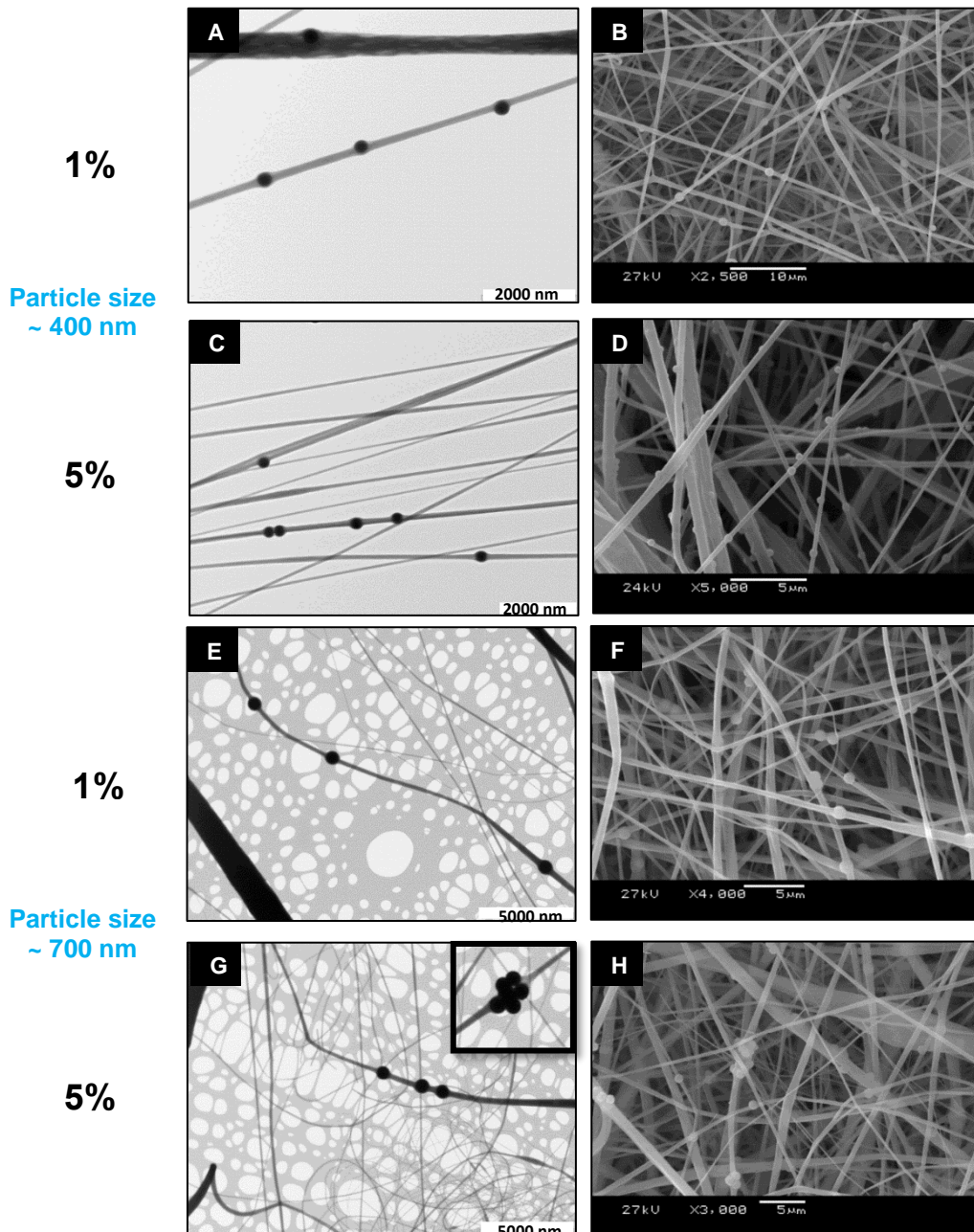


Figure 3.17: The influence of silica nanoparticle size and concentration on the morphology of silica-PVC hybrids: At silica particle concentration = 1% w/v: TEM and SEM images of particle-fibre hybrids prepared using ~ 400 nm (A&B) and ~ 700 nm (E&F) silica nanoparticles. At silica particle concentration = 5% w/v: TEM and SEM images of particle-fibre hybrids prepared using ~ 400 nm (C&D) and ~ 700 nm (G&H). The insets are magnified TEM images.

3.4.4. Advanced Characterisation of Particle-Fibre Hybrids

Characterisation of the hybrid systems is essential to understand and analyse various facets of particle-fibre hybrids such as the chemical interaction between the hybrid components and the effect of process parameters on the morphology and properties. In addition, analysis of a wide spectrum of properties is essential to ascertain the application potential of the hybrid systems.

In section 3.4.3.2, the effect of process parameters on the morphology was investigated using scanning electron microscopy (SEM) and transmission electron microscopy (TEM). In this section, further characterisation of the different particle-fibre hybrids structures fabricated in section 3.4.3.2 will be described. A wide range of advanced analytical techniques was applied to obtain elemental (EDX analysis), vibrational (Raman spectroscopy) and surface (ToF-SIMS) information of the hybrid systems. In addition, super-resolution fluorescence microscopy characterisation of the Alexa 647 silica-fibre hybrids was performed to explore the potential of this hybrid structure to be used as a calibration standard and a test sample to evaluate the performance of super-resolution microscopes.

3.4.4.1. Transmission Electron Microscopy/Energy Dispersive X-ray

Spectroscopy

Hybrid elemental composition and distribution were investigated using EDX combined with TEM. Scanning TEM (STEM) and EDX elemental mappings confirmed the composition of different particle-fibre hybrid structures with carbon, chlorine, oxygen and silicon as the principal elemental components (Figure 3.20). The silicon (Si) and oxygen (O) maps characterise the silica

particle surface, revealing that the entire particle's surface consists of Si and O. The carbon (C) and chlorine (Cl) maps support the composition of the PVC fibre.

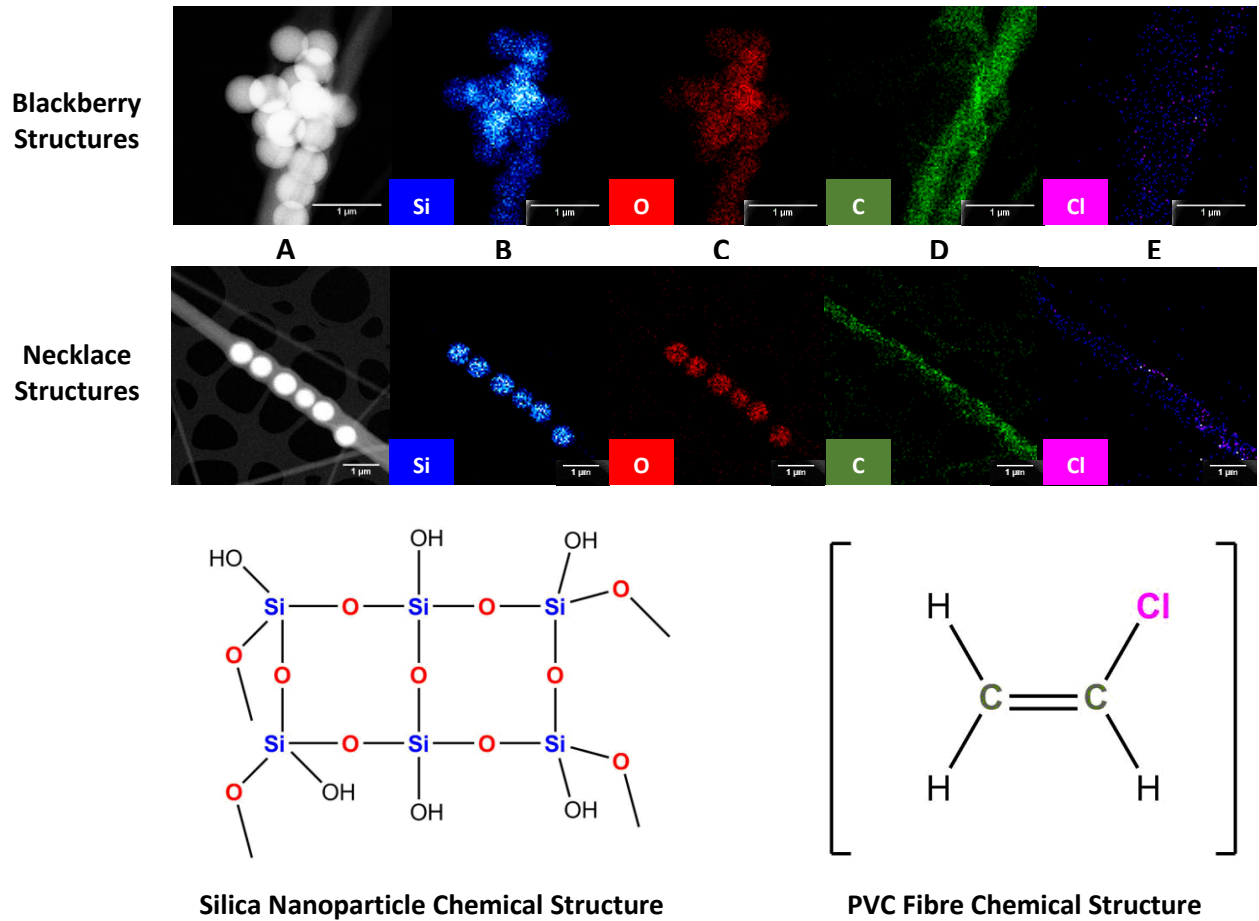


Figure 3.18: STEM-EDX elemental mapping of particle-fibre hybrid. (A) High-angle annular dark-field imaging (HAADF) STEM image; (B) Silicon map (Blue); (C) Oxygen map (Red); (D) Carbon map (Green); (E) Chlorine map (Purple)

The combination of TEM and EDX as complementary characterisation techniques has been proven to be a powerful strategy for comprehensive morphological and elemental characterisations of particle-fibre hybrid systems. The data facilitate the transition into investigating multi-elemental hybrid systems with complex geometric structures.

3.4.4.2. Raman Spectroscopy

Raman scattering is molecular spectroscopy widely used to obtain information on hybrid systems from their vibrational properties. Figure 3.19 depicts the Raman spectra of the pure bulk silica particles, plain PVC fibres and particle-fibre hybrids. Silica particles exhibit a strong and distinct peak at 490 cm^{-1} corresponding to the breathing mode of 4-membered rings and a peak at 980 cm^{-1} , which represents the vibration of the (OH)-group with respect to silicone (Si) [184]. Polyvinyl chloride exhibits two main peaks between 600 to 750 cm^{-1} , which correlates to the C-Cl stretching vibration [185]. It is important to note that the electrospun PVC fibres are Raman inactive in 490 cm^{-1} region, which can be used to discriminate the presence of silica particles inside the PVC fibres.

A single point Raman spectrum was recorded on the blackberry-like structure and the single particle (necklace-like structure) to obtain spectra for both particle-fibre hybrids morphologies and compare them with the reference spectra. The single particle spectrum showed no distinctive peak compared to the baseline at the same wavelength. It is likely that the very low concentration of the silica particles in the necklace hybrid structures reduced the intensity of the Raman signal, which led to a weak signal to noise spectra. In addition, the spatial resolution limit is dictated by the diffraction limit, which is estimated to be around $1.0\text{ }\mu\text{m}$ when a visible laser is employed. Therefore, the Raman spectrum of the necklace-like hybrid structure did not show any significant peak correlation to the single silica particles, which are smaller than the spatial resolution limit of Raman spectroscopy.

On the other hand, a small peak was observed at 490 cm^{-1} in the blackberry-like structure hybrids along multiple peaks corresponds to the PVC fibres. The 490 cm^{-1} peak indicated the existence of silica particles inside the electrospun fibres. It is likely that the closely packed silica

nanoparticles in the blackberry-like structure increased the density of the particles in the area of analysis by several order of magnitude providing enough concentration for Raman detection.

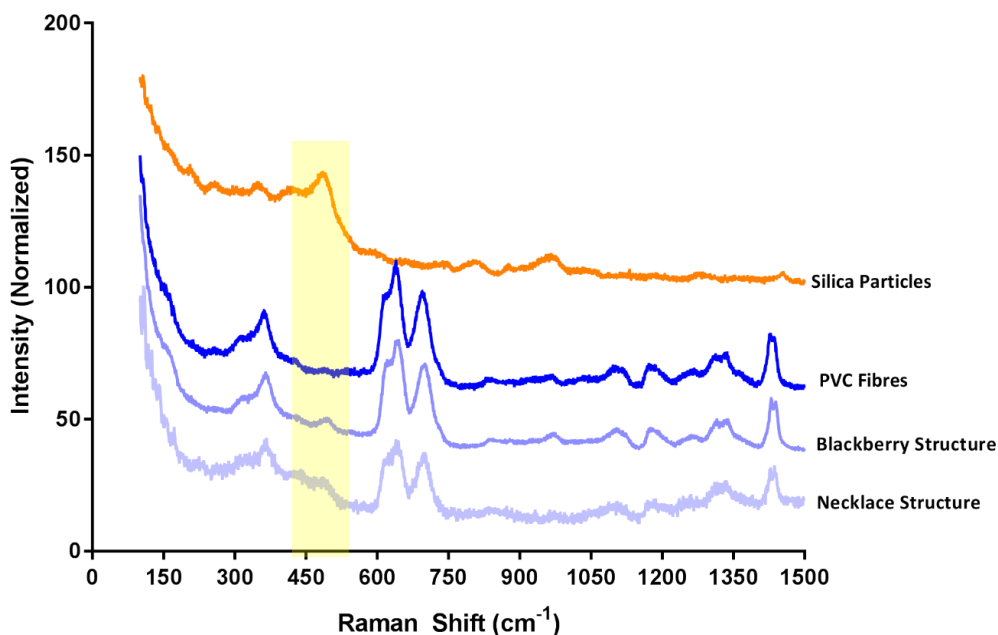


Figure 3.19: Raman spectra of pure silica particles, plain PVC fibres and silica-PVC hybrids over the range of 100 cm⁻¹ to 3400 cm⁻¹.

3.4.4.3. Time of Flight Secondary Ion Mass Spectroscopy

ToF-SIMS analysis was conducted to elucidate surface chemistry and spatial distribution of the various components within the particle-fibre hybrid at the micron-scale. The silica-PVC colloidal suspension was electrospun directly onto a TEM gold grid. The resulting particle-fibre hybrids were imaged optically using a profilometer and analysed using ToF-SIMS.

Chemical maps were retrospectively reconstructed from the ToF-SIMS data by employing an understanding of the specific chemistry of the particle and the fibre materials. In addition, reference materials of the PVC only fibres and silica nanoparticles were analysed using ToF-SIMS to confirm the characteristic fragment ions. The silica particles exclusively contained silicone

while PVC contained chlorine thereby allowing the SiO_2^- and Cl^- secondary ions to be used as characteristic markers for particle and fibre, respectively.

The first sample was analysed over an area of $150 \times 150 \mu\text{m}$. The optical image for particle-fibre hybrids (Figure 3.20-A) shows several beaded fibres suggesting the presence of encapsulated silica particles in the scanned area. The Cl^- secondary ions, indicative of the PVC fibres, were distributed across the hybrid, suggesting a complete and continuous coverage of the fibre polymer (PVC) over the particle-fibre surface (Figure 3.20-C). However, the intensity of the Cl^- ions was varied across the fibres, which is due to the fact that the analysed sample is not flat [186]. This topography-induced intensity differences between the individual spectra can be reduced by data normalisation [187]. No secondary ions diagnostic of the silica particles was detected in the fibre area, although the presence of silica particles was confirmed using the optical profilometer.

SiO_2^- ions were uniformly distributed across the gold frame of the TEM grid, which could be related to poly-dimethyl-siloxane (PDMS) contamination (Figure 3.20-D). The source of the PDMS can be traced to various materials such as the latex gloves that used to handle the sample or the adhesives that used to hold the TEM grid during electrospinning [54]. The significant PDMS transfer onto the TEM grid gold surfaces is due to the high affinity of lower free-energy molecules such as PDMS to cover the gold high free-energy surface [188]. Similar results were found when the second sample was scanned in a smaller area ($50 \times 50 \mu\text{m}$) as shown in Figure 3.21.

These findings can be explained by the ability of ToF-SIMS to provide a qualitative assessment of the chemical composition of the uppermost 1 - 2 nm of the outer surface [189]. Therefore, it is likely that the thickness of the PVC fibre cover layer was larger than 2 nm, which prevented the dissemination of secondary ions from the underlying silica particles.

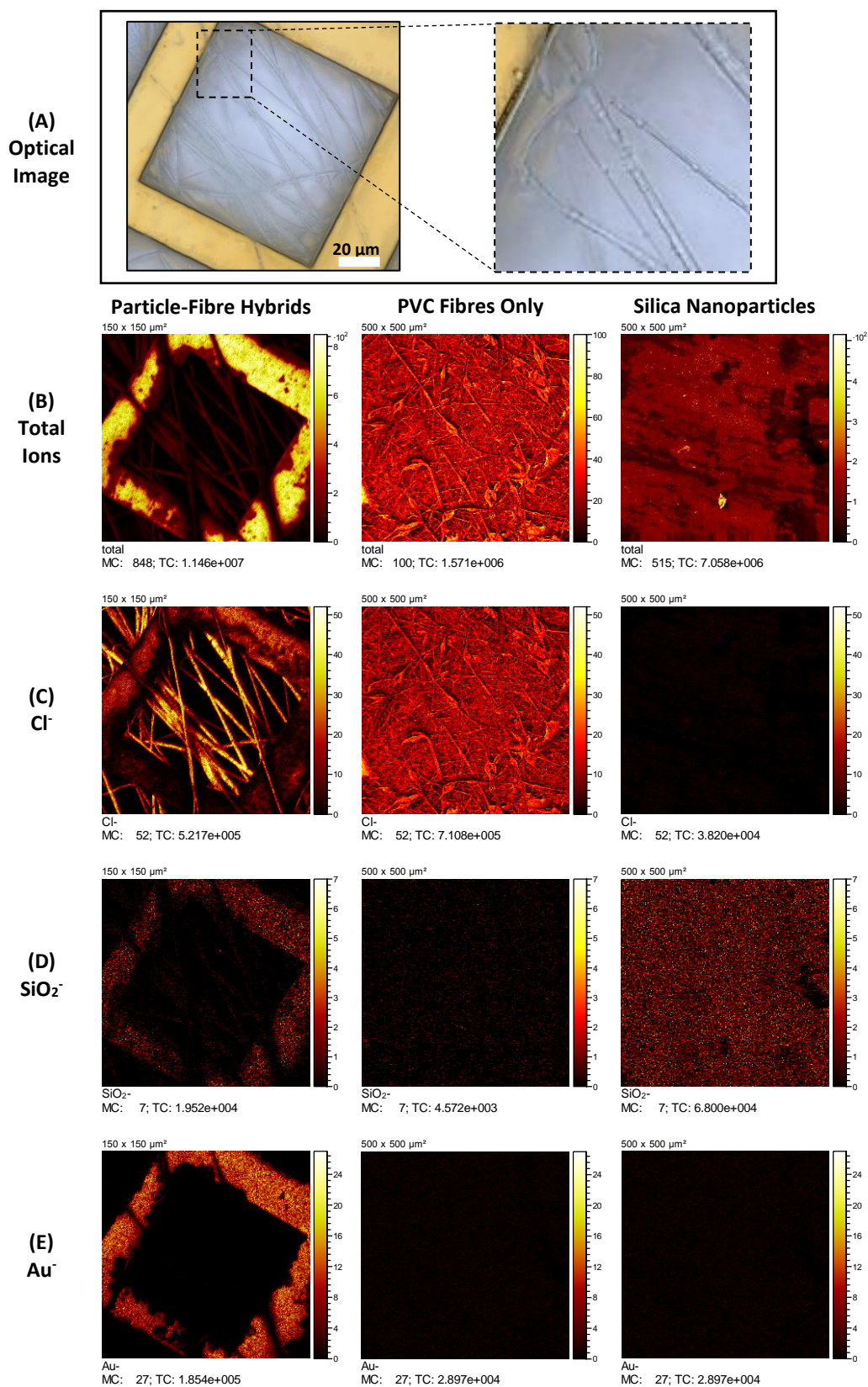


Figure 3.20: (A) Optical image of the particle-fibre hybrids deposited on TEM finder grids. (B-D) ToF-SIMS intensity maps for the surface of particle-fibre hybrids, PVC only fibres and silica nanoparticles. Row (B) shows the results of the total intensity signal. Rows (C) and (D) show negative polarity images of Cl⁻ and SiO₂⁻, respectively. Row (E) shows the negative polarity image of Au⁻ characterising the frame of the TEM gold grid. Scanned area= 150 ×150 µm.

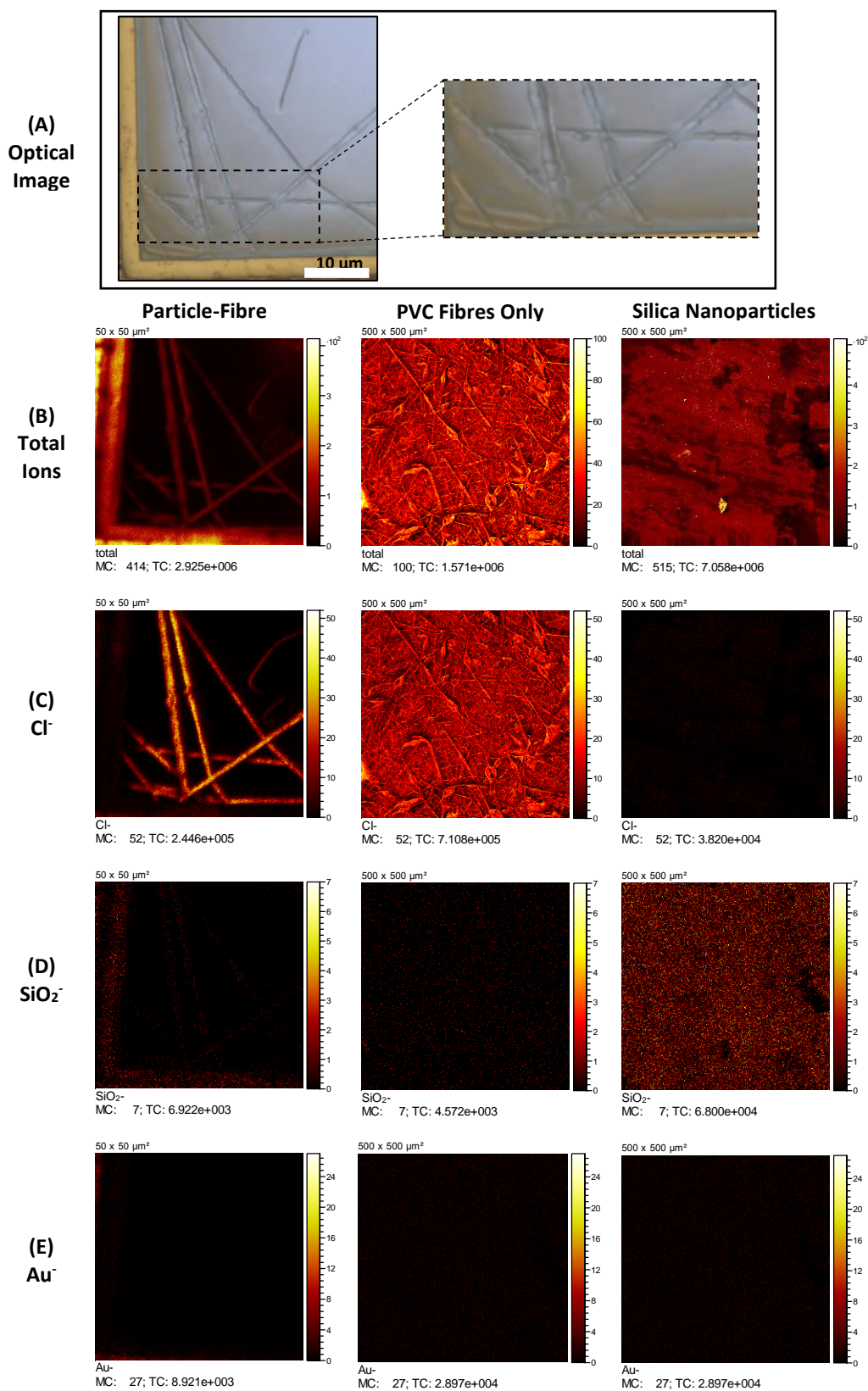


Figure 3.21: (A) Optical image of the particle-fibre hybrids deposited on TEM finder grids. (B-D) ToF-SIMS intensity maps for the surface of particle-fibre hybrids, PVC only fibres and silica nanoparticles. Row (B) shows the results of the total intensity signal. Rows (C) and (D) show negative polarity images of Cl⁻ and SiO₂⁻, respectively. Row (E) shows the negative polarity image of Au⁻ characterising the frame of the TEM gold grid. Scanned area= 50 × 50 μm.

3.4.4.4. Super-Resolution Fluorescence Microscopy

Validating and testing a super-resolution microscopy method requires defined samples that can be used as standards. Fluorescent silica particles (containing Alexa 647 fluorophore) encapsulated into the electrospun fibre can exhibit a defined separation. Therefore, particle-fibre hybrids can provide a versatile calibration standard for super-resolution fluorescence microscopy based on subsequent localisation techniques, such as stochastic optical reconstruction microscopy (STORM). As a proof of concept, photoswitchable Alexa 647 silica nanoparticles with a diameter below 100 nm were encapsulated into PVC fibres, which is well below the optical diffraction limit.

Figure 3.22-B and E shows a wide field image of the particle-fibre hybrid mounted with PVA/glycerol medium. The glycerol-based medium has a high optical index, which makes it convenient for high numerical aperture (NA) imaging. It is also a non-hardening medium that can maintain samples for up to several weeks at low temperature [190]. The image appears as blurred intensity spots for multiple Alexa 647 silica particles (Diameter <100 nm) with no discernible morphological details. It is likely that the distance between the individual particle was smaller than the diffraction limit. Therefore, the position of the single nanoparticles cannot be determined because of their overlapping point spread function (PSF- Section 3.1.4).

The STORM technique was used to experimentally detect the size of the fluorescent silica nanoparticles incorporated into the electrospun fibre. The ON/OFF blinking indicating the fluorescent transient of Alexa 647-functionalised silica nanoparticles was induced by simultaneous excitation at 405 and 642 nm. The subsequent localisation of all Alexa 647 molecules in silica nanoparticles enables reconstruction of super-resolution image as depicted in Figure 3.22-C and F. Single Alexa 647 silica nanoparticle positions are clearly resolved. The

circumference of a single nanoparticle (Figure 3.22-G) was determined from the STORM image, which yielded a particle diameter of 87.5 ± 20 nm (Mean \pm SED). The mean nanoparticle diameter is in good agreement with the Alexa 647 silica nanoparticle mean diameter of 76.5 ± 2.5 nm measured using DLS before incorporating into the electrospun fibre (Section 3.4.2).

Another mounting medium, such as water, was also compared (Figure 3.23), as it may be important to use the particle-fibre hybrids under different conditions. Mounting particle-fibre hybrids with water resulted in very similar results to the PVC/glycerol mounted medium. The silica nanoparticle size obtained from the super-resolution image was around 100 ± 13 nm (Mean \pm SED) as shown in Figure 3.23-G.

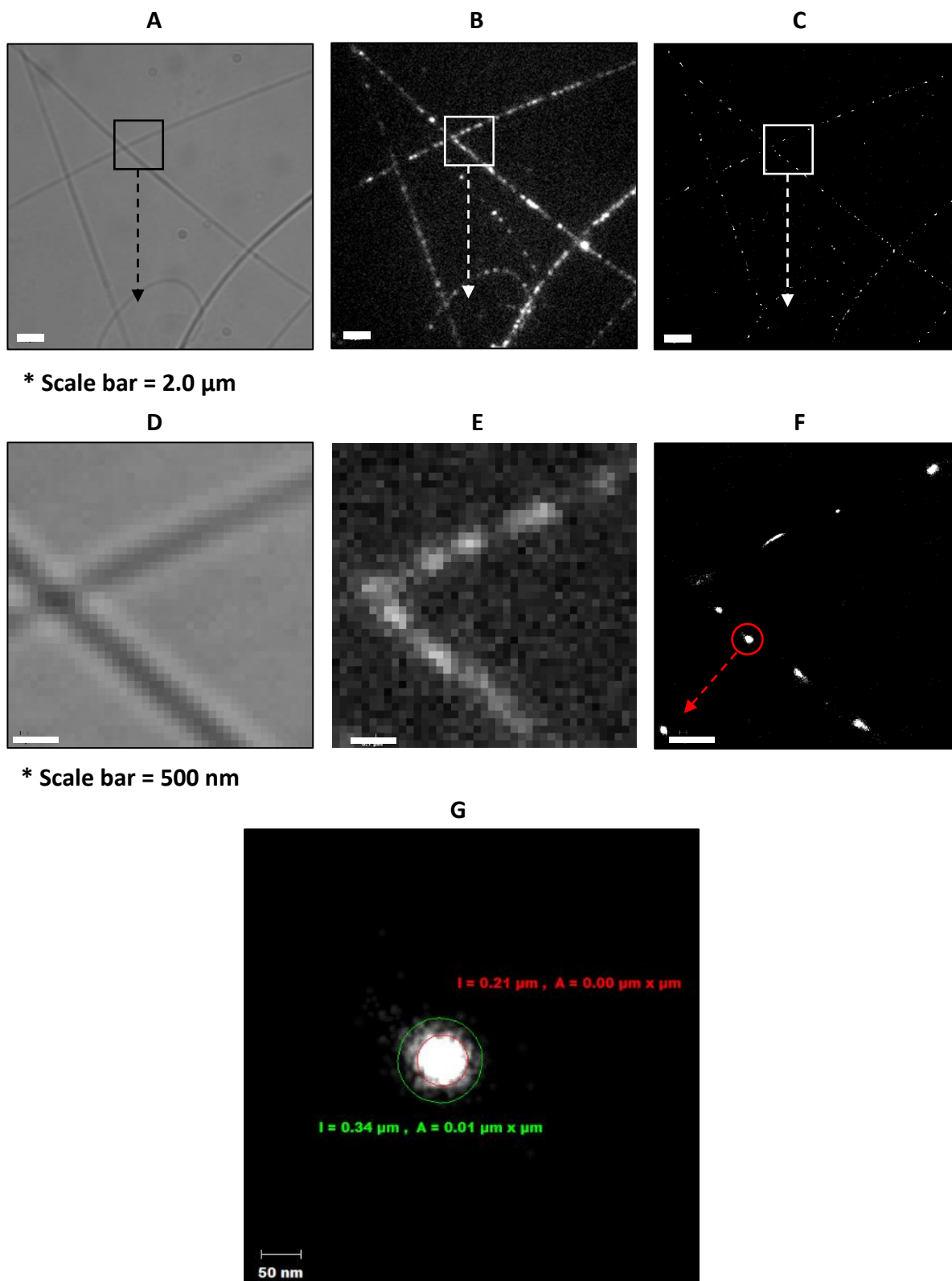


Figure 3.22: (A&D) Bright field image, (B&E) wide field image and (C&F) super-resolution image of the same region of particle-fibre hybrid systems mounted with PVC/glycerol medium. (G) The measured circumferences of a single nanoparticle

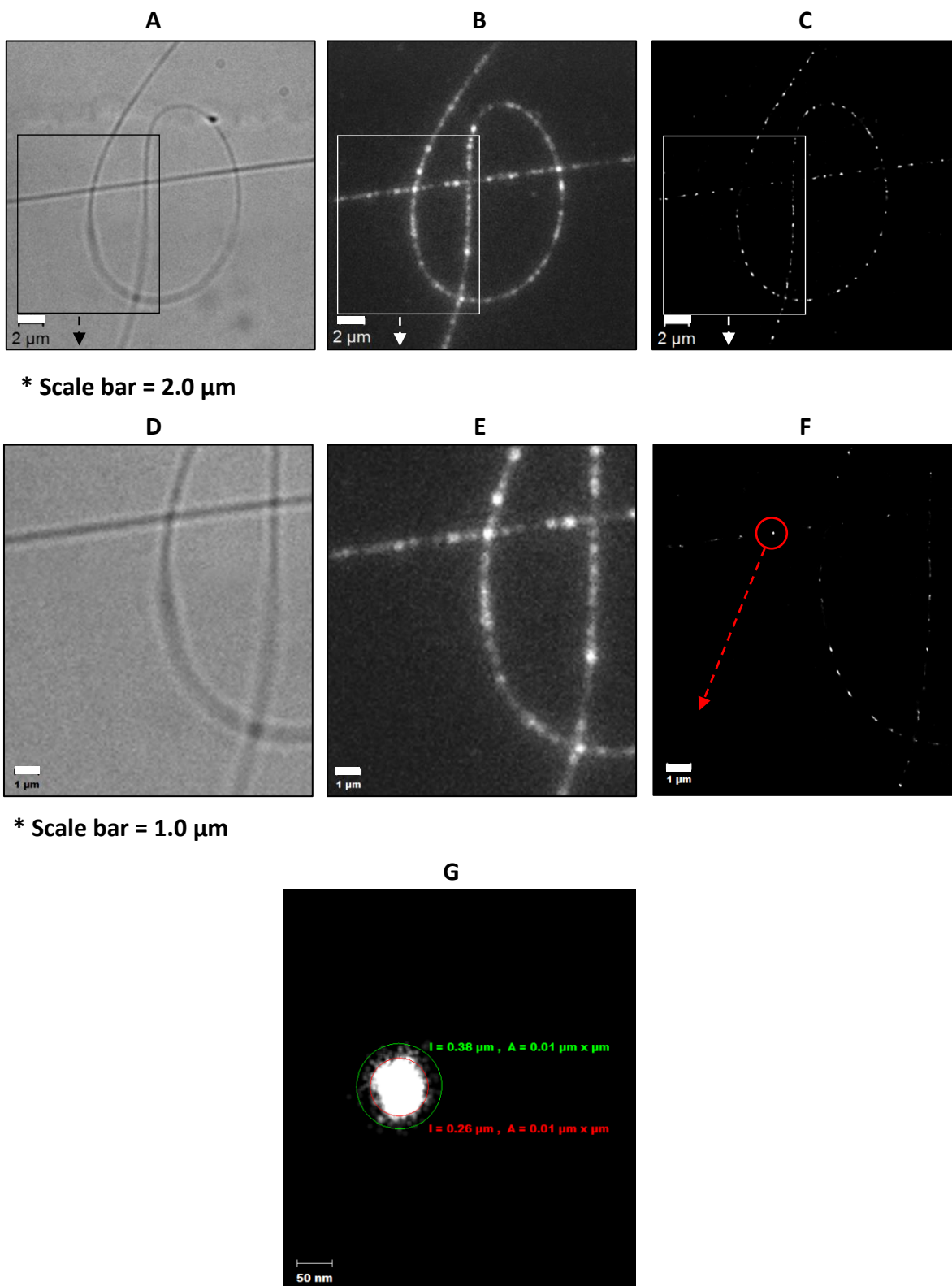


Figure 3.23: (A&D) Bright field image, (B&E) wide field image and (C&F) super-resolution image of the same region of particle-fibre hybrid systems mounted with water. (G) The measured circumferences of a single nanoparticle

3.4.5. Summary of the Results and Discussion

In this chapter, fabrication and characterisation of silica nanoparticles (SNPs) and polyvinyl chloride (PVC) nanofibre hybrids using colloidal electrospinning process were performed for designing calibration standards for super-resolution fluorescence microscopy.

Initially, size tuneable silica nanoparticles were prepared over a range of 20–650 nm by varying the amount of the NH_4OH , TEOS and by using the seed growth techniques. Figure 3.24 summarised the range of silica particle size prepared in section 3.4.1. In addition, below 100 nm fluorescent silica particles covalently linked to different fluorophore molecules were prepared.

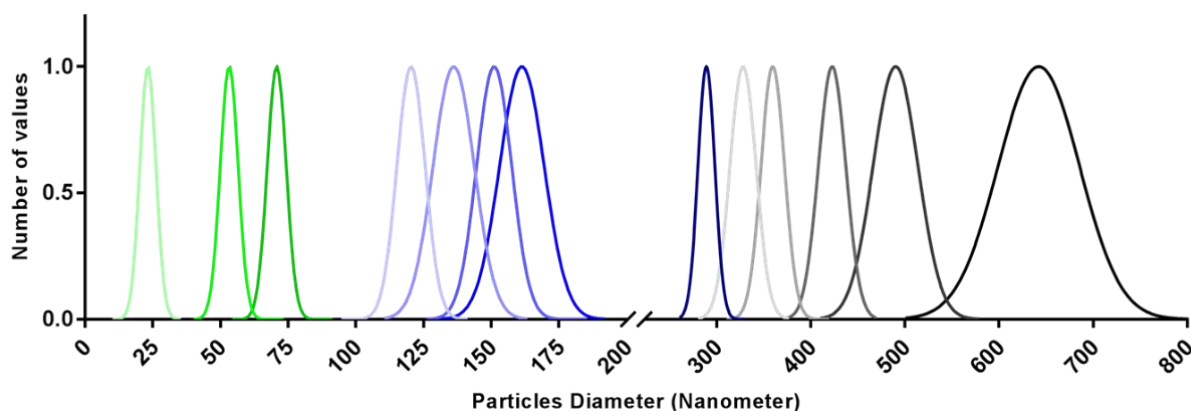


Figure 3.24: Size distribution histogram of the resulting silica particles batches (Size range 20-650 nm)

Subsequently, the effect of the silica particle size and concentration on the particle-fibre hybrid morphologies were investigated. Based on section 3.4.3.2 results, the formation mechanism of different morphologies of the particle-fibre hybrids prepared via colloidal electrospinning can be summarised in Figure 3.25. At low particle concentration, silica particles were evenly distributed in the polymer solution and confined into electrospun fibres. Similar structures were found for different silica particle sizes when used at low concentrations. At high particle concentration, silica particles tend to form aggregates (i.e. blackberry-like structures) of particles during the electrospinning process. Poor particle dispersity in the polymer solution is a

possible explanation for these aggregates. Another explanation involves the formation of a thin polymer shell on the surface of the silica particles. This shell acts as a binder to generate an adhesive force between silica particles, causing them to aggregate in the electrospun fibres [191].

The results confirm that the nanoparticle size, concentration and particle dispersibility in the polymer solution are essential parameters that can significantly influence the morphology of the particle-fibre hybrids.

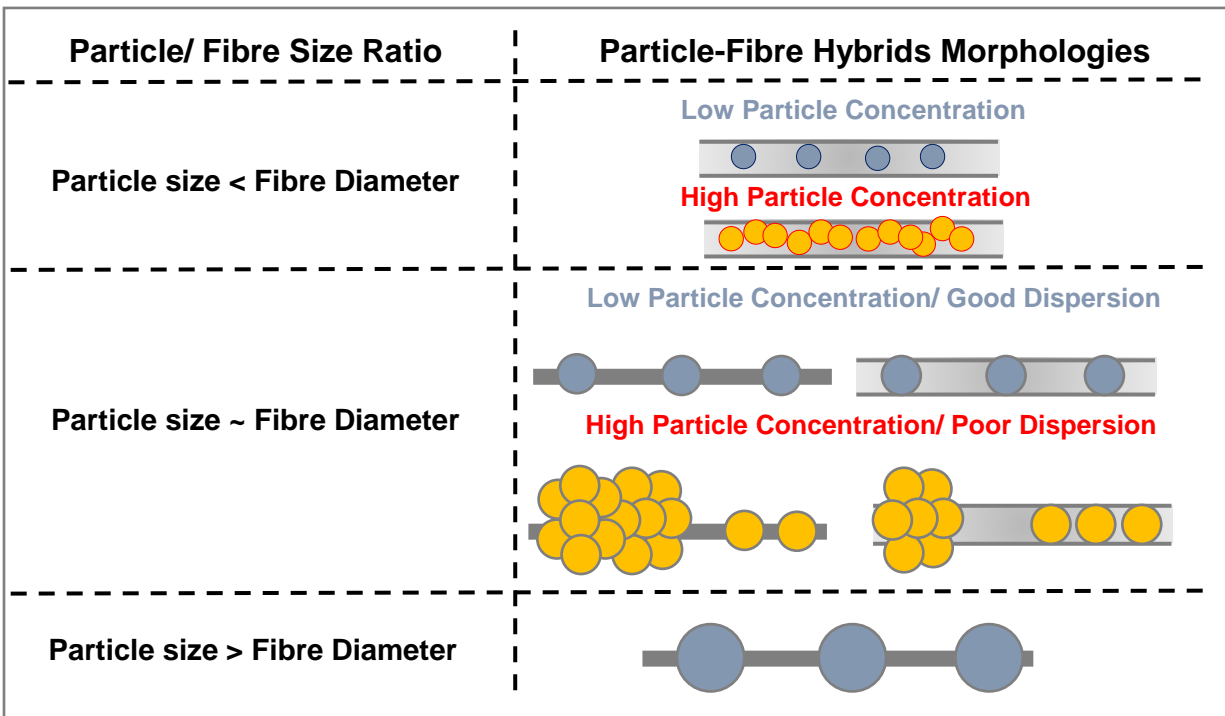


Figure 3.25: Morphologies obtained under different particle sizes and concentrations via colloidal electrospinning of particles and polymer solutions.

The application of advanced analytical strategies demonstrated both an effective and systemic analysis of the structure and composition of the particle-fibre hybrid systems. TEM shows high functionality in observing silica nanoparticles in electrospun fibres at the nano level. Both results coming from TEM-EDX and Raman spectroscopy are demonstrating the ability of both techniques to confirm the presence of particles inside electrospun fibres elementally and chemically.

EDX is a sensitive, fast and practical qualitative technique for the characterisation of the main elements of particle-fibre hybrids. Raman spectroscopy was able to detect silica nanoparticles in the blackberry hybrid structures. However, due to the limited spatial resolution, precise characterisation of individual silica nanoparticles in the necklace hybrid structure was not possible using the conventional Raman spectroscopy.

ToF-SIMS was used to probe the surface of the particle-fibre hybrids. Time-of-flight secondary ion mass spectrometry analysis of the hybrids revealed a thick continuous film of polyvinyl chloride (PVC) fibre polymer at the surface of the hybrids. Figure 3.26 summarises the detection capability of the advanced analytical techniques used to investigate the particle-fibre hybrid systems.

Finally, calibration standard design for super-resolution fluorescence microscopy based on incorporating fluorescent silica nanoparticles into electrospun fibres was evaluated. The findings reported in section 3.4.4.4 indicate that particle-fibre hybrid structure represents an excellent, easy and robust tool to precisely assess the performance of advanced imaging techniques such as STORM as well as used as a calibration standard for fluorescence microscopy.

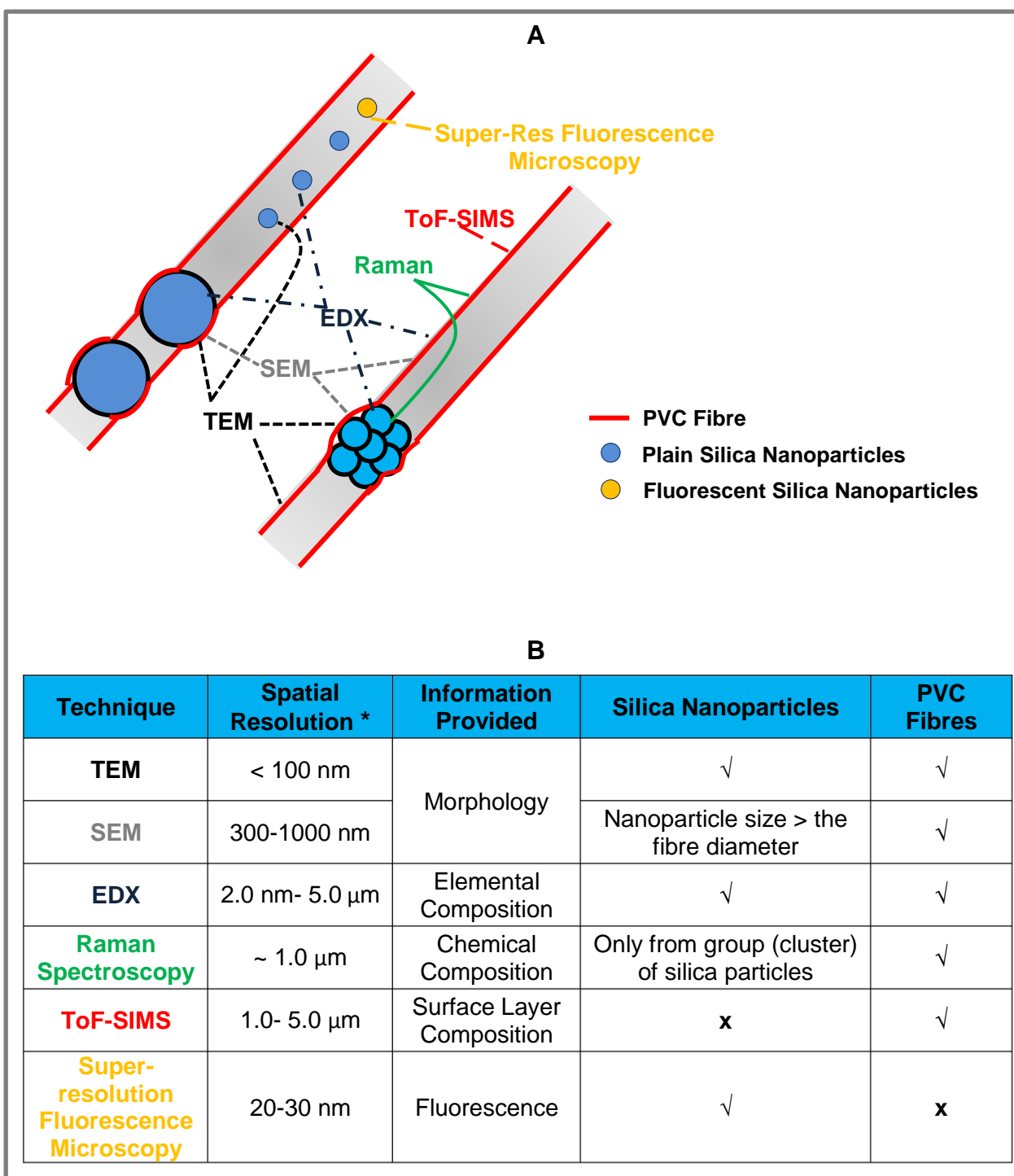


Figure 3.26: Summary (A) diagram and (B) table of the detection capabilities of the advanced analytical techniques used to investigate the particle-fibre hybrid systems.

* Spatial resolution data were obtained from the following references [192]–[195].

3.5. Conclusion

Size-tunable silica particles were prepared, with diameters ranging from 20 to 650 nm. This was achieved by optimising the amount of each reactant and catalyst required for particle synthesis. In addition, fluorescent SNPs covalently linked to fluorescent dye molecules were produced to be used for potential super-resolution fluorescence microscopy application.

Electrospinning process optimisation was carried out to fabricate smooth, beads-free fibres with relatively narrow fibre diameter (271 ± 12.4 nm). Fabrication of particle-fibre hybrids can be successfully achieved by utilising co-electrospinning. The particle size and concentration influenced the morphology of the hybrids forming necklace-like and blackberry-like structures. TEM was found to be a particularly efficient method to investigate the particle-fibre hybrid's morphology and image the encapsulated particles in electrospun fibres. To further characterise the particle-fibre hybrids, EDX analysis, Raman spectroscopy and ToF-SIMS were also utilised to provide valuable information on such complicated systems. EDX was able to define the main elements of particle-fibre hybrids, while Raman spectroscopy provided the chemical composition of the blackberry hybrid structures. ToF-SIMS analysis of the hybrids indicated the complete coverage of the polyvinyl chloride (PVC) fibre polymer of the surface of the hybrids.

These new hybrid systems have potential applications in various fields. The feasibility of using fluorescent particle-fibre hybrids as a new tool for validating and testing super-resolution fluorescence microscopy was examined. The results suggested that fluorescent particle-fibre hybrids have the potential to be used as a convenient and effective calibration tool by incorporating fluorescent nanoparticles into a confined geometry. The versatility and flexibility in the design of particle-fibre hybrids microscopy standards make them suitable for the broad variety of emerging super-resolution microscopy methods.

Chapter4: Investigation of Salt Disproportionation using *In-Situ* Optical Imaging

In this Chapter, the use of *in-situ* optical imaging microscopy equipped with a controlled humidity chamber was investigated for exploring the stability of the pharmaceutical salt stored at high relative humidity when formulated with a range of commonly used excipients. The inspiration for this chapter arises from the fact that the drug salt can convert back to the free form during solid dosage form storage. In this Chapter, a series of binary mixtures were prepared from Pioglitazone HCl (Weak base model drug), and Ibuprofen sodium (Weak acid model drug) mixed with a range of acidic and basic excipients. These mixtures were examined at high relative humidity. *In-situ* optical microscopy was used to monitor changes in the salt crystal morphology as an indication of the salt disproportionation.

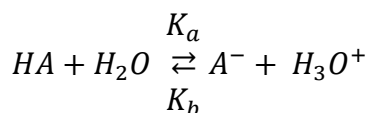
4.1. Introduction

4.1.1. Pharmaceutical Salts

Oral solid dosage forms, such as tablets and capsules, are one of the most commonly used and popular methods to administer drugs. They are simple to manufacture and design; cost-effective and have high patient compliance [196]. However, a large fraction of pharmaceutical drug candidates are poorly soluble in aqueous media and thus have low bioavailability [197]–[201]. According to an FDA recent analysis, there has been a continuous rise in lipophilicity and a decrease in aqueous solubility of approved drugs in the past 30 years [202]. As a result, the bioavailability of these compounds is expected to be limited by the drug solubility.

Strategies aimed at enhancing the bioavailability of such drug substances have thus been extensively used and explored [203]–[209]. Examples of these strategies include, but are not limited to, prodrugs [210], [211], salts [212]–[214], particle size reduction [214], co-crystal [215], [216] and amorphous solid dispersions [217]. One of the simplest means to improve the dissolution properties is to formulate the active pharmaceutical ingredient (API) as salt [201], [214], [218]. It is estimated that at least 50-70% of the APIs are manufactured and formulated as salts [201], [219], [220]. Generally, ionisable drug substances can form salts by pairing with an appropriate counterion. Salts exhibits higher solubility than the corresponding free, unionised form. The solubility of salts significantly depends on the selection of counter-ion, or salt former. For acidic drugs, sodium (Na⁺) is the most common counter-ion, while hydrochloride (Cl⁻) is the most popular counter-ions for basic drugs [218].

For a drug molecule to exist as a stable salt and be able to form ionised species under specific environmental conditions, it must be either a weak acid or weak base [221]. As most APIs contain either an acidic or basic functional group (sometimes both) within their chemical structure, this should, in theory, allow salt to be formed with counterions. According to Brønsted–Lowry theory, acids are compounds that can donate protons and bases are compounds that can accept protons [222]. The equilibrium for the dissociation of a weak acid drug (HA) may be expressed by:

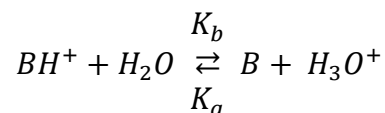


Where HA is the free acid, (A⁻) is the deprotonated acid, and the acid dissociation constant

K_a can be given by:

$$K_a = \frac{[A^-][H_3O^+]}{[HA]} \quad (4.1)$$

Analogously, for a weak base drug (BH⁺), the proton transfer can be expressed by the following equilibrium:



where BH⁺ is the protonated base, (B) is the free base, and the acid dissociation constant K_a can be given by:

$$K_a = \frac{[B][H_3O^+]}{[BH^+]} \quad (4.2)$$

The acid dissociation constant for both the weak acid and the weak base drug can also be expressed by pK_a:

$$pK_a = -\log K_a \quad (4.3)$$

For an acidic drug, strong acids indicate a higher concentration of the ionised species [A⁻], which means a larger numerical value of K_a (Equation 4.1). Because of the way the log function works, a larger K_a means smaller pK_a. Whereas for the basic drug, the high concentration of the ionised species [BH⁺] will result in a small numerical value of K_a (Equation 4.2) and larger pK_a. The relation of the pK_a value and the strength of the acid and base is summarised in Table 4.1 [218].

Table 4.1: Classification of acids and bases according to their pK_a.

Attribute	pKa Value	
	Acids	Bases
Very Strong	< 0	14
Strong	0 -4.5	9.5-14
Weak	4.5-9.5	4.5-9.5
Very Weak	9.5-14	0-4.5
Extremely Weak	14	<0

4.1.2. pH-Solubility Profile and pH_{max}

The solubility of an acidic or basic drug in an aqueous environment as a function of pH provides some critical information such as the propensity of drugs to form salts and the best

counter-ions to choose [214], [223]. In addition, it dictates how easily the salts may convert back into their free forms and their dissolution performance under different gastrointestinal (GI) pH conditions [223].

In general, the total solubility (S_T) of salts can be derived by the sum of the intrinsic solubility of the free form (Unionised species) and the concentration of the salt (Ionised species) [224].

$$S_T = [Ionised] + [Unionised] \quad (4.4)$$

Bearing this in mind, the total solubility of salts varies significantly over the range of physiological pH due to the different degrees of ionisation at different pH. When the salt of an acidic drug is dissolved in water, the equilibrium constant (K_a) can be given by Equation 4.1. The pH solubility profile may be expressed by two regions as shown in Figure 4.1: one where the free acid is at saturation or equilibrium and the other where the solution is saturated with respect to the ionised salt species. The pH point at which the two regions intersect is termed pH_{max} , the pH of maximum solubility. At the pH_{max} , an equilibrium is formed between the ionised and neutral species in solution. Solids of both salt and the free form are considered to co-exist [220], [225], [226].

The total solubility of the salt of acidic drug (S_{Tacid}) at pH higher than pH_{max} , where the salt (ionised) is the dominating species is expressed as follows:

$$\begin{aligned} S_{Tacid}(pH > pH_{max}) &= [A^-]_s + [HA] \\ &= [A^-]_s + \frac{[A^-]_s[H_3O^+]}{K_a} \\ &= [A^-]_s \left(1 + \frac{[H_3O^+]}{K_a}\right) \end{aligned} \quad (4.5)$$

$$S_{Tacid}(pH > pH_{max}) = [A^-]_s(1 + 10^{pK_a - pH})$$

Where the subscript “s” represents the saturation species. On the other hand, when the free acid is the saturation species (i.e. the pH is less than the pH_{max}), the total solubility is:

$$\begin{aligned}
 S_{Tacid}(pH < pH_{max}) &= [HA]_s + [A^-] \\
 &= [HA]_s + \frac{[HA]_s K_a}{[H_3O^+]} \\
 &= [HA]_s \left(1 + \frac{K_a}{[H_3O^+]}\right)
 \end{aligned}
 \tag{4.6}$$

$$S_{Tacid}(pH < pH_{max}) = [HA]_s(1 + 10^{pH-pK_a})$$

Figure 4.1 demonstrates the pH-solubility profile of an acidic drug. When the pH is lower than the pH_{max} , the solid phase contains only the free acid form, whereas the solid phase consists only of the salt when the pH is higher than the pH_{max} . Increasing the pH of the saturated solution with the free acid solid phase from below the pH_{max} up to above the pH_{max} facilitate the conversion of the free acid to the salt. The opposite is true for the transformation of the salt to the free acid; the free acid will precipitate out when the pH is lowered below the pH_{max} . As a result, maintaining the pH higher than the pH_{max} helps the salt formation of the acidic drugs.

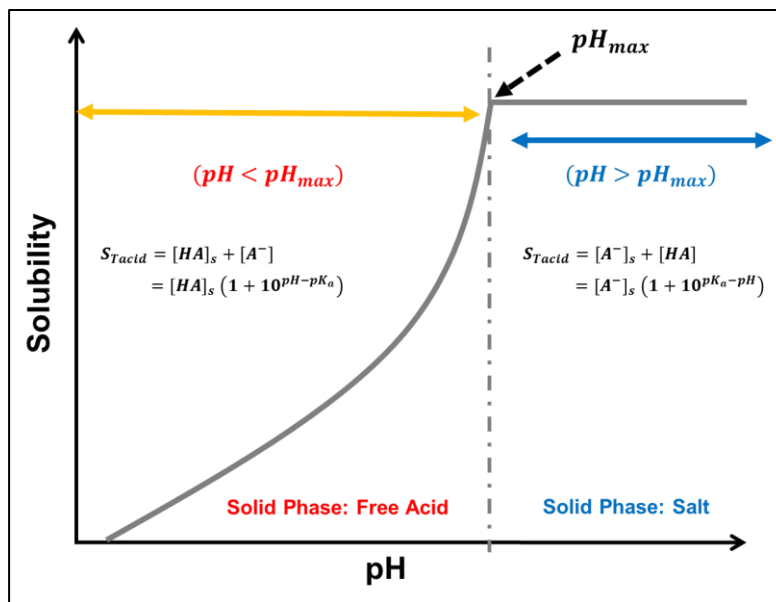


Figure 4.1: Schematic representation of the pH-solubility profile of an acidic drug presenting the pH_{max} point and indicating that the solubility may be expressed by two independent regions[29].

Figure 4.2 illustrates the pH-solubility profile of a free base and its salt form. The free base would be the equilibrium species at a pH above pH_{max} , and it would transform into salt only if it is equilibrated with a solution at a pH below pH_{max} by adding an adequate quantity of acid. On the other hand, to convert the solid phase from the salt to base, the addition of base is needed to increase the pH more than the pH_{max} . Therefore, in order to preserve the salt forms of basic drugs, pH must be kept lower than the pH_{max} . The total solubility at pH greater or less than pH_{max} are as follows:

$$\begin{aligned}
 S_{Tbase}(pH > pH_{max}) &= [B]_s + [BH^+] \\
 &= [B]_s + \frac{[B]_s K_a}{[H_3O^+]} \\
 &= [B]_s \left(1 + \frac{K_a}{[H_3O^+]}\right)
 \end{aligned} \tag{4.7}$$

$$S_{Tbase}(pH > pH_{max}) = [B]_s(1 + 10^{pK_a - pH})$$

$$\begin{aligned}
 S_{Tbase}(pH < pH_{max}) &= [BH^+]_s + [B] \\
 &= [BH^+]_s + \frac{[BH^+]_s [H_3O^+]}{K_a} \\
 &= [BH^+]_s \left(1 + \frac{K_a}{[H_3O^+]}\right)
 \end{aligned} \tag{4.8}$$

$$S_{Tacid}(pH < pH_{max}) = [BH^+]_s(1 + 10^{pH - pK_a})$$

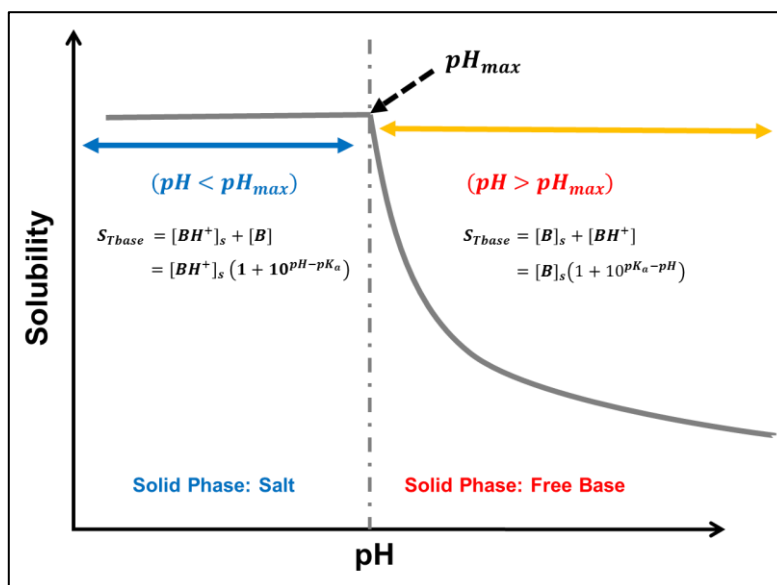


Figure 4.2: Schematic representation of the pH-solubility profile of a basic drug presenting the pH_{max} point and indicating that the solubility may be expressed by two independent regions[29].

The pH_{max} is a critical concept in the physical chemistry of salts [214]. It is apparent from Figure 4.1 and Figure 4.2 that pH_{max} plays a crucial role in determining whether the salt will remain stable or would convert back to the corresponding free form. As mentioned previously, salt and free forms coexist at pH_{max} . Therefore, the total solubility at pH_{max} calculated from Equation 4.5 and 4.6 for acid drug and Equation 4.7 and 4.8 for the basic drug is the same. Bogardus and Blackwood [227] suggested that, for the basic drug, the pH_{max} can be derived from a combination of Equation 4.7 and 4.8 to give the following relationship as shown in Equation 4.9:

$$pH_{max} = pK_a + \log \frac{[B]_s}{\sqrt{K_{sp}}} \quad (4.9)$$

The equivalent relationship for an acid is:

$$pH_{max} = pK_a + \log \frac{\sqrt{K_{sp}}}{[AH]_s} \quad (4.10)$$

Where K_{sp} represents the solubility product of the salt form and $\sqrt{K_{sp}}$ is therefore the salt solubility. According to the pH_{max} equations, there are three parameters that influence the pH_{max} value: The dissociation constant (pK_a), the solubility of the free form (denoted as S_0 for acid and

base drugs) and the solubility of the salt form ($\sqrt{K_{sp}}$). Figure 4.3 demonstrates the relationship between the three factors and the pH_{max} [228]. pH_{max} will increase by one unit if the pK_a increases one unit. An increase in the intrinsic solubility (S_0) of the free form by one order of magnitude increases the pH_{max} by one unit. Furthermore, a decrease in the salt solubility product (K_{sp}) by one order of magnitude also increases the pH_{max} by one unit. In summary, for a basic drug, lower salt solubility with higher pK_a and free base intrinsic solubility values will lead to higher pH_{max} values, which in turn favour the formation of the salt and increase the pH range where the salt is the stable form. In contrast, for an acidic drug, higher intrinsic solubility and lower pK_a and salt solubility values will yield lower pH_{max} and favour acidic salt formation with also a wider range of pH where the salt will be stable.

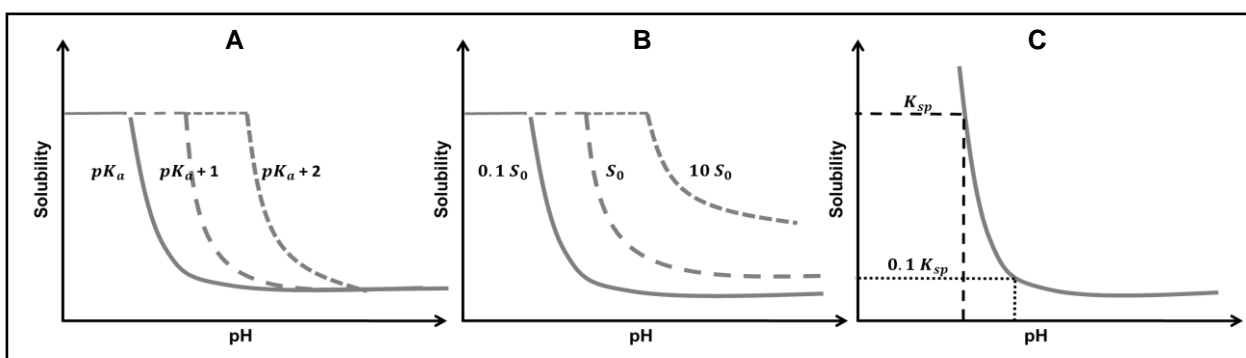


Figure 4.3: Effects of (A) pK_a , (B) S_0 and (C) K_{sp} on pH_{max} (Adapted from Ref [220]).

The pH_{max} , controlled by different factors, has a significant impact on salt solubility and the physicochemical stability of drug salts in the solution and solid state [225], [228].

4.1.3. Salt Disproportionation

4.1.3.1. What is Salt Disproportionation?

Salt formation does not only modify a drug substances solubility and dissolution rate but can also influence other important physicochemical properties such as chemical stability, hygroscopicity, melting point and crystal morphology [201], [219], [220], [226]. However, there is a significant risk associated with salts, which is related to long-term stability [201].

Selecting the best salt form for multicomponent solid dosage form is not a trivial task, and many aspects must be considered during formulation development. It is essential to consider the long-term physical, and chemical stability in multicomponent dosage forms as the salt will potentially be exposed to different excipients and different conditions such as humidity or temperature during manufacturing and storage [220].

Salt solid-state chemical instability in solid dosage forms can be a consequence of the interaction between the salt and one or more of the excipients used in the formulation [220]. Excipients or impurities in excipients may react directly with the salt molecule, act as a catalyst for drug degradation chemical reaction or change the pH of the microenvironment such that the rate of chemical reaction is enhanced [24]. One of the potential risks of using salt formation is that salt forms of APIs have a propensity to revert to the unionised free form, which often exhibits lower solubility and dissolution rate properties [31], [201], [229]. This process is termed salt disproportionation.

Salt disproportionation is an acid-base reaction involving proton exchange in the presence of water [201], [229], [230]. The conversion of the salt to the free form is undesired since it has detrimental effects on solid-state properties and pharmaceutical product performance such as reduced dissolution rate and bioavailability [24], [219], [220], [225], [229], [231]–[233].

Salt disproportionation is largely influenced by a number of factors, which involve physiochemical properties of the drug and the environmental conditions during storage and in-vivo performance [29], [214], [219], [220], [226], [233]. Examples of the drug physiochemical properties that mediate salt disproportionation include the pH_{max} and the solubility difference between the salt form and the free form. The pH_{max} concept and role have been explained in the previous section (Section 4.1.2). Thermodynamically, the salt disproportionation reaction is driven by the low solubility of the free-form relative to the salt solubility. The high solubility difference between the salt and the free-form lead to a high Gibbs free energy difference. As a result, preparing salt with high solubility compared to the free form may significantly increase the risk of disproportionation. Guerrieri and Taylor [219] investigated the disproportionation propensity of the mesylate and napsylate salt of two different drugs stored with excipients at high humidity. The aqueous solubility of mesylate salts was reported to be more than three orders of magnitude greater than the napsylate salts for both drugs. The study found that the napsylate salts were more resistant to disproportionation compare to the mesylate salt stored at the same conditions [219]. In another study, the HCl, HBr, heminapadisylate salts and the adipic acid co-crystal of a corticotropin-releasing hormone receptor-1 antagonist were investigated for their disproportionation propensity in the presence of magnesium stearate [234]. The more soluble HCl and HBr salts exhibited disproportionation during stability assessment, while the less soluble heminapadisylate salt and the adipic acid co-crystals were stable [234]. Hence, salt selection should be based on the desired solubility and salt stability, rather than very high aqueous solubility.

Environmental conditions, such as the presence of water as a dissolution medium or as a moisture layer adsorbed on the solid surface, have a significant role in enhancing the rates of

disproportionation reactions [235], as water (moisture) presence provides the platform for the solution-mediated reactions [31], [32], [219]. The presence of water during dissolution is normal; however, in the solid state, it is less obvious to have water inside solid dosage forms. A considerable amount of evidence exists, particularly in studies investigating the surfaces of inorganic salts, to support the existence of thin-film surface water at ambient relative humidity [219], [226], [236]. The formation of this microscopic aqueous layer on the solid surface is unavoidable due to the presence of residual water from manufacturing or moisture sorption from the atmosphere during storage. This microscopic water layer can mediate the salt disproportionation reaction [214].

The solution mediated phase transformation (SMPT) is a thermodynamic theory that can be used to understand the salt disproportionation mechanism [237]. Thermodynamically, a certain level of supersaturation must precede precipitation at which point the solution becomes unstable, causing the molecules to rearrange and recrystallise. It is suggested by multiple studies [32], [201], [214], [219] that for the salt to revert back to the free-form, the drug must dissolve in the microscopic layer around the solid drug salt crystal. When the drug salt is in its solution phase, nucleation and crystal growth are two critical processes that are expected to happen after reaching the supersaturation level [237]. When the microscopic water layer is highly supersaturated with the ionised form (Salt), there is sufficient thermodynamic driving force for molecules to rearrange and form stable nuclei of the free form.

After nucleation has been initiated, crystal growth ensues if the equilibrium between the solid phase and solution phase has not been reached. The precipitation of the free-form has a significant impact on the total solution concentration and therefore influences the dosage form performance and drug bioavailability [217], [238]–[241].

The microenvironment pH refers to the hydrogen ion activity (i.e. pH) in the microscopic layer of water adsorbed at the solid surface [219], [225], [242], [243]. Microenvironment pH commonly estimated using the slurry method due to its simplicity, in which a sample of the formulation is placed in solution, and the pH of its saturated solution is measured [220], [226]. In the case of solid dosage forms, the microenvironmental pH may be significantly impacted by the excipients possessing acidic/basic functionalities that are in intimate contact with the salt drug in a multi-component formulation. As a result, the salt propensity to disproportionate can be anticipated based on an assessment of the microenvironment pH and knowledge of the salt pH_{max} as illustrated previously in Figure 4.1 and 4.2.

For a salt of a weak base (Figure 4.2), when the microenvironment pH is lower than the salt pH_{max} , the equilibrium is between the solid salt, and the ionised form in solution and therefore, salt disproportionation cannot occur. On the other hand, disproportionation can potentially occur when the microenvironment pH suppresses the pH_{max} of salt. In this case, excipients that can elevate the microenvironment pH values above the drug salt can promote disproportionation. For the salt of a weak acid (Figure 4.1), the salt disproportionation occurs only when the microenvironment pH is below the pH of maximum solubility (pH_{max}). Therefore, a problematic excipient is viewed as being able to decrease the microenvironment pH of the microscopic water layers below the pH_{max} . Stephenson et al. reviewed four oral dosage forms in, which the disproportionation detected was generally justified by higher estimated tablet pH microenvironment values compared to the salt's pH_{max} [220].

4.1.3.2. Salt Disproportionation during Storage: Role of Excipients

Pharmaceutical excipients are crucial and essential components of pharmaceutical formulations. Excipients have a wide range of functionalities that used to improve pharmaceutical dosage form properties and performance, such as making up the bulk of the total dosage like fillers and improve dissolution rate like disintegrant [244], [245]. However, excipient selection is critical, as some excipients may impact the stability and interact with active pharmaceutical ingredients in multicomponent formulations [246], [247].

The ability of some acidic or basic excipients to change the microenvironment pH that influenced salt disproportionation in solid dosage forms is well documented [31], [32], [225], [232], [243], [248]. For example, mixtures of delavirdine mesylate salt with different excipients were prepared to determine which excipient participated in the salt conversion to the free form in tablets stored at 60-75% relative humidity [31]. The study concluded that the presence of the croscarmellose sodium disintegrant in the tablet matrix is essential for the salt disproportionation [31]. Zannou et al. [32] reported disproportionation of maleate salt in multicomponent tablets prepared for late-stage clinical trials. The microenvironment pH of the tablets measured by the slurry method was found to be (4.3) which is higher than the pH_{max} of the salt (3.3-3.5) thus favouring the salt to base conversion. The tablet stored at 40°C/ 75% RH showed a significant loss of potency within six weeks [32].

In another study, physical mixtures of the mesylate salts of miconazole and benzocaine with seven basic excipients (50/50 w/w) stored at 60% relative humidity for around 40 days [219]. The basic excipients investigated include magnesium stearate, anhydrous tribasic phosphates (sodium and calcium) and croscarmellose sodium. The study concluded that excipient basicity, solubility and surface area had substantial roles in the disproportionation of the mesylate salt of

both drugs [219]. John et al. [201] studied the disproportionation of an HCl salt of a weakly basic drug formulated with nine common excipients in binary mixture compacts. The compacts were stressed at 40°C/ 75% RH and 40 °C/ 35% RH for 28 days. The salt disproportionation was detected in compacts containing magnesium stearate, sodium croscarmellose, and sodium stearyl fumarate. Magnesium stearate was the most deleterious excipient for HCl salts due to the formation of the deliquescent salt magnesium chloride, which increased in the water uptake by the compacts even at low relative humidity (RH= 35%) [201].

In another study, Hsieh et al. selected several basic excipients (croscarmellose sodium, magnesium stearate, sodium bicarbonate, tribasic sodium phosphate dodecahydrate and sodium starch glycolate) to study their ability to induce salt conversion of various sertraline salts in 1:1 w/w powder blends stored at 25°C 57% RH [230]. Sertraline salts mixed with tribasic sodium phosphate dodecahydrate (TSPd) were found to undergo a significant extent of conversion from salt to free form due to the strong basic properties of TSPd compared to the other excipients investigated [230]. The same group investigated the extent of the salt disproportionation of four sertraline salts and five miconazole salts blended individually with tribasic sodium phosphate dodecahydrate (TSPd; 50:50 w/w) incubated at 25°C 57% RH [248]. The authors observed a strong correlation between the pH_{max} and moisture uptake of the binary mixture with the rate and extent of disproportionation. Salts that had high weight gain due to moisture sorption and low pH_{max} experienced a significant increase in the extent of disproportionation [248].

4.1.4. Solid State Excipient Compatibility Testing

Pharmaceutical excipients have been previously viewed as “inert substances”; however, this view has changed. Drug and excipient compatibility tests have gained increased attention as they can influence the stability of the drug in a formulated drug product [224], [249]. Therefore, excipient compatibility studies are essential in the drug development process to predict the potential incompatibility between the drug and the excipients in the final dosage form. These studies and tests are conducted mainly to provide valuable information that can be used to select the suitable type and concentration of excipients, delineate stability profile of the drug and help to adopt strategies to mitigate the instability of the drug in solid dosage forms [224]. Consequently, methodical, precise and simple planned compatibility tests can lead to savings regarding resources and time delays related to stability issues arising during the late-stage product development [29], [224].

Sample preparation, storage conditions and method of analysis are essential attributes of drug-excipient compatibility studies [250]. Samples are prepared traditionally based on a one factor at a time approach, in which binary blends of the API with excipients are prepared to be used in compatibility screening [250]. High relative humidity is the most common storage condition that has been used during drug-excipient compatibility studies [224], [249]. The drug and excipient binary mixtures are incubated under controlled humidity condition using a humidity chamber. The humidity chamber ensures stable maintenance of equilibrium moisture level in the solid state; therefore, water-mediated drug-excipient reactions can be investigated in the solid state.

Presence of water in the solid-state systems has a significant impact on the salt stability, by participating as a reaction medium and by increasing the molecular mobility of the reactant

species [224]. It is evident based on the previous section (Section 4.1.3.2) that excipients can induce salt phase transformations in the presence of moisture. The pH of the microenvironment controlled by the acidic or basic excipient can have a significant impact on the chemical stability of the salt. Therefore, excipients can be included in or excluded from the final formulation based on the excipient pH profiles, which can help in the design of the excipient compatibility study [224]. However, the slurry measured pH value of excipients is insufficient on its own to describe the role of excipient on disproportionation [30], [201], [226].

Other important excipient properties including aqueous solubility, physical state (e.g. amorphous or crystalline), particle size, surface area and the formulation hygroscopicity were found to increase the risk and extent of salt disproportionation significantly [219], [248]. All of these factors are competing to induce or prevent salt disproportionation in solid dosage form during storage which could dramatically increase the data interpretation complexity of excipient-drug compatibility tests. Therefore, simple screening analytical techniques are generally preferable in studying the effect of excipients on salt disproportionation [29].

4.1.5. Advanced Analytical Techniques

Several analytical methods can be utilised to fully characterise the physical transformation of salt in excipient mixtures following preparation and accelerated stress testing at high relative humidity. Examples of analytical techniques that are commonly used in drug-excipients compatibility studies includes thermal analysis such as differential scanning calorimetry (DSC) and thermal gravimetric analysis (TGA) [251], [252], solid-state nuclear magnetic resonance spectroscopy (SS-NMR) [31], X-ray powder diffractometer (XRPD) [201], [225], [226], [232], [233], Fourier transform infrared (FTIR) spectroscopy [31], [201], [219], [225], [232], [253], [254], Raman

spectroscopy [219], [226], [229], [232], [233], [248], [253], [254] and optical microscopy [224], [249].

Thermal analysis techniques, such as DSC, were proven to be the most sensitive and specific in assessing the compatibility [255]. However, the interaction reported at DSC operating high temperature might not always be relevant at ambient drug storing condition [256], [257]. In addition, conventional stability testing includes prolonged storage of the sample at elevated humidity and temperatures to determine the undegraded or degraded fraction of drug as a function of time. Moreover, most of these analytical techniques are time-consuming and offline analytical techniques. Offline analytical techniques may provide misleading information regarding the drug phase transformation due to the non-representative sampling and system perturbations introduced during post-sampling preparation [40]. Therefore, it would be desirable to have a rapid, simple and online analytical method that can precisely define any drug conversion transit in real time during drug-excipient compatibility studies [29], [40]. *In-situ* analytical techniques fit the previous criteria typically.

In-situ analytical techniques provide key advantages over offline techniques in defining the drug transformation transient through the collection of many data points rapidly without the need of sampling [232]. Raman spectroscopy, for example, has been employed to investigate salt disproportionation in solid dosage form during dissolution [253], [254]. Another example is the *in-situ* optical microscopy, which can be used to monitor the drug transformation process from one form to another in real-time. *In-situ* optical screening can be used to detect drug-excipient incompatibility by studying the evolution of crystal morphology of the drug substance during the transformation process [258]. Optical microscopy is one of the most widely used technique for analysing crystal morphology in laboratory studies [259]. Scot et al. utilised an in-line camera for

qualitative investigation of particle-particle interactions [255]. Multiple studies reported the use of *in-situ* optical microscopy for monitoring the shapes of crystals during different crystallisation processes [260]–[263]. The previous studies reported the advantages of using *in-situ* optical microscopy; including the simple experimental set-up, the low cost and the intuitive interpretation of the image data. These advantages present *in-situ* optical microscopy as an appealing online analytical technique to study systems undergoing phase transformation.

It has been reported that the conversion of the salt to the free-form produce both change in the internal structure and crystal habit (i.e. crystal morphology) [264], [265]. However, no study, to the best of our knowledge, has used *in-situ* optical microscopy to investigate salt disproportionation by monitoring the change in salt crystal morphology during transformation. *In-situ* optical microscopy can be used to investigate the role of excipient properties in inducing or preventing salt disproportionation at stressed condition (high relative humidity) as part of drug-excipient compatibility investigation.

4.2. Motivation and the Aim

Excipient compatibility studies were conducted with the main goal of selecting dosage form components that are compatible with the drug. The ability of formulation components to induce or prevent the conversion of the salt to the free form by influencing the microenvironmental pH is well documented. Microenvironmental pH within moisture located at surfaces of the salt crystals would be expected to be influenced by the excipient's properties including, but not limited to, acidity/basicity, aqueous solubility and hygroscopicity [225]. The pH of excipients is usually assessed using the slurry method. However, these pH measurements are considered poor surrogates for the exact microenvironmental pH conditions at a solid surface [266]–[270], especially for less soluble, hygroscopic excipients, and excipients that show unique behaviour. This may make the correlation between the measured pH values and the effect of the excipients in the solid state difficult [225]. Therefore, the ability to anticipate the disproportionation propensity in the early stages of drug development by considering all the excipient properties would be highly valuable. Currently, drug-excipient compatibility studies anticipate salt disproportionation by storing the binary mixture of the salt and excipient in stressed storage conditions, then applying offline analytical techniques to measure the amount of salt converted into the free form. This experimental design can be time-consuming, costly and generate complicated data.

Therefore, this chapter aimed to investigate the effect of excipients on salt disproportionation in binary mixtures stored at high humidity as part of drug-excipient compatibility study using a simple, fast and online analytical technique. *In-situ* optical screening equipped with a controlled humidity chamber was used for monitoring salt disproportionation by tracking the changes in the salt crystal morphology mixed with specific excipients at high relative

humidity. Offline Raman spectroscopy was used in the screening studies in parallel with the online optical imaging system for validation and benchmarking purposes.

Pioglitazone HCl and Ibuprofen sodium were used as two model systems in this chapter (Figure 4.4). Pioglitazone is a weak base drug ($pK_a = 5.2$) used for type II diabetes treatment, while Ibuprofen is a weak acid drug ($pK_a = 4.4$) used as a non-steroidal anti-inflammatory drug. Twelve common excipients (Table 4.2) that can provide a wide range of microenvironmental pH were chosen for this study:

The specific objectives of this chapter are:

- To identify the difference between the salt and the free-form crystal morphology and Raman spectra.
- To rationalise the stability of model salt drugs, Pioglitazone HCl and Ibuprofen sodium, without any excipients at high relative humidity during *in situ* optical imaging experiments. The salt disproportionation to the free form of the drug during storage at 75-90% relative humidity was monitored.
- To investigate the influence of commonly used excipients in inducing or preventing salt disproportionation during accelerated stability testing at high RH. Binary mixtures of the drug salt with the excipients were tested at high RH by monitoring the salt crystal morphology changes using *in situ* optical microscopy.

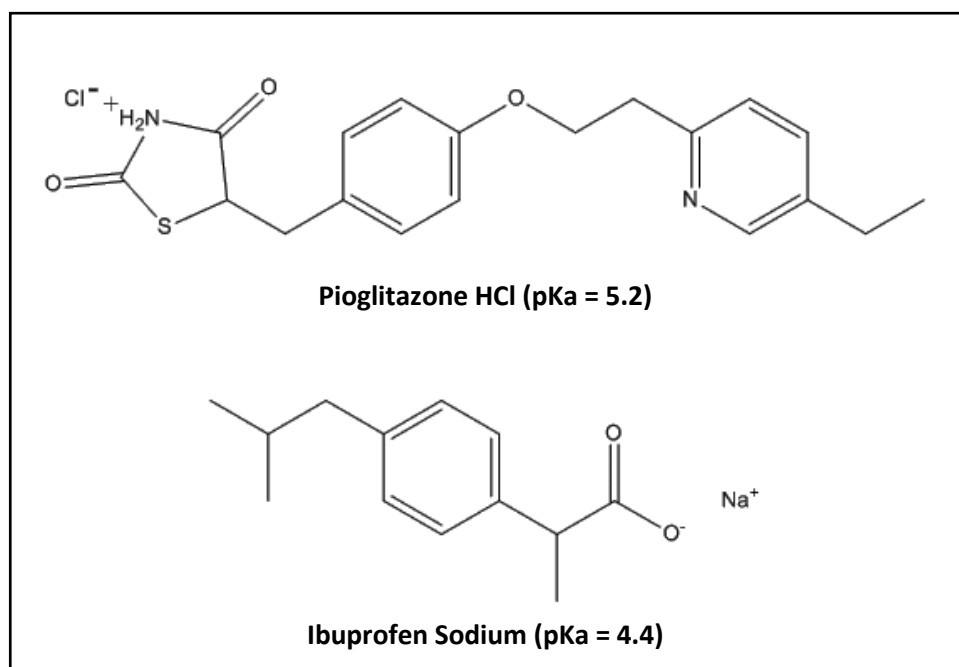
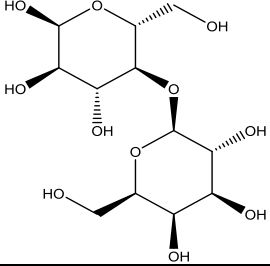
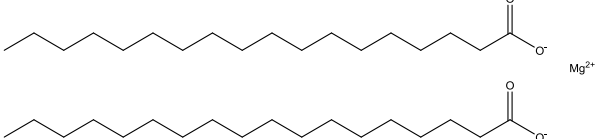
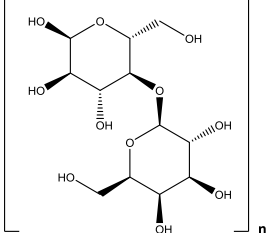
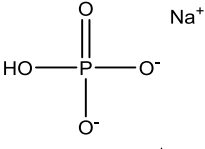
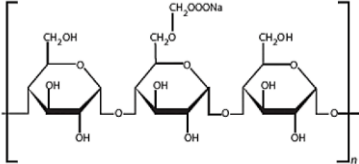
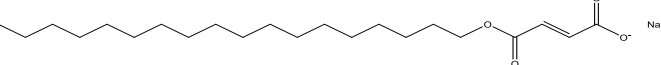
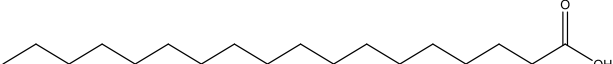


Figure 4.4: Chemical structure of Pioglitazone HCl salt and Ibuprofen sodium salt.

Table 4.2: Summary of the selected excipients role and chemical structures.

Excipient Name	Excipient Role [244]	Chemical Structure
Ascorbic Acid	Antioxidant	
Calcium Phosphate Dibasic	Binder Filler	
Citric Acid	Acidic Buffering Agent	
Croscarmellose Sodium (AC-DI-SOL)	Disintegrant	
Hydroxypropyl Methylcellulose (HPMC)	Binder Extended-release-matrix former	

where R is H or CH₃ or CH₂CH(OH)CH₃

Lactose Monohydrate	Binder Filler	
Magnesium Stearate	Lubricant	
Microcrystalline Cellulose (MCC)	Binder Filler	
Sodium Phosphate Dibasic	Basic Buffering Agent	
Sodium Starch Glycolate	Disintegrant	
Sodium Stearyl Fumarate	Lubricant	
Stearic Acid	Lubricant	

4.3. Materials and Methods

4.3.1. Materials

Active Pharmaceutical Ingredients (APIs): Pioglitazone hydrochloride (Salt ≥ 98.5) was obtained from Kemprotec Limited (UK). Pioglitazone free base (98%), Ibuprofen free acid (98%) and Ibuprofen sodium (Salt 98%) were purchased from Sigma-Aldrich (UK). All APIs were used as received, without any further purification.

Excipients: Citric acid monohydrate (≥ 99.0 %), ascorbic Acid (99.0 %) sodium phosphate dibasic (Pharma grade), calcium phosphate dibasic (98.0-105 %), and magnesium stearate (Technical grade) were purchased from Sigma-Aldrich (UK). Stearic acid (General grade) was obtained from Fisher Scientific (UK). Lactose monohydrate (InhaLac™ 70-Pharma Grade) and sodium croscarmellose (AC-DI-SOL™ SD-711) were supplied by Meggle Pharma - Excipients & Technology (Germany). Hydroxypropyl methylcellulose (Metolose™- SM type) was obtained from Shin-Etsu Chemical (Japan). Microcrystalline cellulose (Avicel™ PH-102-Pharma Grade) was supplied by FMC Health and Nutrition (USA). Sodium stearyl fumarate (Pruv™) and sodium starch glycolate were supplied by JRS Pharma (Germany). All excipients were used as received, without any further purification.

Instruments:

Jenway™ 3510 pH meter (Cole-Parmer, UK) was used to measure the pH of the excipient's slurry in water.

Pestle and mortar, 50 μm sieve (Endecotts Ltd, UK) and 3-dimensional shaker/mixer (TURBULA T2F) used for preparing the API and excipient binary mixtures.

Optical Screening Humidity System: EVOS™ Auto-FL inverted microscopy (Fisher Scientific, UK) and ibidi™ gas incubation system for humidity control (ibidi, Germany).

4.3.2. Formulation and Binary Mixture Preparation

All excipients were ground and screened through a 50 µm sieve before mixing with the APIs for three reasons. The first reason is that the grinding was performed so that the small excipient's particle will adsorb on the drug salt surface. This adsorption will bring the drug and excipient particles into intimate physical contact, which resembles the type of contact in solid dosage forms such as tablets. The second reason is to increase the surface area of the excipient particles, which will enhance the interaction rate with the moisture and change the pH around the drug salt particle rapidly. Finally, the size difference between the drug and excipient particle size will ease the differentiation of the two solids during optical imaging.

A binary mixture of the drug salt and each excipient was prepared at 1:1 weight ratio according to the ICH (International Conference on Harmonisation of Technical Requirements for Registration of Pharmaceuticals for Human Use) Q8 [271] and ANDA (Abbreviated New Drug Application) guidelines [272]. The excipient selection was based on the acidic and basic strength of the excipient, and their different functionalities (i.e. filler, disintegrant, lubricant). The excipients name, role and chemical structures are detailed in Table 4.2. The binary mixtures were thoroughly blended for 15 min using Turbula T2F™ mixer. The blended powders were then sprinkled on glass coverslip to be tested.

4.3.3. APIs and Excipients Characterisations

4.3.3.1. Measurement of the Microenvironment pH

A slurry of each excipient was prepared in glass vials. A known amount of solid, approximately 10-20 % w/v (i.e. more than needed to saturate the medium), was added to

deionised water and mixed for 24 hours. The pH of the saturated solution was measured by a Jenway™ 3510 pH meter equipped with a Jenway™ glass electrode.

4.3.3.2. Scanning Electron Microscopy (SEM)

The crystal morphologies of the as-received drug salts and the free forms of both model drugs (i.e. Pioglitazone and Ibuprofen) were investigated by scanning electron microscopy (JEOL™ 6060LV, UK). Samples were mounted on aluminium stubs using a 12 mm carbon adhesive film and were subsequently coated with gold employing a Leica EM™ sputter coater (SCD005, Germany) at 25 mA, 10^{-3} vacuum for 300 seconds. The images were acquired at acceleration voltages of 15–20 kV and a working distance of 10-15 mm.

4.3.3.3. Raman Spectroscopy

Both crystalline forms (i.e. salt and free form) for Pioglitazone HCl and Ibuprofen sodium obtained by sampling before and after transition were subjected to off-line Raman spectroscopy analysis to verify the solid form. Raman spectra were acquired using a Horiba LabRAM HR confocal microscopy/spectroscopy. Sample excitation was performed using a near-IR laser (785 nm) of 250 mW power. Spectra were acquired using a 50x objective and a 300 μ m confocal pinhole. A 600 mm rotatable diffraction grating was used to scan a range of Raman shifts simultaneously. Raman spectra were collected using a SYNAPSE CCD detector (1024 pixels). Data acquisition time was set at 3 seconds, and two accumulations were averaged for all samples. GraphPad Prism™ was used for spectra visual inspection in this section.

4.3.4. Optical Screening Control Humidity System

Figure 4.5 illustrates the experimental set-up of the system. An inverted optical microscopy equipped with a controlled humidity chamber was used to investigate the salt conversion during storage at high humidity of binary drug/excipient mixtures via tracking the change in the salt crystal morphology in real-time.

Time-lapse imaging was performed on an EVOS FL inverted microscopy with 20x/0.45 NA, and 40x/0.65 NA objectives and a CCD camera (High-sensitivity monochrome, Sony™ ICX285AL CCD) mounted with a humidity control chamber (ibidi™). The time-lapse parameters are controlled to take one picture every 10 seconds for a maximum of 10-40 minute. A video for each mixture was produced, which can be found on the USB attached to this thesis. The samples are only illuminated during image acquisition. The binary mixture was sprinkled on a coverslip placed into the stage of the humidity controlled chamber. The humidity of the chamber is maintained by a feedback loop system using a humidity sensor located in the humidity chamber. The humidity is increased by streaming the dry compressed air through the heated water column if the humidity is too low. The relative humidity was kept around $75\% \pm 10\%$ for the duration of the imaging period based on the guidance from the FDA entitled “Stability Testing of Drug Substances and Drug Products.” [273]. The chamber temperature was maintained at $25^{\circ}\text{C} \pm 1.0$ in all measurements

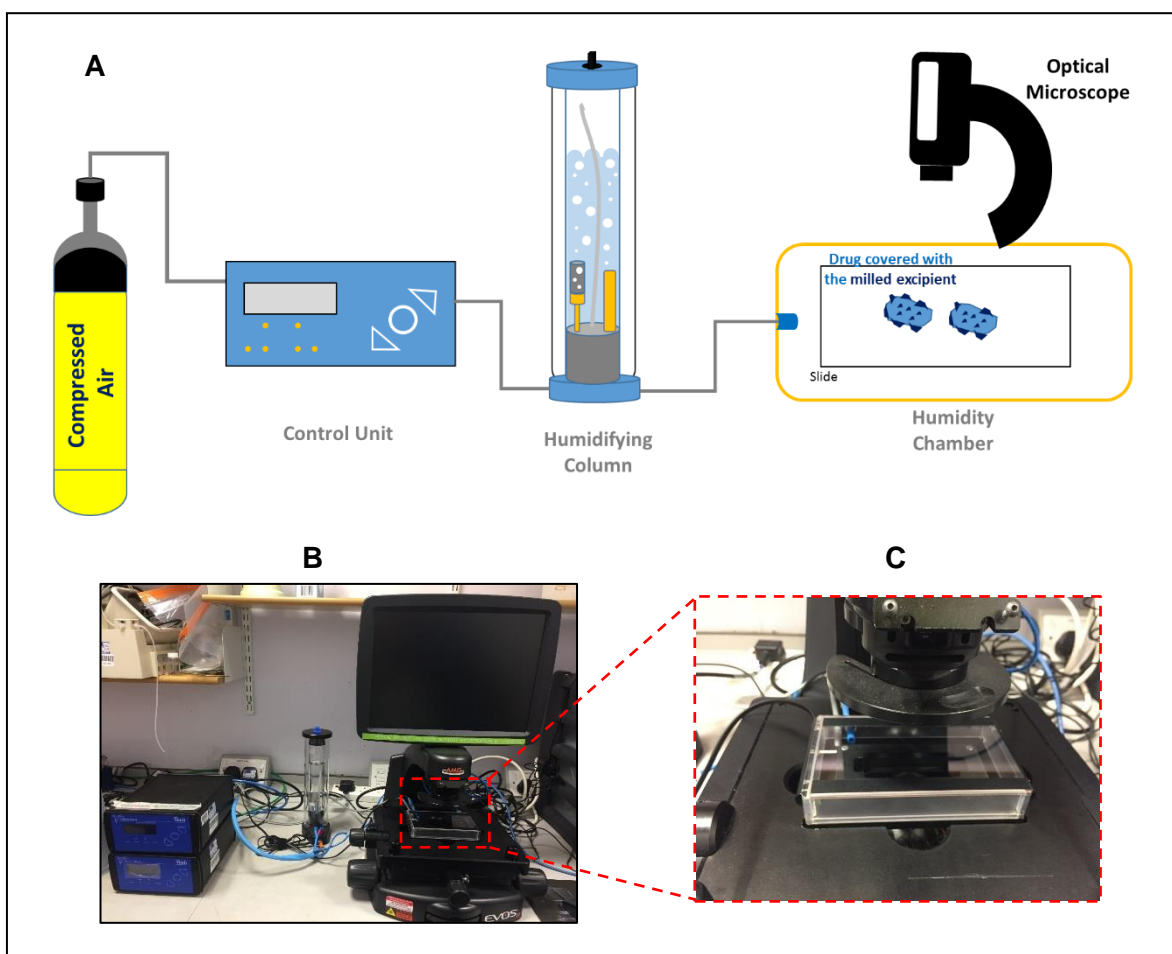


Figure 4.5: (A) Schematic diagram of the optical screening-controlled humidity system. (B) Front view of the humidity control unit and the stage-top humidity chamber. (C) Humidity chamber.

4.4. Results and Discussion

The effect of the excipient on the microenvironment pH to induce or prevent salt disproportionation was investigated using an optical screening controlled- humidity system. The *in situ* imaging system enables temporal crystal morphology information to be observed in real-time throughout the stability test run. Pioglitazone HCl and Ibuprofen sodium were selected as a weak base and weak acid drug salt model, respectively. Time-lapse optical imaging was used to track the crystal morphology changes of the drug salts formulated with a range of commonly used excipients in high relative humidity. Videos are included in the USB attached to this thesis.

4.4.1. Slurry pH Values of Excipients

For crystalline APIs subjected to pH-dependent degradation mechanisms such as disproportionation, the pH of maximum solubility (pH_{max}) and the microenvironmental pH are two pivotal parameters required to predict the likelihood of disproportionation occurring [214], [220]. The pH_{max} values of the two salts being investigated in this chapter have been reported previously in the literature [226], [274]. The microenvironment pH within the adsorbed moisture located at surfaces of the salt would be expected to be influenced by excipients exhibiting acidic/basic functionalities, which are in intimate contact [219]. For example, basic excipients which can raise microenvironmental pH values above the weak base drug salt pH_{max} value can promote disproportionation.

The pH of a slurry of a given excipient is most commonly used technique to measure the pH due to its simplicity, in which a sample of the excipient is placed in deionised water, and the pH of its saturated solution measured [220]. It is generally employed as an empirical approach to

roughly estimate the microenvironmental pH and to provide an indication of the possible drug-excipient compatibility [219], [269], [275].

Slurry pH values of excipients measured by a pH meter are listed in Table 4.3. The excipients are ranked according to their pH values (From low pH to high pH). The excipients pH values range from 1.6 for citric acid to around 9.6 for sodium stearyl fumarate. The data is in good agreement with a previous study that measured the pH using a similar method [270]. In the coming sections, the pH_{max} of the model salt drug will be compared to the measured pH values of the excipient to explain the results.

Table 4.3: Excipients microenvironment pH measured by the slurry pH method.

Excipient Name	Excipient Role [244]	Measured pH
Citric acid	Acidic Buffering Agent	1.6
Ascorbic acid	Antioxidant	2.1
Stearic acid	Lubricant	3.4
Croscarmellose Sodium (AC-DI-SOL)	Disintegrant	4.9
Sodium Starch Glycolate	Disintegrant	6.1
Lactose monohydrate	Binder Filler	6.3
Hydroxypropyl Methylcellulose (HPMC)	Binder Extended-release-matrix former	6.8
Microcrystalline Cellulose (MCC)	Binder Filler	7.1
Calcium Phosphate Dibasic	Binder Filler	7.8
Magnesium Stearate	Lubricant	8.5
Sodium Phosphate Dibasic	Basic Buffering Agent	9.1
Sodium Stearyl Fumarate	Lubricant	9.6

4.4.2. Salt Disproportionation in Solid-State during Storage

In this section, the salt disproportionation of the hydrochloride salt of Pioglitazone, a weak base with a pK_a of 5.2 and pH_{max} of 2.8 [226] and the sodium salt of Ibuprofen, a weak acid with

a pKa of 4.4 [276] and pH_{max} 6.9-7.0 [274], will be investigated. This investigation will improve the fundamental understanding of the salt stability of the two model drugs during storage in high relative humidity.

Pioglitazone HCl may disproportionate back to the free base at high pH (Basic microenvironment) as shown in Figure 4.6. Whereas, Ibuprofen sodium may disproportionate back to the free acid at low pH (Acidic environment) as shown in Figure 4.7.

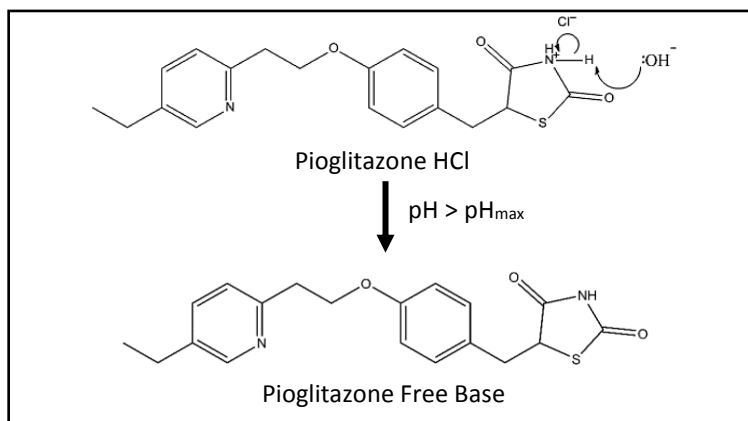


Figure 4.6: Mechanism of the salt disproportionation reaction of Pioglitazone HCl at $pH > pH_{max}$.

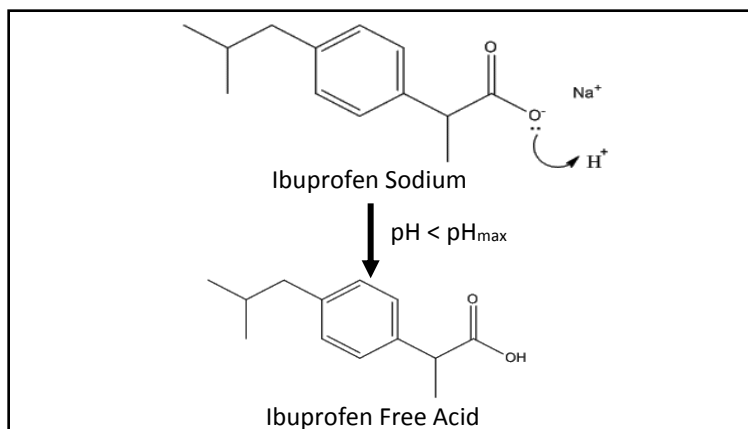


Figure 4.7: Mechanism of the salt disproportionation reaction of Ibuprofen sodium at $pH < pH_{max}$.

The effect of moisture and excipient acidity or basicity on salt disproportionation were explored by monitoring any change in the salt crystals shape using *in-situ* optical microscopy combined with humidity control chamber.

4.4.2.1. Identification of the Salt and Free Form

A crystalline solid is described by a specific external and internal structure [277]. The internal structure or polymorphic state represents the molecular arrangement within a crystal, which is mainly controlled by the intermolecular and intramolecular interactions [278]. While crystal habit (i.e. morphology) describes the overall external shape of a particular crystal [277]. Generally, differences in external crystal shape are not necessarily indicative of a change in the internal structure. For examples, changes in several external parameters such as solvent, supersaturation level, temperature, and impurities may lead to significant modifications in crystal morphology [277], [279]. This could explain the crystal habit diversity of the same chemical entity grown under various crystallisation conditions.

However, changes in internal packing usually (but not always) give an easily distinguishable change in the crystal morphology [265]. Therefore, changes in the intermolecular interactions, like the one observed in drug-excipient interactions, could have a tremendous impact on the external crystal morphology [277]. The similar effect can be observed if an API is able to undergo a phase transformation, like salt disproportionation, resulting in a crystalline form with different crystal habit.

Therefore, tracking crystal shape changes via video microscopy can be used to assess the role of moisture and excipients in salt disproportionation reaction. The prerequisite is that the salt and the free-form manifest a characteristic morphology that is sufficiently distinguished to permit assignment of crystals to a specific form based on particle shape. Crystal shape information was obtained through optical and electron microscopy. Both crystalline forms (i.e. Salt and free form) were also subjected to Raman spectroscopy analysis to verify their forms.

Pioglitazone HCl: The scanning electron microscopy (SEM) optical microscopy images of Pioglitazone HCl and the free base are shown in Figure 4.8. Pioglitazone HCl (Salt) exhibits an irregular plate-like morphology, whereas the free base presents a needle-like morphology. These significant differences can be employed to differentiate between the two forms and monitor the crystal transformation (i.e. salt disproportionation).

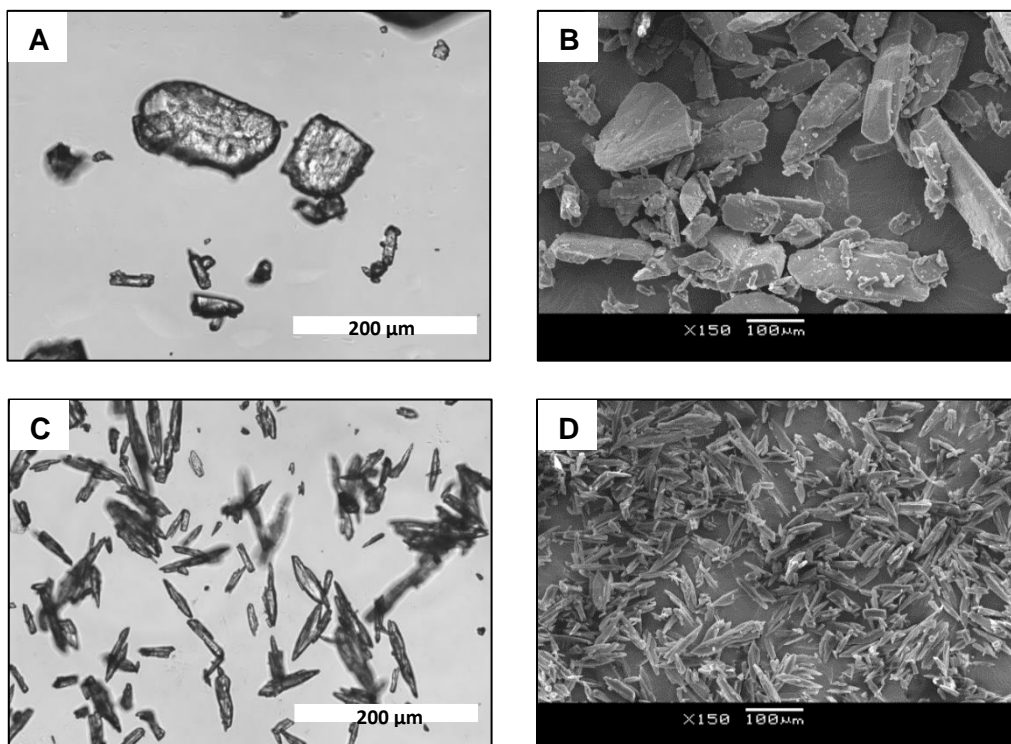


Figure 4.8: Microscopic images of Pioglitazone salt and free-form as received material: A & C: optical microscopic image of Pioglitazone HCl and Pioglitazone free base, respectively; B & D: SEM images of Pioglitazone HCl and Pioglitazone free base, respectively.

Pioglitazone salt and free base form were also subjected to Raman spectroscopy analysis to verify their forms. The Raman spectra of both forms, shown in Figure 4.9, exhibit several clear differences. Specifically, Pioglitazone HCl salt demonstrated a doublet peak found at the region 1600 to 1650 cm^{-1} , whereas the free base displayed a unique single peak at 1610 cm^{-1} . This spectral difference can be explained by the protonation of pioglitazone that changes the vibrational modes of the pyridine ring and the carbonyl group [280]–[282].

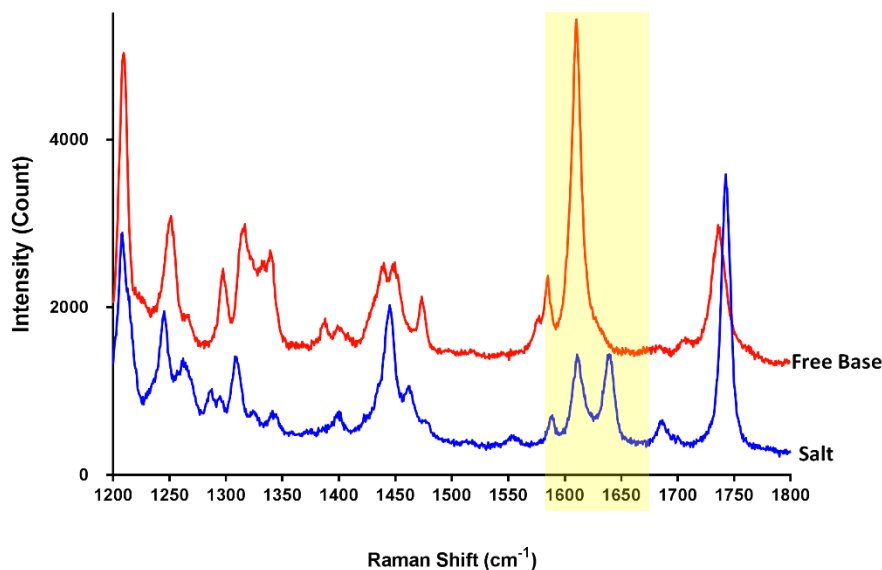


Figure 4.9: Raman spectra of Pioglitazone HCl salt and Pioglitazone free base as received material over the range 1200 cm^{-1} to 1800 cm^{-1} .

Ibuprofen Sodium: Figure 4.10 shows optical microscopy and SEM images of Ibuprofen sodium and Ibuprofen free acid crystals. The crystal form of ibuprofen free acid (Figure 4.10-B&D) appears as acicular (i.e. needle) shape crystals with round edges. On the other hand, Ibuprofen sodium shows irregular block-like crystals with rough surfaces comprising of flat-shaped ibuprofen crystals sticking together to make bigger particles (Figure 4.10- A&C). In general, the Ibuprofen salt and free acid crystals are showing different crystal morphology that can be differentiated under the microscope.

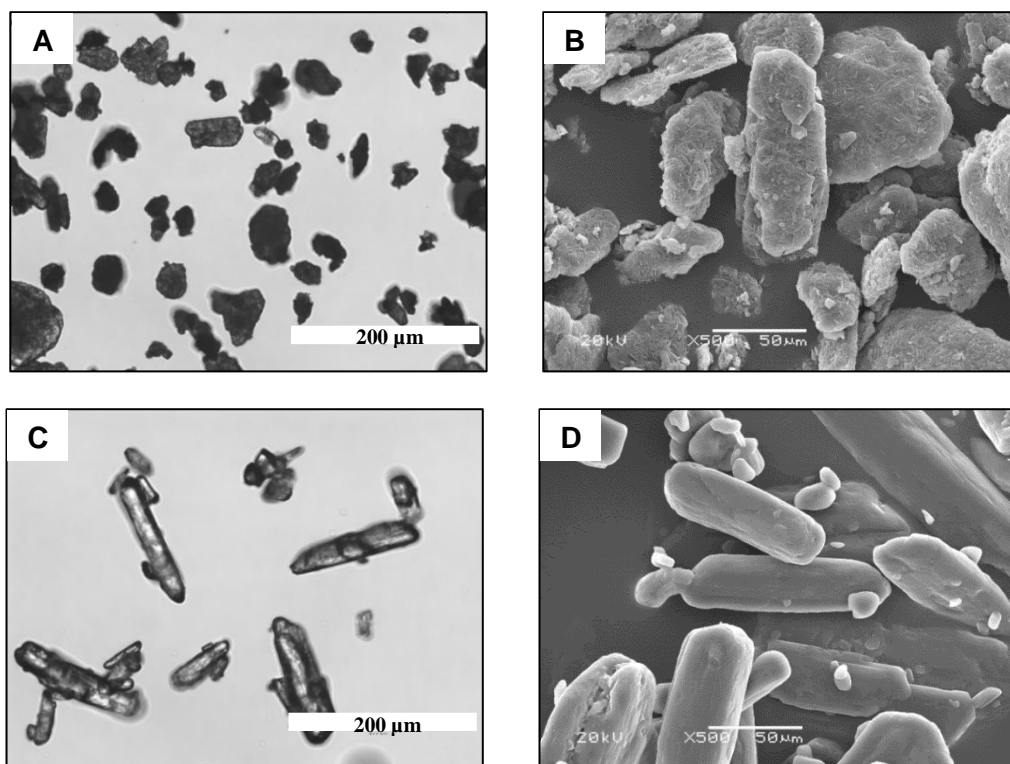


Figure 4.10: Microscopic images of Ibuprofen salt and free-form as received material: A & C: optical microscopic image of Ibuprofen sodium and Ibuprofen free acid, respectively; B & D: SEM images of Ibuprofen sodium and Ibuprofen free acid, respectively.

The Raman spectra (Spectral region 200 to 1500 cm^{-1}) of Ibuprofen sodium salt and Ibuprofen free acid are presented in Figure 4.11. The two spectra are showing some clear spectral differences between the salt and free acid forms. Specifically, Ibuprofen sodium salt demonstrates a small single peak located at 1250 cm^{-1} due to the stretching of (OC), bending of (HCC) and torsion of (HCCC) vibrational modes [283], while the free acid form demonstrated no peaks at 1250 cm^{-1} . In addition, Ibuprofen sodium salt demonstrates a single broad peak located at 800 to 850 cm^{-1} region due to the (CC) stretching, whereas the free acid displays two sharp peaks at the same region due to the (CH) bending and in-plane (CC) ring deformation [284]. All the spectral difference can be elucidated by the protonation of Ibuprofen that changes the vibrational modes of the phenyl ring and the carboxyl group.

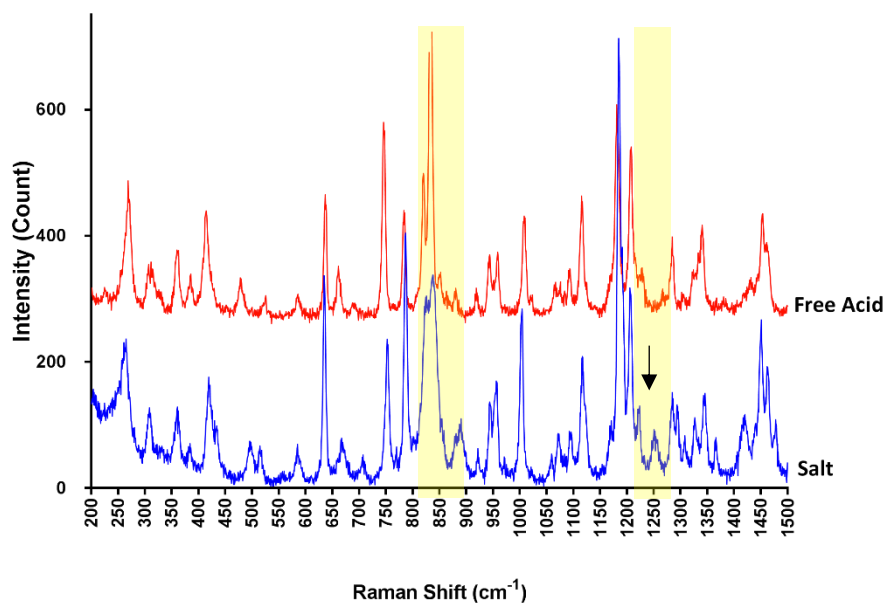


Figure 4.11: Raman spectra of Ibuprofen sodium salt and Ibuprofen free acid form over the range 200 cm^{-1} to 1500 cm^{-1} .

4.4.2.2. The Impact of Relative Humidity on Salt Disproportionation in Solid State

Water itself may participate in a chemical reaction or may perform as a solvent to provide a platform for chemical reactions [29]. During storage, the presence of an even small amount of moisture in solid dosage forms may facilitate the salt disproportionation [243], [248]. Therefore, the influence of moisture on the salt transformation process was investigated.

Pioglitazone HCl: Crystals of pure Pioglitazone HCl were incubated in high relative humidity (75-90% RH), and *in-situ* monitoring of the crystal morphology changes was performed. The single crystal of Pioglitazone salt form was, within minutes, covered by needle-like crystallites as shown in Figure 4.12-B - D. The change in the crystal structure can be related to the phase transition between the salt form and free base form. It is likely that a local increase in the supersaturation level in the microscopic water layer surrounding the salt crystal may be occurred due to the high pH of water (around 7) compared to the salt pH_{max} (2.8). This supersaturation

would increase the probability of precipitation of the free base form in the vicinity of the salt crystal.

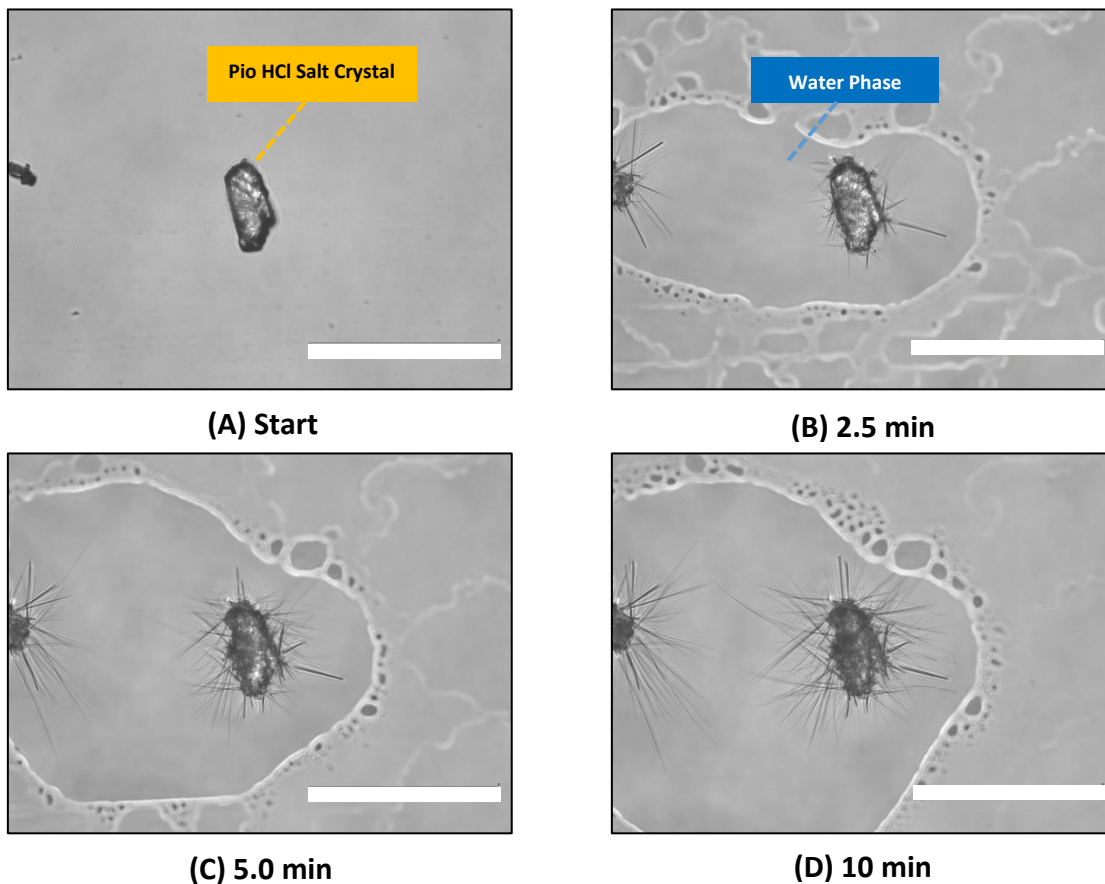


Figure 4.12: *In situ* optical microscopy images of Pioglitazone HCl crystal morphological variation during salt disproportionation stored at 75-90% RH: (A) Start (B) 2.5 min (C) 5.0 min (D) 10 min. Scale bar for images is 100 μm .

To support this observation, Raman spectra of Pioglitazone HCl crystals before and after the transformation was compared. The Raman spectrum of the needle crystals formed after the transformation in the high humidity environment matched that of Pioglitazone free base completely (Figure 4.13). It indicates that the formation of the needle crystals was due to the transformation of the salt form to the free base. Therefore, optical screening can be used to investigate salt disproportionation by monitoring the change in crystal shape from plate crystals to needle crystals.

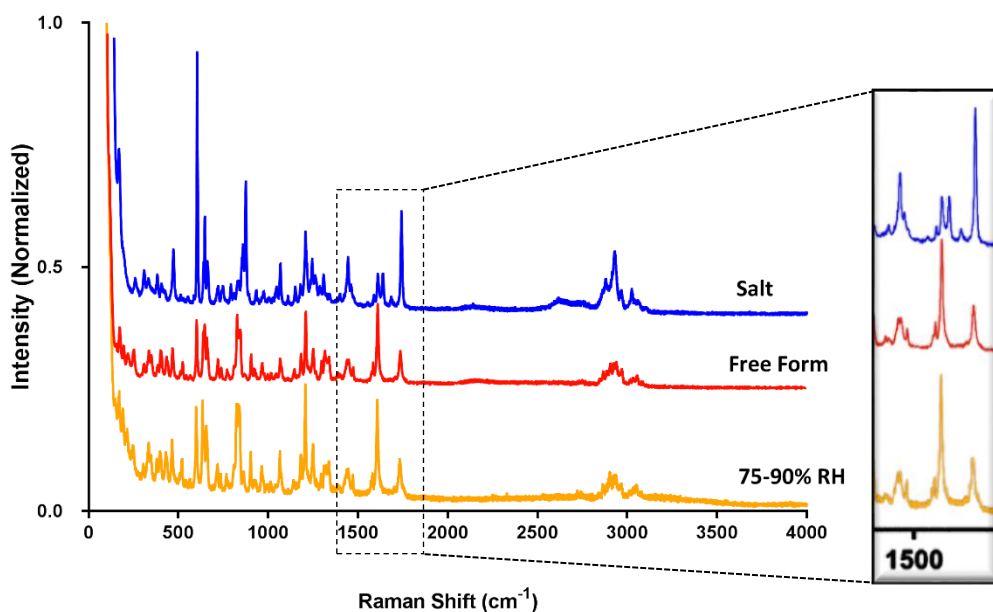


Figure 4.13: Raman spectra (100 to 4000 cm^{-1}) of Pioglitazone HCl (Blue spectra), Pioglitazone free base (red spectra) and Pioglitazone HCl after incubation in 75-90% RH. Y-axis offsets were applied for presentational purposes.

Ibuprofen Sodium: Similar to Pioglitazone, Ibuprofen sodium crystals were exposed to high relative humidity (75-90% RH), and *in-situ* monitoring of the crystal morphology change was performed. Ibuprofen sodium crystals were disintegrated rapidly after 1.0 min of storing at high humidity followed by complete dissolution in the surrounding water layer at time = 1.5 min (Figure 4.14). No re-crystallisation of the free acid (i.e. Disproportionation) was optically detected after the crystal dissolution, which indicates the formation of a stable solution of ibuprofen sodium in the water layer (i.e. moisture). It is likely that the compatibility of the water pH with the pH_{max} of ibuprofen sodium (approximately 7) favours the salt dissolution over the free acid precipitation.

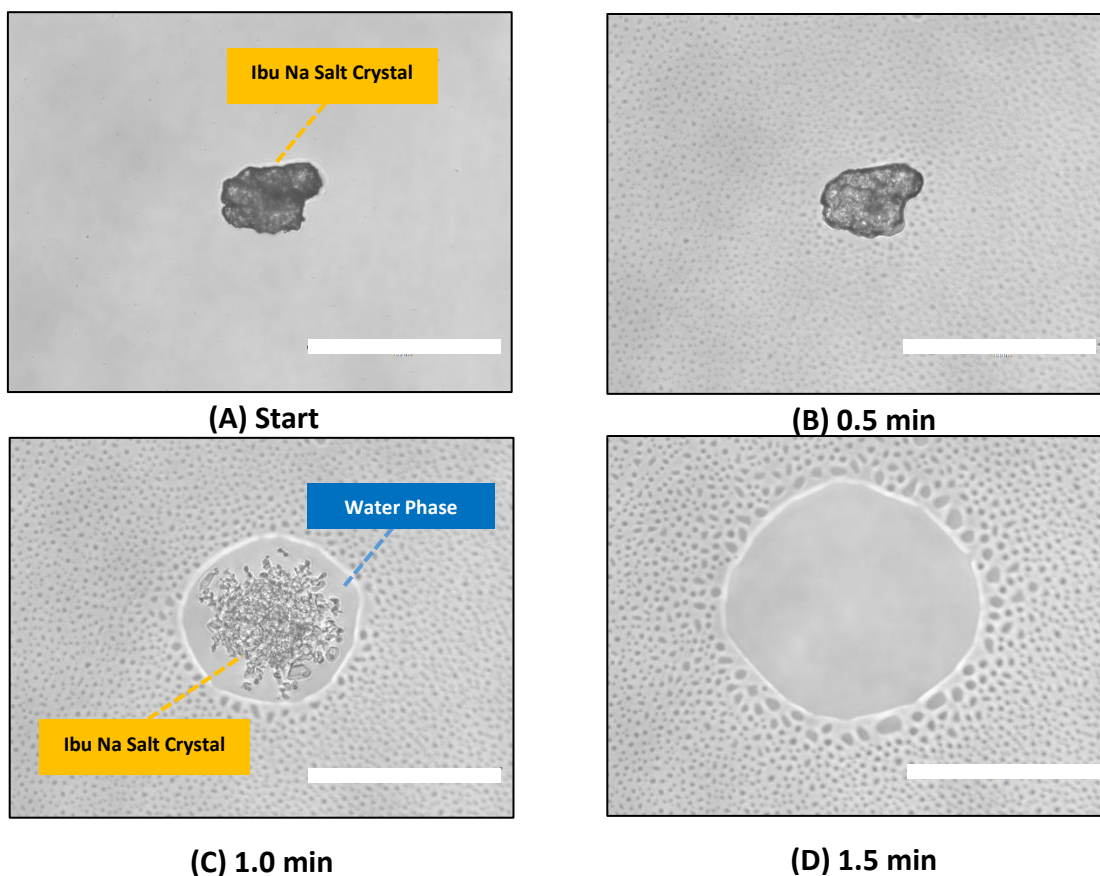


Figure 4.14: *In situ* optical microscopy images of Ibuprofen sodium crystal dissolution during the storage at 75-90% RH: (A) Start (B) 0.5 min (C) 1.0 min (D) 1.5 min. Scale bar for images is 100 μm .

4.4.2.3. The Effect of Excipient on Salt Disproportionation in Solid State

Salt disproportionation is thermodynamically controlled by the pH of the microenvironment around the drug crystals relative to its pH_{max} [220]. Microenvironmental pH within the moisture located at surfaces of the salt crystals is expected to be influenced by excipient's properties including, but not limited to, acidity/basicity, aqueous solubility and hygroscopicity [225]. Therefore, the impact of different excipient properties on the disproportionation of Pioglitazone HCl and Ibuprofen sodium was assessed. Binary blends were prepared by mixing the salt with individual excipients at 1:1 ratio. *In-situ* optical screening with

control humidity chamber (RH%= 75-90%) was used to investigate the salt disproportionation in these binary mixtures by tracking the change in the salt crystal morphology.

4.4.2.3.1. Citric Acid Monohydrate

Citric acid is widely used pH modifiers in pharmaceutical formulations, primarily to adjust the microenvironment pH of tablet matrices [244]. pH modifiers, such as citric acid, has been used previously as an effective tool to modulate the microenvironment pH for stability purposes [32], [285], [286]. Therefore, drug salts were mixed with citric acid to investigate the effect of citric acid on Pioglitazone HCl and Ibuprofen sodium stability during storage.

Pioglitazone HCl: Citric Acid: Pioglitazone pH_{max} is equal to (2.8) while the measured pH of citric acid is around (1.6) (Table 4.3-Section 4.4.1), which is below the pH_{max} of the salt. Therefore, the salt is expected to be the most stable species at high RH. Figure 4.15 shows optical microscopy images of Pioglitazone HCl covered with citric acid acquired at 75-90% RH. No significant difference in the crystal shape can be observed after 10 min incubation in high RH. The difference is that the salt crystal was getting smaller in size with time. This indicates the dissolution of the salt crystal in the water layer, which can be clearly seen in the video (attached USB). This observation was significantly different from the one reported early when the drug salt was stored in high RH without any additives (Section 4.4.2.2). It is evident that citric acid plays a significant role in lowering the microenvironment pH below the pH_{max} of the drug and prevent the formation of the needle crystals (i.e. salt disproportionation). Similar findings were reported previously on the role of citric acid in minimising weak basic salt disproportionation in solid dosage forms [287]–[290].

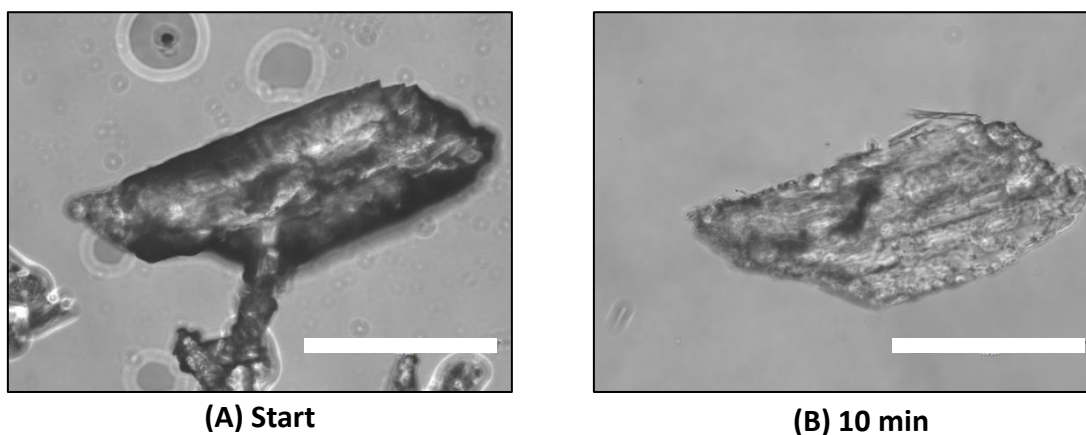


Figure 4.15: *In situ* optical microscopy images of Pioglitazone HCl crystal mixed with citric acid during storage at 75-90% RH: (A) Start (B) 10 min. Scale bar for images is 100 μm .

Ibuprofen Sodium: Citric Acid: In contrast to Pioglitazone HCl, it is expected that the low pH values of citric acid would induce disproportionation of Ibuprofen sodium in the solid state. The crystal shape transformation images obtained at high RH of Ibuprofen sodium and citric acid binary mixture are shown in Figure 4.16. Figure 4.16-A shows few Ibuprofen sodium crystals covered with milled citric acid at the start of the test. The image in Figure 4.16-B was taken after 2.5 min incubation in high RH and showed the initial dissolution of block Ibuprofen crystals. After 5 min (Figure 4.16-C), the formation of small needle-shaped crystals, which enlarge in a dendritic fashion over several tens of microns (Orange arrows), was observed. At $t=10$ min, a new darker contrast appeared near the previously formed dendrites (red arrows, Figure 4.16-D).

Christensen et al. [225] hypothesised the existence of a solution-mediated phase transformation (SMPT) mechanism for salt disproportionation of free acid salts, like Ibuprofen sodium, in the presence of acidic excipient. Figure 4.16 supports the SMPT mechanism that suggested the initial dissolution of the salt (Figure 4.16-B) followed by subsequent nucleation and growth of the free acid form (Figure 4.16- C&D).

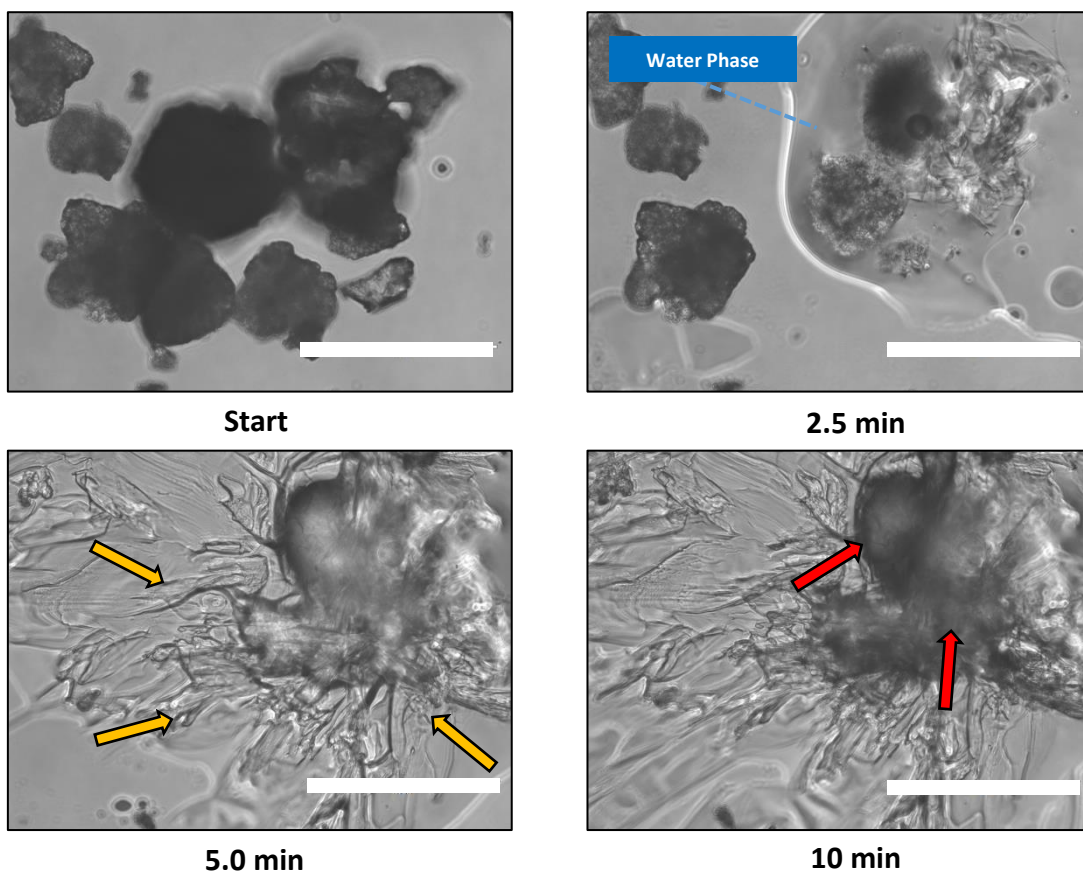


Figure 4.16: *In situ* optical microscopy images of Ibuprofen crystals mixed with citric acid during storage at 75-90% RH: (A) Start (B) 2.5 min (C) 5.0 min (D) 10 min. Scale bar for images is 100 μm

To support this observation, Raman spectra of the Ibuprofen dendritic needle crystals were obtained and compared to the Ibuprofen salt and free acid spectra (Figure 4.17). The Raman spectrum of the needle crystals formed after the transformation in the high humidity environment matched that of Ibuprofen free acid. These results indicate that citric acid can induce Ibuprofen sodium salt disproportionation, which resulted in a change in crystal shape from block crystal to needle-like crystals.

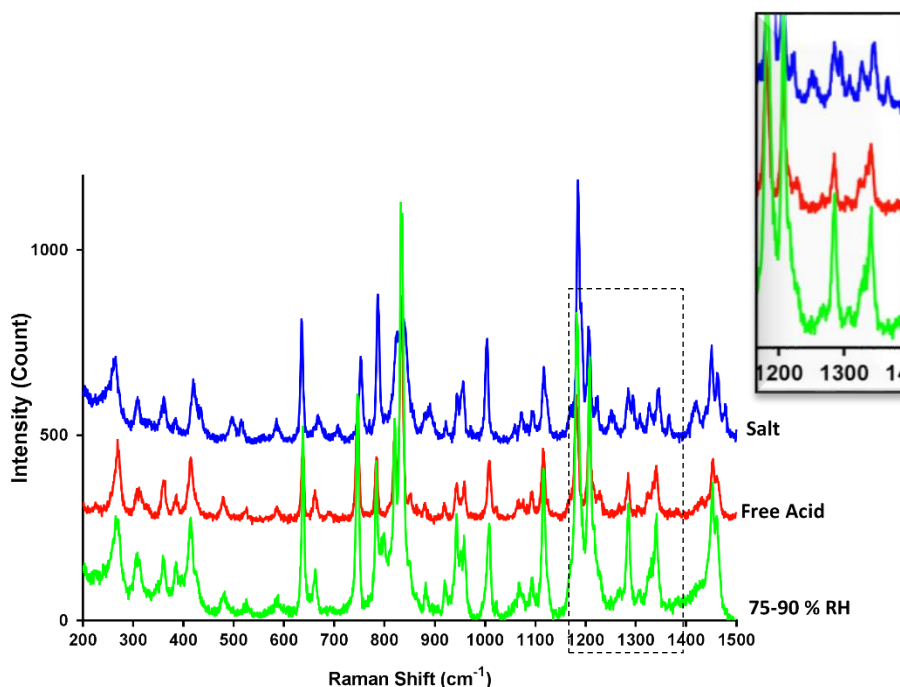


Figure 4.17: Raman spectra (200 to 1500 cm⁻¹) of Ibuprofen sodium (Blue spectra), Ibuprofen free acid (red spectra) and Ibuprofen sodium after incubation in 75-90% RH with citric acid monohydrate. Y-axis offsets were applied for presentational purposes.

4.4.2.3.2. Ascorbic Acid

Ascorbic Acid is a water-soluble organic acid, also called Vitamin C, used as an antioxidant to improve the shelf-life of pharmaceuticals. Antioxidants retard or inhibit the oxidation of active substances and excipients by free radicals in the finished product [244], [291]. Due to the acidity of ascorbic acid in the presence of water (pKa 4.20) [244], it provides labile H⁺ which will be accepted by any free radical to terminate the oxidation reaction [291]. When salts formulated with Ascorbic acid are exposed to relative humidity during storage, the ascorbic acid liberates free H⁺ ions in the microscopic water layer, which leads to lower the microenvironment pH.

Pioglitazone HCl: Ascorbic Acid: Like citric acid, Pioglitazone HCl crystal mixed with ascorbic acid showed no crystal morphological changes (Figure 4.18). The salt crystal exhibited a gradual dissolution behaviour on a microscopic scale with all the crystal surfaces retreated along all directions. The optical screening images essentially showed that the ascorbic acid lowers the

pH below the pH_{max} of the drug preventing the free base from being formed and keeping the drug as the more soluble HCl salt. Sample involving a larger number of Pioglitazone HCl crystals mixed with ascorbic acid showed similar results (Figure A.1 - Appendix A).

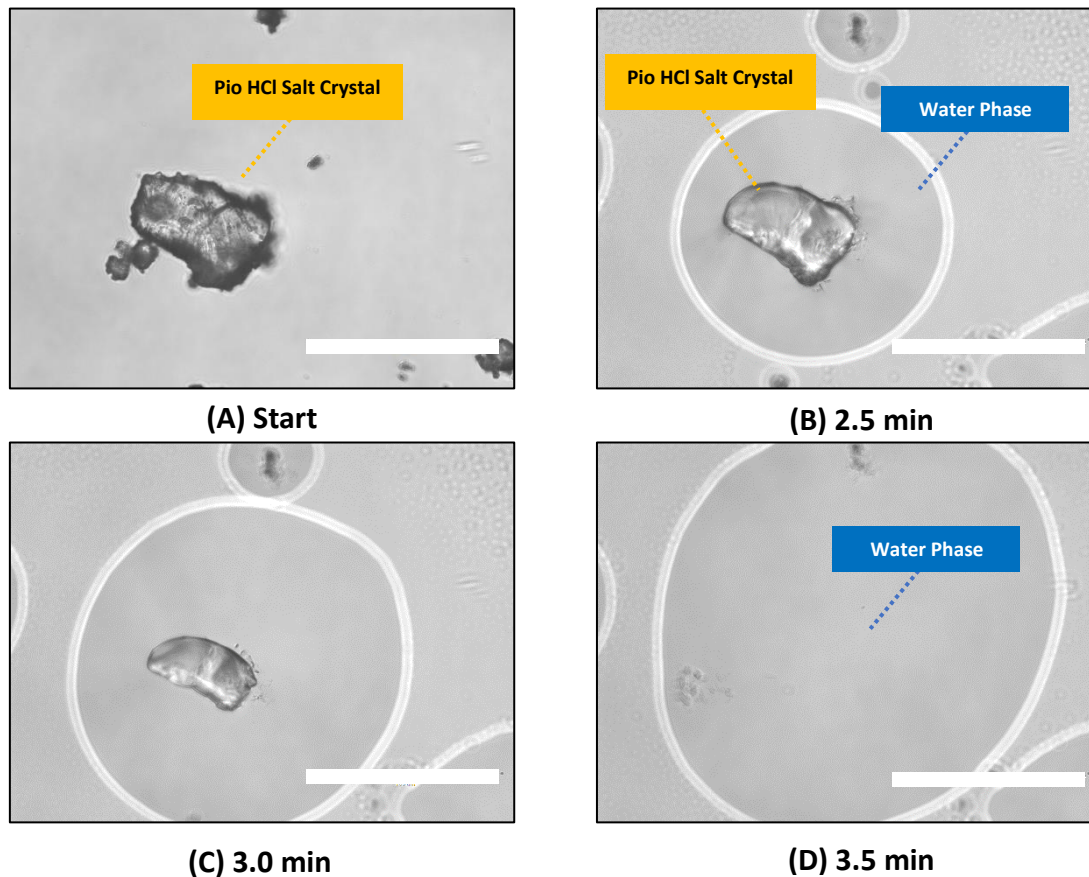


Figure 4.18: *In situ* optical microscopy images of Pioglitazone HCl crystal mixed with ascorbic acid during storage at 75-90% RH: (A) Start (B) 2.5 min (C) 3.0 min and (D) 3.5 min. Scale bar for images is 100 μ m.

Ibuprofen Sodium: Ascorbic Acid: *In-situ* optical imaging of Ibuprofen sodium mixed with ascorbic acid under high RH showed a change in drug crystal morphology (Figure A.2 - Appendix A). Needle shape crystals growing in a dendritic fashion were seen after 5 min. The data revealed the role of ascorbic acid in reducing the microenvironment pH (around 2) below the pH_{max} of Ibuprofen Sodium (approximately 7) facilitating the conversion of the salt drug to the free acid which precipitated in the form of dendrites crystals.

4.4.2.3.3. Stearic Acid

Stearic acid (SA) is a saturated fatty acid that is used as a lubricant in tablet manufacturing to reduce the friction between the surfaces of the metal and that of formulation powders as well as to ensure the continuation of the operation [244], [292], [293]. It is practically insoluble in water, so only small concentrations are added generally to the formulation. The measured pH of stearic acid is (3.4), which is higher than the pH_{max} of Pioglitazone (2.8) and lower than the pH_{max} of Ibuprofen sodium (7.0). Therefore, salt disproportionation is expected to occur in both drug salts.

Pioglitazone HCl: Stearic Acid: Figure 4.19 illustrates the optical monitoring of Pioglitazone HCl and stearic acid binary mixture at high RH. The image in Figure 4.19-A was taken at the beginning of the experiment before increasing the RH to 75-90% RH. After 5 min, large needle-like crystals were observed, which could potentially indicate the formation of the free base form or the less-soluble Pioglitazone stearate salt (Figure 4.19-B).

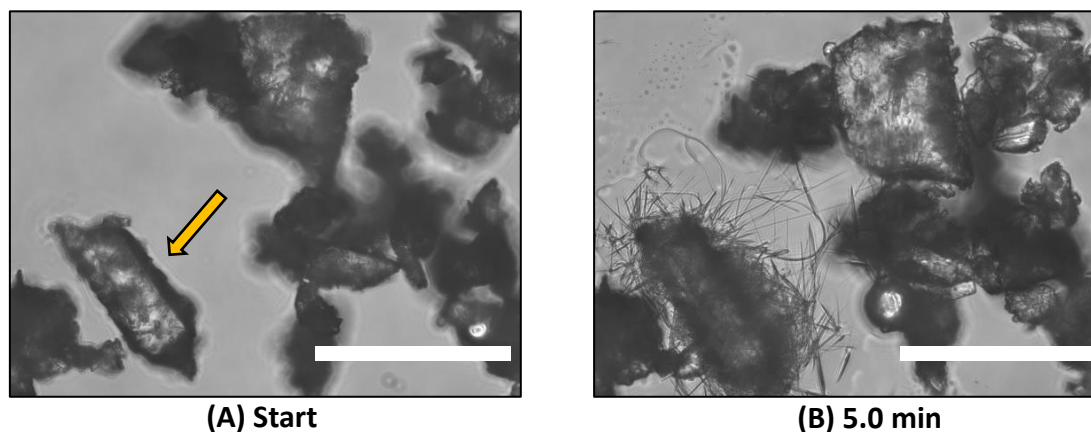


Figure 4.19: *In situ* optical microscopy images of Pioglitazone HCl crystal (Orange arrow) mixed with stearic acid during storage at 75-90% RH: (A) Start (B) 5 min. Scale bar for images is 100 μm .

However, weak acids, that have a pK_a greater than 1.5 such as stearic acid, often do not yield Pioglitazone salt [294]. Therefore, it was reasonably believed that the needle-crystals

formed were attributed to the precipitation of the free base. The results match the prediction based on the measured pH of the excipient and the pH_{max} of the salt.

Ibuprofen Sodium: Stearic Acid: As shown earlier (Section 4.4.2.3.1), the salt disproportionation process is mainly accompanied by the dissolution of the salt form and subsequent nucleation and growth of free acid form. Figure 4.20 shows images of Ibuprofen crystal mixed with stearic acid at different times during the optical screening experiment conducted at 75-90% RH. The sodium salt crystal disappeared after 1.0 min (dissolution). After about 2.0 min, a small number of fine, needle crystals were suspended in the solution, which indicates the nucleation and growth of a new, less-soluble form. The successful formation of a less-soluble Ibuprofen salt (i.e. Ibuprofen stearate) is linked to the difference in the pK_a values of Ibuprofen and stearate counterion. For the synthesis of salt forms of acidic drugs like Ibuprofen, the pK_a of the counterion should be at least two units higher than the pK_a of the drug in order to confirm that the proton transfer is energetically favourable [218]. The pK_a value of stearic acid is 4.8 [295], which is just slightly higher than the pK_a of Ibuprofen ($\text{pK}_a = 4.4$). The significantly small difference in pK_a between Ibuprofen sodium and stearic acid reduces the probability of the salt formation and confirm the precipitation of Ibuprofen free acid as small needle crystals.

The formation of Ibuprofen free acid is also supported with the incompatibility between the measured pH of stearic acid and the pH_{max} of Ibuprofen sodium. It is important to note that stearic acid is used as a lubricant in some Ibuprofen sodium tablet formulation such as Advil® [296], which could increase the risk of salt disproportionation during storage and affect the product performance and bioavailability *in vivo*.

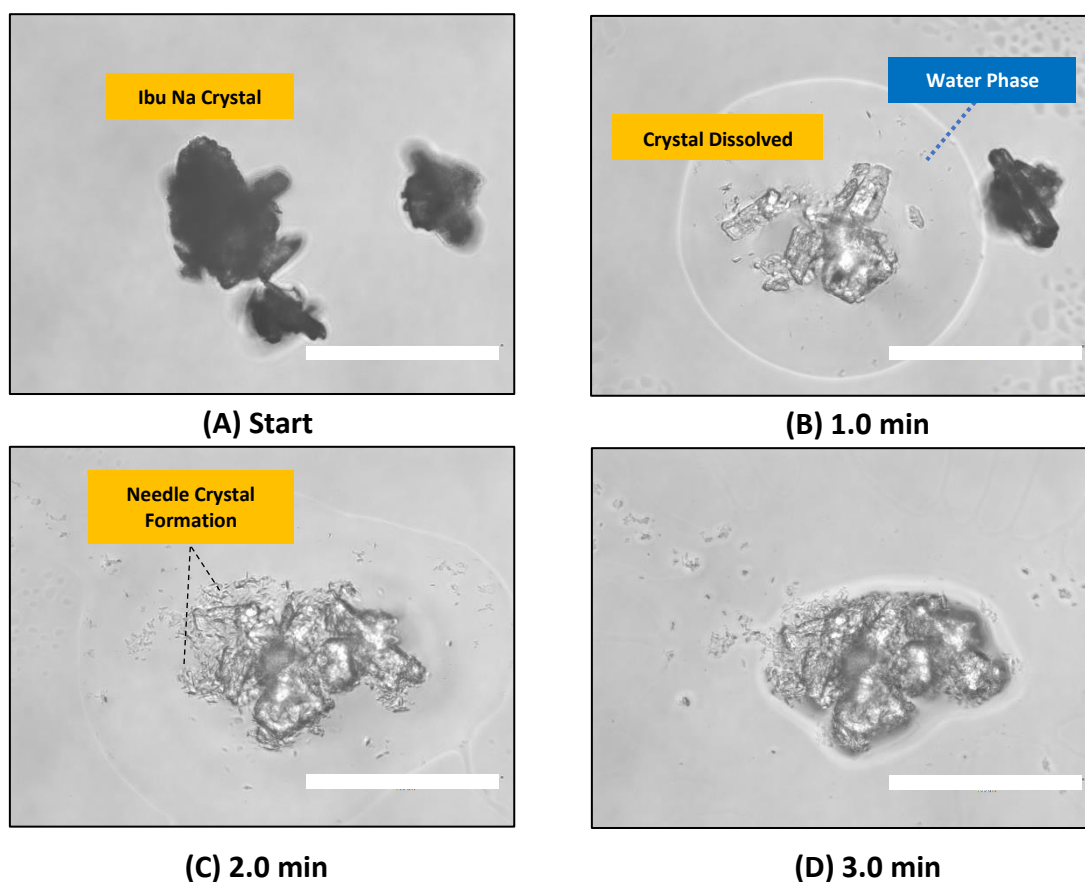


Figure 4.20: *In situ* optical microscopy images of Ibuprofen crystals mixed with stearic acid during storage at 75-90% RH: (A) Start (B) 1.0 min (C) 2.0 min (D) 3.0 min. Scale bar for images is 100 μm .

4.4.2.3.4. Croscarmellose Sodium (AC-DI-SOL)

Croscarmellose sodium (CCNa) is used as a super-disintegrant in oral pharmaceutical formulations. Despite being water insoluble, croscarmellose sodium rapidly swells to 4–8 times its original volume in the presence of water [244]. Therefore, it is expediting tablet disintegration by increasing the internal pressure within the tablet matrix [297]. Due to the water insolubility, the measured pH of croscarmellose sodium has lower predictive power of salt disproportionation comparing to water-soluble excipients. Therefore, optical screening is suitable to investigate the effect of CCNa on salt stability stressed at high relative humidity.

Pioglitazone HCl: Croscarmellose Sodium: As seen in Figure 4.21-A, the Pioglitazone HCl plate crystal was surrounded by fibre, straw-like particles of CCNa before increasing the relative

humidity. After increasing the relative humidity from ambient to 75-90%, the CCNa particles were growing due to the swelling behaviour in the presence of water while the Pioglitazone HCl crystal showed no significant difference in crystal shape after 10 min. Incubating the binary mixture for a longer time (Figure 4.21-C to D) did not reveal any change in the salt crystal structure. It is likely that a large part of the water consumed or bound with the excipient particle and thus unavailable to dissolve the drug. As salt disproportionation is a solution mediated reaction, the drug dissolution is an essential step for the transformation of the salt to the free base. These results contradict the results reported previously; showing the effectiveness of croscarmellose sodium at causing disproportionation of the weakly basic salt drug [30], [201], [229], [233]. However, the salt disproportionation in these studies was investigated after several days of incubation in high relative humidity, which is significantly different from the optical screening time frame (minutes). Therefore, it is expected that salt disproportionation may occur after the saturation of the disintegrant particle with water, which allows the excess water to facilitate the disproportionation reaction.

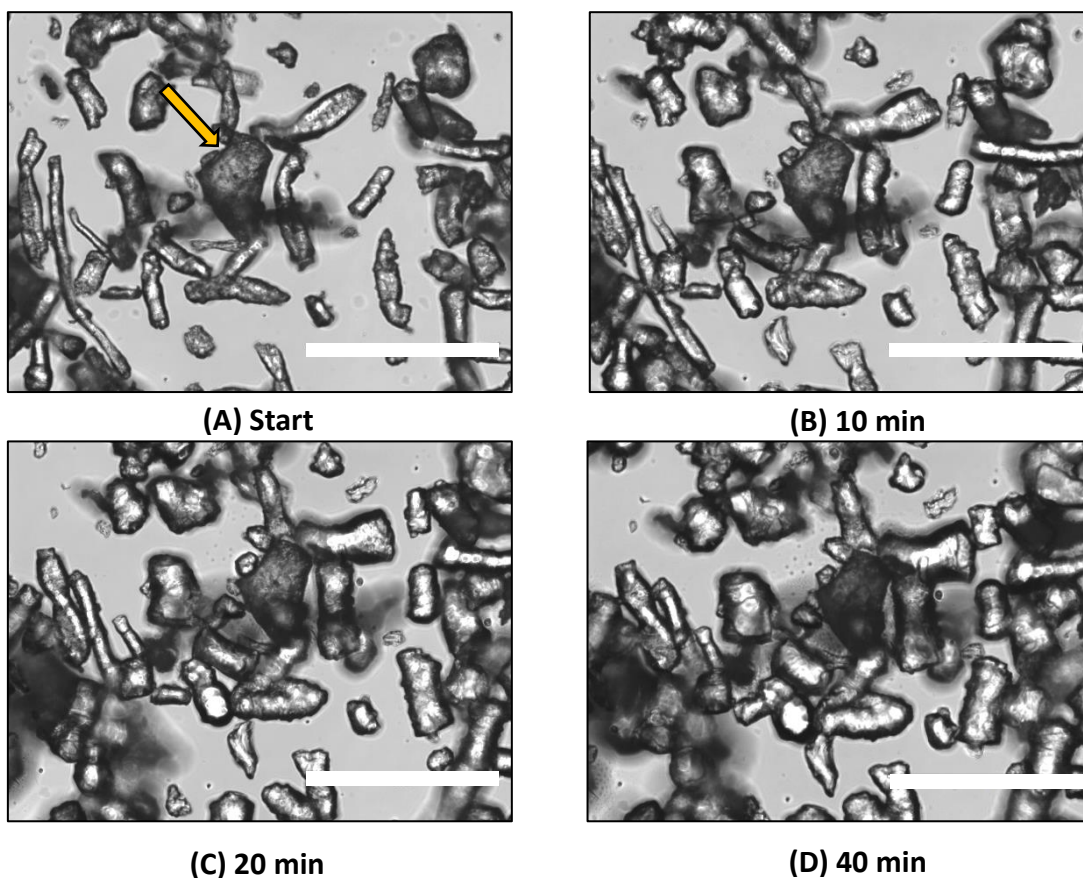


Figure 4.21: *In situ* optical microscopy images of Pioglitazone HCl crystal (Orange arrow) mixed with croscarmellose sodium during storage at 75-90% RH: (A) Start (B) 10 min (C) 20 min (D) 40 min. Scale bar for images is 200 μm .

Ibuprofen Sodium: Croscarmellose Sodium: Snapshots of the Ibuprofen sodium behaviour mixed with CCNa at high relative humidity using the *in-situ* optical microscopy are illustrated in Figure A.3 (Appendix A). The size of the CCNa particles increased, but the shape of the Ibuprofen sodium did not seem to change while stressed in high RH. Ibuprofen sodium crystals started dissolving, when the disintegrant particle stopped growing (i.e. saturated with water) at time = 3.0-4.0 min. The presence of the CCNa did not induce any salt disproportionation during storage at 75-90% RH.

4.4.2.3.5. Sodium Starch Glycolate

Sodium starch glycolate (SSG) is a widely used disintegrant in tablet formulations [244]. Similar to the croscarmellose sodium, disintegration occurs by the rapid uptake of water followed by rapid and enormous swelling [298]–[300]. In the presence of water, sodium starch glycolate swells to up to 300 times its volume [244]. The *in-situ* optical screening was used to investigate the stability of Pioglitazone HCl and Ibuprofen sodium mixtures with SSG.

Pioglitazone HCl: Sodium Starch Glycolate: The data showed a similar trend to the one seen in croscarmellose sodium. The SSG oblong, semi-spherical particles showed an increase in size due to the swelling behaviour in the presence of water while the Pioglitazone HCl crystal showed no significant difference in crystal shape during the whole experiment (Figure A.4-Appendix A). The absence of water around the drug crystals minimised the transformation of the salt to the free base.

Ibuprofen Sodium: Sodium Starch Glycolate: The *in-situ* optical monitoring of ibuprofen sodium crystals mixed with SSG showed Ibuprofen crystal dissolution once the disintegrant particle saturated with water at time= 5.0 min (Figure A.5-Appendix A).

4.4.2.3.6. Lactose Monohydrate

Lactose monohydrate (LM) is a widely used filler in solid dosage forms [244]. Fillers are commonly used to provide bulk for the active ingredient to be measured accurately and improve the formulation properties such as cohesion. The measured pH value of lactose monohydrate is around (6.3) (Section 4.4.1-Table 4.3), which is higher than the pH_{max} of Pioglitazone HCl and bordering on the pH_{max} of Ibuprofen sodium.

Pioglitazone HCl: Lactose Monohydrate: *In situ*, optical screening images indicate a change in shape of the Pioglitazone HCl crystals, as shown in Figure 4.22. A rapid dissolution of lactose monohydrate fine crystals followed by subsequent salt crystals conversion from irregular plates to a needle-like shape after 5.0 min was observed (Figure 4.22-C). This change indicates that lactose monohydrate contributed to the increase of the microenvironment pH above the pH_{max} of the drug, which allowed the salt disproportionation in the shape of the observed morphology change. It is important to note that, the FDA approved Pioglitazone HCl tablet, Actos[®], contains lactose monohydrate as a filler [301], which increases the risk of disproportionation in solid dosage form during storage.

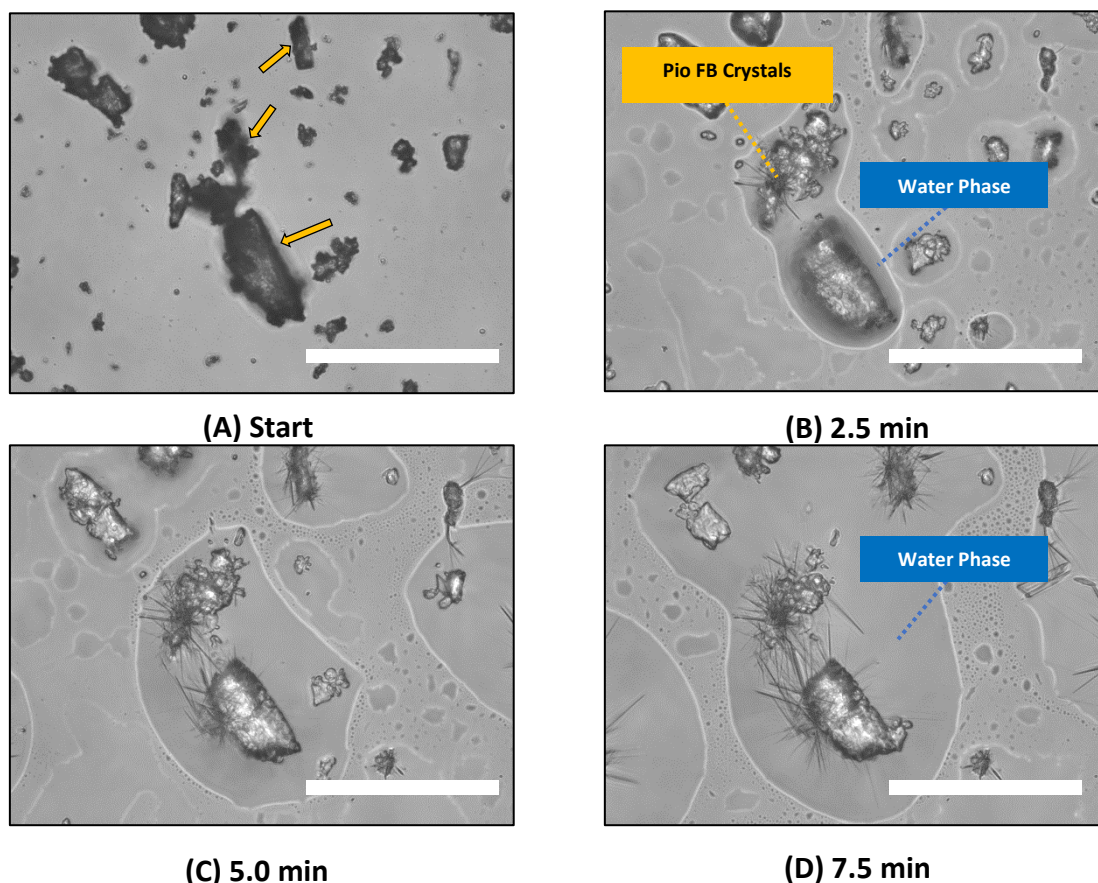


Figure 4.22: *In situ* optical microscopy images of Pioglitazone HCl crystals (Orange arrows) mixed with lactose monohydrate during storage at 75-90% RH: (A) Start (B) 2.5 min (C) 5.0 min (D) 7.5 min. Scale bar for images is 100 μ m.

Ibuprofen Sodium: Lactose Monohydrate: Optical microscopy images of Ibuprofen sodium covered with lactose monohydrate acquired at 75-90% RH are shown in Figure A.6 (Appendix A). The Ibuprofen sodium salt crystal started disintegrating after 2.0 min and then completely dissolved after 5.0 min leaving the lactose monohydrate particles suspended in the water layer dissolving slowly. The results indicated the stability of Ibuprofen sodium when formulated with lactose monohydrate

4.4.2.3.7. Hydroxypropyl Methylcellulose (HPMC)

Hydroxypropyl methylcellulose is a hydrophilic polymer that is primarily used in tablet formulations as a binder [302] and as extended-release-matrix former [303]–[305]. In addition, HPMC is commonly used as drug precipitation inhibitors in supersaturating drug delivery systems, by interfering with the crystal nucleation and growth stages [306]. As salt disproportionation is a solution mediated reaction that involves the dissolution of the salt and the nucleation and growth of the free-form crystals[31], [32], the use of drug precipitation inhibitors such as HPMC can minimise or prevent salt disproportionation during storage at high relative humidity. Therefore, Pioglitazone HCl and Ibuprofen sodium were mixed with HPMC and the crystal morphology was monitored using an *in-situ* optical microscopy at high relative humidity.

Pioglitazone HCl: Hydroxypropyl methylcellulose: Figure 4.23 shows images at different times of Pioglitazone crystals mixed with HPMC at 75-90% RH. After 3.0 min (Figure 4.23-B), HPMC particles dissolved, forming a water layer around the drug salt crystal. After 5.0 min, tiny fine needle crystals were seen at the surface of the salt crystal. No major change on the crystal structure was observed at time= 10 min. It is evident that adding HPMC delayed and prevented the growth of larger needle crystals as seen in Pioglitazone HCl-only powder stressed at high

humidity (Section 4.3.2.2), drug salt mixed with stearic acid (Section 4.4.2.3.3) and lactose monohydrate (Section 4.4.2.3.6). The role of HPMC as a precipitation inhibitor might have minimised the salt disproportionation by preventing the significant nucleation of the free base as well as inhibiting the growth of the free base crystal. Several possible mechanisms of inhibition of drug precipitation by HPMC might be responsible for preventing the salt disproportionation. These mechanisms include the intermolecular interaction between the drug and polymer via hydrogen bonding [307]–[309], steric hindrance of recrystallisation or a combination of both [306], [308], [310], [311]. The hydroxyl groups (hydrogen bond donor) of HPMC are capable of forming hydrogen bonding with drugs, which lead to an inhibition in drug nucleation and subsequent crystal growth. The dissolution of HPMC in the microscopic water layer is expected to increase water layer viscosity, which will result in a greater steric hindrance of recrystallisation. The high viscosity in water layer will retard the diffusion rate of the drug in the surrounding environment and inhibit nucleation and crystal growth [306].

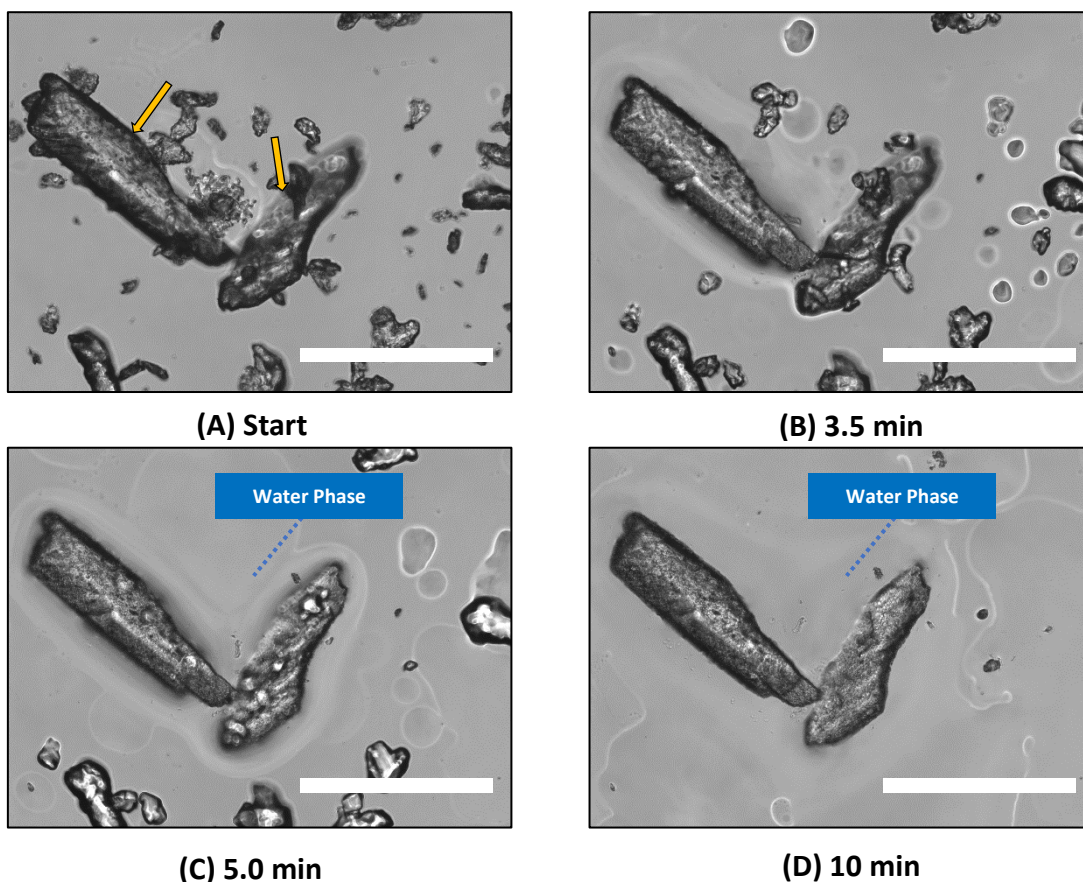


Figure 4.23: *In situ* optical microscopy images of Pioglitazone HCl crystals (Orange arrows) mixed with hydroxypropyl methylcellulose (HPMC) during storage at 75-90% RH: (A) Start (B) 3.5 min (C) 5.0 min (D) 10 min. Scale bar for images is 100 μm .

Ibuprofen Sodium: Hydroxypropyl methylcellulose: Figure 4.24 demonstrates the change of the Ibuprofen crystal shape during the *in-situ* optical screening experiment against HPMC conducted at high relative humidity. The crystals slowly disintegrated and decreased in size (i.e. dissolution), but the crystal shape did not seem to change to a needle-like crystal during the whole experiment (time= 10 min, Figure 4.24-D). The drug precipitation inhibition properties of the HPMC and the compatibility of the HPMC measured pH (6.8) and pH_{max} of Ibuprofen sodium (~ 7.0), prevented the salt disproportionation at high relative humidity.

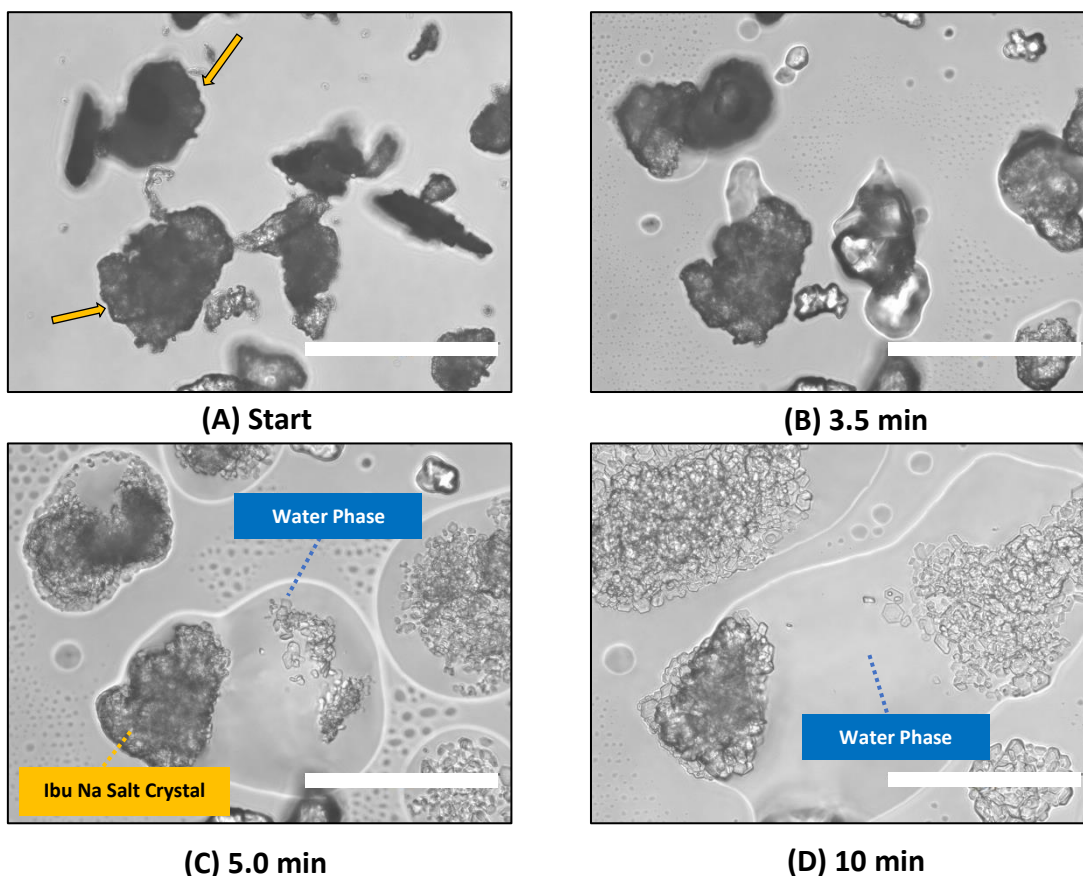


Figure 4.24: *In situ* optical microscopy images of Ibuprofen sodium crystals (Orange arrows) mixed with hydroxypropyl methylcellulose (HPMC) during storage at 75-90% RH: (A) Start (B) 2.5 min (C) 5.0 min (D) 10 min. Scale bar for images is 100 μm .

4.4.2.3.8. Microcrystalline Cellulose (MCC)

Microcrystalline cellulose (MCC) is mainly used as a binder/diluent in oral tablets prepared by direct-compression [244].

Pioglitazone HCl: Microcrystalline Cellulose: The *in-situ* optical imaging (Figure A.7 - Appendix A) shows an apparent transformation of the plate-like crystal into needle-like crystals at time=5.0 min as shown in Figure A.7-C. The measured pH of MCC is significantly higher than the pH_{max} of Pioglitazone HCl which favours the salt conversion to the free base.

Ibuprofen Sodium: Microcrystalline Cellulose: Figure 4.25 illustrates the stability of Ibuprofen sodium crystals mixed with MCC at high relative humidity. The *in-situ* optical imaging shows a complete dissolution of the ibuprofen sodium crystal in the water layer in less than 5.0

min, leaving the water-insoluble MCC particles suspended in the medium. The microenvironment pH affected by the MCC favoured the salt crystal dissolution over the free acid formation (i.e. Disproportionation).

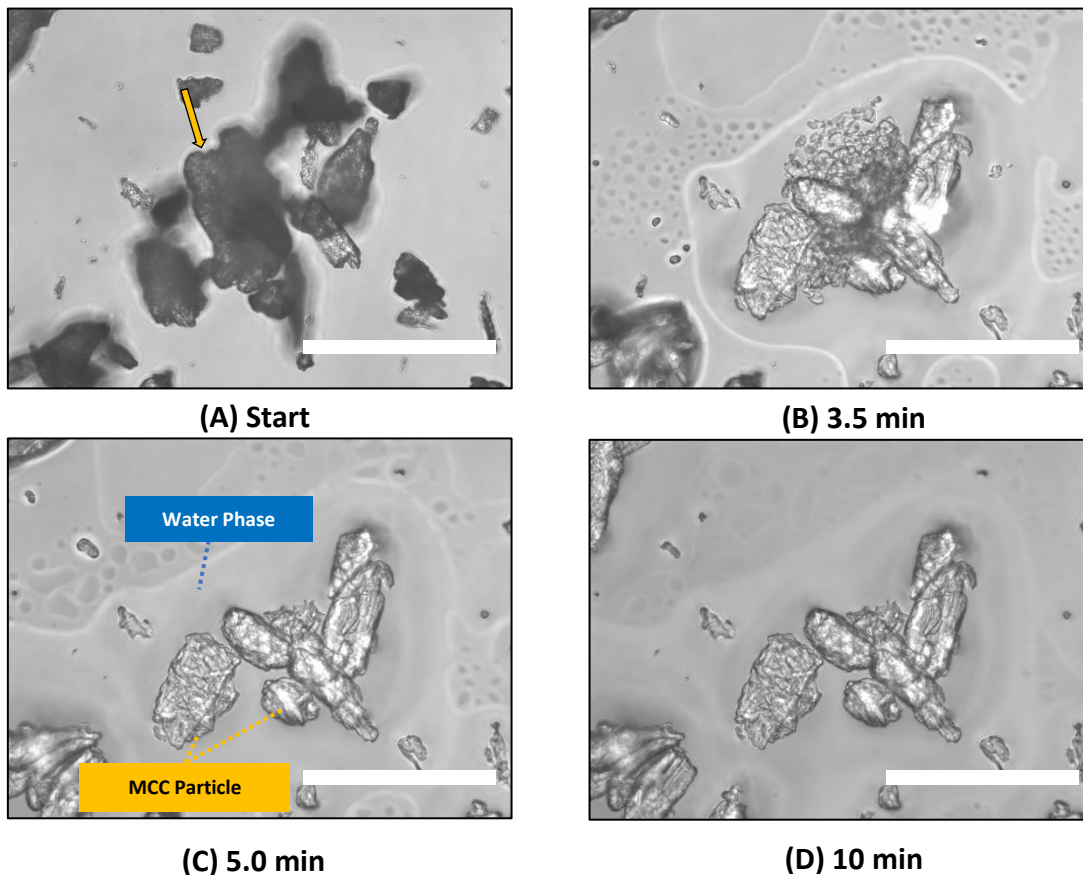


Figure 4.25: *In situ* optical microscopy images of Ibuprofen sodium crystals (Orange arrows) mixed with microcrystalline cellulose (MCC) during storage at 75-90% RH: (A) Start (B) 3.5 min (C) 5.0 min (D) 10 min. Scale bar for images is 100 μ m.

4.4.2.3.9. Calcium Phosphate Dibasic

Calcium phosphate dibasic (CPD) is a commonly used pharmaceutical excipient as binder and filler in tablets [312]. CPD exhibits some good properties such as excellent flowability and high compactibility, which is highly suitable for direct compression tableting processes [244], [312], [313]. Binary mixtures of CPD with Pioglitazone HCl and Ibuprofen sodium were prepared to test the compatibility between the drug salt and the excipient at high relative humidity using the *in-situ* optical microscopy system.

Pioglitazone HCl: Calcium Phosphate Dibasic: Pioglitazone HCl crystals morphology changes were monitored at high relative humidity by *in-situ* optical microscopy. The Pioglitazone HCl crystal mixed with CPD particles were, with less than 5 minutes, covered by needle crystallites as shown in Figure A.8 (Appendix A). The CPD measured pH (7.8) is higher than the pH_{max} of Pioglitazone HCl, which might facilitate salt disproportionation to the needle-shape free base crystals. The formation of Pioglitazone phosphate or Pioglitazone calcium salts is also possible, however, there are no reports for the existence of these compounds in literature.

Ibuprofen Sodium: Calcium Phosphate Dibasic: Ibuprofen sodium crystals did not show any crystal morphology change from the block-like structure to the needle shape when mixed with CPD (Figure A.9 - Appendix A). Ibuprofen sodium conversion to the free acid form was inhibited due to the alternation of the microenvironment pH as a result of the presence of CPD. Therefore, the dissolution of the Ibuprofen sodium crystals was noticed, leaving the insoluble CPD particles suspended in the water layer.

4.4.2.3.10. Magnesium Stearate

Magnesium stearate (MgSt) is used widely as a lubricant in tablet manufacturing in order to reduce the friction between the surfaces of the metal and that of formulation powders as well as to ensure the continuation of the operation [244], [292], [293]. Magnesium stearate exhibits hydrophobic nature as well as alkaline nature, which is ascribed to the presence of basic impurities such as magnesium oxide [226]. Therefore, the measured pH was found to be around 8.5 (Table 4.3-Section 4.4.1).

Pioglitazone HCl: Magnesium Stearate: Figure 4.26 illustrates the optical monitoring of Pioglitazone HCl crystals mixed with magnesium stearate (MgSt) stored at 75-90% RH. After

increasing the relative humidity to 75-90% RH, the Pioglitazone HCl crystal covered with fine MgSt particles maintained its crystal morphology for more than 5.0 min due to the low water adsorption at the surface of the drug salt crystal. After 10 min (Figure 4.26-C), a rapid formation of large needle crystals was observed indicating the salt conversion to another less soluble form. The formation of Pioglitazone stearate salt is less probable because the pKa values of the drug and the counterions are comparable, which make the reaction energetically unfavourable [218]. Therefore, it was more reasonable that the needle-crystals formed were attributed to the precipitation of Pioglitazone free base. The results match the prediction based on the measured pH of the excipient and the pH_{max} of the salt.

The hydrophobic nature of MgSt can explain the increase in the lag time between the time of increasing the relative humidity and the induction time of salt disproportionation in comparison to previous results. Magnesium stearate can decrease the wettability of the active pharmaceutical ingredient crystals due to its pronounced hydrophobic nature. As a result, it can cause delayed water ingress into the powder and prolonged dissolution of the drug salt. Therefore, the presence and distribution of the hydrophobic lubricant, MgSt, in the blend would alter the wetting behaviour of Pioglitazone HCl within the blend leading to a delay in the salt dissolution in the water layer and a delay in the salt disproportionation.

The role of magnesium stearate in inducing salt disproportionation reaction when blended with weak-base salts has been reported before [30], [201], [219], [226]. However, the FDA approved Pioglitazone HCl, Actos[®]; formulation contains magnesium stearate [301] as a lubricant, which could increase the risk of salt disproportionation during storage.

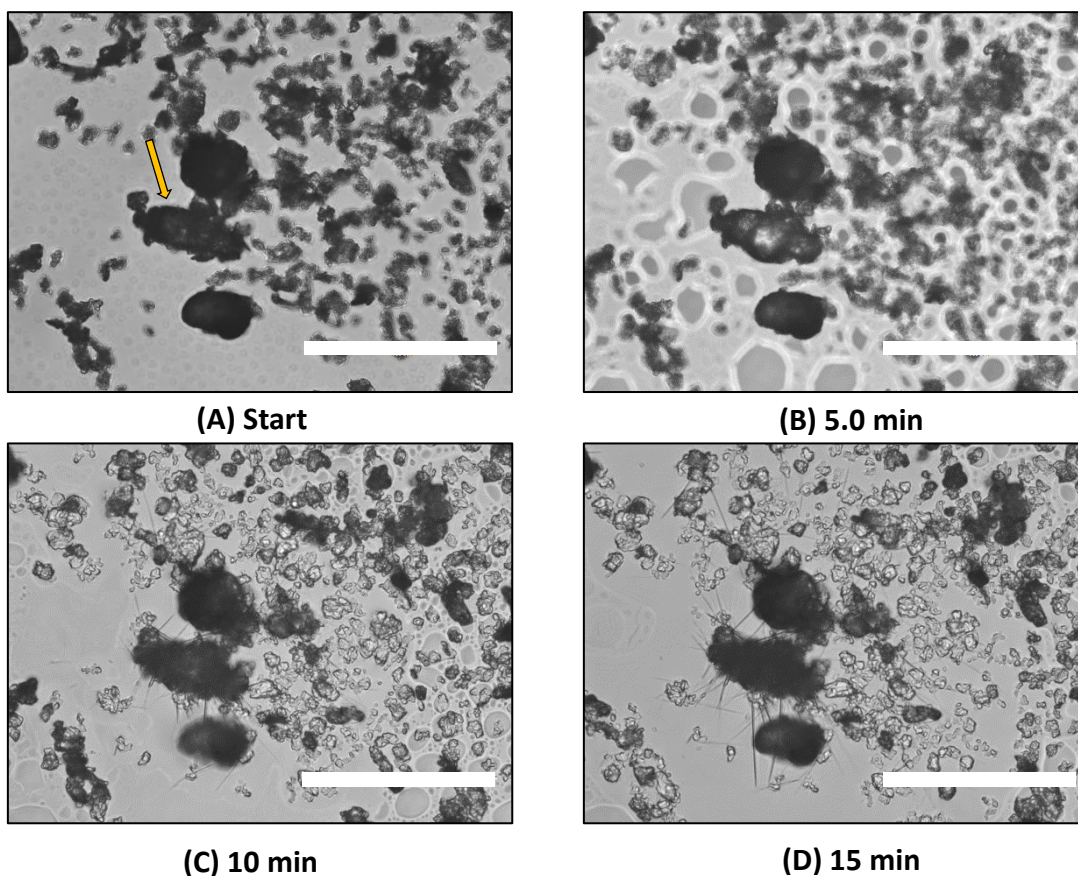


Figure 4.26: *In situ* optical microscopy images of Pioglitazone HCl crystal (Orange arrow) mixed with magnesium stearate during storage at 75-90% RH: (A) Start (B) 5.0min (C) 10 min (D) 15 min. Scale bar for images is 100 μm .

Ibuprofen Sodium: Magnesium Stearate: The Ibuprofen sodium crystals mixed with MgSt particles had, within less than 2.0 minutes, disintegrated then dissolved leaving the insoluble MgSt particles suspended in the water layer (Figure A.10 - Appendix A). The MgSt measured pH is higher than the pH_{max} which prevented the salt conversion to the free form.

4.4.2.3.11. Sodium Phosphate Dibasic

Sodium phosphate dibasic (NPD) is a buffering agent that is used in pharmaceutical formulations, primarily to control the microenvironment pH and to control the drug release from the solid dosage forms [244], [314]. Sodium phosphate dibasic possess high alkalinity ($\text{pH}= 9.1$) that can elevate the microenvironment pH to above the pH_{max} of the salt leading to induce salt

disproportionation for Pioglitazone HCl or preserve the ibuprofen sodium salt from disproportionation during storage at high relative humidity.

Pioglitazone HCl: Sodium Phosphate Dibasic: The stability of Pioglitazone HCl: NPD binary mixture at 75-90% humidity was investigated. *In-situ* optical images of the salt crystal morphology changes are presented in Figure 4.27. Real-time optical images showed rapid changes in the salt crystal structure after 2.0 min (4.27-C). The formation of needle crystals indicates the formation of the free base or Pioglitazone sodium.

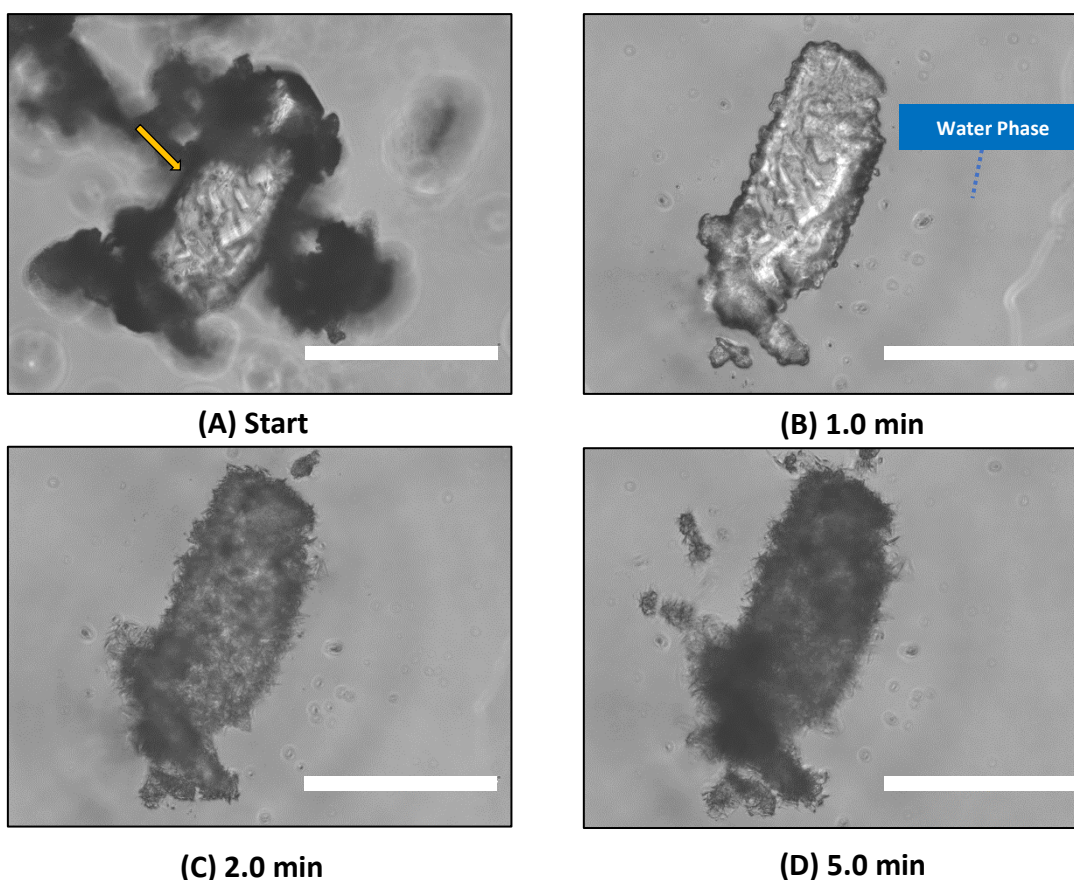


Figure 4.27: *In situ* optical microscopy images of Pioglitazone HCl crystal (Orange arrow) mixed with sodium phosphate dibasic during storage at 75-90% RH: (A) Start (B) 1.0min (C) 2.0 min (D) 5.0 min. Scale bar for images is 100 μ m.

Pioglitazone may form salts with bases such as sodium. However, the water solutions of such salts (if dissolved) are not completely stable and eventually precipitate into Pioglitazone base [294]. Therefore, it is likely that the addition of sodium phosphate dibasic raised the

microenvironment pH above the pH_{max} of the salt allowing the salt to disproportionate back to the free base form.

Ibuprofen Sodium: Sodium Phosphate Dibasic: *In-situ* optical images of Ibuprofen sodium crystal mixed with NPD at high RH are shown the fast dissolution of the salt drug in the water layer in less than 2.0 min (Figure A.11 - Appendix A). Needle crystals indicating salt disproportionation were not optically detected throughout the experiment. It is likely that the NPD raised the microenvironment pH above the pH_{max} of Ibuprofen sodium which reduced the risk of the salt conversion to the free acid form.

4.4.2.3.12. Sodium Stearyl Fumarate

Sodium stearyl fumarate (SSF) is used as a lubricant in capsule and tablet formulations [244]. SSF has been suggested as a suitable alternative to magnesium stearate due to its fewer negative impacts on tablet strength and dissolution rate [315], [316].

Pioglitazone HCl: Sodium Stearyl Fumarate: *In situ* optical images of Pioglitazone HCl: SSF binary mixture reveal a change in the salt crystal morphology to the needle-like shape after 10 minutes of incubation in high RH (Figure 4.27). Needle-shaped crystals were formed after 10 min indicating the formation of either the free base form, Pioglitazone stearyl fumarate or Pioglitazone sodium. Pioglitazone stearyl fumarate formation is less energetically favourable as the pK_a difference between Pioglitazone and fumarate counterion is less than two [218]. In addition, Pioglitazone sodium is not stable salt in aqueous solution and tend to precipitate eventually to the free form [266]. Therefore, it was reasonably believed that the needle-crystals formed were attributed to the precipitation of the free base. The results show high similarity in the disproportionation kinetics to the magnesium stearate images (Section 4.3.2.3.10). The delay

in the salt disproportionation induction time of Pioglitazone HCl crystal is due to the hydrophobic nature of the excipients.

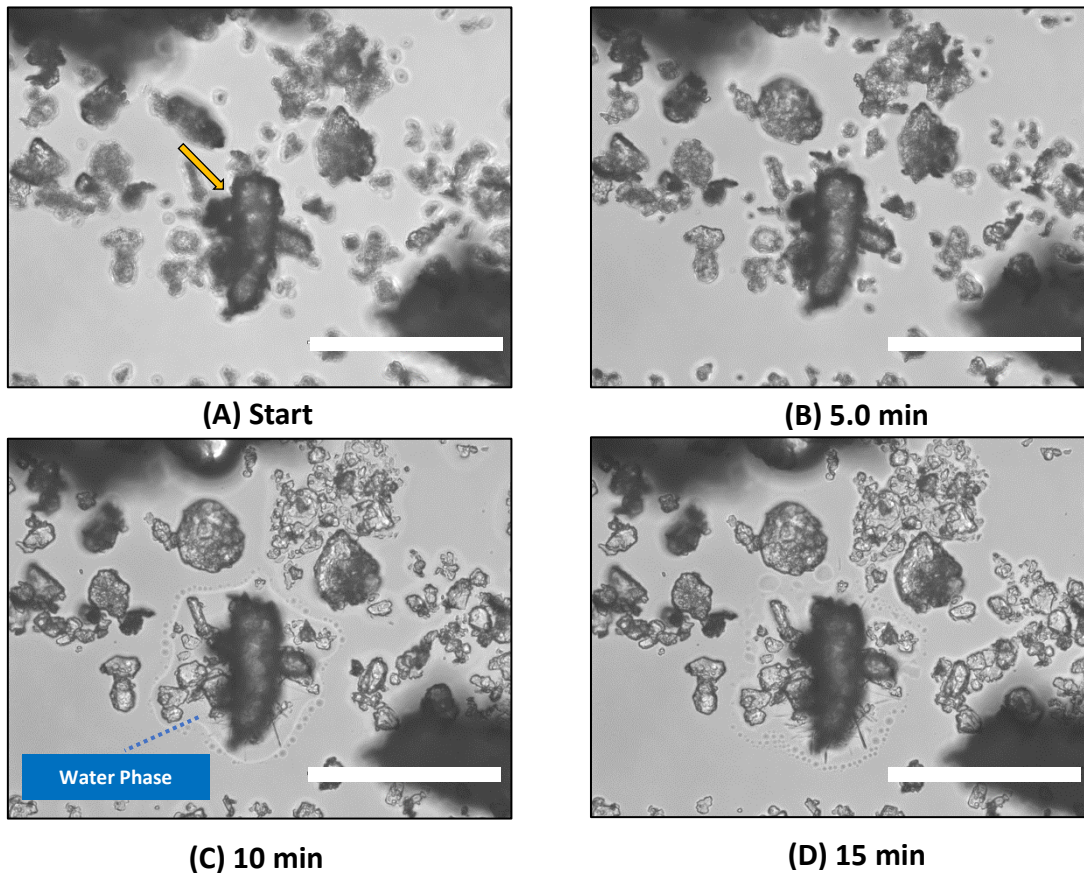


Figure 4.28: *In situ* optical microscopy images of Pioglitazone HCl crystal (Orange arrow) mixed with sodium stearyl fumarate during storage at 75-90% RH: (A) Start (B) 5.0min (C) 10 min (D) 15 min. Scale bar for images is 100 μ m.

Ibuprofen Sodium: Sodium Stearyl Fumarate: Similar to magnesium stearate, Ibuprofen sodium crystals mixed with SSF showed rapid disintegration and dissolution within 2.0min (Figure A.12 - Appendix A). No formation of needle crystals was observed during the experiment.

4.4.3. Results and Discussion Summary

In situ optical microscopy equipped with a controlled humidity chamber was used to investigate the propensity of salt disproportionation during storing at high humidity. For the weak base drug salt, Pioglitazone HCl, a change in the crystal morphology from plate-like crystal to needle crystal was observed when stored at high humidity. This change in crystal morphology represents the salt conversion to the free base, which was confirmed by offline Raman spectroscopy analysis. On the other hand, Ibuprofen sodium, a weakly acid drug salt, crystals stored at high humidity showed crystal size reduction and dissolution, which indicates the stability of Ibuprofen sodium at high humidity condition.

In the second part of this chapter, the role of excipients in inducing or preventing salt disproportionation by changing the microenvironment pH was investigated. For Pioglitazone HCl, acidic excipients such as citric acid and ascorbic acid reduced the microenvironmental pH below the pH_{max} of the Pioglitazone HCl. The *in-situ* optical images showed the dissolution of the salt crystal at high relative humidity, which indicates the stability of Pioglitazone HCl when formulated with acidic pH excipients. Stearic acid, lactose monohydrate, calcium phosphate dibasic, magnesium stearate, sodium phosphate dibasic and sodium stearyl fumarate all exhibited pH higher than the pH_{max} of Pioglitazone HCl, which led to the conversion of the salt to the free base form or to lower solubility salt. The salt crystals mixed with these excipients showed a change in the crystal morphology from the plate-like structure to the needle structure. Excipient properties, such as solubility and hydrophobicity controlled the extent and the onset of salt disproportionation. *In-situ* optical screening successfully demonstrated the unique behaviour of some excipients and their effect on Pioglitazone HCl stability at high RH. Disintegrant, such as croscarmellose sodium and sodium starch glycolate, showed high absorption of water, which

decreases the reactivity of water in the system. The reduction of water reactivity led to a delay in the salt disproportionation of Pioglitazone HCl at high RH compared to the drug only powder. Hydroxypropyl methylcellulose (HPMC) had the ability to inhibit the nucleation and growth of the free base needle crystals, which results in small needle crystal formation. Due to the hydrophobic nature of some excipients such as magnesium stearate, poor water wettability of the drug crystals and delayed salt conversion was observed.

Ibuprofen sodium exhibited good stability in most of the salt-excipient binary mixtures. However, the formation of small needle-shaped crystals, which enlarge in a dendritic fashion, was seen in mixtures containing citric acid, ascorbic acid and stearic acid. These acidic excipients protonated Ibuprofen sodium, which led to the precipitation of Ibuprofen free acid form at high RH. Citric acid, ascorbic acid and stearic acid slurry pH values were well below the pH_{max} of Ibuprofen sodium. The other binary mixtures tested reported the dissolution of the Ibuprofen sodium crystals, which demonstrates the stability of Ibuprofen sodium in these mixtures.

4.5. Conclusion

In this chapter, the salt disproportionation of two model drug salts, Pioglitazone HCl and Ibuprofen sodium, mixed with different commonly used excipients were tested at high relative humidity. *In-situ* optical screening with controlled humidity chamber was employed to monitor any salt crystal morphology changes due to the conversion of the salt to the free form. Binary mixtures of the drug salt and excipients that exhibited different measured pH and properties were stored at high relative humidity to simulate accelerated stability test conditions.

Salt disproportionation to the free form can be detected by monitoring the change in the crystal shape to the needle-like structure in real-time using *in-situ* optical microscopy system. Offline Raman spectroscopy analysis obtained from the formed needle crystals confirmed the formation of the free form. Lactose monohydrate, calcium phosphate dibasic, magnesium stearate, sodium phosphate dibasic and sodium stearyl fumarate all have the potential to facilitate disproportionation of Pioglitazone HCl due to their high alkalinity and capacity to accept protons in the presence of moisture. Whereas, citric acid and ascorbic acid both show the ability to lower the microenvironment pH below the pH_{max} of the salt and stabilise the salt at high relative humidity.

In the case of Ibuprofen sodium, acidic excipients such as citric acid, ascorbic acid and stearic acid all have the potential to induce disproportionation of Ibuprofen sodium due to their high acidity and ability to donate protons in the presence of moisture. The conversion of Ibuprofen sodium to the free acid resulted in the formation of needle-shaped crystals that were imaged by the *in-situ* optical microscopy system. Whereas basic excipients such as lactose monohydrate, microcrystalline cellulose, calcium phosphate dibasic and sodium phosphate dibasic increased the microenvironment pH above the pH_{max} of Ibuprofen sodium, facilitating the

salt dissolution rather than disproportionation. The optical microscopy imaging method successfully showed the behaviour of some excipients such as disintegrant (swelling due to water absorption), controlled release polymer (HPMC precipitation inhibitor) and lubricant (hydrophobic nature) and their effect on salt stability and the onset of the salt disproportionation.

The results presented in this chapter suggest that the *in-situ* optical microscopy imaging system equipped with a controlled humidity chamber has the potential to investigate the ability of the different excipients to induce or prevent salt disproportionation. To the best of our knowledge, this is the first time that monitoring change of salt crystal shape using optical microscopy has been employed to study salt disproportionation in drug-excipient binary mixtures stored at high RH. The success of applying optical microscopy as a qualitative analytical technique to detect the ability of excipients to induce salt disproportionation will help formulation scientists better understand drug-excipients compatibility. Hence, the findings of this chapter could profoundly impact the formulation design of solid dosage forms containing pharmaceutical salts.

Chapter5: The Effect of Excipients on Salt Disproportionation during Dissolution: Novel Application of *In-Situ* Raman Imaging

In this Chapter, *In situ* Raman UV-Vis flow system has been used to investigate the behaviour of tablets containing salt drug when formulated with carefully selected excipients during dissolution experiments. The flow cell system includes an in-line UV-Vis spectroscopy, which enables changes in the amount of drug in solution (Tracked by UV-Vis) to be directly related to physicochemical changes that occur in the solid-state to the tablet (monitored by Raman). The motivation for this chapter arises from the fact that ionised drugs (salts) can revert back to their thermodynamically favourable free forms during the formulation preparation or delivery stages. This conversion has a significant impact on the dissolution performance of active pharmaceutical ingredients (APIs). In this Chapter, a series of tablets were made from Pioglitazone HCl (Weak base model drug), and Ibuprofen sodium (Weak acid model drug) formulated with acidic and basic excipients were investigated in different aqueous pH environments.

5.1. Introduction

It is reported that 50-70 % of drugs are manufactured as salts, and the success of using these ionised species in tablets significantly depends on their stability both before and during drug release [254]. However, there is a tendency for the salt to convert back to its free (unionised) form under certain conditions via a reaction known as disproportionation [220]. Salt disproportionation can have a negative impact on the dissolution behaviour of the drug, which can compromise the potency and reliability of the API [219].

5.1.1. Salt Disproportionation during Dissolution

Salt disproportionation does not only occur in the solid state as described in Chapter 4 (Section 4.1.3.2) but may also happen in the solution during dissolution. Salts have pH-dependent solubility due to the solubility difference between the ionised and unionised forms (Chapter 4-Section 4.1.2). The ionised forms generally have a significantly higher solubility than the unionised forms. The conversion from the ionised state (Salt) to the unionised state (Free-form) during dissolution could be induced by the incompatibility between the dissolution medium pH with the pH_{max} of the salt or pH changes, which is due to the transition of the drug through the GI tract. In order to understand the likelihood of salt disproportionation during dissolution, background on the salt dissolution mechanism and the precipitation in solution thermodynamics must be covered.

Based on Noyes–Whitney equation [317], the relationship between the dissolution rate (J) and solubility (C_s) can be expressed by:

$$J = KA (C_s - C) \quad (5.1)$$

Where K is a constant, A is the surface area of the dissolving solid, and C is the concentration in the medium. Equation 5.1 may be modified according to the Nernst–Brunner diffusion layer model [237], which assumes that when the dissolution medium is introduced, the outermost layer of the drug dissolves promptly into a thin film to form a saturated solution (C_s) around the drug particle, known as the diffusion layer. The transfer of the dissolved drug to the bulk solution occurs by diffusion of the drug molecule through the diffusion layer. If the diffusion layer thickness may be represented by (h) and the diffusion coefficient of the solute in this layer by D , then K in Equation (5.1) becomes equal to D/h , and the equation may then be rephrased as:

$$J = \frac{DA}{h} (C_s - C) \quad (5.2)$$

Figure 5.1 illustrates the diffusion layer model for drug dissolution. Salts have the ability to enhance their dissolution rate by effectively acting as their own buffer. The self-buffering allows the salts to alter and control the pH of the diffusion layer to favour the salt dissolution (i.e. increase solubility) in the diffusion layer to reach the supersaturated state.

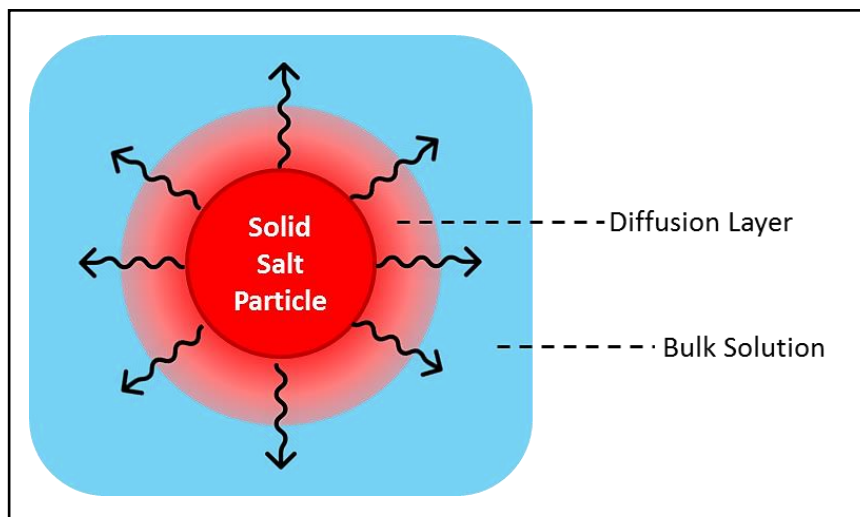


Figure 5.1: Diffusion layer model for drug dissolution.

Equation (5.2) works well when the pH is compatible with the pH_{max} of the salt (i.e. $\text{pH} > \text{pH}_{\text{max}}$ of free acid salt or $\text{pH} < \text{pH}_{\text{max}}$ of free base salt). However, when the pH is not compatible with the pH_{max} of the salt, the dissolution medium would be considered reactive, and salt is expected to convert to the free form (i.e. Salt disproportionation). In this case, because the unionised form usually has lower solubility than the ionised form, local areas of supersaturated concentrations of dissolved drug in the diffusion layer can initiate precipitation and recrystallisation from the solution as free-form upon salt disproportionation.

Only a couple of examples of salt disproportionation during dissolution have been reported in the literature. Binary mixture tablets of a new drug candidate HCl salt and Avicel (50:50 w/w) were prepared to investigate the dissolution performance of the tablet in 0.1 M HCl

medium and water [254]. The results revealed that the HCl salt underwent conversion to the free base when the water was used as the dissolution medium. The conversion did not occur when 0.1 M HCl was used because the pH of the dissolution medium was well below the pH_{max} of the salt. The data also confirmed that disproportionation follows solution mediated phase transformation, where the HCl salt initially dissolved before starting to precipitate out as a free base [254]. Ewing et al. [253] investigated the salt disproportionation of formulated tablets containing an ionised free acid drug (Sodium salt) during dissolution in different aqueous pH environments. A clear release of the sodium salt from the tablet was shown during dissolution in neutral medium. Dissolution in acidic (0.1 M HCl) medium exhibited rapid disproportionation upon contact with the medium, forming the free acid form. A shell of the free acid form was detected around the tablet edges slowing the medium ingress into the tablet before the full conversion of the API in the main bulk of tablet [253].

5.1.2. Advanced Analytical Techniques & Mitigation Strategies:

Salt disproportionation can dramatically increase the cost of development and delay the approval process if it is detected in the late stages of drug development. Therefore, it is crucial to find a proper analytical technique to study the disproportionation propensity of newly developed drug salt during early stages of drug development.

A number of analytical techniques have been employed to investigate and reveal the factors responsible for salt disproportionation, including solid-state nuclear magnetic resonance spectroscopy (NMR) [31], powder X-ray diffractometer (XRPD) [201], [225], [226], [232], [233], Fourier transform infrared (FTIR) spectroscopy [31], [201], [219], [225], [232], [253], [254], and Raman spectroscopy [219], [226], [229], [232], [233], [248], [253], [254]. Most of these techniques

have been used to study salt disproportionation during storage by taking offline measurements. However, vibrational spectroscopic approaches such as infrared and Raman spectroscopy can also be used as online techniques to study chemical and physical changes during dissolution [232]. The ability to investigate salt disproportionation and its effects upon dissolution *in situ* would be beneficial for understanding how it occurs and developing strategies to mitigate the issue. Ewing et al. and Wray et al. employed Raman and FT-IR with flow-through dissolution cells to investigate salt conversion to the free form during dissolution [253], [254]. Both studies showed the advantage of using the two spectroscopic approaches to study the behaviour of the drug salt tablet dissolving in different aqueous pH environment in real time. However, the studies did not investigate the role of formulation components (i.e. excipients) in inducing or preventing the salt disproportionation during dissolution.

Disproportionation can be prevented by selecting suitable salts or modifying the formulation appropriately [29]. Formulation strategies have been used to reduce the risk of disproportionation in pharmaceutical products. For example, pH modifiers are deliberately added in the formulation to modulate the pH. Organic acids such as citric, tartaric, and succinic acid have been used in solid dosage forms of weakly basic drugs to enhance their stability and dissolution performance [287], [318]–[321]. Zannou et al. [32] used citric acid to acidify the microenvironmental pH of a maleate salt of a basic drug formulation. The formulation modification succeeded to stabilise the product for a shelf-life of 3 years [32]. Similarly, incorporation of tartaric acid in the hydrochloride salt of a factor Xa inhibitor (Razaxaban) tablet formulation increased the dissolved fraction of the drug at basic pH medium [287]. The study suggested that tartaric acid increased the solubility of the drug in the microenvironment of the

dissolving dosage form (i.e. the diffusion layer), leading to a lower degree of supersaturation in the microenvironment, therefore, preventing the free base precipitation during dissolution [287].

Another approach using crystalline solid dispersion has been used by Nie et al. [233]. Pioglitazone HCl salt crystals were dispersed into a polymeric carrier. The solid dispersion acts as a mean to protect the salt from interacting with problematic excipients. The solid dispersion strategy showed effective ability in reducing the extent of disproportionation [233].

5.2. Motivation and the Aim

Although salts represent one of the most common formulation platforms for improving the dissolution properties of poorly water-soluble drugs, this approach often fails to achieve the required bioavailability due to the salt disproportionation (salt conversion to the less soluble free form). This form conversion can pose a potential risk to the desired dissolution behaviour of the dosage form and the *in vivo* efficacy. The ability to investigate salt disproportionation and its effects upon dissolution *in situ* would be very valuable for understanding how it occurs and developing strategies to mitigate the issue. Real-time vibrational spectroscopy has been employed before to investigate salt disproportionation during dissolution [253], [254]. However, both studies investigated the effect of aqueous media with different pH on drug salt disproportionation without exploring the role of the other formulation components (i.e. excipients) in inducing or preventing salt disproportionation during dissolution.

Gaps in the current knowledge of salt disproportionation include the lack of the mechanistic understanding of how the physiochemical properties of excipients lead to salt disproportionation in tablets during dissolution. In addition, the effectiveness of formulation strategies, such as pH modifiers, to reduce the risk of the salt conversion during dissolution is yet to be confirmed directly in the tablet matrix *in-situ* using online analytical techniques.

Therefore, the primary aim of this chapter is to fill the gap related to the understanding of the effect of excipients on salt conversion in the tablet matrix (solid-state) during dissolution. This will be attempted by using Raman spectroscopic mapping in conjunction with a custom designed flow-dissolution as the main analytical technique. The novelty of this system for investigating the salt disproportionation during dissolution derived from collecting Raman data *in situ* during the course of the dissolution experiment. Raman data were analysed using a different

mathematical approach, which originates from the use of concatenated maps of the tablet to explicitly track the changes as a function of time and space. In-line ultraviolet-visible (UV-Vis) spectroscopy was used in parallel with Raman spectroscopy as a complementary analytical technique that allows the changes in drug release from the tablet (monitored by the UV-Vis) to be directly related to physicochemical changes that occur to the drug salt in the tablet matrix. This combination provides a more global view of the effect of salt disproportionation on tablet performance.

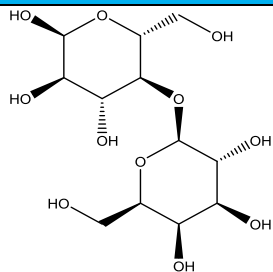
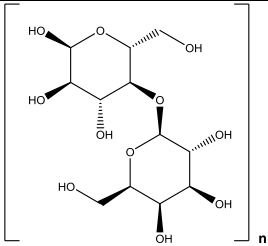
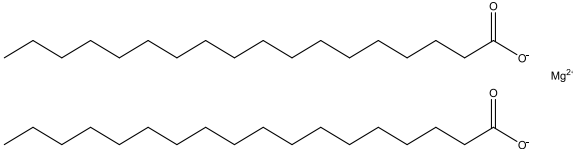
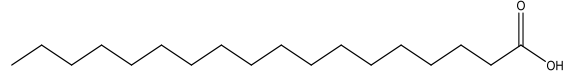
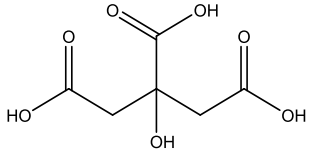
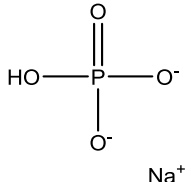
Two salts were employed in this chapter as model systems, Pioglitazone HCl and Ibuprofen Sodium. Six common excipients (shown in Table 5.1) are chosen for this study: two diluent/fillers (Lactose and Microcrystalline Cellulose (MCC)), two lubricants (Magnesium stearate and stearic acid) and two pH modifiers (Citric Acid and sodium phosphate dibasic). The excipients have been selected not only due to their common usage in the two salts formulations but also to specifically provide a wide range of microenvironmental pH between 2.0 to 9.0.

The specific objectives of this chapter are:

- To rationalise the stability and dissolution behaviour of model salt drugs, Pioglitazone HCl and Ibuprofen sodium, in drug only tablet during *in situ* tablet dissolution experiments. The salt disproportionation to the free form of the drug during dissolution in pH 1.2 (0.1 M HCl) and pH 6.8 (0.1 M sodium phosphate) media was monitored to mimic the stomach and duodenum condition, respectively.
- To investigate the influence of commonly used excipients in inducing salt disproportionation during dissolution in the tablet matrix. pH modifiers excipients were investigated as an effective formulation approaches to minimise the salt disproportionation during manufacturing and dissolution. Binary mixture tablets of

the drug salt with the excipients were tested in acidic and basic media to probe the effect of excipient on the microenvironment pH to induce or inhibit disproportionation.

Table 5.1: Summary of excipients used in the binary mixture tablets.

Excipient Name	Excipient Role	Slurry pH *	Chemical Structure
Lactose Monohydrate	Binder-Filler	6.0-7.0	
Microcrystalline Cellulose (MCC)		5.0-6.0	
Magnesium Stearate	Lubricant	8.5	
Stearic Acid		3.0	
Citric Acid	pH Modifiers	2.0	
Sodium Phosphate Dibasic		9.0	

* The slurry pH values of the excipients were reported in Chapter 4- Section 4.4.1.

5.3. Materials and Methods

5.3.1. Materials

Active Pharmaceutical Ingredients (APIs): Pioglitazone hydrochloride (Salt $\geq 98.5\%$) was obtained from Kemprotect Limited (UK). Pioglitazone free base (98%), Ibuprofen free acid (98%) and Ibuprofen sodium (Salt 98%) were purchased from Sigma-Aldrich (UK). All APIs were used as received, without any further purification. Infrared spectroscopy was used to confirm the identity of the received salts and free forms.

Excipients: Citric acid monohydrate ($\geq 99\%$), sodium phosphate dibasic (Pharma Grade) and magnesium stearate (Technical Grade) were purchased from Sigma-Aldrich (UK). Stearic acid (General Grade) was obtained from Fisher Scientific (UK). Lactose monohydrate (InhaLac[®] 70-Pharma Grade) was supplied by Meggle Pharma - Excipients & Technology (Germany). Microcrystalline cellulose (Avicel PH-102-Pharma Grade) was supplied by FMC Health and Nutrition (USA). All excipients were used as received, without any further purification.

Buffers: Hydrochloric acid (12 M), sodium phosphate dibasic and sodium phosphate monobasic were purchased from Sigma-Aldrich (UK).

Instruments used for preparing the formulations and tablets: 3-dimensional shaker/mixer (TURBULA T2F) and Manual 15 Ton Hydraulic Press (Specac-Atlas).

Raman Ultraviolet-Visible Flow Cell System: The Raman 3D printed tablet flow-cell was designed and manufactured by the medical engineering unit at the University of Nottingham. The flow-cell consists of a rectangular section of poly(methyl methacrylate) (PMMA), with flow channels drilled through it to allow the flow of dissolution medium. The cell dimensions are 75 mm in length, 40 mm in width, and 3.0 cm in height. The tablet is positioned within the flow cell cavity, which has an internal diameter of 14 mm. The dissolution cell cover with a glass window

is then bolted into place on top of the sample, which seals with the O-ring to create a chamber for dissolution. The UV-Vis flow cell, deuterium light source and the CCD spectrometer were all obtained from Ocean Optics (USA). The peristaltic pump was purchased from Ismatec (Switzerland).

Post-Dissolution Sample Preparation Kit: PowerTome XL CR-X Ultramicrotome (RMC Products, Broeckeler Instruments Inc., AZ, USA) was used to cross-section the tablet after the dissolution experiment.

5.3.2. Formulation and Tablet Preparation

All excipients were ground and screened through a 50 µm sieve before mixing with the APIs. The grinding and sieving were performed to narrow the particle size distribution, prevent segregation and ensure blend homogeneity [322].

A binary mixture of the drug salt and each excipient was prepared at a different weight ratio. The selection of the excipients was mainly driven by the excipients used in the branded-drug tablet formulation. Citric acid and sodium phosphate dibasic were used to investigate the role of pH modifiers to prevent salt disproportionation during dissolution.

Pioglitazone HCl (Pio HCl) was combined with citric acid (CA), lactose monohydrate (LM), and magnesium stearate (MgSt). The compositions of formulation A, formulation B and formulation C are detailed in Table 5.2. The excipients were mixed with Pioglitazone HCl according to the ratio used in the branded drug product (Actos[®])[301] or according to the standard excipient ratio stated in the Handbook of pharmaceutical excipients [244].

Table 5.2: Pioglitazone HCl formulations compositions, excipients role and the mixture weight ratio of each formulation.

Formulation	Excipient Name	Excipient Role	Measured pH	Pioglitazone HCl: Excipient weight ratio (w/w %)
F _A	Citric acid Monohydrate	Acidic Buffering Agent	1.6	70:30
F _B	Lactose monohydrate	Binder- Filler	6.3	20:80
F _C	Magnesium Stearate	Lubricant	8.5	90:10

Ibuprofen sodium (Ibu Na⁺) was mixed with sodium phosphate dibasic (NPD), microcrystalline cellulose (MCC) and stearic acid (SA). The compositions of formulation E, formulation G and formulation H are detailed in Table 5.3. Similar to Pioglitazone HCl, the excipients were mixed with Ibuprofen sodium according to the ratio used in the branded drug product (Advil[®]) [296] or according to the standard excipient ratio stated in the Handbook of pharmaceutical excipients [244].

Table 5.3: Ibuprofen sodium formulations compositions, excipients role and the mixture weight ratio of each formulation.

Formulation	Excipient Name	Excipient Role	Measured pH	Ibu Na: Excipient weight ratio (w/w %)
F _E	Sodium Phosphate Dibasic	Basic Buffering Agent	9.1	70:30
F _G	Microcrystalline Cellulose	Binder- Filler	7.1	50:50
F _H	Stearic Acid	Lubricant	3.4	90:10

The formulations were thoroughly blended for 15 min using Turbula T2F mixer. The blended powders were then gravimetrically dispensed (Approximately 50 mg for Pioglitazone formulations and 100 mg for Ibuprofen formulations) into a 20 ml glass vial. Afterwards, the mixture was compacted into tablets, 5 mm in diameter, using a manual hydraulic press (Specac). A consistent compression force of ca. 20 kN was applied for all tablets for 15-20 seconds. Pure Pioglitazone HCl and Ibuprofen sodium tablets were also prepared similarly, serving as a control

such that the salt conversion to the free-form resulting from the pH of the dissolution buffer is distinguished from those due to the excipients in the formulation. All tablets were stored in a desiccator before the dissolution experiment for a maximum of 24 hours. A photographic image of the 50 mg and 100 mg tablets is presented in Figure 5.2.

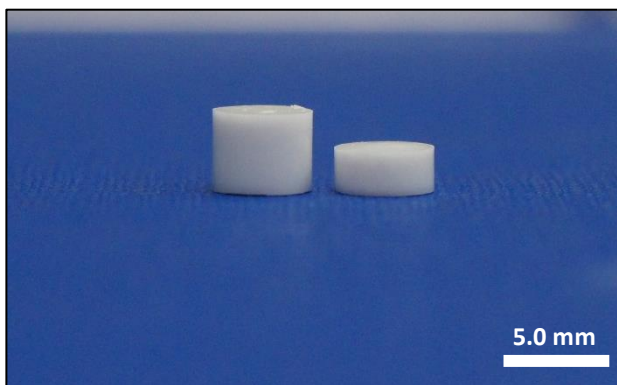


Figure 5.2: Photographic image of the 100 mg (Left) and 50 mg (Right) tablets.

5.3.3. Buffer Preparation:

Two different dissolution media were used in this investigation, 0.1 M hydrochloric acid (HCl) buffer (pH=1.2) and 0.1M sodium phosphate buffer (pH=6.8). The 0.1 M HCl buffer solution was prepared by diluting 8.30 mL of 12 M HCl in 1 L of deionised water. Whereas, the 0.1M sodium phosphate buffer solution was prepared by mixing 245 ml of 0.2 M of sodium phosphate dibasic and 255 ml of 0.2 M sodium phosphate monobasic then making up the volume to 1 L using deionised water.

5.3.4. Raman Spectroscopy

Raman spectroscopy was used to acquire reference spectra of the salts and free forms of both model drugs (i.e. Pioglitazone and Ibuprofen). Reference spectra for the excipients listed in Table 5.2 and 5.3 were also obtained. Raman spectra were acquired using a Horiba LabRAM HR

confocal microscopy/spectroscopy from 100 to 4000 cm^{-1} . Sample excitation was performed using a near-IR laser (785 nm) of 250 mW power. Spectra were acquired using a 50x objective and a 300 μm confocal hole. A 600 mm rotatable diffraction grating was used to scan a range of Raman shifts. Raman spectra were collected using a SYNAPSE CCD detector (1000 pixels). Data acquisition time was set at 3 seconds, and two accumulations were averaged for all samples. GraphPad Prism was used for spectra visual inspection in this section.

5.3.5. Raman Ultraviolet-Visible Flow Cell System

Raman Spectroscopy: The same Raman system described in section 5.2.4 equipped with a 3D printed flow cell was used to investigate the salt conversion during the dissolution of compressed drug/excipient formulations. Each formulation was performed in acidic ($\text{pH}=1.2$) and basic ($\text{pH}=6.8$) buffer to resemble gastric and duodenal pH condition, respectively. In all investigated cases, no change in the dissolution media pH (checked by pH meter) was noticed after the termination of the dissolution experiment. Each experiment was run for 2.0 hours in each buffer, which matches the mean residence time of tablet in the stomach and duodenum [323]. The total buffer volume was 500 ml, and the flow rate was set at 5.0 ml/min. Figure 5.3 illustrated the experimental set-up of the system.

The flow cell was placed under the objective of the Raman microscopy fixed to a motorised XYZ stage (Märzhäuser) for mapping. The spectra were collected as a function of time (15 min intervals) across a mapping area of 500 μm x 500 μm with 50 μm step along the x and y-axes (121 spectra per map). The whole map required approximately 15 min as each spectrum was acquired for 2 seconds and repeated once to remove the spikes. The z-axis was corrected between each

map during the dissolution experiment. The spectral region was changed according to the drug, and the excipient investigated to get the least interference between peaks.

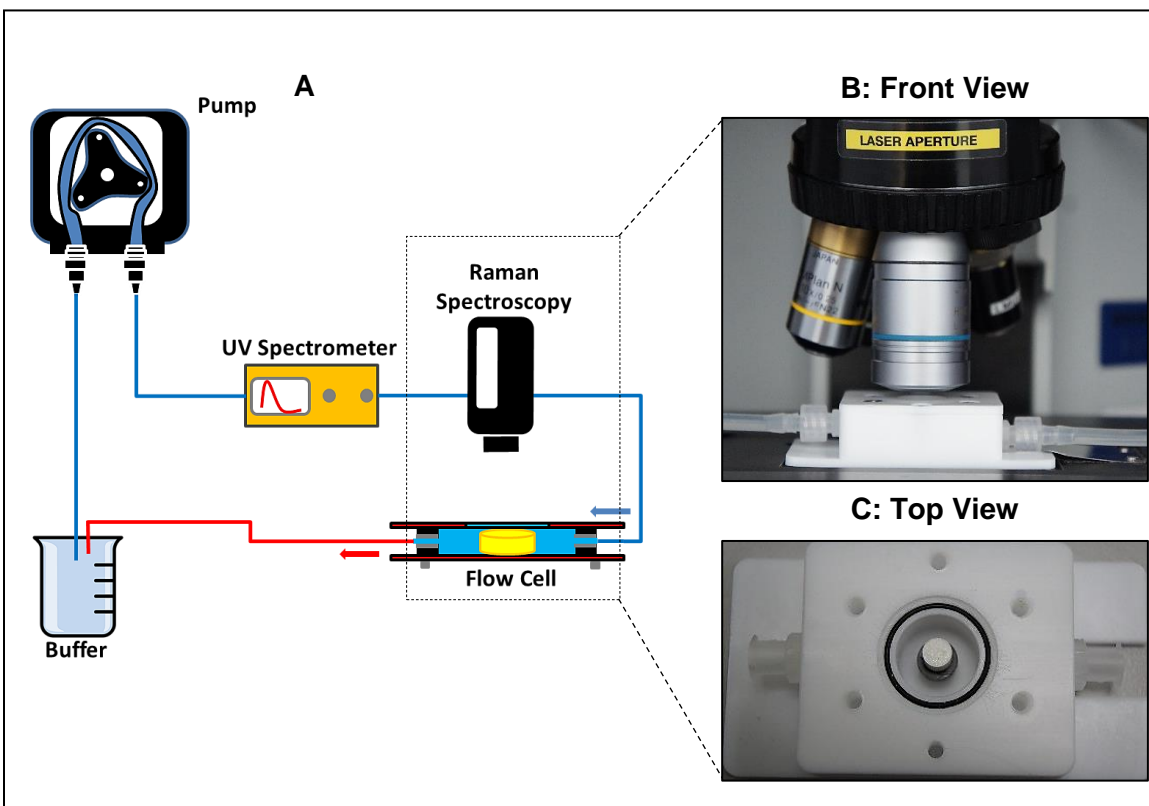


Figure 5.3: (A) Schematic diagram of the Raman Ultraviolet-Visible Flow Cell System. (B) Front view of the flow-cell under the Raman spectroscopy objective. (C) Top view of the tablet placed inside the flow-cell.

For Raman data analysis, spectra from each time-point map were averaged to generate a single spectrum. Averaging produced spectra with good signal to noise ratio and facilitated the determination of any spectral changes occurring to the salt during the dissolution test. False colour maps were created using classical least square (CLS) and alternate least square multivariate curve resolution (ALS-MCR). Prior to the CLS chemical mapping, all spectra were baseline corrected and normalised to reduce the effect of variability in Raman spectra. In CLS analysis, the distribution of the tablet components was identified using a computerised model function build in the LabSpec software (Horiba). The algorithm is based on modelling the spectra found in each pixel across the Raman map as the linear combination (the weighted average) of the pure

component spectra (i.e. Reference spectra). This results in an overlay chemical image for each time point, illustrating the distribution of each component across the map. In ALS-MCR, a single data matrix, including all the spectra collected across the dissolution experiment at all time points, was produced in order to probe any salt conversion as a function of both x-y position and time. Numerical codes for statistical analyses were written in the "R" language (R software version 3.2.2), which is free open-source software [323]. All numerical routines were adapted from a previous study [323].

Through this chapter, in MCR, colours from white/red to black/blue denoted the component concentrations from high to low. In CLS, the blue colour represented the salt spectrum, the red colour represented the free-form spectrum, and the yellow represented the excipient (only in formulation tablets) spectra.

Ultraviolet-Visible (UV-Vis): Drug release data were collected using UV-Vis data were collected using a combined miniature light source flow-cell UV-Vis spectrometer system. A Z-shaped flow cell (FIAZ-SMA) with a 10 mm path length was simultaneously connected to a deuterium light source (DT-MINI-2) through optical fibres and a CCD spectrometer (USB2000). A peristaltic pump (IPS) pumped the dissolution buffer through the UV-Vis flow cell and the Raman flow cell in a closed circle flow (Figure5.3). The dissolution profiles of Pioglitazone HCl [324] and Ibuprofen Sodium [325], [326] were both acquired by measuring the absorbance at 270 nm every 10 seconds.

A calibration curve for each drug was performed to calculate the drug mass release and the percentage release. Quantification was determined by dissolving a measured mass of Pioglitazone HCl and Ibuprofen sodium in methanol and diluting the solution with further known

aliquots of methanol to construct a calibration plot (Concentration vs Absorbance). The Beer-Lambert law was used to relate the concentration to the UV absorbance (Equation 5.3):

$$A = \epsilon bC \quad (5.3)$$

Whereas A is the absorbance, ϵ is the molar absorptivity ($\text{ml mg}^{-1} \text{cm}^{-1}$), b is the path length (cm) and, C is the concentration (mg/ml). The free form (unionised) has a negligible water solubility in comparison with the salt form (ionised). Therefore, the molar absorptivity of the salt is expected to be representable for both ionised (salt) and unionised form (free form) amount released in the acidic and basic pH buffer. This equation will allow to measure the amount and percentage of drug release and directly compare the different formulation performance. Tablets total weight (50 mg for Pio HCl and 100 mg for Ibu Na) and the volume of the dissolution medium (500 ml) were kept constant for all experiments to ensure the accuracy of the calculations.

5.3.6. Post-Dissolution Analysis:

Tablets that maintained their structural integrity (stayed intact) after dissolution were cross-sectioned in order to be subjected to further analysis. Raman mapping of the cross-sectioned tablet was performed to spatially identify the tablet's surface components and the inner core of the tablet after dissolution.

Ultramicrotome: Tablets were cross-sectioned using PT-X & PT-XL PowerTome Ultramicrotomes. At the end of the experiment, the remaining tablet was removed from the flow-cell and left to dry at room temperature. Each tablet was placed perpendicular to the surface of the aluminium sample holder, embedded in an epoxy resin solution. The resin was left to dry at room temperature. First, a thin section of about 1.0 mm thickness was cut from the top of the sample with a razor. Then, each sample was placed in a die, which was subsequently levelled in

the microtome (PowerTome XL CR-X Ultramicrotome) to permit smooth vertical cuts of the edge of the tablet to expose the interior using glass and diamond knives. The cross-sectioned tablets were stored in desiccators until the analysis was performed.

Raman Spectroscopy Mapping: The cross-sectioned tablet was placed under the objective of the Raman microscopy fixed to a motorised XYZ stage (Märzhäuser) for mapping. The spectra were collected across a mapping area covering the whole tablet (around 3000 μm x 5000 μm) with a 100 μm step along the x and y-axes. The whole map required approximately 90-120 minutes as each spectrum was acquired for 2 seconds and repeated once to remove the spikes. False colour maps were created using CLS. Before the chemical mapping, all spectra were baseline corrected and normalised to reduce the effect of variability in Raman spectra.

5.4. Results and Discussion

The effect of buffer pH and excipients on salt disproportionation was investigated using Raman UV-Vis flow cell system. Pioglitazone HCl and Ibuprofen sodium were selected as a free base and free acid drug model, respectively. Raman averaged spectra, Raman mapping and UV-Vis drug release profile were used to study the behaviour of the two model drugs in acidic and basic buffer media.

5.4.1. Pioglitazone HCl: Free Base Case Study

In this section, the excipient-induced disproportionation of the hydrochloride salt of Pioglitazone, a weak base with a pKa of 5.2, was investigated in order to improve the basic understanding of the salt stability and tablet dissolution performance in acidic and basic environment. Pioglitazone HCl may disproportionate back to the free base at high pH (Basic environment). By using Raman ultraviolet-visible flow cell system, the effect of dissolution medium pH and excipient physiochemical properties (mainly pKa) on salt disproportionation was explored.

5.4.1.1. Dry Pure Material Spectra

The Raman spectra (Spectral region 1200 to 1800 cm^{-1}) of all tablet ingredients are shown in Figure 5.4, including Pioglitazone (HCl salt and free base), citric acid, lactose monohydrate, and magnesium stearate. Starting with the salt and the free base, it is evident that there are some clear spectral differences between the salt and free base forms. Specifically, Pioglitazone HCl salt demonstrates a doublet peak located at the region 1600 to 1650 cm^{-1} , whereas the free base displays a unique single peak at 1610 cm^{-1} . This spectral difference can be elucidated by the

protonation of pioglitazone that changes the vibrational modes of the pyridine ring and the carbonyl group [280]–[282].

With respect to the excipient's spectra, all the excipients used in the formulations are mainly Raman inactive in this specific region (1600 to 1650 cm^{-1}). Therefore, this spectral range will be used to discriminate between the salt and the free base peaks with minimum interference from the excipients spectra used in this study.

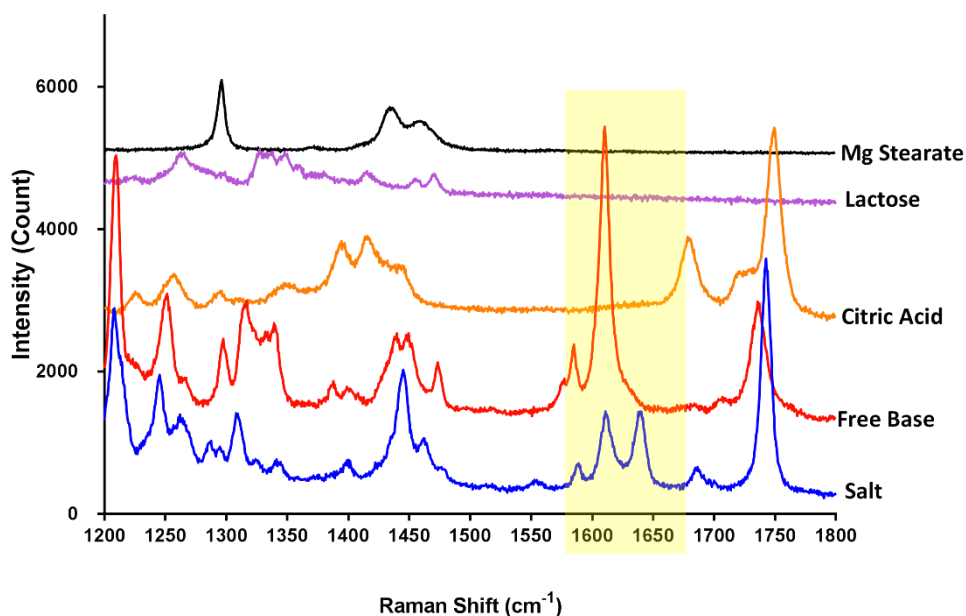


Figure 5.4: Raman spectra of Pioglitazone HCl salt, Pioglitazone free base and excipients used in formulations over the range 1200 cm^{-1} to 1800 cm^{-1} .

5.4.1.2. Dissolution Experiments

5.4.1.2.1. The Effect of the Buffer pH

For an initial investigation to study the dissolution behaviour of the salt in acidic and basic environments, tablets of pure drug salt were prepared. This type of experiment was employed to discriminate the role of excipients in inducing or preventing salt disproportionation from the buffer effect.

The pH_{max} of Pioglitazone HCl published by Nie et al. indicates a pH_{max} of 2.8 [226]. Therefore, at pH values below 2.8, the salt is expected to be the most stable form, whereas the free base form will be stable above pH 2.8. The acidic environment may thus stabilise the salt, whereas the basic buffer may lead to the conversion of the salt into a free form of the drug.

Pure Pioglitazone HCl Tablet-Acidic Buffer:

Averaged Raman spectra of the pure salt tablet in the acidic buffer are presented in Figure 5.5. Examination of the data revealed some minor changes in the spectra after 60 min. The peak located at 1610 cm^{-1} showed an increase in the intensity over the second peak at 1640 cm^{-1} . The slight increase in the 1610 cm^{-1} peak intensity is an indication of the conversion of some salt molecules to the free form [226]. This was unexpected as the buffer pH is below the pH_{max} of the Pioglitazone HCl salt, thus no disproportionation is expected to occur. Other factors, might have influenced the salt stability during dissolution.

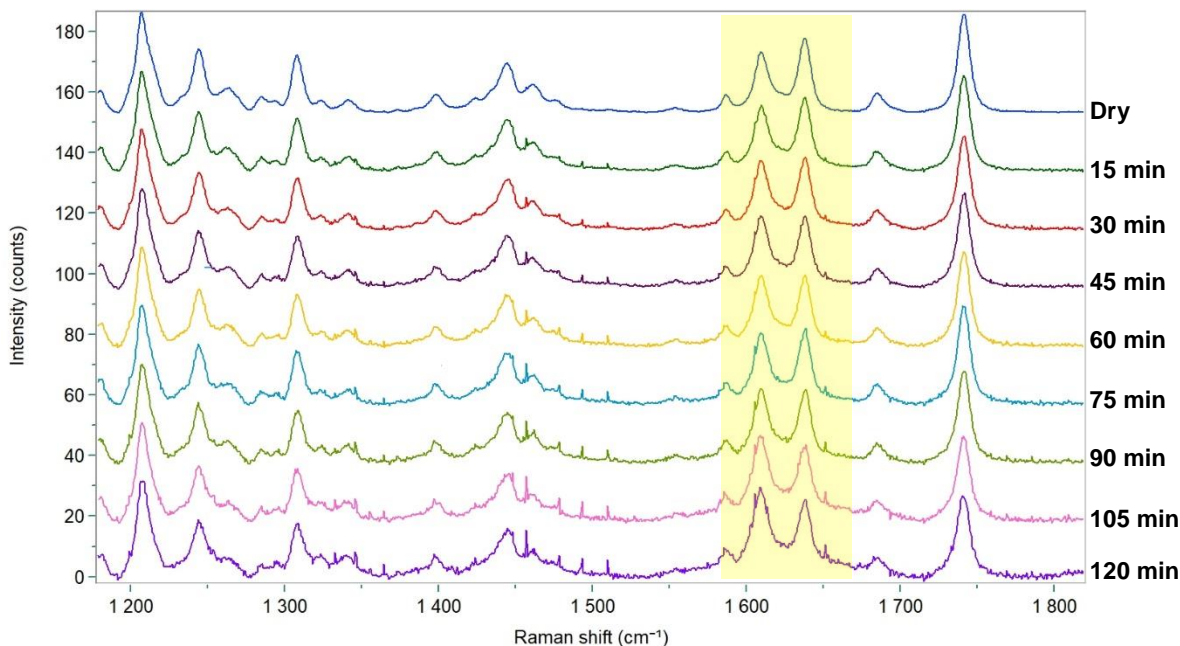


Figure 5.5: Averaged Raman spectra (1200 to 1800 cm^{-1}) of the dissolution of the pure Pioglitazone HCl tablet in the acidic buffer. Y-axis offsets were applied for presentational purposes.

Therefore, the MCR and CLS models were both employed to spatially and spectrally deconvolute any change in the salt state during dissolution in acidic pH (Figure 5.6). Starting with the MCR, two components were required to deconvolute the mapped data. Comparison with the reference spectra indicates that the first component, MCR1, can be associated with the salt (Doublet peak at 1600 to 1650 cm^{-1}).

The second component, MCR2, shows an increase in the 1610 cm^{-1} intensity over the second peak. Increasing the 1610 cm^{-1} intensity by increasing the Pioglitazone free form in a physical mixture with the salt form has been reported previously [226]. As a result, MCR2 components can be associated with the mix of both salt and free-form spectra. The scores' plots show that the salt (MCR1) is distributed throughout the mapped compact surface before the dissolution experiment start. Corresponding MCR2 scores' plots indicated some small co-existence of salt and the free-form material in the mapped area of the dry compact. This may be explained by the formation of the free form due to the humidity during the powder mixing and tablet compression.

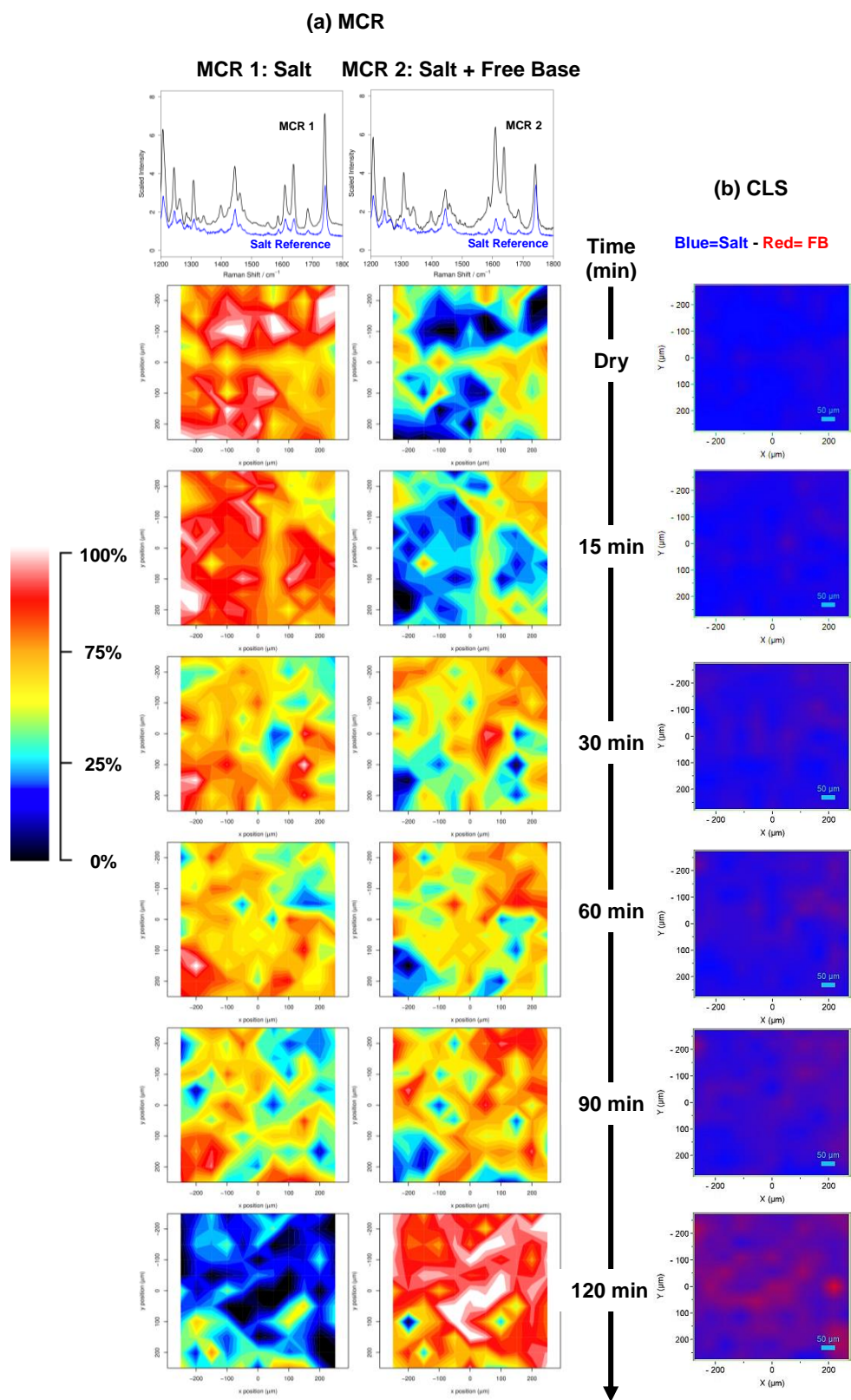


Figure 5.6: Raman maps of the pure Pioglitazone HCl tablet during dissolution in the acidic buffer as a function of time, generated by (a) MCR analysis (b) CLS analysis.

During the dissolution, the amount of the salt-free form mixture increased at the expense of the pure salt (MCR1). It is apparent that limited salt conversion to the free form has occurred during dissolution. The salt disproportionation is likely linked with the presence of the free form in the tablet matrix, which facilitated the solution-mediated phase transformation (SMPT) of the salt. It is well known that SMPT consists of three phases; initial dissolution of the metastable phase (i.e. salt) to reach saturation or supersaturation, then nucleation of the stable phase (i.e. free form) and finally crystal growth [224]. There are some factors that influence each step, for example, controlling the first phase by reducing the supersaturation level of the salt can be achieved by keeping the pH below the pH_{max} of the free base. This pH condition was maintained in the previous experiment by using the acidic buffer. Bearing this in mind, the free-form nucleation can be triggered by the presence of secondary nucleation. Therefore, the presence of the free base in the tablet due to the humidity during tablet manufacturing led to the conversion of the salt to the free form.

The spectra of both pure Pioglitazone salt (Blue) and the free form (Red) were used with the CLS fitting algorithm to determine the proportion of each form during the dissolution experiment. The false colour map in Figure 5.6-b indicated the dominant presence of the salt form of the dry tablet. As the dissolution experiment progressed, the free base formation across the mapped area is noticed by the faint red colour. The faint red colour indicates that the spectra are a mixture of the salt and the free base, which is in agreement with the map generated using MCR.

Pure Pioglitazone HCl Tablet-Basic Buffer:

The results from the dissolution experiments in the 0.1M sodium phosphate buffer (pH=6.8) significantly differ from those recorded in the acidic buffer. Averaged Raman spectra of the pure salt tablet in the basic buffer are presented in Figure 5.7. Raman data showed that the

spectrum changed after 15 min (Figure 5.7, 15 mins). The intensity of the doublet peak at 1640 cm^{-1} appeared to decrease in relation to the other peak at 1610 cm^{-1} . The spectra collected between 30 and 120 min showed a strong correlation with the Pioglitazone free base spectrum. It is likely that the rise of the pH above the pH_{max} of the salt led to an increase in the supersaturation concentration of the unionised form in the solution. This high supersaturation led to the precipitation of the free form to reach equilibrium [226], [229], [233], [327], [328].

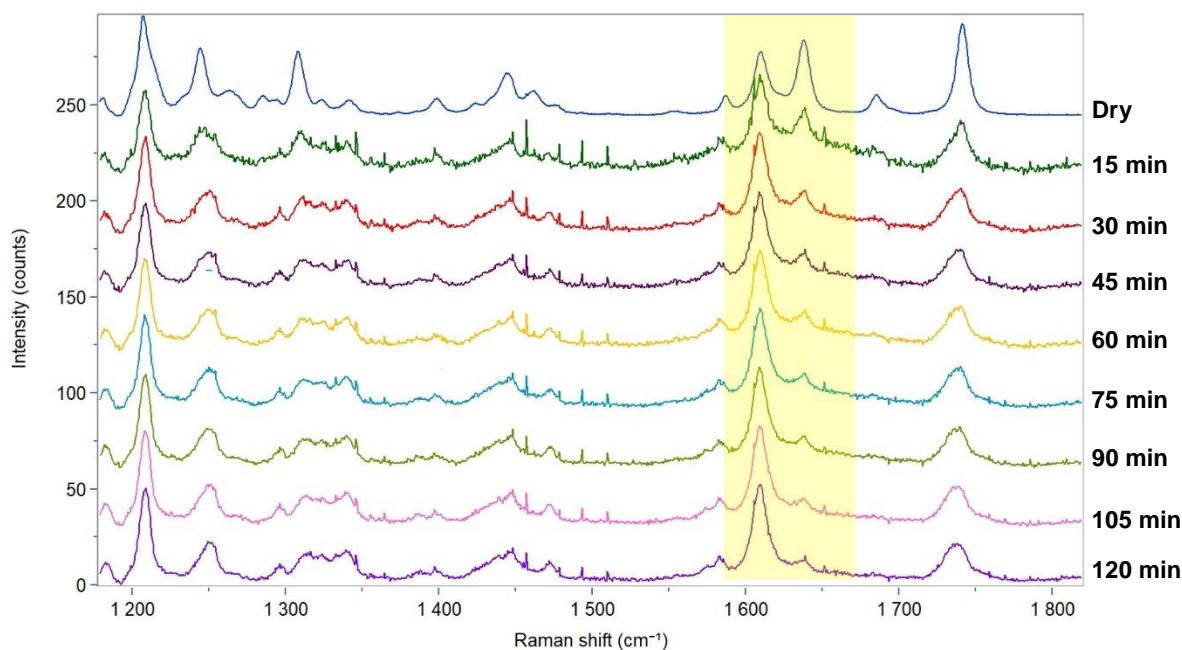


Figure 5.7: Averaged Raman spectra (1200 to 1800 cm^{-1}) of the dissolution of the pure Pioglitazone HCl tablet in the basic buffer. Y-axis offsets were applied for presentational purposes.

The MCR and CLS model were both used mainly to spatially and spectrally visualise the salt conversion to the free form during dissolution in basic pH (Figure 5.8). Starting with the MCR, again, two components were required to deconvolute the mapped data. The white/red colours represent areas where a phase is present at its maximum, whereas black/blue colours indicate areas where it is present at its minimum. A continuum of white-red-orange-yellow-cyan-blue-black colours represents areas with a variable weighting of that phase. Comparison of the MCR

loadings with reference spectra clearly showed that the data had been resolved into components, which agree remarkably well with Pioglitazone HCl salt (MCR1) and Pioglitazone free base (MCR2).

The images in Figure 5.8-(a) show the behaviour of the tablet every 15 min for the duration of the experiment. These results confirmed that there was the rapid formation of the free base form after the basic medium contacted the tablet. A complete conversion of the salt form to the free base form had occurred after 60 min of the dissolution experiment started. The concentration map generated by CLS in Figure 5.8-(b) is significantly in agreement with the MCR-ALS maps. The dominance of the free base form (red) was observed after 30 min.

It is expected that the chemical changes that occurred to the Pioglitazone HCl in the basic conditions had implications for the overall release of the drug. The drug release results will be discussed later in this chapter.

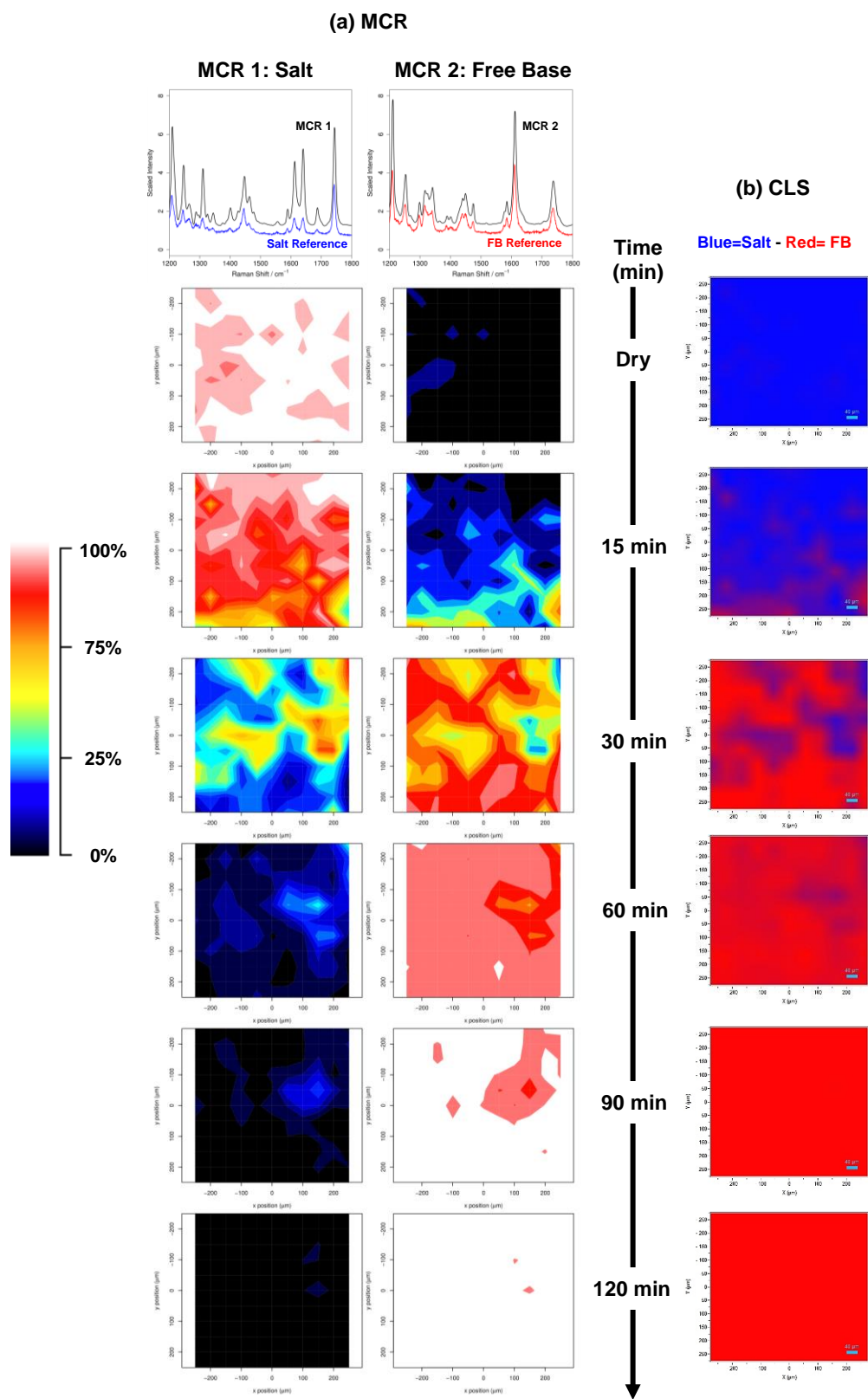


Figure 5.8: Raman maps of the pure Pioglitazone HCl tablet during dissolution in the basic buffer as a function of time, generated by (a) MCR analysis (b) CLS analysis

At the end of the experiment, the tablet was recovered from the flow cell nearly intact. The tablet was cross-sectioned using ultramicrotome to expose the interior of the tablet. Raman mapping was performed to analyse the edge and the core of the whole cross-sectioned tablet. Data are presented in Figure 5.9. The salt disproportionation of the Pioglitazone HCl salt to the free base occurs on the outside of the tablet (top and bottom surface and edges), with the interior consisting of unchanged salt form. Under basic conditions, Pioglitazone salt disproportionation resulted in the formation of the free base form of the drug that initially manifested itself as an impermeable layer around the outside of the tablet which inhibited the ingress of the dissolution medium. Serajuddin et al. theorised a situation where the free-form precipitated at the surface of the salt which may exist below the surface layer not available for dissolution [214]. These results confirmed the previous theory experimentally using Raman spectroscopy.

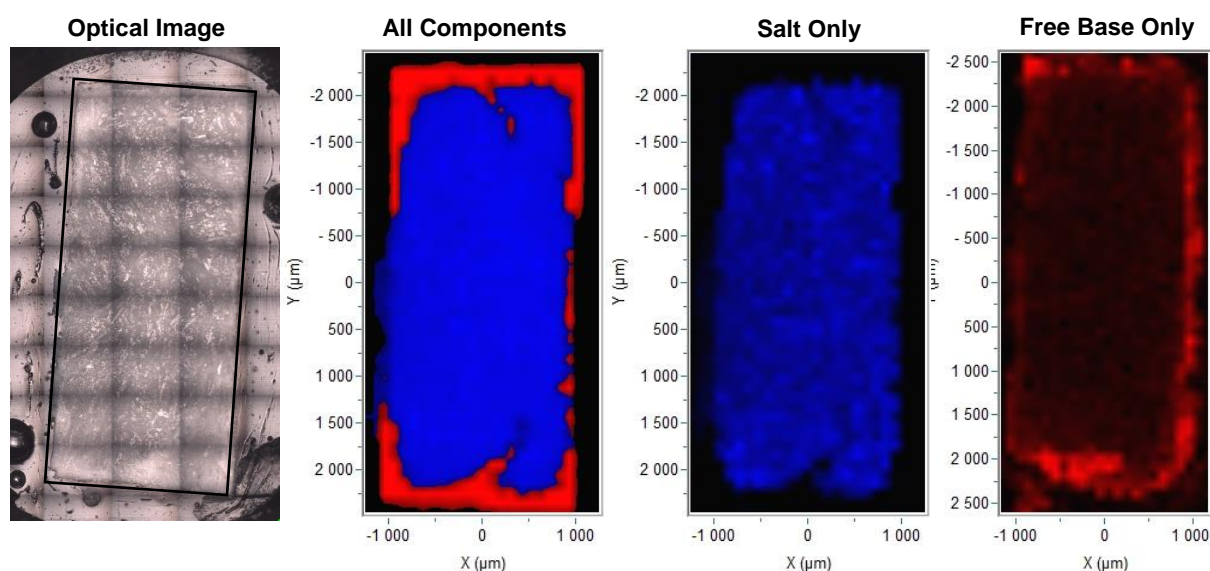


Figure 5.9: Optical image and Raman maps of the pure Pioglitazone HCl cross-sectioned tablet after dissolution in the basic buffer generated by CLS fittings.

5.4.1.2.2. The Effect of the Excipients

The excipient's effect on salt disproportionation will be investigated in this section. It has been reported that excipients possessing acidic/basic functionalities can modulate the microenvironmental pH within sorbed moisture located at surfaces of the salt [24], [31], [327], [328], [32], [201], [220], [225], [226], [229], [232], [233]. The change in the microenvironmental pH may induce or prevent salt disproportionation depending on the pH_{max} of the drug salt.

In this section, Pioglitazone HCl was formulated with different types of excipients that possess different physiochemical properties and roles in tablet formulation. The results in this section will be compared to the results obtained in section 5.4.1.2.1 (The Effect of the Buffer pH). Therefore, any changes in the drug salt stability will be influenced by the excipient, not the buffer used.

5.4.1.2.2.1. Formulation A-Pioglitazone HCl: Citric Acid

Citric acid is widely used pH modifiers in pharmaceutical formulations, primarily to adjust the microenvironment pH of tablet matrices [244]. pH modifier, such as citric acid, has been used before as an effective tool to modulate the microenvironment pH to enhance stability [32], [285], [286] and minimise salt disproportionation during dissolution [287]–[290]. Therefore, Pioglitazone HCl was formulated with citric acid to prevent the conversion to the free form during tablet manufacturing and dissolution in basic medium. The weight ratio (Pio HCl: Citric Acid- 70:30 w/w) was adapted from a previous study that used pH modifiers in tablet formulations [329].

Formulation A: Acidic Buffer: Averaged Raman spectra of formulation (A) tablet in the acidic buffer are presented in Figure 5.10. Examination of the data did not reveal significant changes in the spectra across the entire period of the dissolution experiment (0 to 120 min). The

doublet peak located at the region 1600 to 1650 cm^{-1} was preserved throughout the whole dissolution test. The Raman data essentially showed that when the pH is below the pH_{max} of the drug, the free base did not form, and the drug remained as the more soluble HCl salt.

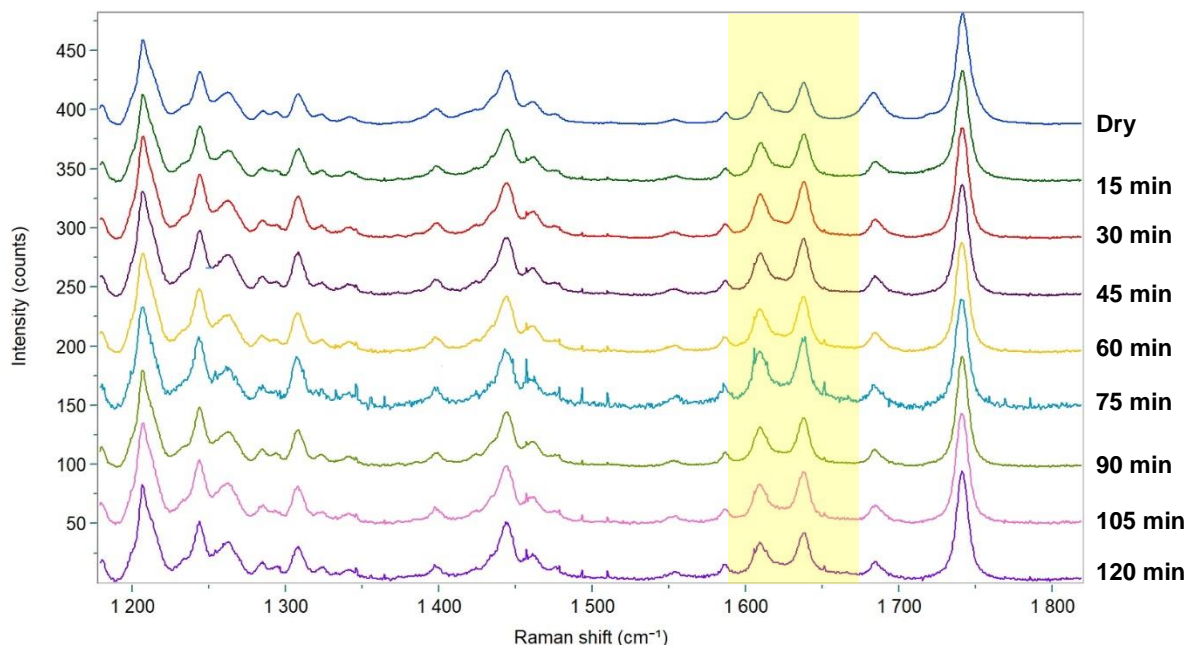


Figure 5.10: Averaged Raman spectra (1200 to 1800 cm^{-1}) of the dissolution of formulation A (Pio HCl: Citric Acid) tablet in the acidic buffer. Y-axis offsets were applied for presentational purposes.

The results of the MCR and CLS analysis are presented graphically in Figure 5.11. In the MCR analysis, trial runs indicated that a suitable choice of the number of components for this data set was two. The MCR component related to the citric acid cannot be generated due to the lack of significant variance between the citric acid and the salt spectra (Figure 5.11). The first MCR component unambiguously correlates to the pure salt reference spectra (Doublet peak at 1600 to 1650 cm^{-1}). The second component showed the doublet peak at 1600 to 1650 cm^{-1} , which were correlated to the salt spectra. However, a broad peak at 1600 cm^{-1} was also seen in the second component that is not entirely comparable to the salt or the free base reference spectra. Therefore, raw data checking was performed to investigate the source of this peak.

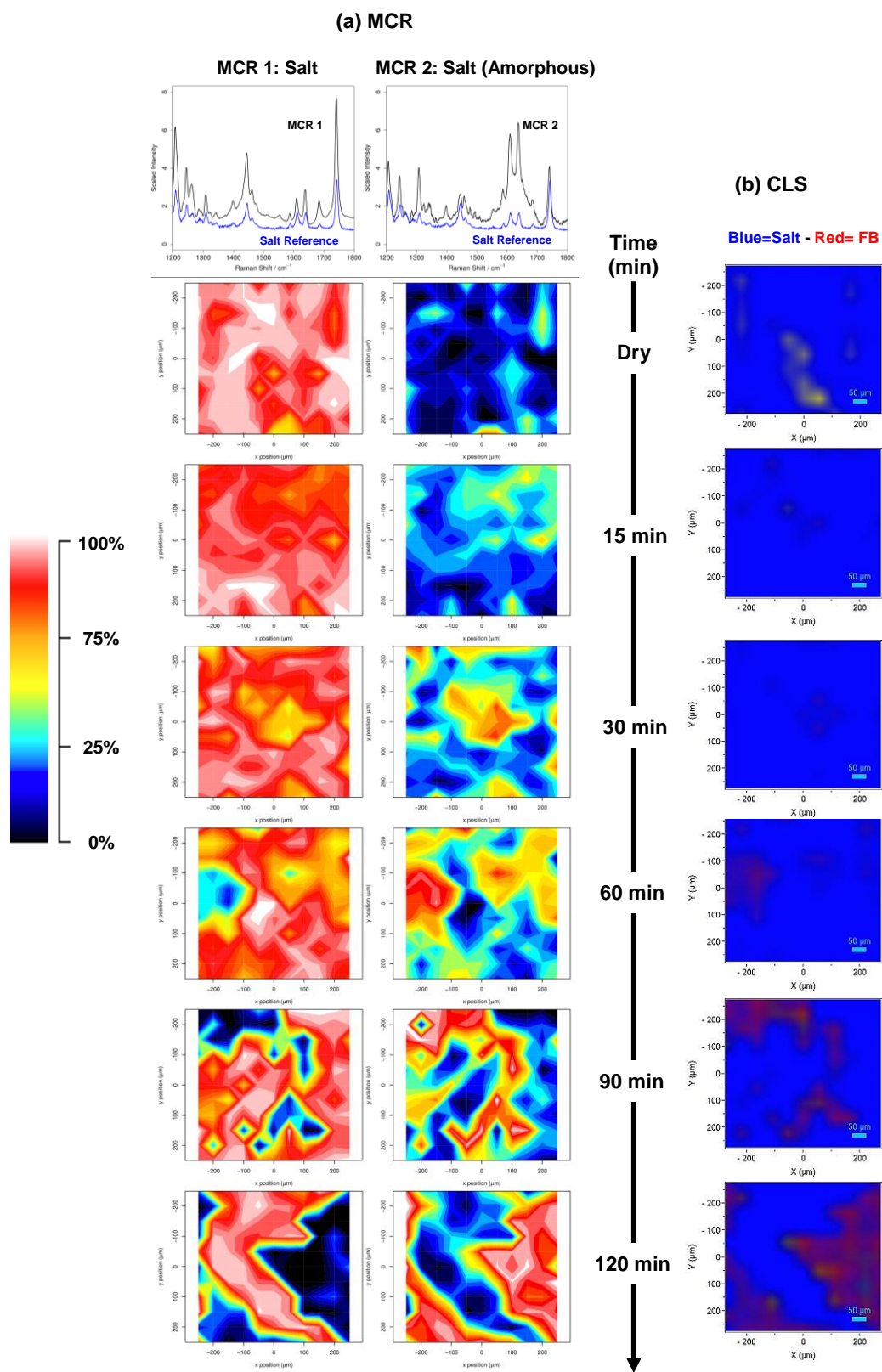


Figure 5.11: Raman maps of formulation A tablet (Pio HCl: Citric Acid) during dissolution in the acidic buffer as a function of time, generated by (a) MCR analysis (b) CLS analysis.

It is likely that the broad humps in the Raman spectra were due to the amorphous drug component produced during dissolution (Figure B.1 - Appendix B). There was no spectroscopic evidence of conversion from the salt to the free base form during this experiment in any of the measured data. This result is confirmed by the information in the CLS maps showing the dominance of the salt form (Blue colour) across all the maps (Figure 5.11-b).

Incorporation of citric acid in the Pioglitazone HCl tablet formulation preserved the salt form during tablet preparation, which is evident by the absence of the free base spectra in the dry tablet map (Figure 5.11, Dry). Furthermore, citric acid may have enhanced the apparent solubility of the hydrochloride salt by lowering the microenvironment pH of the dissolution medium surrounding the tablet; therefore, minimising free base precipitation during dissolution. A similar effect of the pH modifier has been reported previously [287].

Formulation A: Basic Buffer: Dissolution of formulation (A) tablet in basic buffer was investigated. Reduction of the salt disproportionation during dissolution was expected due to the role of citric acid in lowering the microenvironment pH below the pH_{max} of salt regardless of the bulk dissolution medium pH [320], [321]. Figure 5.12 shows the averaged Raman spectra of formulation (A) tablet in the basic buffer. Raman data showed rapid and significant changes in the spectrum after 15 min. The increase of 1610 cm^{-1} peak intensity supports the formation of the free base. The addition of citric acid did not reduce or prevent the salt disproportionation in the basic medium. It is likely that the faster dissolution of citric acid with respect to Pioglitazone HCl led to a rapid leach of citric acid from the tablet matrix. This resulted in high microenvironment pH values and thus led to the salt disproportionation. This effect has been reported before in multiple studies [321], [330], [331].

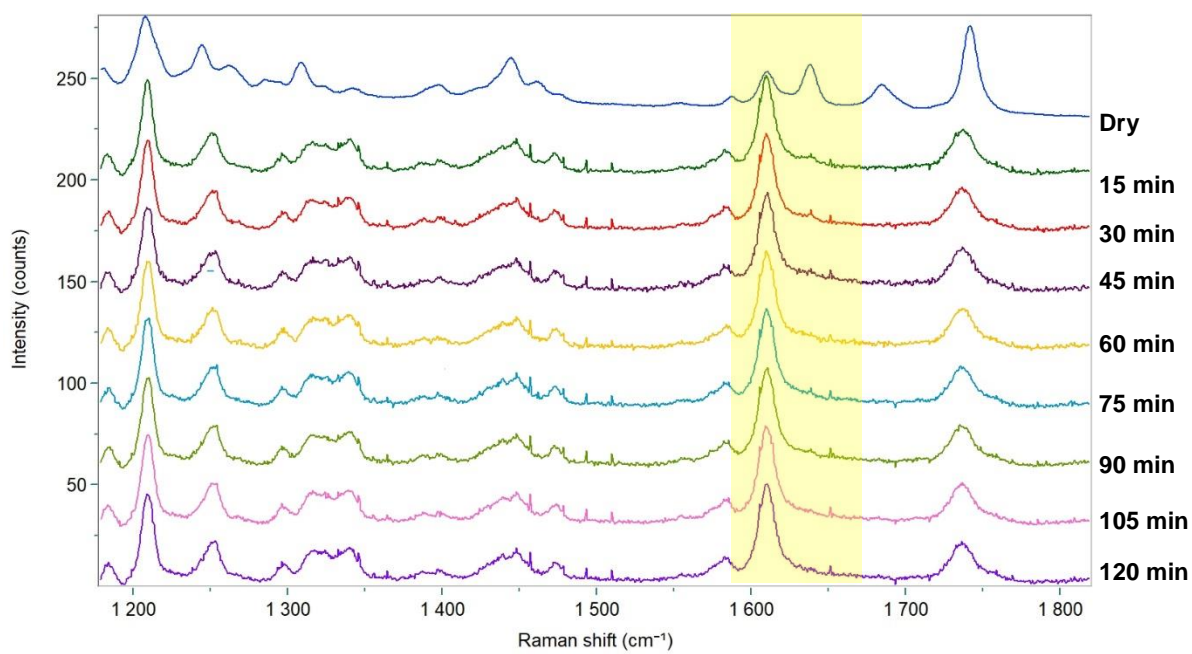


Figure 5.12: Averaged Raman spectra (1200 to 1800 cm^{-1}) of the dissolution of formulation A (Pioglitazone HCl: Citric Acid) tablet in the basic buffer. Y-axis offsets were applied for presentational purposes.

MCR data analysis shows that the data have been resolved into components which agree remarkably well with Pioglitazone HCl salt (MCR1) and Pioglitazone free base (MCR2) in Figure 5.13. The data are showing rapid conversion to the free form in less than 30 min. The salt conversion in the formulation (A) was faster than that in pure Pioglitazone HCl tablet during dissolution in basic media.

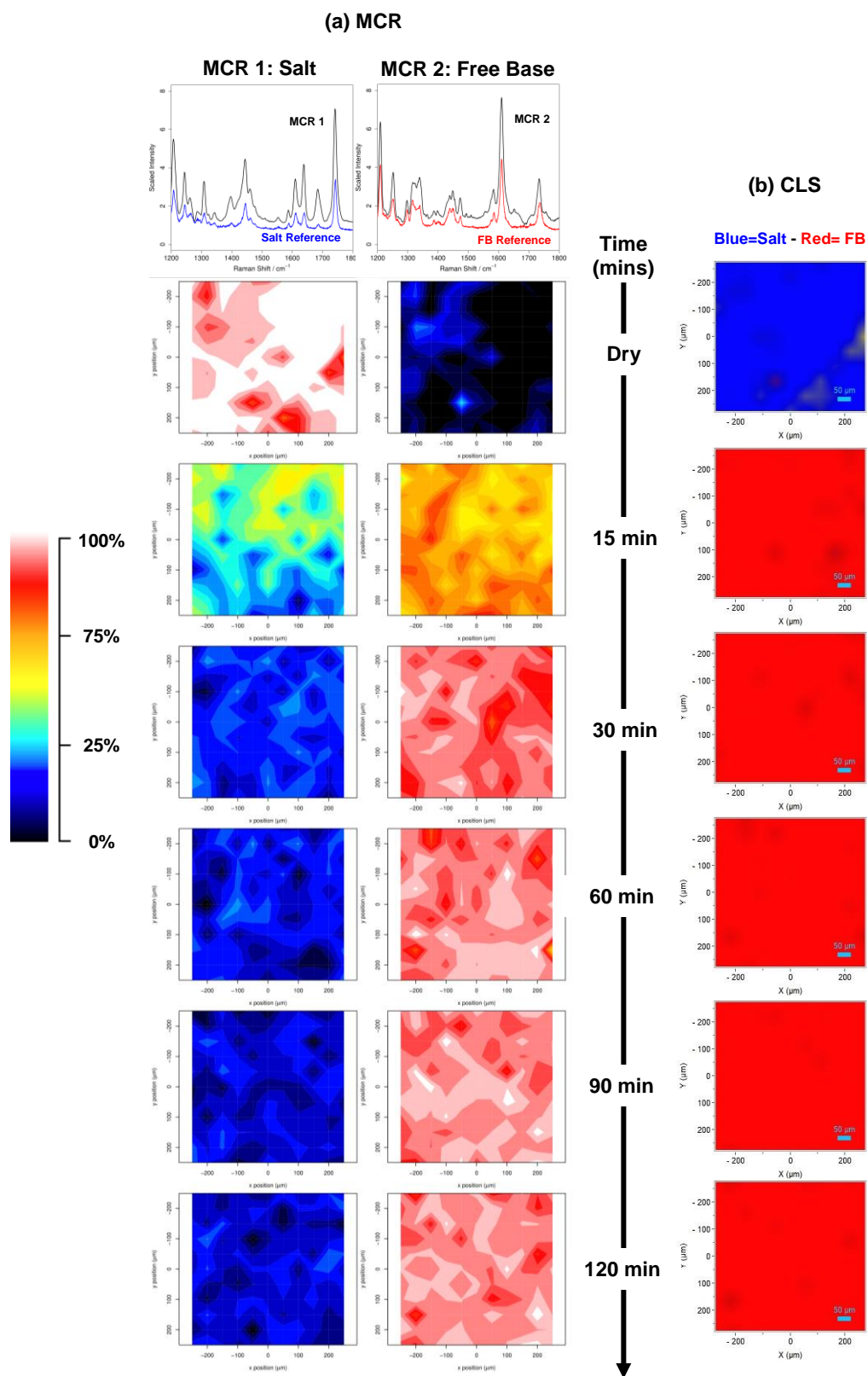


Figure 5.13: Raman maps of formulation A tablet (Pio HCl: Citric Acid) during dissolution in the basic buffer as a function of time, generated by (a) MCR analysis (b) CLS analysis.

It is likely that the citric acid leached out of the tablet matrix, possibly leaving pores upon contact with the basic buffer medium. These pores may have increased the basic medium ingress inside the tablet and exposed more surfaces of the salt drug to the medium resulting in rapid and significant conversion to the free form. Similarly, CLS data shows the domination of the free base around the outer surface and edges of the tablets similar to the pure Pioglitazone HCl tablet (Section 5.4.1.2.1, Figure 5.9). However, the thickness of the free form layer in formulation (A) tablet is larger than the drug only tablet. This could be related to the high solubility of the citric acid leaving pores in the free form layer, therefore allowing more basic media to penetrate.

Unlike the acidic medium, formulation (A) tablet was recovered from the flow-cell after the dissolution experiment in the basic buffer. Raman maps generated by CLS on Figure 5.14 show the formation of the free base around the outer surface and edges of the tablets similar to the pure Pioglitazone HCl tablet (Section 5.4.1.2.1, Figure 5.9). However, the thickness of the free form layer in formulation (A) tablet is larger than the drug only tablet. This could be related to the high solubility of the citric acid leaving pores in the free form layer, therefore allowing more basic media to penetrate.

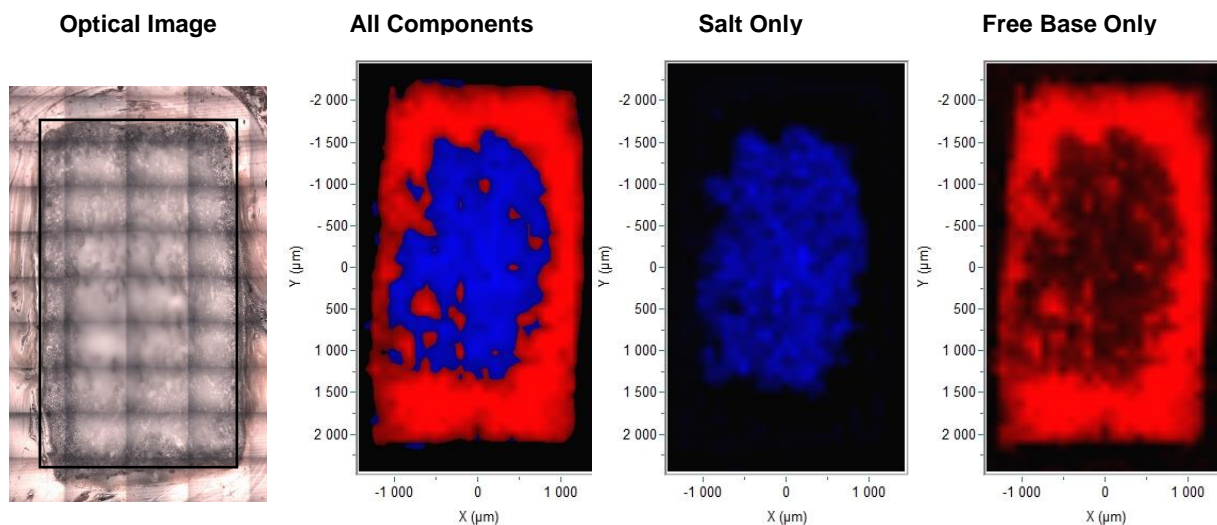


Figure 5.14: Optical image and Raman maps of the formulation A (Pio HCl: Citric Acid) cross-sectioned tablet after dissolution in the basic buffer generated by CLS fittings.

5.4.1.2.2.2. Formulation B-Pioglitazone HCl: Lactose Monohydrate

Lactose monohydrate (LM) is a carbohydrate that is widely used as a filler and diluent in solid dosage forms [244]. Fillers are usually used to provide bulk for the active ingredient to be measured accurately and improve the formulation properties, such as cohesion. Generally, Lactose monohydrate exhibits some good properties that contribute to its popularity, including low hygroscopicity, compatibility with active ingredients and excellent physical and chemical properties [332].

The FDA approved Pioglitazone HCl tablet, Actos™ formulation contains lactose monohydrate as a filler [301]. However, the slurry measured pH for LM is around 6.0, which exceed the pH_{max} of Pioglitazone HCl. This indicates that LM in the presence of water may elevate the microenvironment pH in the tablet and induce salt disproportionation. Therefore, Pioglitazone HCl was formulated with lactose monohydrate to study the stability of the salt tablet during dissolution in the acidic and basic medium. According to the ingredient's percentage used in Actos™ formula, lactose monohydrate makes up about 80% of the total formulation compared to 14% for the drug salt. Therefore, 80%: 20% weight ratio (Pio HCl: LM) was used in the tablet formulation.

Formulation B- Acidic pH: Averaged Raman spectra of formulation (B) tablet in the acidic buffer are presented in Figure 5.15. Raman data show that the spectrum does not change after 15 min (Figure 5.15, 15 min). The double peak of the Pioglitazone salt at 1600 to 1650 cm^{-1} region preserved the same ratio as in the spectrum of the dry tablet compact. Proceeding with the analysis, after 60 min the intensity of the 1640 cm^{-1} peak appears to decrease in relation to the 1610 cm^{-1} peak. After 90 min, the average Raman spectrum shows only a single peak at 1610 cm^{-1} , which correlate well with Pioglitazone free base spectrum.

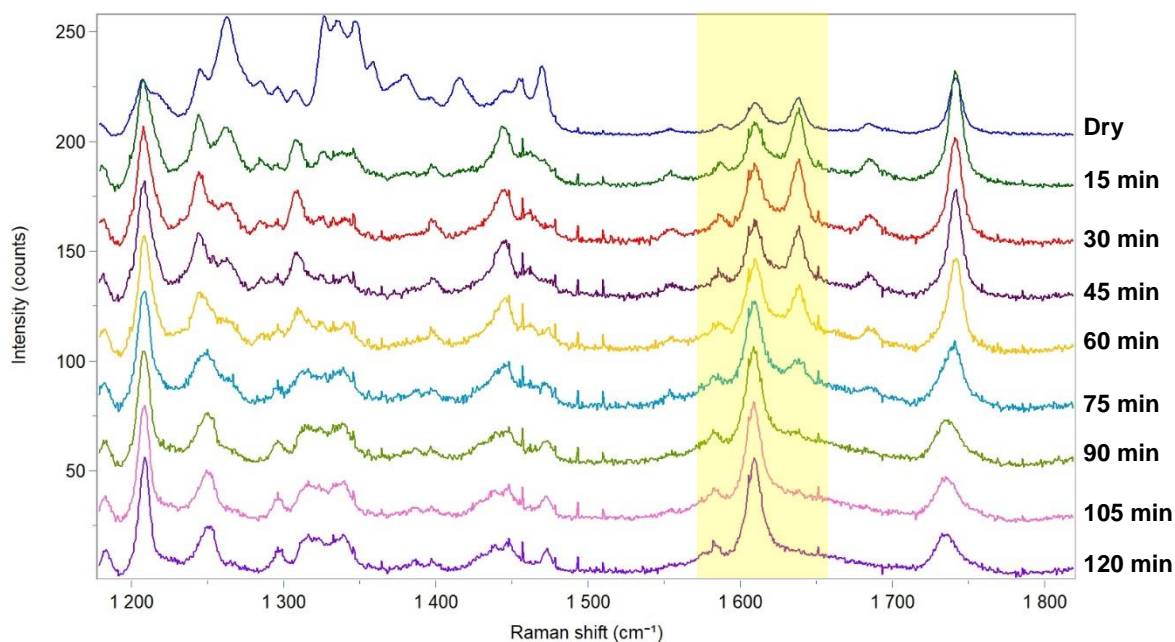


Figure 5.15: Averaged Raman spectra (1200 to 1800 cm^{-1}) of the dissolution of formulation B (Pio HCl: LM) tablet in the acidic buffer. Y-axis offsets were applied for presentational purposes.

The MCR model was used to spatially and spectrally visualise the components distribution in the tablet and track the salt conversion to the free form during dissolution in acidic pH (Figure 5.16). Three components were applied to deconvolute the mapped data. The first and the third components can be associated with the salt and the free base, respectively.

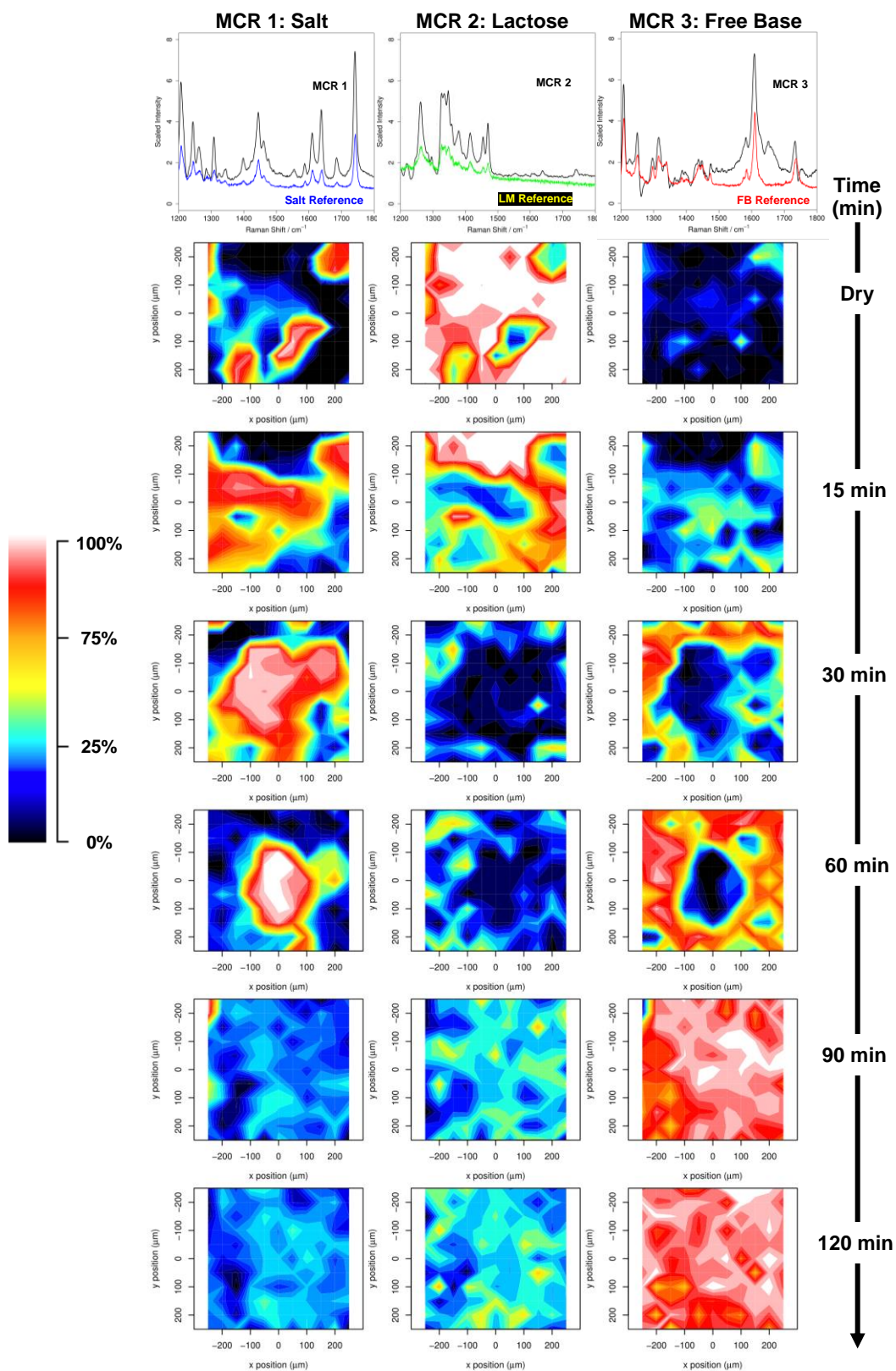


Figure 5.16: Raman maps of formulation B tablet (Pio HCl: LM) during dissolution in the acidic buffer as a function of time, generated by MCR analysis.

MCR 2 mostly correlate to the lactose monohydrate. The vibration bands at 1200 to 1500 cm^{-1} are due to movements of C-CH and O-CH in lactose monohydrate molecules[333]. The scores' plots show that the Pioglitazone HCl salt (MCR1) and lactose monohydrate (MCR2) are distributed throughout the mapped compact surface before immersion in the dissolution medium. Then, after 30 minutes the amount of the free base (MCR3) increased whereas the salt and the lactose monohydrate amount decreased. It is likely that lactose monohydrate rapidly dissolved in the dissolution medium whereas the salt dissolved and then precipitated in the form of a free base.

CLS model showed similar features to the MCR maps especially at 30 and 60 min (Figure 5.17). After 90 min, a complete conversion to the free form in the mapped area was noticed.

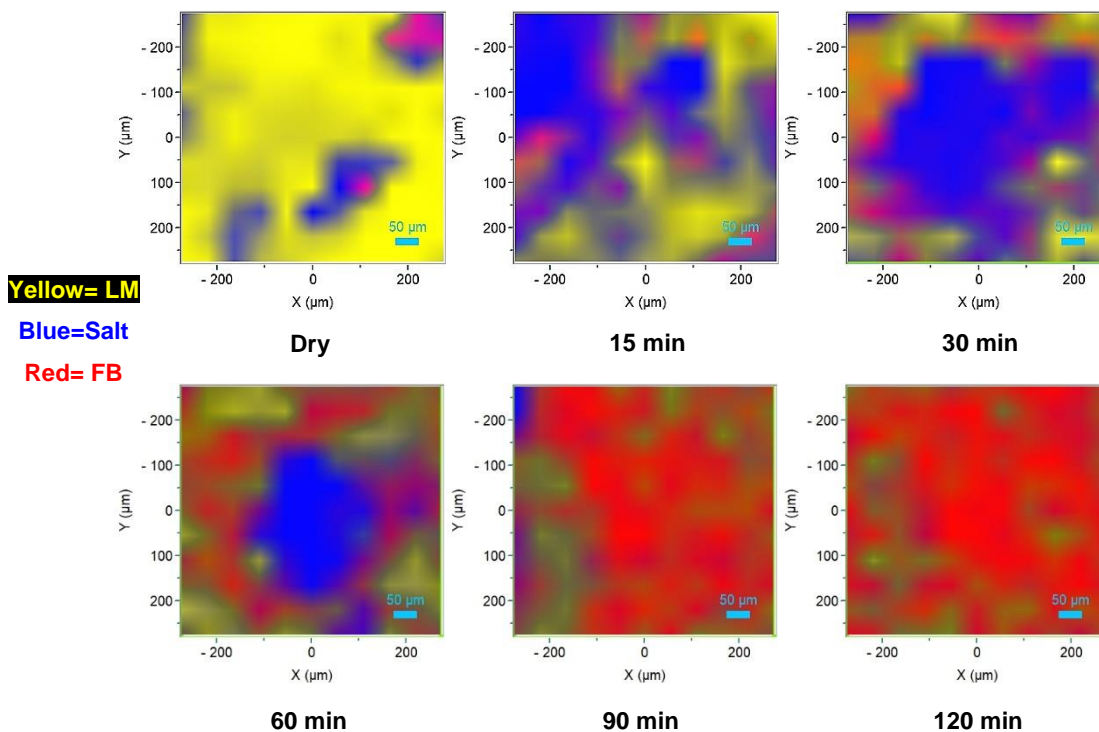


Figure 5.17: Raman maps of formulation B tablet (Pio HCl: LM) during dissolution in the acidic buffer as a function of time, generated by CLS analysis.

In comparison to the pure Pioglitazone HCl tablet (Section 5.4.1.2.1-Figure 5.5 & 5.6), formulation (B) tablet showed a significant difference in the salt disproportionation kinetic. In

comparison to the salt-only tablet, a complete salt conversion to the free base supported by the absence of the 1640 cm^{-1} peak was shown in formulation (B) during dissolution in acidic medium. It is possible that lactose monohydrate elevated the microenvironment pH significantly, which impacted the salt stability in the tablet. This effect of lactose monohydrate has not been reported before in the literature to the best of our knowledge.

Formulation B- Basic pH: Average Raman spectra (Figure B.2 - Appendix B), MCR maps (Figure B.3 - Appendix B) and CLS maps (Figure B.4 - Appendix B) are all shown the rapid conversion of the salt drug to the free base. The high solubility of the lactose monohydrate facilitated the ingress of the basic dissolution medium into the tablet matrix and induced the salt disproportionation. It was not possible to recover any tablet after the dissolution test due to the high solubility of lactose monohydrate, which accounts for ~70% of the tablet mass.

5.4.1.2.2.3. Formulation C-Pioglitazone HCl: Magnesium Stearate

Magnesium stearate (MgSt) is used primarily as a lubricant in tablet manufacturing to reduce the friction between the surfaces of the metal and that of formulation powders, as well as to ensure the continuation of the operation [244], [292], [293]. It works by coating the surface of the particles when mixed with the active ingredients and other excipients [219]. As a result, magnesium stearate was added to the formulation in a small concentration (0.25 - 5.0 % w/w) due to the hydrophobic nature that may retard the dissolution of the drug from the tablet [244], [292]. Furthermore, magnesium stearate exhibits an alkaline nature, which is ascribed to the presence of basic impurities such as magnesium oxide [226].

It is well-documented that magnesium stearate induces and accelerates disproportionation reaction when blended with free-base salts [30], [201], [219], [226]. The FDA

approved Pioglitazone HCl tablet, Actos™; formulation includes magnesium stearate as a lubricant. However, the measured pH for MgSt is around 8.5, which highly exceeds the pH_{max} of Pioglitazone HCl. The addition of MgSt in the tablet formulation may induce Pioglitazone HCl salt disproportionation during manufacturing and dissolution. Therefore, Pioglitazone HCl was formulated with magnesium stearate to investigate the stability of the salt tablet during dissolution in the acidic and basic medium. Pioglitazone HCl salt was mixed with magnesium stearate were at a 90% to 10% weight ratio, which is a sensible representation of the percentage of MgSt found in Pioglitazone HCl commercial tablet [301].

Formulation C- Acidic pH: Averaged Raman spectra of formulation (C) tablet in the acidic buffer are presented in Figure 5.18. Raman data show that after 30 minutes the intensity of the 1640 cm^{-1} peak decreased gradually in relation to the 1610 cm^{-1} peak till the end of the experiment. After 90 min, the average Raman spectra shows only a single peak at 1610 cm^{-1} , which correlates well with Pioglitazone free base spectrum. The prompt conversion to the free base was due to the role of magnesium stearate in elevating the microenvironment pH above the pH_{max} of the salt. These findings are supporting the importance of the microenvironment pH in salt stability and performance.

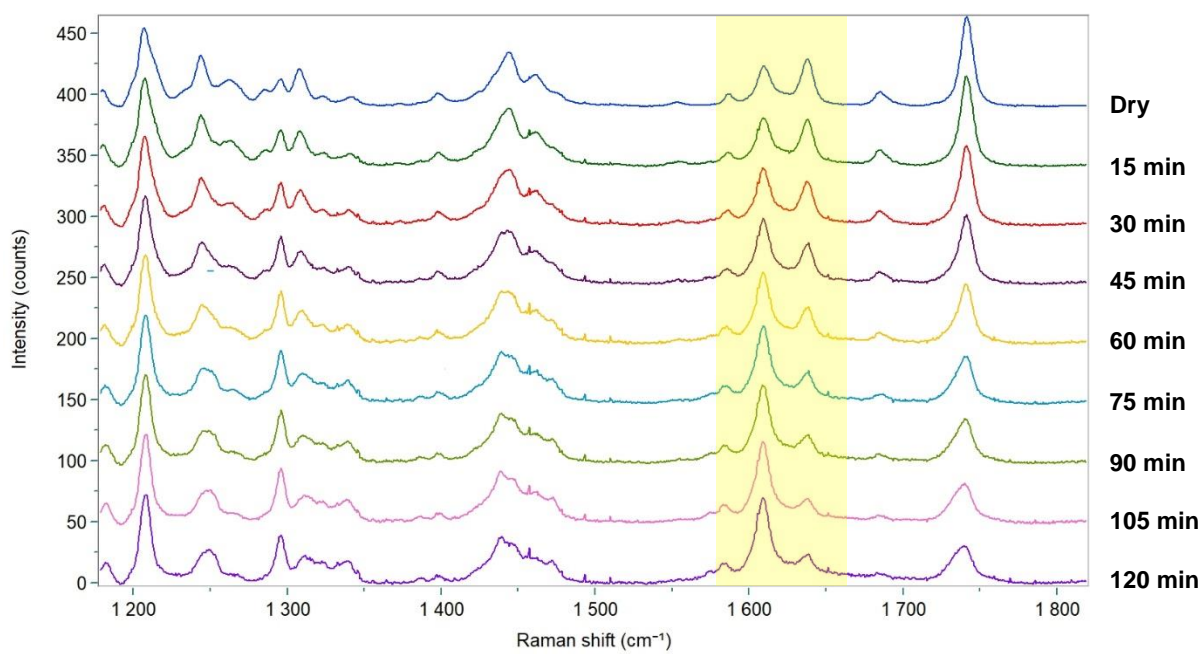


Figure 5.18: Averaged Raman spectra (1200 to 1800 cm^{-1}) of the dissolution of formulation C (Pio HCl: MgSt) tablet in the acidic buffer. Y-axis offsets were applied for presentational purposes.

The results of the MCR and CLS analysis are presented graphically in Figure 5.19 and 5.20, respectively. Three components were applied to deconvolute the mapped data in the MCR analysis. The first and the second components can be associated with the salt and the free base, respectively. MCR 3 mostly correlate to the magnesium stearate. The two vibration strong bands at 1294 and 1437 cm^{-1} in MgSt are due to in-plane scissoring movements (bending) of CH_2 [334]. The scores' plots show that the Pioglitazone HCl salt (MCR 1) are distributed throughout the mapped compact surface before immersing in the dissolution medium. Small distribution of the magnesium stearate (MCR 3) can be identified in the middle of the tablet (Figure 5.20, Dry). After 30 min, the amount of the free base (MCR2) increased, whereas the salt amount decreased. It is interesting to note that the free base formation started around the magnesium stearate's high concentration region at time=30 min. This confirms the deleterious effect of magnesium stearate to induce salt disproportionation [201], [226].

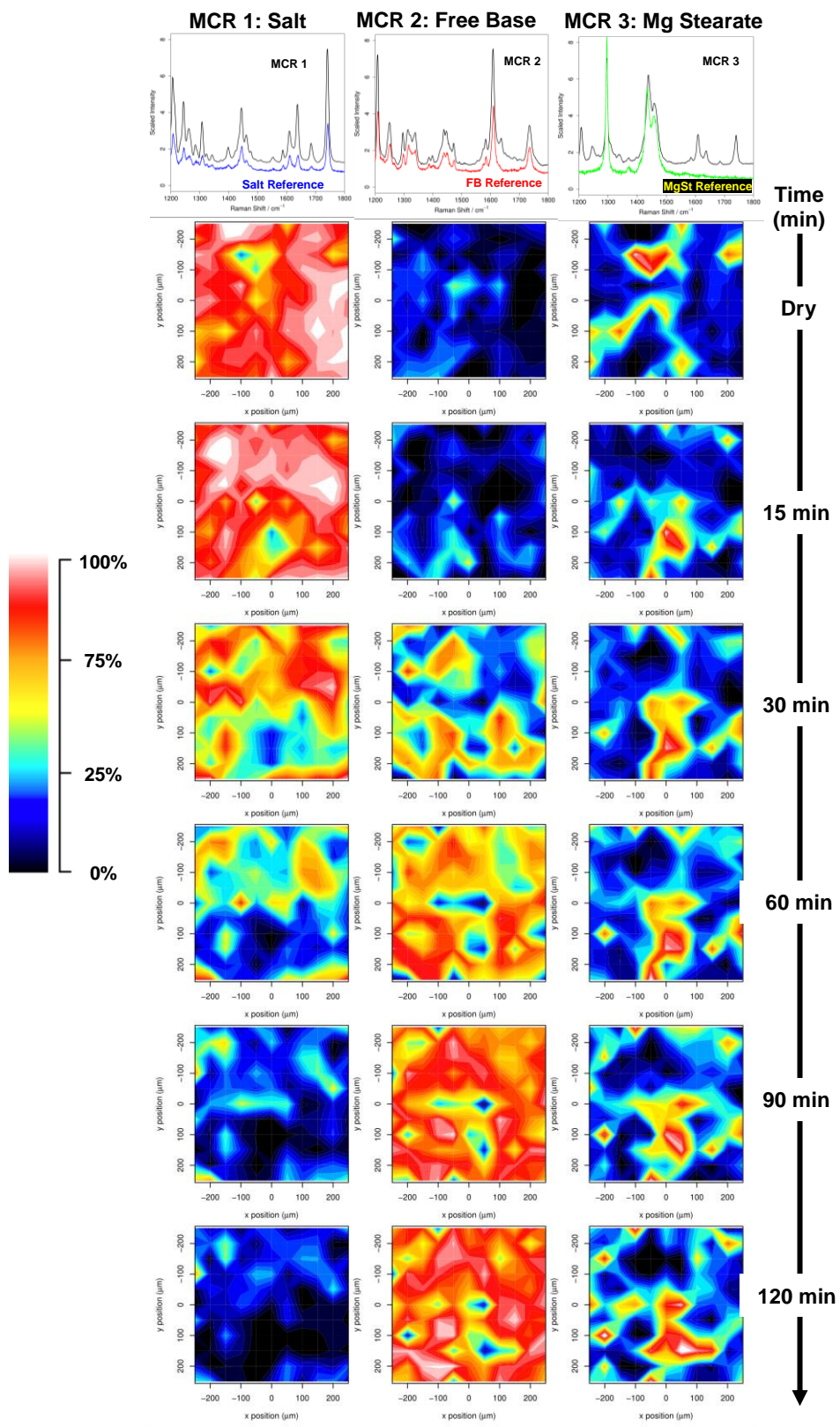


Figure 5.19: Raman maps of formulation C tablet (Pio HCl: MgSt) during dissolution in the acidic buffer as a function of time, generated by MCR analysis.

CLS maps show similar disproportionation kinetics and the co-localisation effect of magnesium stearate to the MCR.

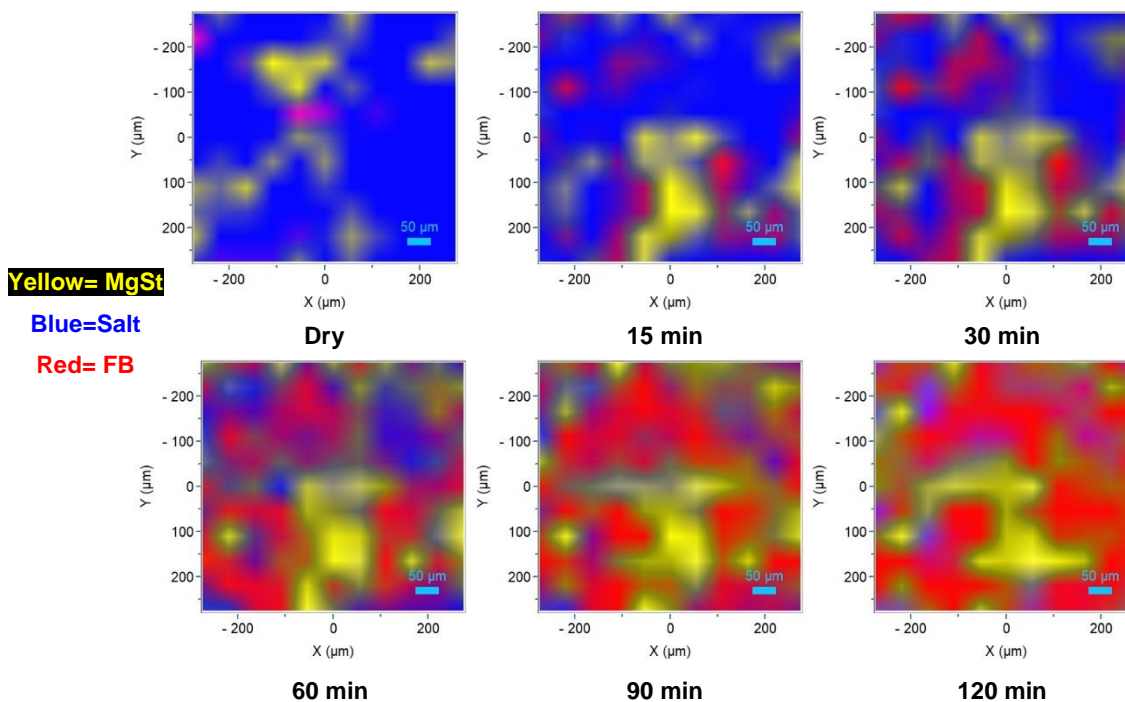


Figure 5.20 Raman maps of formulation C tablet (Pio HCl: MgSt) during dissolution in the acidic buffer as a function of time, generated by CLS analysis.

At the end of the experiment, the tablet was recovered from the flow cell and cross-sectioned. Raman mapping was performed to analyse the edge and the core of the whole cross-sectioned tablet (Figure 5.21). A thin layer of the free form is observed on the outside surface of the tablet with the salt located below the surface, which was not available for dissolution. The formation of the insoluble free form shell affected the penetration of the solution towards the core of the tablet, which had a significant impact on the amount of the drug released into the surrounding medium. These findings prove the detrimental effect of magnesium stearate on the dissolution performance when formulated with the salt of the weakly basic drug.

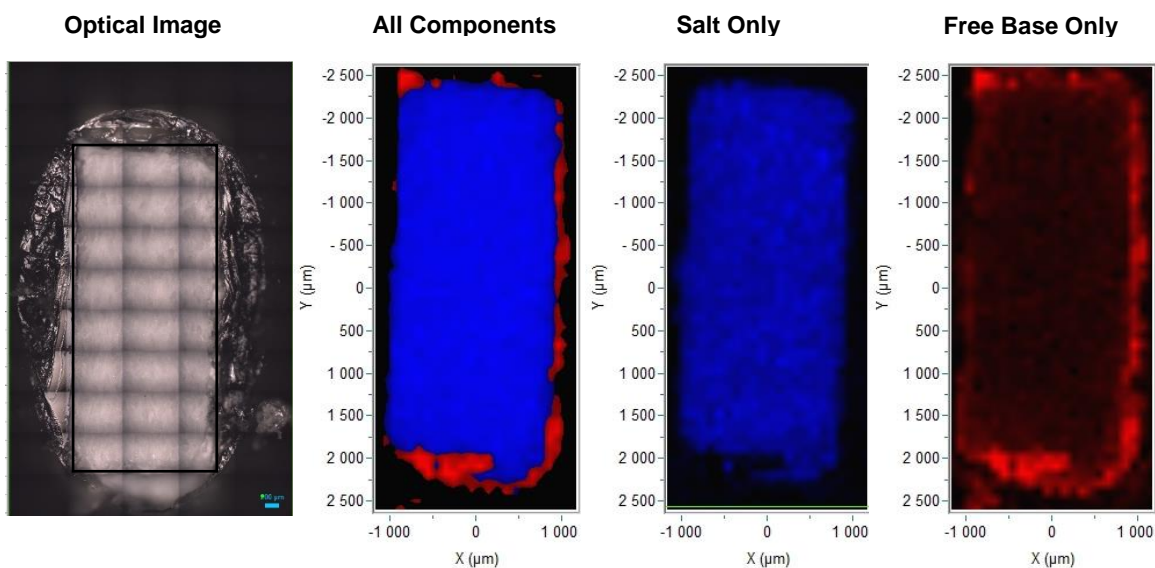


Figure 5.21: Optical image and Raman maps of the formulation C (Pio HCl: MgSt) cross-sectioned tablet after dissolution in the acidic buffer generated by CLS fittings.

Formulation C- Basic pH: The dissolution performance and salt stability of Pioglitazone HCl: Mg stearate formulation tablet in basic buffer medium was investigated. Figure 5.22 shows the averaged Raman spectra of formulation (c) tablet in the basic buffer. Surprisingly, a slow decrease in the 1640 cm^{-1} intensity in relation to the other peak at 1610 cm^{-1} was noticed. At the end of the dissolution experiment (Time=120 min), the average spectrum showed a small peak at 1640 cm^{-1} , which indicates the presence of the salt in the tablet matrix at a very low percentage. These data are significantly different from the one obtained in pure drug (Section 5.4.1.2.1-Figure 5.7), formulation A (Section 5.4.1.2.2.1-Figure 5.12) and formulation B (Section 5.4.1.2.2.2-Figure B2 in Appendix B) tablets dissolved in the basic medium.

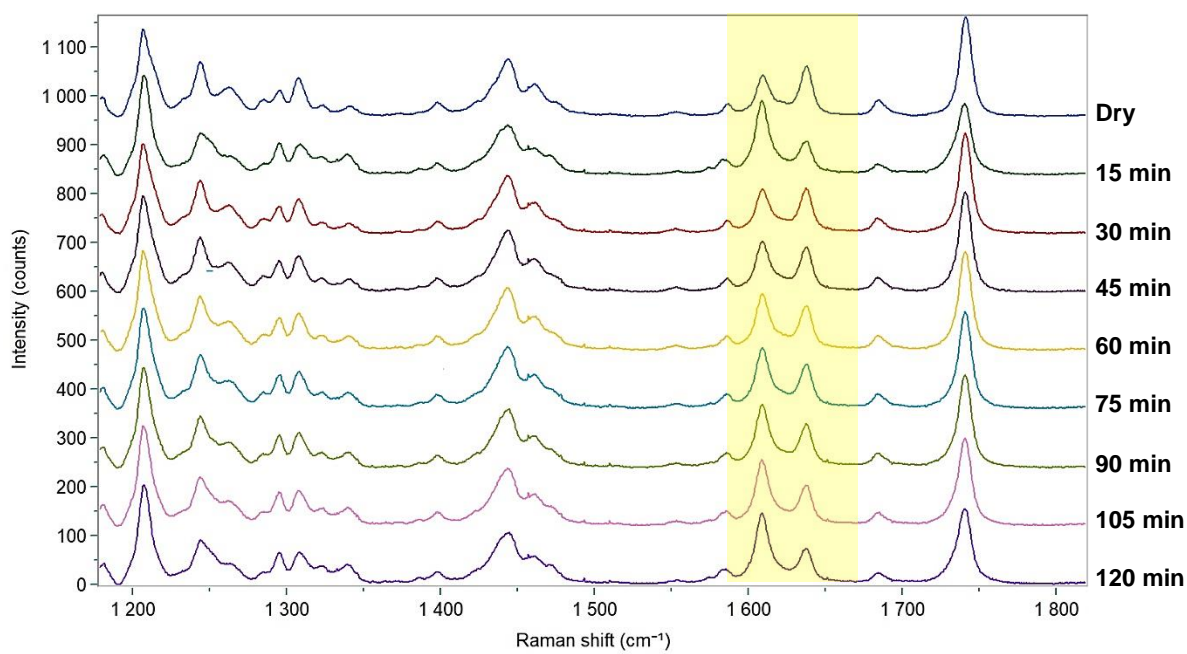


Figure 5.22: Averaged Raman spectra (1200 to 1800 cm^{-1}) of the dissolution of formulation C (Pio HCl: MgSt) tablet in the basic buffer. Y-axis offsets were applied for presentational purposes.

Three components were required to deconvolute the mapped data using MCR (Figure 5.23). Comparison of the MCR loadings with reference spectra shows that the data have been resolved into components, which agree well with Pioglitazone HCl salt (MCR 1), Pioglitazone free base (MCR 2) and magnesium stearate (MCR 3). The MCR maps confirm that there was the slow formation of free base form around high concentration MgSt regions (Figure 5.23, time = 15 min, 30 min and 60 min). A high concentration of mass correlated to the salt form was located at the bottom left corner after the end of the dissolution experiments. This agrees with the average spectra visualisation in Figure 5.22. The Raman maps generated by CLS are in good agreement with the MCR-ALS maps (Figure B.5 - Appendix B).

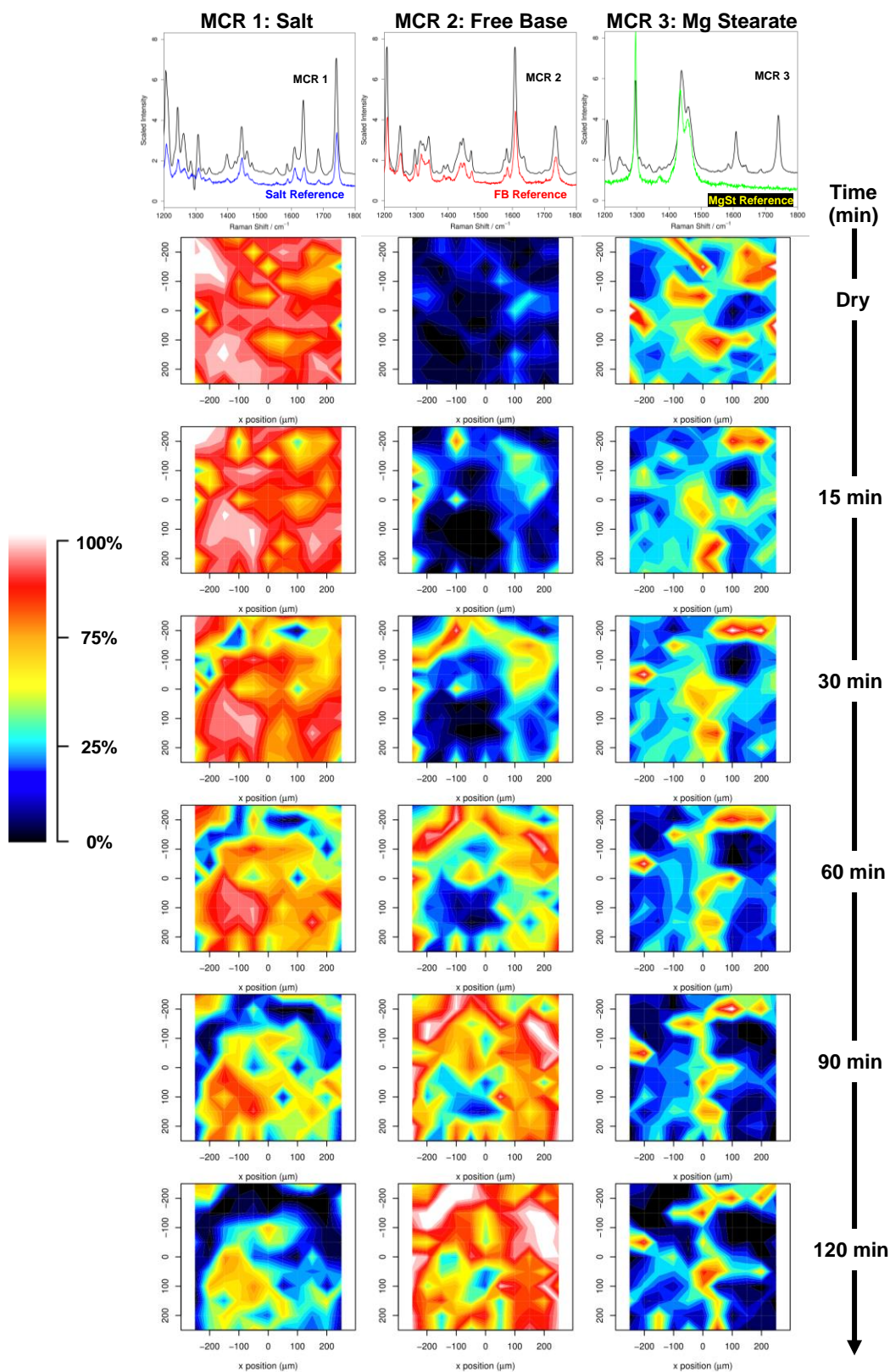


Figure 5.23: Raman maps of formulation C tablet (Pio HCl: MgSt) during dissolution in the basic buffer as a function of time, generated by MCR analysis.

Disproportionation is a solution-mediated reaction, which involves the dissolution of the salt reaching the supersaturation level then precipitation out of the solution into the free form [224]. In formulation C, basic pH medium system, a synergetic effect of both the hydrophobic nature of the magnesium stearate and the low salt solubility in basic medium led to the slow disproportionation kinetics. The hydrophobic surface coverage of the salt particles by the MgSt led to a decrease in the water ingress inside the tablet and a reduction in the salt dissolution rate. The reduction in the dissolution rate led to an increase in the time required to reach the supersaturation concentration to start precipitating as the free base.

The cross-sectioned tablet of the formulation (C) dissolved in basic buffer was analysed using Raman mapping (Figure 5.24). The Raman maps showed a similar effect when the same formulation tablet dissolved in acidic buffer (Figure 5.21) where the free form was detected on the surface, and the edge of the tablet and the interior remained an unchanged salt. However, the thickness of the free form layer formed at the surface of the tablet dissolved in basic medium was bigger due to the relatively higher dissolution rate and solubility of magnesium stearate in basic medium [335].

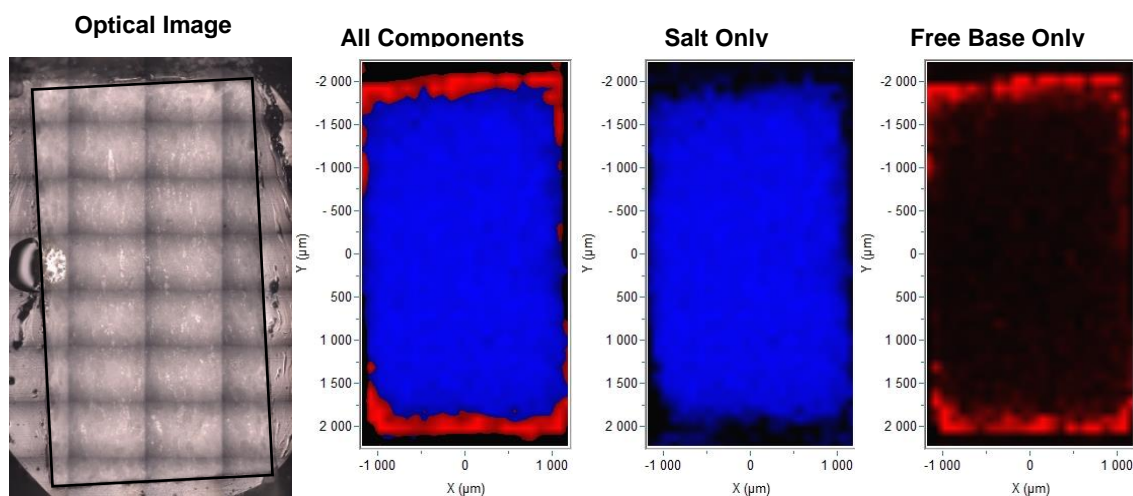


Figure 5.24: Optical image and Raman maps of the formulation C (Pio HCl: MgSt) cross-sectioned tablet after dissolution in the basic buffer generated by CLS fittings.

5.4.1.2.2.4. Dissolution Profile: Ultraviolet-Visible Data

To provide additional analytical insight, the dissolution profiles of Pioglitazone HCl released from pure drug salt, formulation (A) and formulation (C) tablet were obtained in parallel with the flow-cell experiment in acidic and basic dissolution. Formulation (B) UV-Vis data were excluded due to lactose monohydrate that absorbs UV in the same range ($\lambda \sim 260$ nm) as Pioglitazone, which causes interference with the drug release measurement [324]. This interference causes an overestimation of the Pioglitazone concentration in the release medium due to the UV analytical incapability of determining drug concentration separately from other components present in the formulation.

By using the equation of the trend line from the calibration plot (Figure B.6 - Appendix B), the amount of Pioglitazone HCl released from tablets in the acidic and basic medium was determined as shown in Figure 5.25 and Figure 5.26, respectively.

Figure 5.25 presents the dissolution profile for the different formulations in acidic buffer. The dissolution rate of the tablets containing citric acid showed fast drug release during the experiment period, releasing 70% of the drug. In contrast, the dissolution rate of the tablets containing pure Pioglitazone salt and magnesium stearate showed slower drug release during the same period. However, the pure Pioglitazone HCl tablet has a higher dissolution rate compared to the formulation C tablet (Magnesium stearate), where 18% and 10% of the Pioglitazone was dissolved from the 50 mg tablet after 120 min, respectively. The UV dissolution profiles supported the Raman spectroscopic images recorded for the experiments, which confirms that the link between the salt disproportionation incident in the tablet and the percentage of the drug released from the tablet.

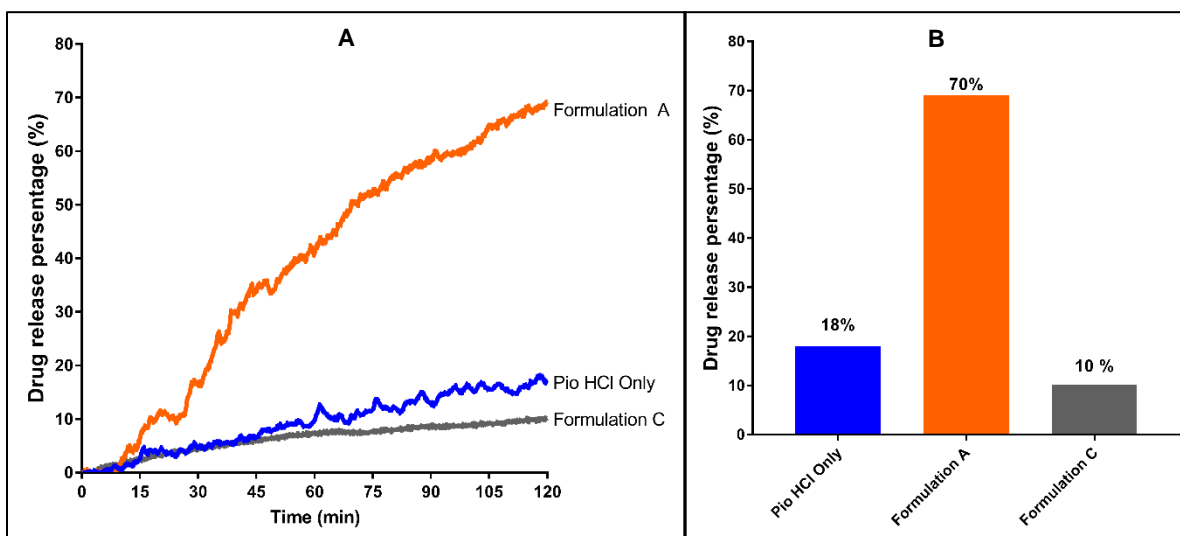


Figure 5.25:(A) Dissolution profiles obtained using UV-Vis detection that presents the percentage of Pioglitazone HCl released from the tablet as a function of time for the pure drug and different formulation tablets studied in the acidic medium. (B) The maximum drug release percentage.

The Raman average spectra and maps in Figure 5.10 and Figure 5.11, respectively, (Section 5.4.1.2.2.1, Acidic buffer) represent the dissolution of formulation (A) tablet showed that there was no detectable formation of the free base in the mapped area across the experiment time. The inhibition of the salt disproportionation resulted in a significant release of Pioglitazone as shown in UV dissolution profile for this formulation (Orange line within Figure 5.25). While, the Raman spectra and images of pure drug salt tablet (Section 5.4.1.2.1-Acidic buffer) and formulation (C) tablets (Section 5.4.1.2.2.3-Acidic buffer) showed salt conversion to the free form during dissolution, which contributed to the low drug release in the UV dissolution profile for Pure salt tablet (Blue line) and formulation C (Black line) presented in Figure 5.25. These findings confirm the protective role of citric acid in preventing salt disproportionation and the deleterious effects of magnesium stearate in inducing salt disproportionation during dissolution.

The Pioglitazone HCl release in the basic medium is presented in Figure 5.26. All tablets showed a considerably low drug release (1.0-2.0 %) which reflects the tablet's failure to dissolve in basic medium. These results were in agreement with the Raman average spectra and maps

presented previously (Section 5.4.1.2.1-Basic buffer, Section 5.4.1.2.2.1, Basic buffer and section 5.4.1.2.2.3-Basic buffer) showing the rapid conversion of the salt to the free base form after the basic medium contacted the tablet surface.

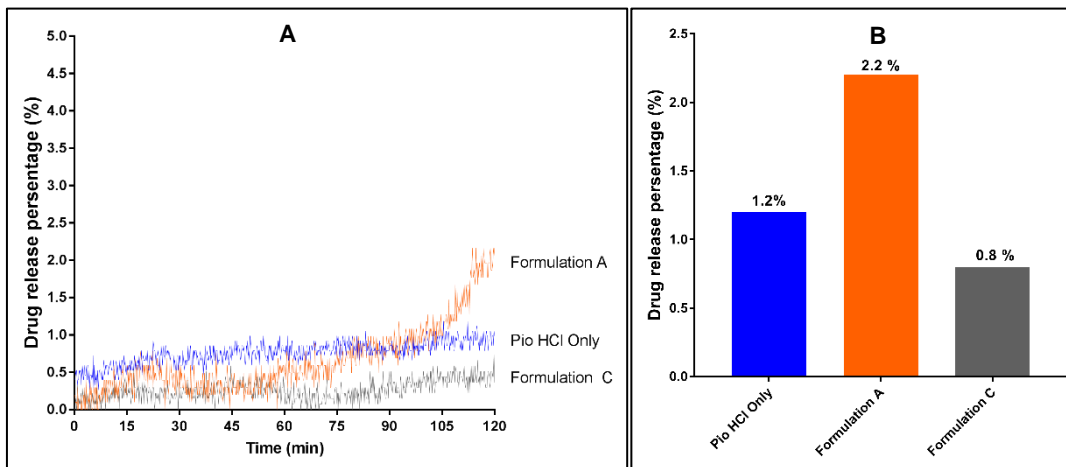


Figure 5.26: (A) Dissolution profiles obtained using UV-Vis detection that presents the percentage of Pioglitazone HCl released from the tablet as a function of time for the pure drug and different formulation tablets studied in the basic medium. (B) The maximum drug release percentage.

5.4.2. Ibuprofen Sodium: Free Acid Case Study

In this section, the excipient-induced disproportionation of the sodium salt of Ibuprofen, a weak acid with a pKa of 4.4 [276], will be investigated in order to improve the basic understanding of the salt stability and tablet dissolution performance in acidic and basic environment. Ibuprofen sodium may disproportionate back to the free acid at low pH (Acidic environment). By using Raman ultraviolet-visible flow cell system, the effect of dissolution medium pH and excipient physiochemical properties (mainly pKa) on salt disproportionation was explored.

5.4.2.1. Dry Pure Material Spectra

The Raman spectra (Spectral region 200 to 1500 cm^{-1}) of Ibuprofen sodium salt and Ibuprofen free acid are shown in Figure 5.27. The two spectra are showing some clear spectral differences between the salt and free acid forms. Specifically, Ibuprofen sodium salt demonstrated a small single peak, located at 1250 cm^{-1} , due to the stretching of (OC), bending of (HCC) and torsion of (HCCC) vibrational modes [283]. On the other hand, the free acid form demonstrated no peaks at 1250 cm^{-1} . In addition, Ibuprofen sodium salt demonstrated a single large peak located at 800-850 cm^{-1} region due to the (CC) stretching, whereas the free acid showed two sharp peaks at the same region due to the (CH) bending and in-plane (CC) ring deformation [284]. All the spectral difference can be elucidated by the protonation of Ibuprofen that changes the vibrational modes of the phenyl ring and the carboxyl group.

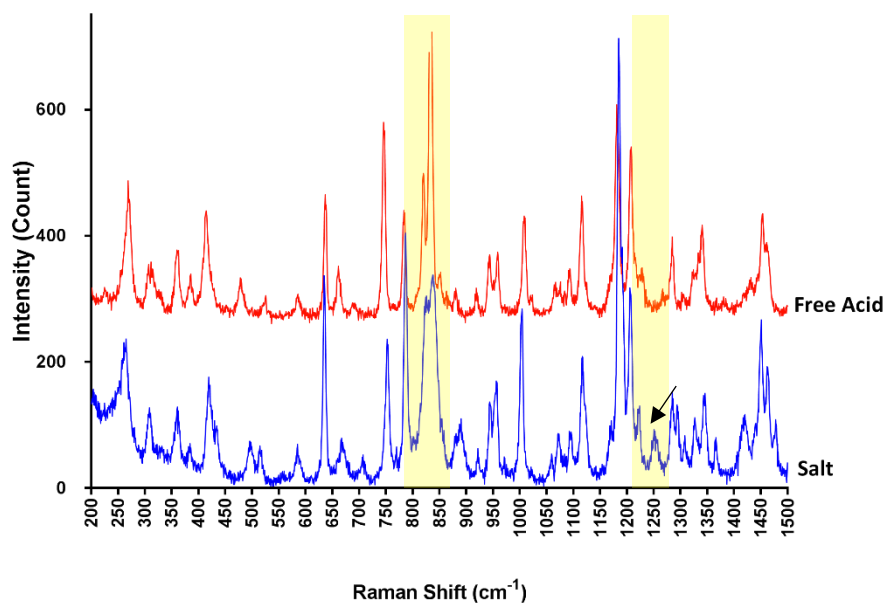


Figure 5.27: Raman spectra of Ibuprofen sodium salt and Ibuprofen free acid form over the range 200 cm^{-1} to 1500 cm^{-1} .

Figure 5.28 presents the Raman spectra (Spectral region 700 to 1500 cm^{-1}) of all tablet ingredients. Sodium phosphate dibasic (NPD) and stearic acid (SA) spectra showed a minimum interference with the Ibuprofen sodium and free acid spectra in 1250 cm^{-1} region. As a result, the absence of 1250 cm^{-1} peak (black arrow) can be used to track Ibuprofen salt disproportionation in the formulation (E) and formulation (H) dissolution experiments. However, microcrystalline cellulose (MCC) had a high fluorescence background that obscured the Ibuprofen sodium small peak at 1250 cm^{-1} spectral region [336]. As a result, the larger peak at 800 to 850 cm^{-1} region (Dashed black box) was used instead. The transformation of the single large peak into two sharp peaks was followed to track salt disproportionation in the formulation (G) during dissolution.

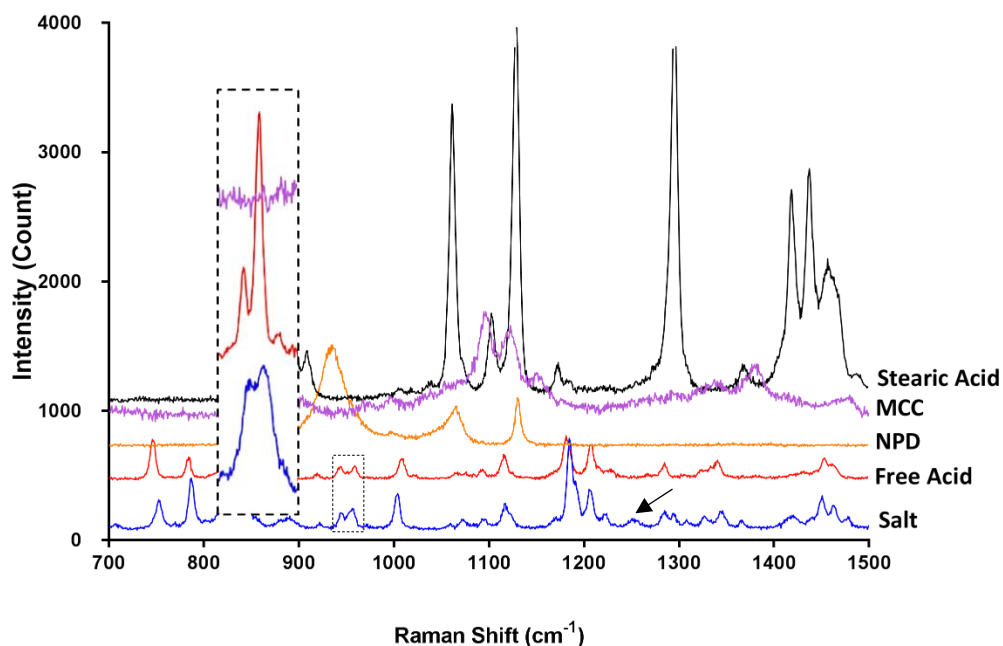


Figure 5.28: Raman spectra of Ibuprofen sodium salt, Ibuprofen free acid and excipients used in formulations over the range 700 cm^{-1} to 1500 cm^{-1} .

5.4.2.2. Dissolution Experiments

5.4.2.2.1. The Effect of the Buffer pH

First, the dissolution behaviour of Ibuprofen salt in acidic and basic environments was investigated using pure drug salt tablets. This type of experiments was used to discriminate the role of excipients in inducing or preventing salt disproportionation from the buffer effect.

Sarveiya *et al.* reported that the pH_{max} of Ibuprofen sodium is 6.9-7.0 [274]. Therefore, at pH values around or above 7.0, the salt is expected to be the most stable species, whereas the free base form will be more stable below pH 7.0. The acidic environment may lead to the conversion of the salt into the free acid, whereas the basic buffer may favour the salt dissolution.

Pure Ibuprofen Sodium Tablet-Acidic Buffer:

Averaged Raman spectra of the pure salt tablet in the acidic buffer are presented in Figure 5.29. Raman data showed that the spectrum changed after 15 min (Figure 5.29, 15 min). The single peak at 1250 cm^{-1} disappeared in addition to the conversion of the double peak at 1280 to 1300 cm^{-1} region into a single peak at 1280 cm^{-1} . The spectra collected between 15 and 60 min showed a strong correlation with Ibuprofen free acid spectrum. It is likely that the acidic pH below the pH_{max} of the salt increased the supersaturation concentration of the unionised form in the solution. This high supersaturation led to the precipitation of the free acid form to reach equilibrium. The fine-suspended Ibuprofen free acid particle blocked the flow-cell after 60 min. The experiment was stopped after obtaining the 60 min Raman map spectra.

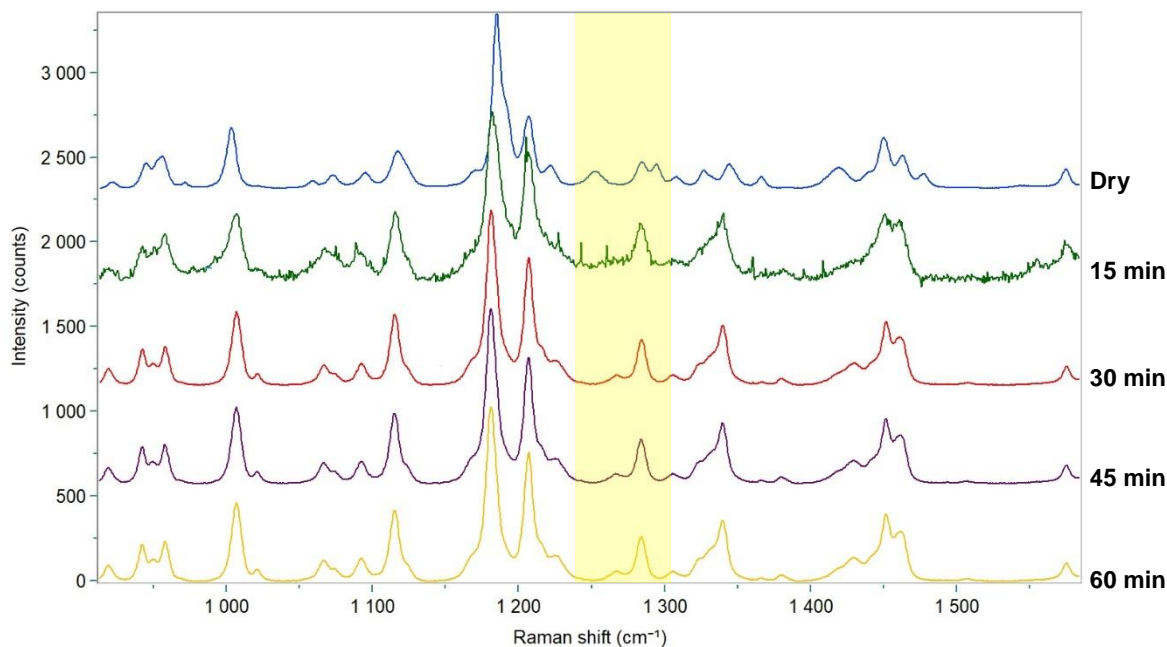


Figure 5.29: Averaged Raman spectra (900 to 1600 cm^{-1}) of the dissolution of the pure Ibuprofen sodium tablet in the acidic buffer. Y-axis offsets were applied for presentational purposes.

The MCR and CLS model were both used to spatially and spectrally visualise the salt conversion to the free form during dissolution in acidic pH (Figure 5.30). Starting with the MCR, two components were required to deconvolute the mapped data. The white/red colours

represent areas where a phase is present at its maximum, whereas the black/blue colours indicate areas where it is present at its minimum. Comparison of the MCR loadings with reference spectra clearly shows that the data have been resolved into components, which correlate with Ibuprofen sodium salt (MCR2) and Ibuprofen free acid (MCR1).

The images in Figure 5.30-(a) show the behaviour of the tablet every 15 min for the duration of the experiment. The results confirmed that there was a rapid formation of free acid form after the acidic medium contacted the tablet. A complete conversion of the map area to the free acid form occurred after 30 min of the start of the dissolution experiment. The concentration maps generated by CLS in Figure 5.30-(b) are significantly in agreement with the MCR-ALS maps. The dominance of the free acid form (red) was observed after 30 min.

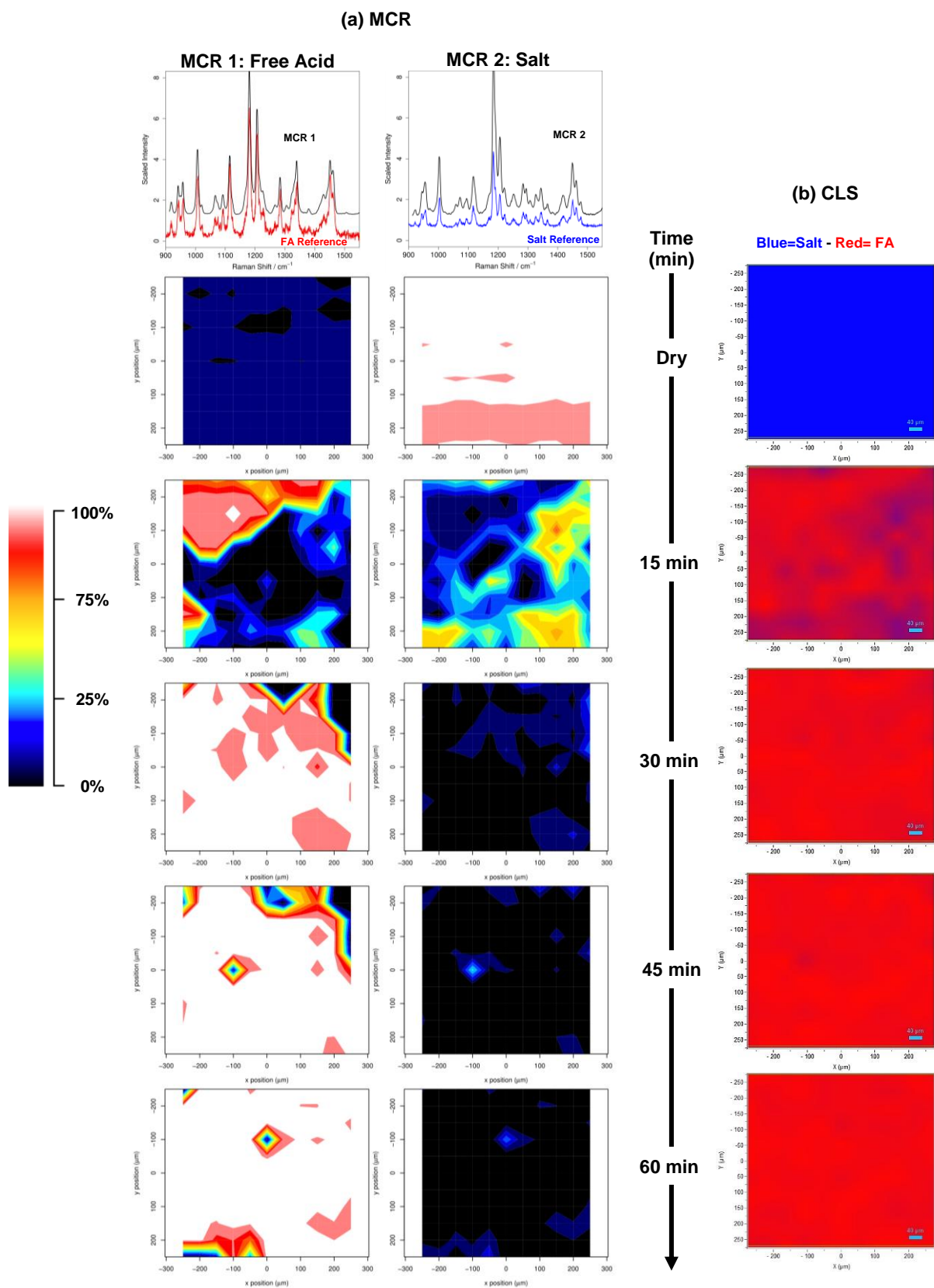


Figure 5.30: Raman maps of the pure Ibuprofen sodium tablet during dissolution in the acidic buffer as a function of time, generated by (a) MCR analysis (b) CLS analysis.

Pure Ibuprofen Sodium Tablet-Basic Buffer:

Figure 5.31 shows the averaged Raman spectra of the pure salt tablet in the basic buffer. The experiment lasted 15 min before most of the tablet dissolved. No good signal to noise Raman spectrum was obtained after 15 min. This can be explained by the high solubility (100 mg/ml) of the Ibuprofen sodium in basic medium [337].

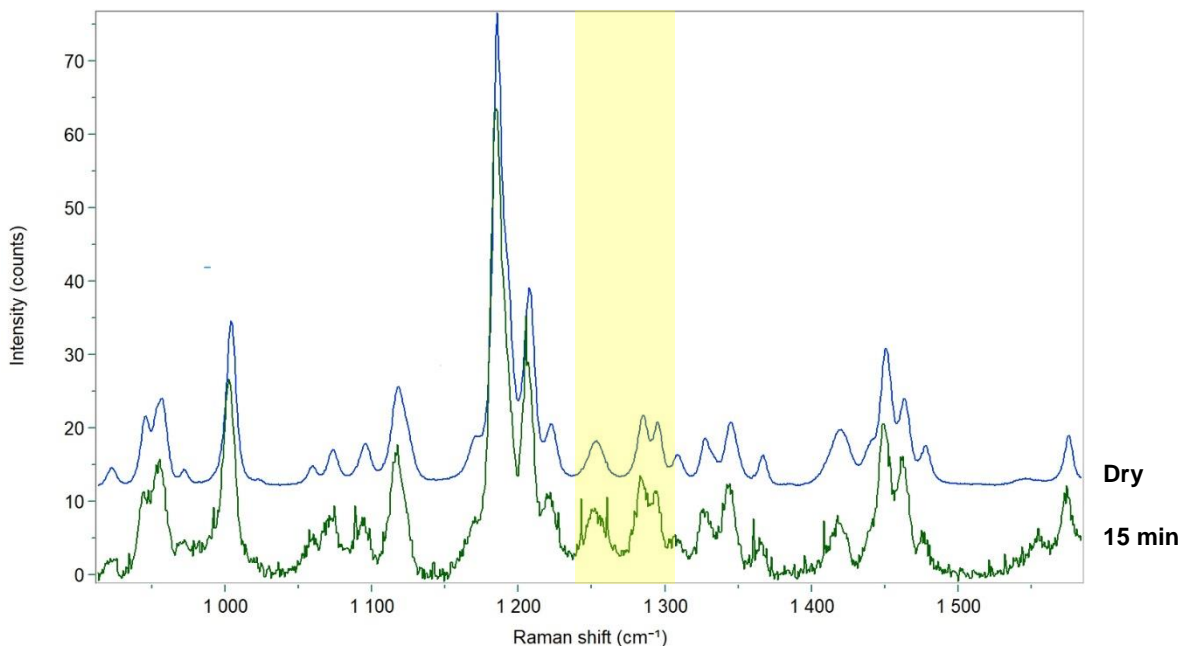


Figure 5.31: Averaged Raman spectra (900 to 1600 cm^{-1}) of the dissolution of the pure Ibuprofen sodium tablet in the basic buffer. Y-axis offsets were applied for presentational purposes.

Examination of the data did not reveal any change in the spectra acquired at time= 15 min. The single peak at 1250 cm^{-1} was preserved until the whole tablet dissolved. The Raman data essentially showed that when the pH is higher than the pH_{max} of the drug, the free acid did not form, and the drug remained as the more soluble sodium salt.

The results of the MCR and CLS analysis are presented graphically in Figure 5.32. Spectra of the two components resolved by MCR analysis. However, the two components correlate to the salt spectra. Both components demonstrate the single peak at 1250 cm^{-1} . The second component (MCR2) is the salt spectra with the background noise generated due to the tablet dissolution.

There was no spectroscopic evidence of conversion from the salt to the free acid form during this experiment in any of the measured data. This result is confirmed by the information in the CLS maps showing the dominance of the salt form (Blue colour) in all the maps.

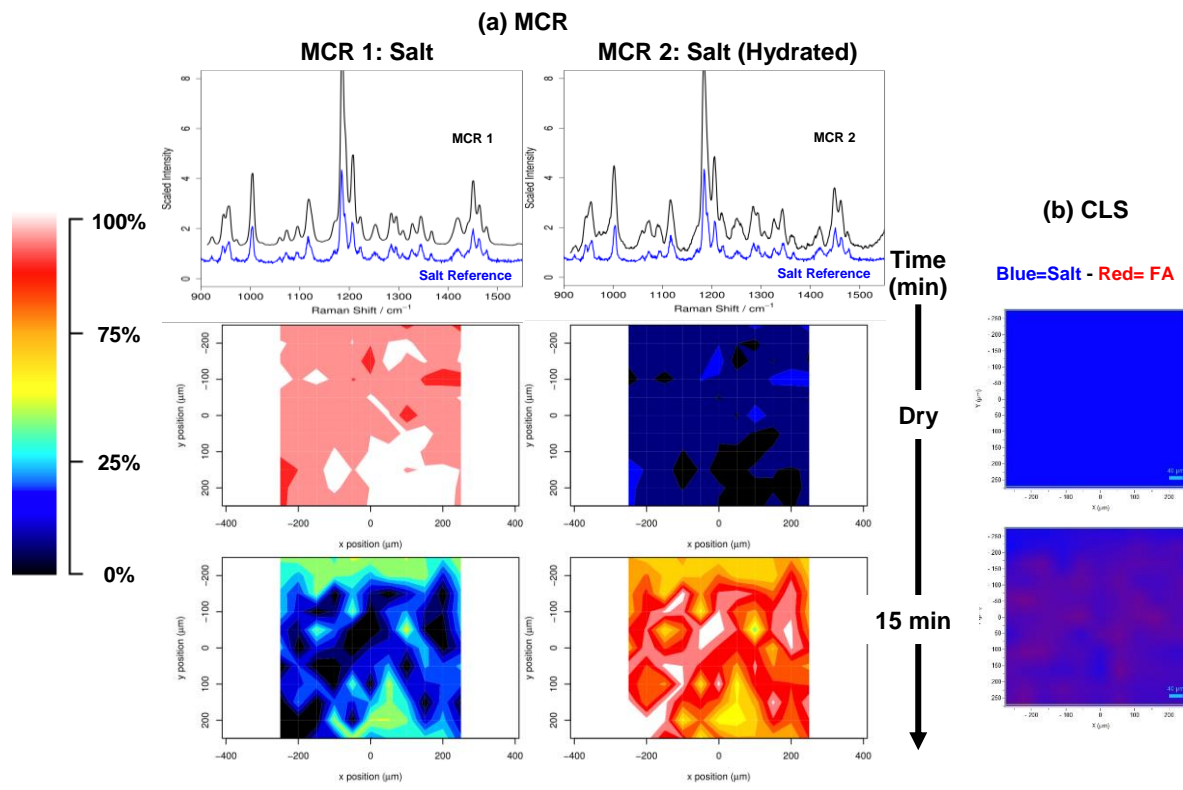


Figure 5.32: Raman maps of the pure Ibuprofen sodium tablet during dissolution in the basic buffer as a function of time, generated by (a) MCR analysis (b) CLS analysis.

5.4.2.2.2. The Effect of the Excipients

Similar to the Pioglitazone HCl experiments (Section 5.4.1.2.2), the excipient's effect on salt disproportionation was investigated in this section. Some of the excipients that used typically in Ibuprofen sodium formulation may change the microenvironment pH inside the tablet matrix, which could induce or suppress salt disproportionation depending on the pH_{max} of the drug salt and the pK_a of the excipient.

In this section, Ibuprofen sodium was formulated with a different type of excipients, which possess different physicochemical properties and role in tablet formulation. The results in this

section will be compared to the results obtained in section 5.4.2.2.1 (The Effect of the Buffer pH). Therefore, any changes in the drug salt stability will be influenced by the excipient, not the buffer used.

5.4.2.2.2.1. Formulation E-Ibuprofen Sodium: Sodium Phosphate

Dibasic

Sodium phosphate dibasic (NPD) is a buffering agent that is frequently used in pharmaceutical formulations, primarily to modulate the microenvironment pH and to control the drug release from the solid dosage forms [244], [314]. Sodium phosphate dibasic possess high alkalinity (pH= 9.1), which can be used as an effective tool to elevate the microenvironment pH above the pH_{max} of the salt and preserve the salt form disproportionation during dissolution [338], [339]. Therefore, Ibuprofen sodium was formulated with sodium phosphate dibasic to prevent the conversion to the free form during dissolution in acidic medium. The weight ratio (Ibu Na: NPD - 70:30 w/w) was generally adapted from a previous study that used pH modifiers in tablet formulations [329].

Formulation E: Acidic Buffer: Dissolution of formulation (E) tablet in acidic buffer was investigated. Reduction of the salt disproportionation during dissolution was expected due to the role of sodium phosphate dibasic in elevating the microenvironment pH above the pH_{max} of salt. Averaged Raman spectra of formulation (E) tablet in the acidic buffer are presented in Figure 5.33. Raman data showed rapid changes in the spectrum after 15 min. The absence of 1250 cm^{-1} peak supports the formation of the free acid. The addition of sodium phosphate dibasic did not reduce or prevent the salt disproportionation in the acidic medium. Sodium phosphate dibasic is highly soluble in water (NPD solubility is 1 part in 8 parts of water for sodium phosphate dibasic [244]).

Therefore, sodium phosphate dibasic leached out rapidly from the tablet matrix, resulting in lowering microenvironmental pH values and thus leading to the disproportionation of the sodium salt. Riis *et al.* reported similar effects using high soluble basic pH modifier [340].

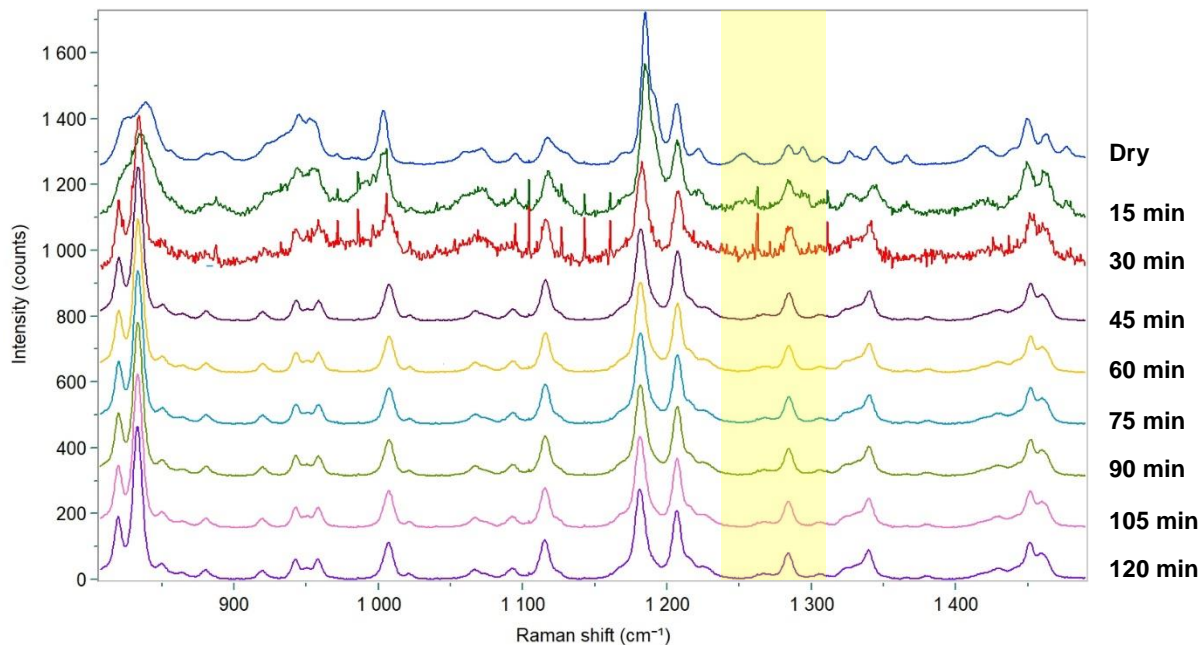


Figure 5.33: Averaged Raman spectra (800 to 1500 cm^{-1}) of the dissolution of formulation E (Ibu Na: NPD) tablet in the acidic buffer. Y-axis offsets were applied for presentational purposes.

For the MCR analysis, the data have been resolved into three components, which agree remarkably well with Ibuprofen sodium salt (MCR1), Ibuprofen free acid (MCR2) and sodium phosphate dibasic (MCR3) as shown Figure 5.34. The third components (MCR3) represent the NPD spectrum in addition to some peaks from the ibuprofen spectrum and background noise. The data show a complete conversion to free acid after 30 min. Similarly, CLS data showed the domination of the free acid form over the tablet map at 15 min after the beginning of the dissolution (Figure 5.35). A similar trend was seen in the pure Ibuprofen sodium tablet during dissolution in acidic media (Section 5.4.2.2.1).

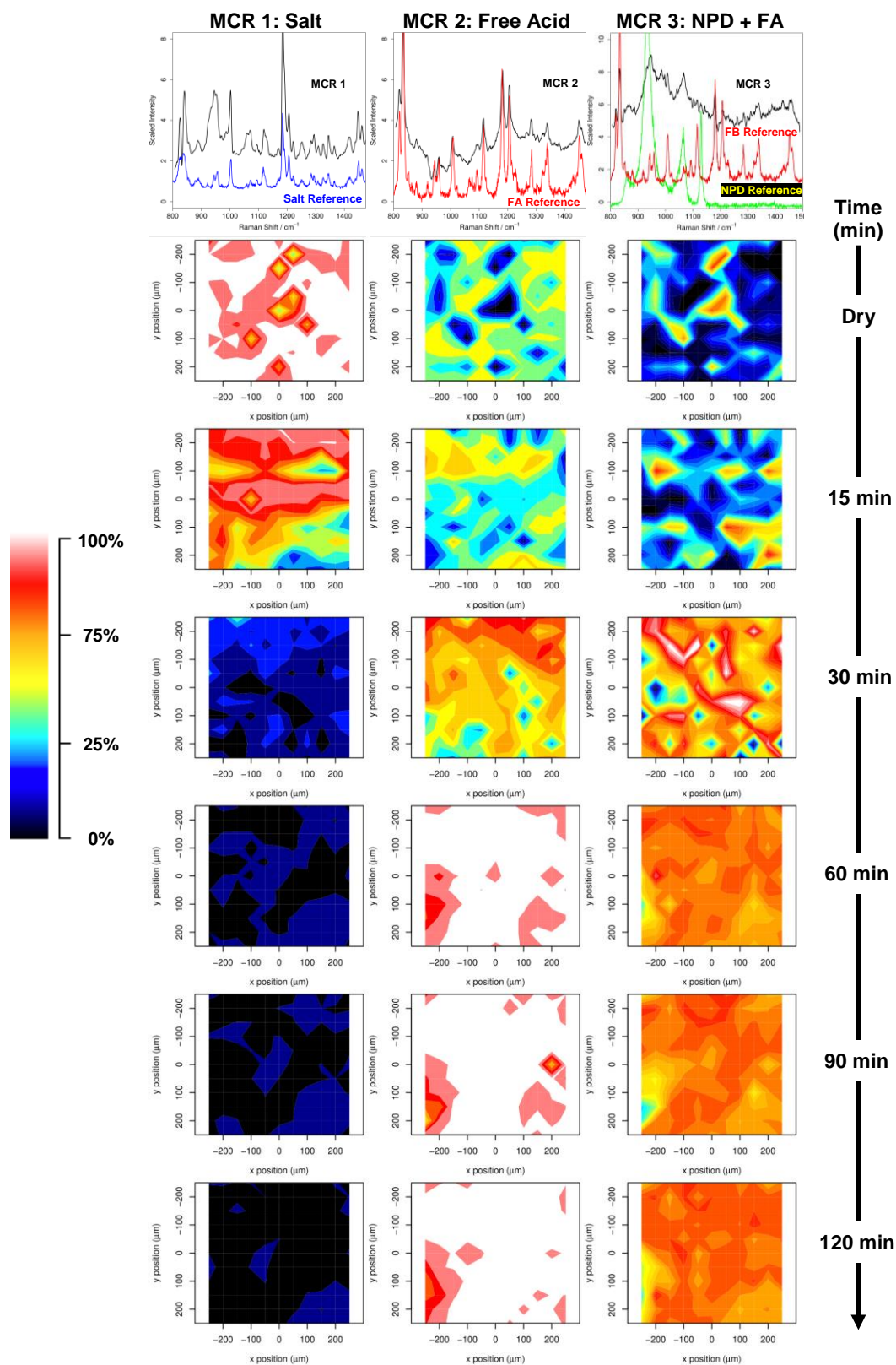


Figure 5.34: Raman maps of formulation E (Ibu Na: NPD) tablet during dissolution in the acidic buffer as a function of time, generated by MCR analysis.

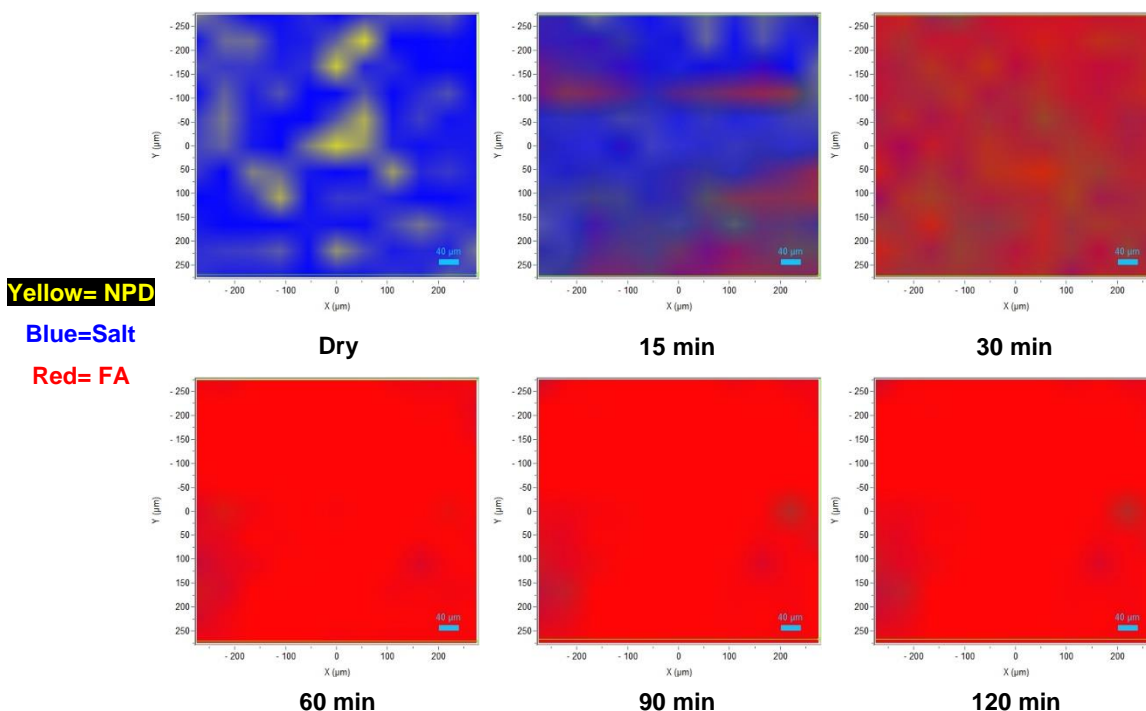


Figure 5.35: Raman maps of formulation E (Ibu Na: NPD) tablet during dissolution in the acidic buffer as a function of time, generated by CLS analysis.

Formulation E: Basic Buffer: Average Raman spectra (Figure B.7 - Appendix B) and the MCR and CLS maps (Figure B.8 - Appendix B) are shown the stable dissolution of the salt drug in the basic medium. No salt disproportionation was detected throughout dissolution. The experiment lasted 30 min before the complete dissolution of most of the tablet. No good signal to noise Raman spectrum can be obtained after 30 min.

5.4.2.2.2. Formulation G-Ibuprofen sodium: Microcrystalline

Cellulose

Microcrystalline cellulose (MCC) is primarily used as a binder/diluent in oral tablet prepared by direct compression. In addition, MCC has some lubricant and disintegrant properties [244]. The FDA approved Ibuprofen sodium tablet, Advil[®], contains MCC as one of the excipients used in the formulation [296]. As a result, Ibuprofen sodium was formulated with MCC to study

the stability of the salt tablet during dissolution in the acidic and basic medium. According to the ingredient's percentage used in Advil[®] formula, microcrystalline cellulose makes up about 40-50% of the total tablet weight while the ibuprofen sodium salt makes the other 50%. Therefore, 50:50% weight ratio (Ibu Na: MCC) was used in the tablet formulation.

Formulation G- Acidic pH:

Averaged Raman spectra of formulation (G) tablet in the acidic buffer are presented in Figure 5.36. Raman data showed a rapid change in the spectrum immediately after the dissolution started. The single peak of the Ibuprofen salt at 800 to 850 cm^{-1} region converted into two sharp peaks, which support the formation of the free acid. Mixing the Ibuprofen sodium salt with MCC did not improve the salt stability in an acidic environment.

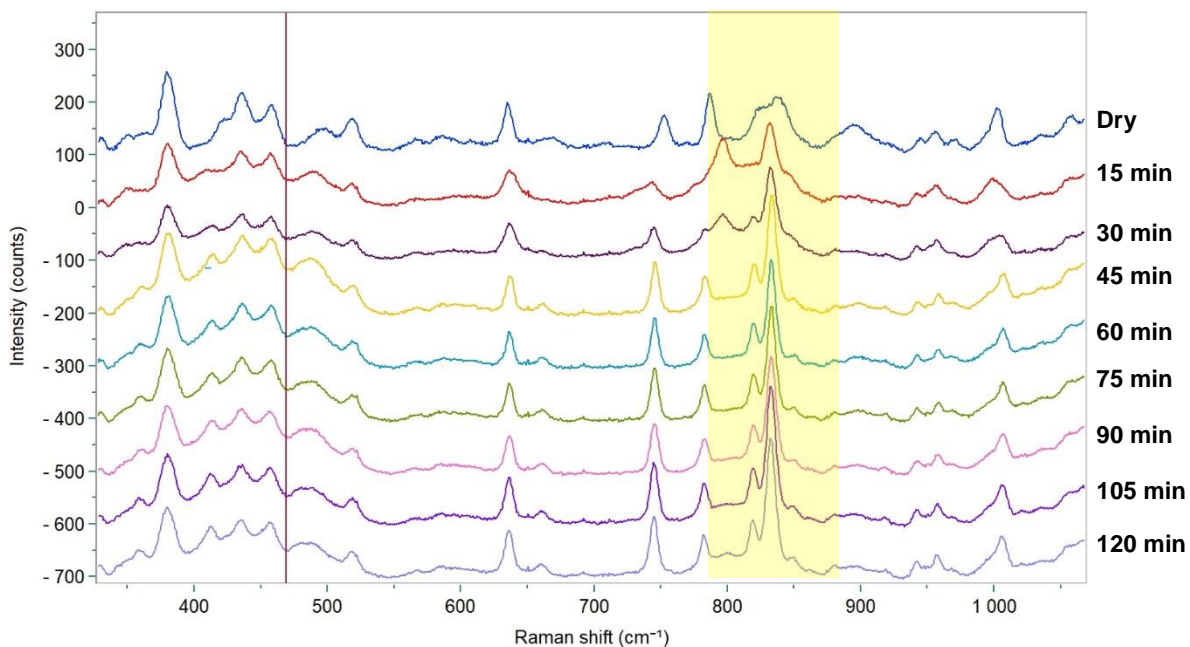


Figure 5.36: Averaged Raman spectra (400 to 1100 cm^{-1}) of the dissolution of the formulation G (Ibu Na: MCC) tablet in the acidic buffer. Y-axis offsets were applied for presentational purposes.

The MCR model was used to spatially and spectrally visualise the components distribution in the tablet and track the salt conversion to the free form during dissolution in acidic pH (Figure 5.37). Three components were applied to deconvolute the mapped data. The first and the third

components can be associated with the salt and the free acid, respectively. MCR 2 mostly correlate to the microcrystalline cellulose (MCC). It can be observed that the Ibuprofen sodium and MCC content were homogeneously dispersed through the surface of the tablet before being immersed in the dissolution medium. Once the dissolution experiment started, a gradual increase in the amount of the free acid (MCR3) was observed whereas the salt amount decreased and the MCC amount remained nearly the same. The rate of the disproportionation in the formulation (G) was slower than that of the pure salt tablet (Section 5.4.2.2.1). Complete salt conversion to the free base supported by the absence of the 1250 cm^{-1} peak was shown in the pure Ibuprofen sodium tablet after 30 min (Section 5.4.2.2.1-Figure 5.30). Formulation (G) showed gradual conversion to the free acid supported by the presence of a significant agglomerate of the remaining salt on the surface of the scanned area after 30 min.

It is likely that the role of the microcrystalline cellulose as a binding agent in tablets resulted in decrease the dissolution rate of the salt [341]. As a result, the time to reach the high supersaturation concentration was prolonged, which delayed the free acid precipitation induction time [341]. This effect can be valuable to prevent or slow down salt disproportionation, by providing the opportunity for the drug to escape precipitation long enough to be absorbed. The CLS results follow similar trends as MCR analysis. A mixture of the MCC (yellow colour) and Ibuprofen free acid was covering the mapped area after 60 min. (Figure B.9 - Appendix B).

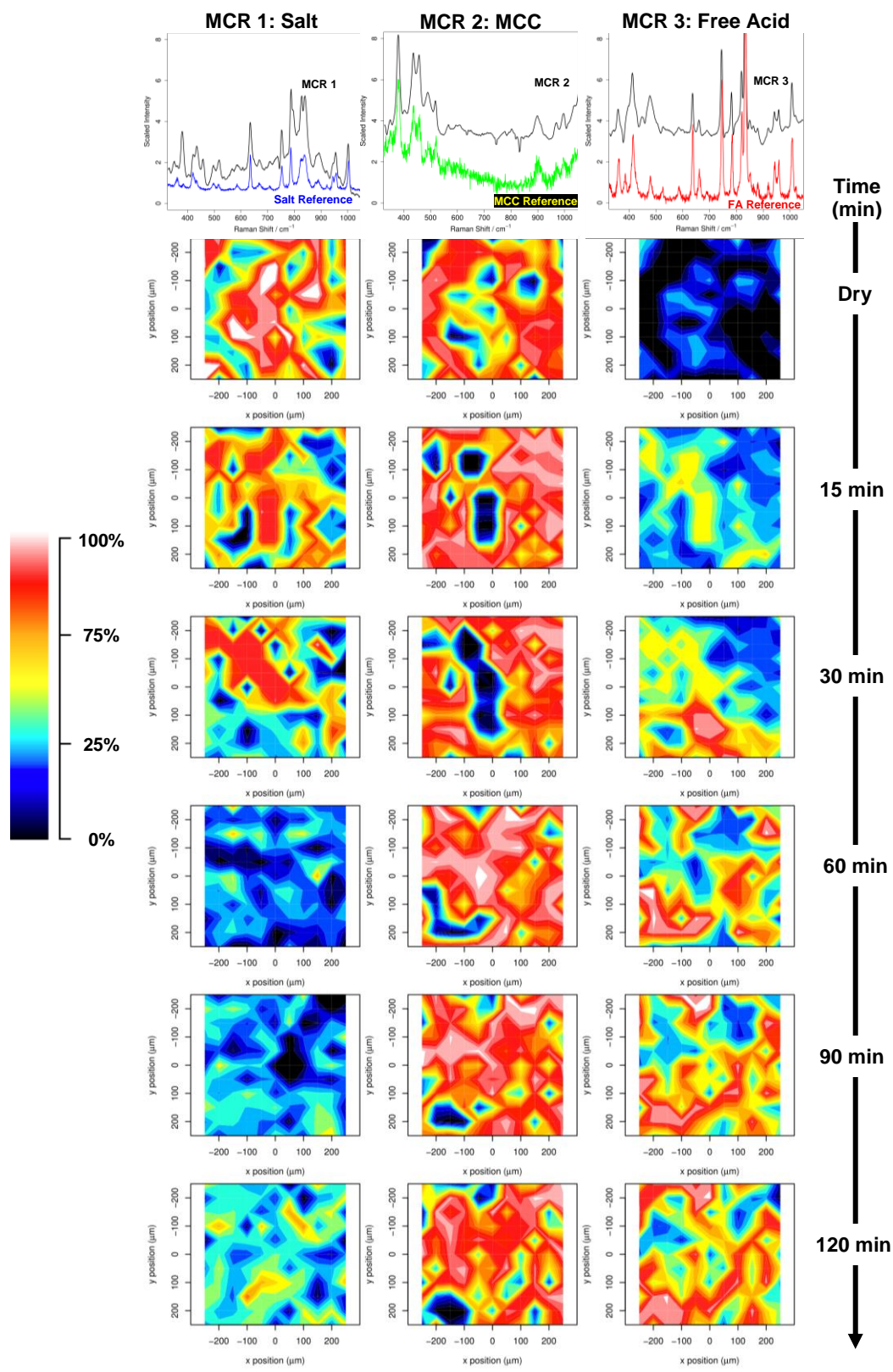


Figure 5.37: Raman maps of the formulation G (Ibu Na: MCC) tablet during dissolution in the acidic buffer as a function of time, generated by MCR analysis.

Formulation G- Basic pH:

The Average Raman spectra (Figure B.10 - Appendix B), MCR maps and CLS maps (Figure B.11 - Appendix B) did not reveal any significant changes in the spectra across the entire period of the dissolution experiment (0 to 120 min). The large peak at 800 to 850 cm^{-1} region was preserved throughout the whole dissolution test. This was expected to happen as the dissolution medium, and the MCC pKa are compatible with the pH_{max} of Ibuprofen sodium. Formulation G tablet maintained its shape until the end of the dissolution experiment (time=120 min), while the pure salt tablet disintegrated entirely after only 15 min (Section 5.4.2.2.1, Figure 5.31 and Figure 5.32). This highlights the binding properties of the MCC that can hold the formulation components together and keep the tablet intact [244].

5.4.2.2.3. Formulation H-Ibuprofen Sodium: Stearic Acid

Stearic acid (SA) is a saturated fatty acid that is used principally as a lubricant in tablet manufacturing [244]. It is practically insoluble in water, therefore only a small concentration (0.25- 5.0 % w/w) is added to the formulation to not interfere with the drug release.

Stearic acid is used in Ibuprofen sodium tablet (Advil™) as a lubricant. However, the measured pH for stearic acid is around (3.4) which is below the pH_{max} of Ibuprofen sodium. The addition of stearic acid in the tablet formulation may induce Ibuprofen sodium salt disproportionation during manufacturing and dissolution. Therefore, Ibuprofen sodium was formulated with stearic acid to investigate the stability of the salt tablet during dissolution in the acidic and basic medium. Ibuprofen sodium salt was mixed with stearic acid at 9:1 w/w ratio, which is the in the same range of what being used in Advil™ formulation [296].

Formulation H- Acidic pH: The effect of stearic acid on the salt disproportionation of Ibuprofen sodium salt during dissolution in acidic medium was investigated. Averaged Raman spectra of formulation (H) tablet in the acidic buffer are presented in Figure 5.38. Raman data showed that after 15 min the 1250 cm^{-1} peak disappeared, which indicates the rapid formation of Ibuprofen free acid spectrum. This quick conversion to the free acid is similar to the one seen in the pure Ibuprofen sodium tablet dissolved in the acidic media (Section 5.4.2.2.1).

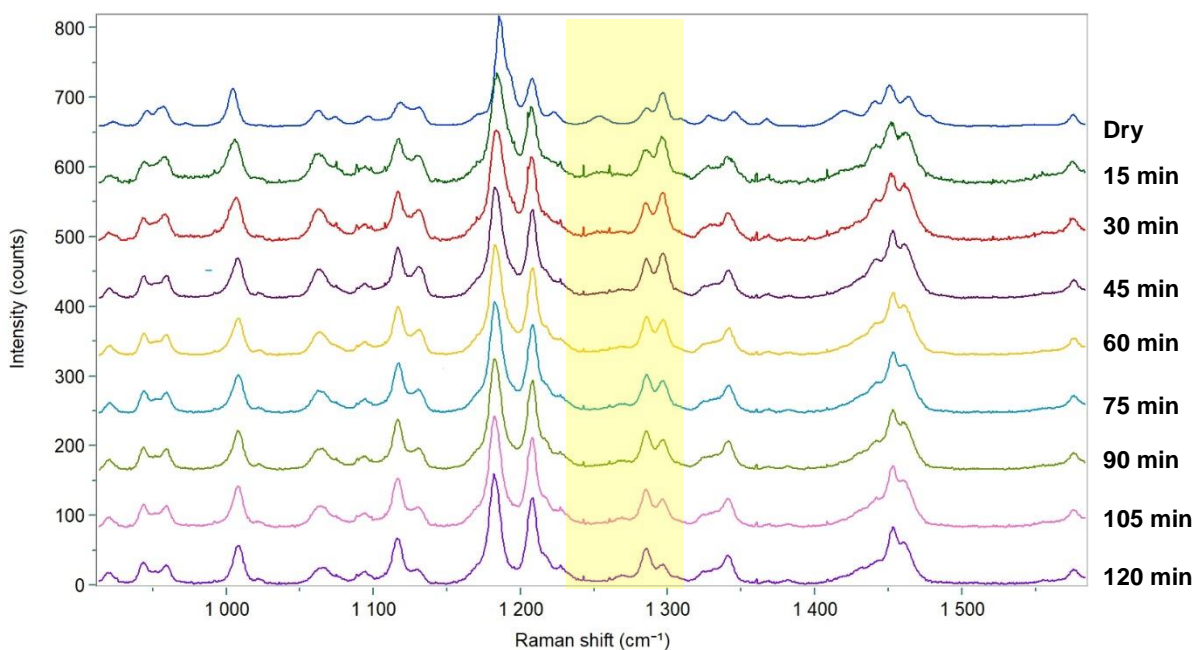


Figure 5.38: Averaged Raman spectra (900 to 1600 cm^{-1}) of the dissolution of formulation H (Ibu Na: SA) tablet in the acidic buffer. Y-axis offsets were applied for presentational purposes.

Three components were applied to deconvolute the mapped data in MCR analysis (Figure 5.39). The first and the third components can be associated with the salt and the free acid, respectively. The second components mostly correlate to the stearic acid. In MCR2 (i.e. stearic acid), very distinct, narrow sharp peaks at 1062 cm^{-1} , 1097 cm^{-1} , 1128 cm^{-1} and 1296 cm^{-1} are observed. The peaks, specifically at 1062 , 1097 , and 1128 cm^{-1} can be allocated to C-C stretching in a hydrocarbon chain and the 1296 cm^{-1} to in-plane scissoring movements (bending) of CH_2 [334]. Some peaks related to Ibuprofen sodium can be found in the second component as well.

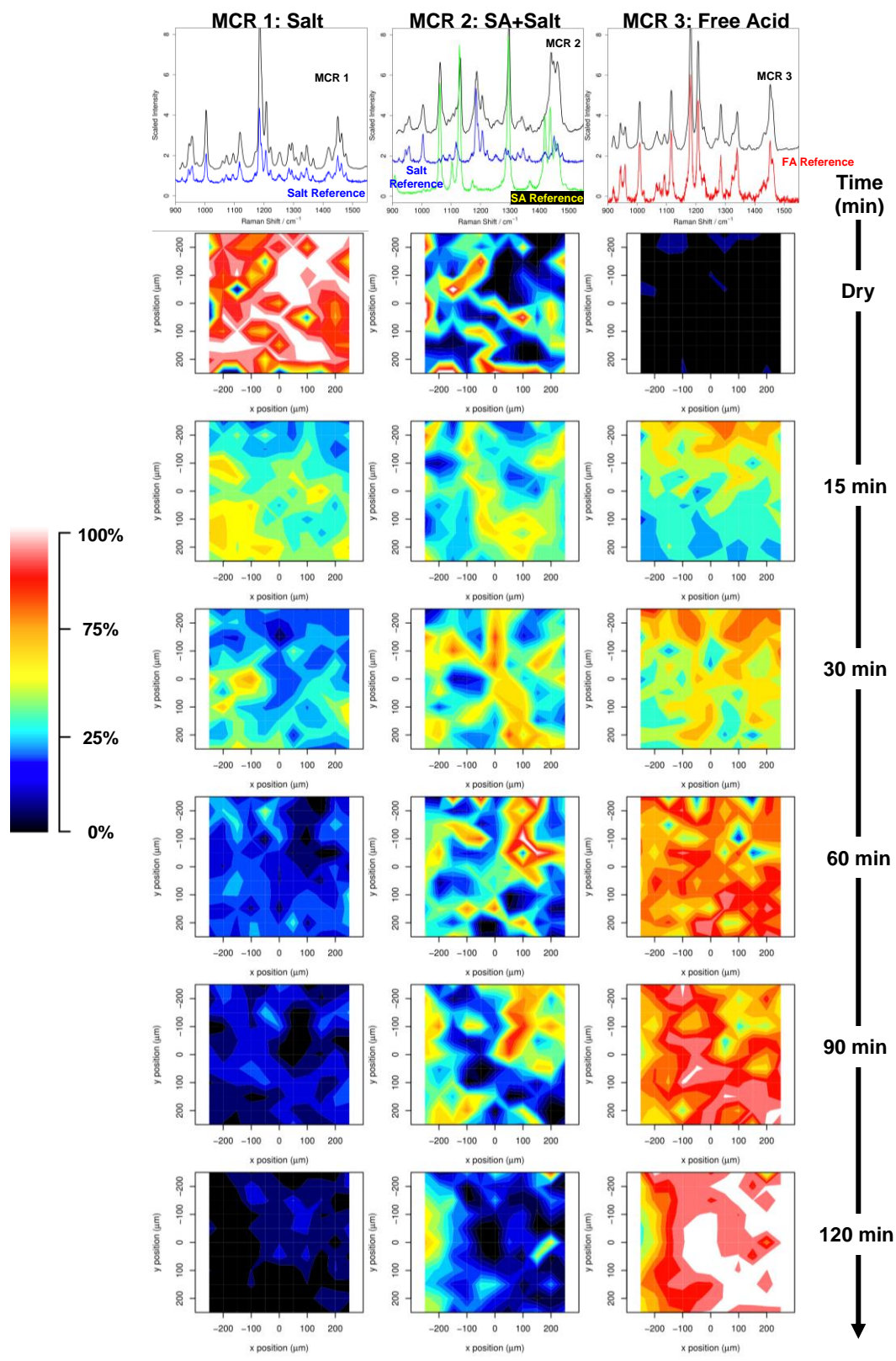


Figure 5.39: Raman maps of the formulation H (Ibu Na: SA) tablet during dissolution in the acidic buffer as a function of time, generated by MCR analysis.

The scores' plots show that the Ibuprofen sodium salt (MCR1) is presented in a high concentration in the tablet before being immersed in the dissolution medium. In addition, stearic acid (MCR2) is distributed across the tablet surface (Figure 5.39, Dry). After introducing the acidic dissolution medium, a gradual conversion of the salt to the free acid can be observed after 15 min. A full conversion to the free acid was observed at the 60 min map. The CLS maps are showing similar disproportionation kinetics to the MCR analysis with full conversion of the mapped area to the free acid at time = 60 min (Figure B.12 - Appendix B). The results did not confirm the role of stearic acid in changing the disproportionation kinetics comparison to the pure Ibuprofen sodium tablet (Section 5.4.2.2.1).

Formulation H- Basic pH: Figure 5.40 presents the averaged Raman spectra of formulation (H) tablet in the basic buffer. The Raman spectrum of the dry tablet showed a high correlation to the salt spectrum. However, the spectrum obtained after 15 min showed a very low signal to noise, which made it hard to interpret or compare with reference spectra. This was due to the rapid dissolution of the tablet, which made the correction of the z-axis very challenging. However, the spectra obtained at 30 min and 60 min showed strong sharp peaks at 1062, 1128 and 1296 cm^{-1} , which correlate well with the stearic acid spectra. It is likely that the ibuprofen sodium leached out the formulation (H) tablet rapidly (15 min) leaving only the water-insoluble excipient in the flow-cell.

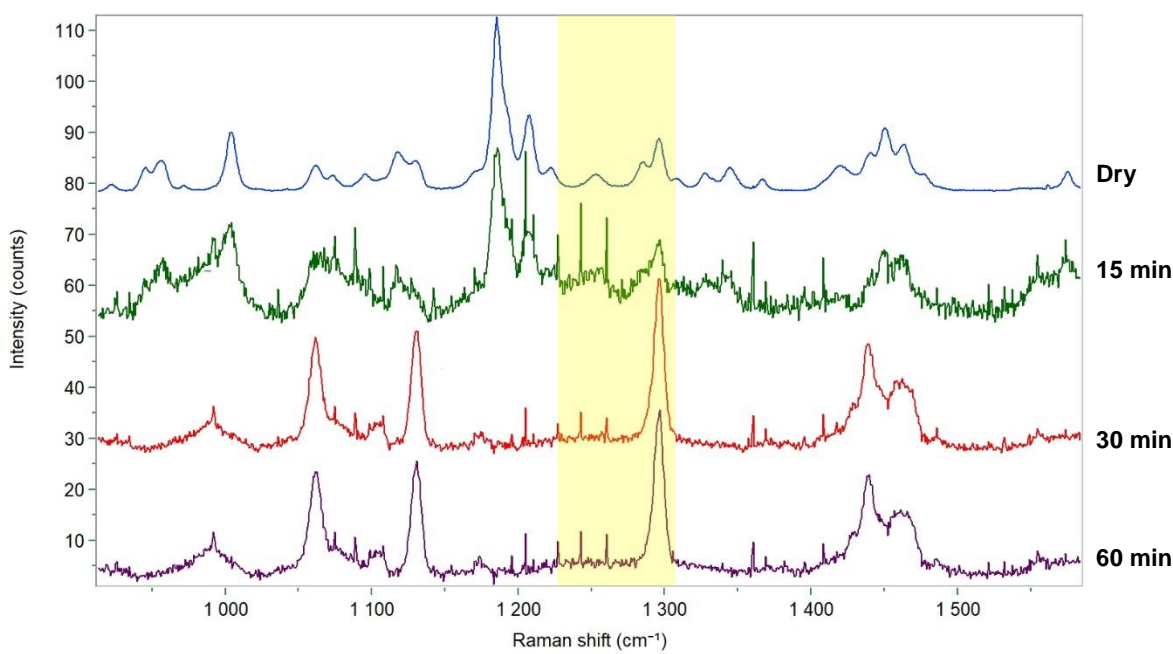


Figure 5.40: Averaged Raman spectra (900 to 1600 cm^{-1}) of the dissolution of formulation H (Ibu Na: SA) tablet in the basic buffer. Y-axis offsets were applied for presentational purposes.

The results of the MCR and CLS analysis are presented graphically in Figure 5.41. In the MCR analysis, trial runs indicated that a suitable choice for a number of components was two. The first component shows the small peak at 1250 cm^{-1} , which is correlated to the salt spectra. The second component shows multiple sharp peaks, which is associated with the stearic acid spectra. The MCR maps show no spectra related to the salt after 15 min. The 30 min and 60 min maps show only the stearic acid in the mapped area. CLS displays a black map after 15 min, which indicates that CLS could not correlate the spectra of the maps to any of the pure components' spectra. The results obtained did not show any role of the stearic acid to induce salt disproportionation. The insolubility of the stearic acid in the dissolution medium may explain the inability of the excipient to lower the microenvironment pH below the pH_{max} of the salt to induce salt disproportionation.

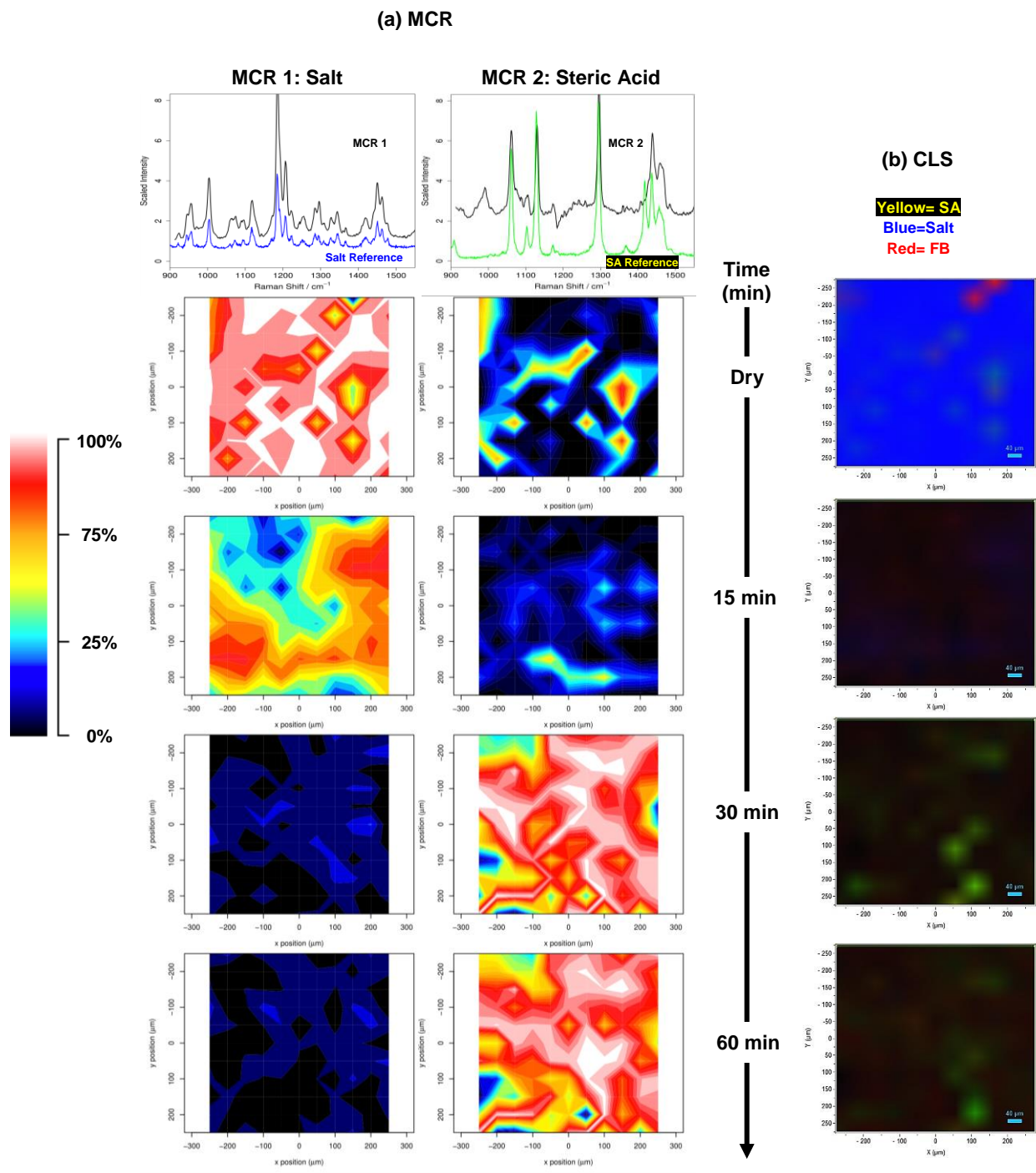


Figure 5.41: Raman maps of the formulation H (Ibu Na: SA) tablet during dissolution in the basic buffer as a function of time, generated by (a) MCR analysis and (b) CLS.

5.4.2.2.2.4. Dissolution Profile: Ultraviolet-Visible Data

The integration of the UV-Vis spectroscopy to the Raman spectroscopy dissolution flow system as a complementary technique is highly advantageous. The drug release measured by the UV-Vis can provide more information about the tablet performance during dissolution and the role of excipients in changing the dissolution profile by inducing or preventing salt disproportionation in tablets. Bearing this in mind, the UV-Vis data becomes more critical when the tablet disintegrates rapidly during dissolution, which reduces the chance to obtain good quality Raman maps. As a result, the dissolution profiles of Ibuprofen sodium released from pure drug salt, formulation (E), formulation (G) and formulation (H) tablet were obtained in parallel with the flow-cell experiment in acidic and basic dissolution.

By using the equation of the trend line from the calibration plot (Figure B.13 - Appendix B), the amount of Ibuprofen sodium released from tablets in the acidic and basic medium was determined as shown in Figure 5.42 and Figure 5.43, respectively.

Figure 5.42 presented the dissolution profile for the different formulations in acidic buffer. All tablets showed a low drug release (3.0 – 8.0%), which reflect the low tablet solubility in acidic medium. Ibuprofen sodium only tablet (Blue line) showed a fast increase in the concentration in 30 min after, which the equilibrium solubility reached (~ 6.0% drug release). A similar trend was seen in the dissolution of the formulation E tablet (Ibu Na: NPD). However, the drug release percentage was slightly higher than that of the drug only tablet (~ 8.0%). Then a slow and steady increase in the concentration was noticed until the end of the experiment. This confirms the ability of sodium phosphate dibasic to raise the microenvironment pH and enhance Ibuprofen sodium solubility in the acidic medium. The effect of sodium phosphate dibasic could not be seen from the Raman map of the tablet surface which shows a rapid formation of the free acid (Section

5.4.2.2.2.1, Acidic Buffer). Formulation G (Ibu Na: MCC) exhibited a slow dissolution rate of the Ibuprofen sodium, where it reaches around 6.0% drug release at 120 min. The slow drug release increased the time needed to reach the high supersaturation concentration in the tablet microenvironment, which allowed the drug to escape precipitation (i.e. recrystallisation to the free acid) long enough to reach the bulk medium. The Raman images of formulation G (Section 5.4.2.2.2.2, Acidic buffer) further support the UV dissolution profiles, thus confirming that the slow salt disproportionation rate was due to the MCC binding effect in slowing the drug release. Finally, formulation H (Ibu Na: SA) showed the lowest drug release, which can be related to poor wettability of the tablet due to the hydrophobic nature of the stearic acid.

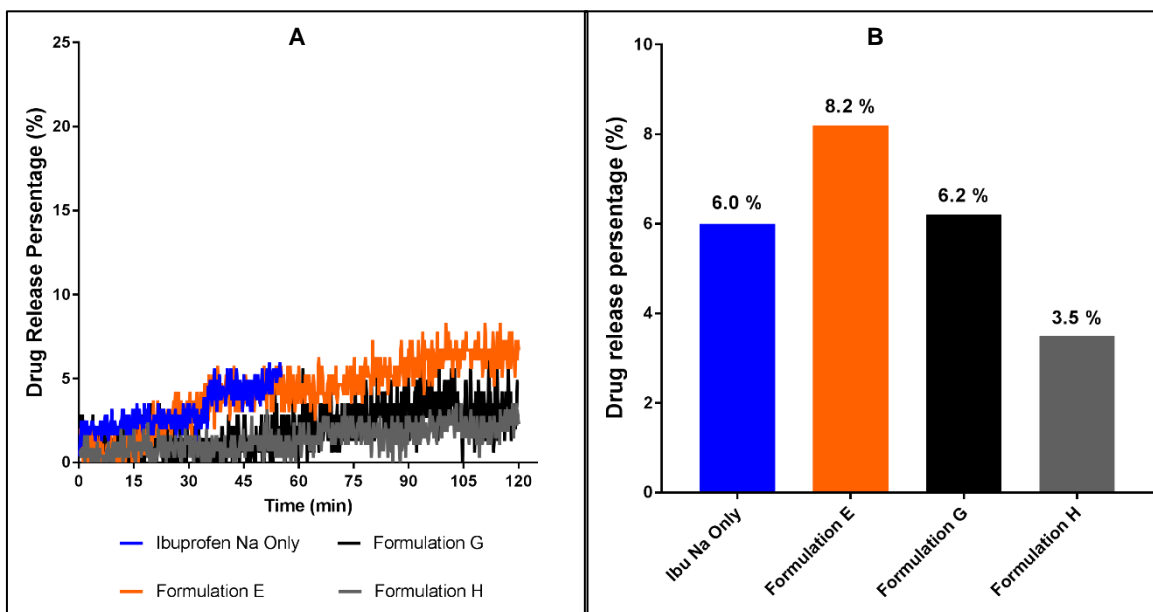


Figure 5.42: (A) Dissolution profiles obtained using UV-Vis detection that presents the percentage of Ibuprofen released from the tablet as a function of time for the pure drug and different formulation tablets studied in the acidic medium. (B) The maximum drug release percentage.

The drug release profiles of Ibuprofen sodium tablets (Drug only and formulation E, G, and H) in alkaline dissolution medium are graphically illustrated in Figure 5.45. Drug release was rapid and complete from tablets containing Ibuprofen sodium only and sodium phosphate dibasic. In contrast, formulation G tablet (Ibu Na: MCC) showed slower drug release from the matrix over the time of the study. The slower drug release is likely due to the high amount of MCC (50%),

which when tableted produced slightly harder tablets [342]. Tablet hardness can influence the rate at which water infuses into the tablet matrix and thus how rapidly the drug releases from the system [342]. Formulation H tablet (Ibu Na: SA) showed similar dissolution profiles to formulation G tablet, with approximately 96% of the drug released after 60 minutes. The UV-vis drug release data are in good agreement with the Raman map, which showed a rapid and complete release of Ibuprofen sodium salt in the basic medium without any conversion of the salt to the free acid.

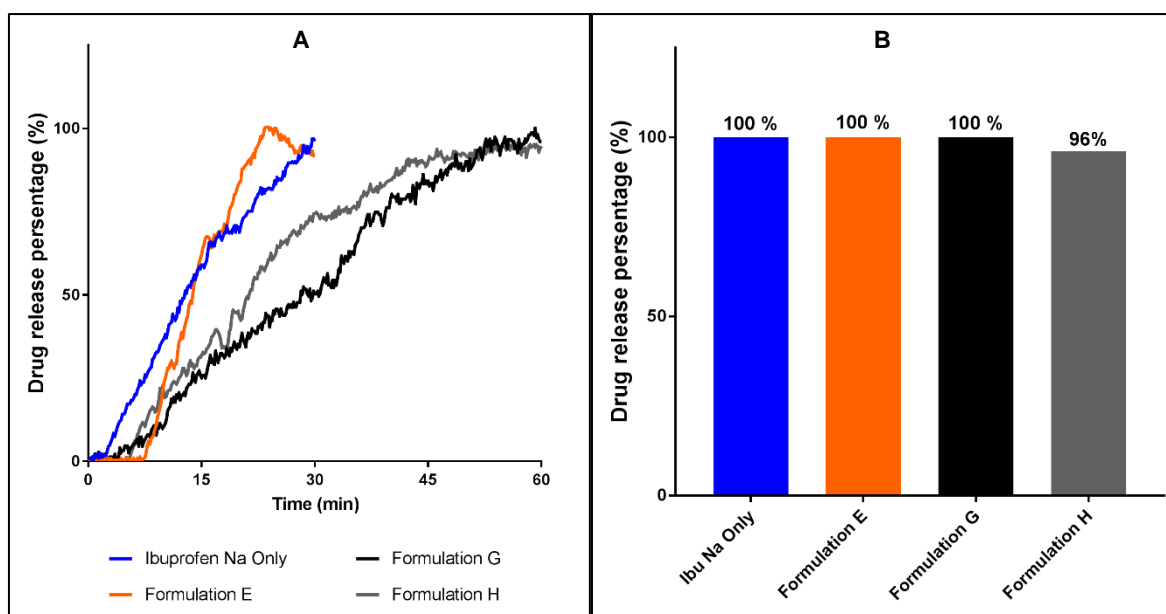


Figure 5.43: (A) Dissolution profiles obtained using UV-Vis detection that presents the percentage of Ibuprofen released from the tablet as a function of time for the pure drug and different formulation tablets studied in the basic medium. (B) The maximum drug release percentage.

5.4.3. Results and Discussion Summary

In situ Raman spectroscopy in conjunction with a custom designed flow-dissolution cell were used to investigate salt disproportionation during the course of the dissolution experiment. In-line UV-Vis spectroscopy was used in parallel with Raman spectroscopy as a complementary analytical technique that allows the changes in drug release from the tablet (monitored by the UV-Vis) to be directly related to physicochemical changes that occur in the tablet matrix to the salt.

For weak basic drug salt, Pioglitazone HCl, dissolution medium with pH higher than the pH_{max} of the salt led to the conversion of the salt to the free base form, whereas acidic dissolution medium ($pH < pH_{max}$) promoted stable salt dissolution. The effect of excipients in inducing or preventing salt disproportionation was investigated by mixing Pioglitazone HCl with citric acid (formulation A), lactose monohydrate (formulation B) and magnesium stearate (formulation C). Both lactose monohydrate and magnesium stearate induced salt disproportionation in the tablet during dissolution in acidic medium. These results highlighted the main role of excipients in controlling the microenvironment pH and its detrimental effect on drug in-vitro performance. The tablets recovered from the dissolution test were cross-sectioned using ultramicrotome for further analysis using Raman spectroscopy. The Raman maps showed the formation of a thin layer of the free base around the edges of the tablet, which slowed the ingress of water into the tablet matrix and stopped the drug release into the dissolution medium as revealed from the UV-vis drug release data.

Ibuprofen sodium (weak acid drug) tablets exhibited complete tablet disintegration and dissolution in the basic medium as shown from the Raman and UV-vis data. No salt disproportionation was detected in ibuprofen sodium tablet during dissolution in alkaline

medium ($\text{pH} > \text{pH}_{\text{max}}$). Decrease the dissolution medium pH to 1.2 ($\text{pH} < \text{pH}_{\text{max}}$) resulted in ibuprofen sodium salt disproportionation to the free acid and significantly decreased the drug release in the dissolution medium. Ibuprofen sodium formulation excipients demonstrated a small effect on delaying the salt disproportionation (formulation G and formulation H) in the tablets or increasing the drug dissolution in acidic medium (formulation E).

5.5. Conclusion:

In this chapter, the salt disproportionation during the dissolution of two model drug salt, Pioglitazone HCl and Ibuprofen sodium, tablets were tested as a function of both the pH of the dissolution medium and the excipient's type. Raman spectroscopy was employed to detect any chemical changes that produced the undesirable free form of the drug in the solid form during the dissolution and directly related it to the change in the concentration of drug in solution measured by in-line UV-vis. Drug salt only tablets and formulated tablets that contained a binary mixture of the API salt and the excipients were investigated at pH 1.2 to mimic the stomach conditions and pH 6.8 to simulate the duodenum conditions.

For Pioglitazone HCl tablets at acidic pH ($\text{pH} < \text{pH}_{\text{max}}$), the Raman imaging data was able to reveal that salt conversion to the free base did not occur significantly in pure drug salt and tablets containing citric acid. Moreover, introducing citric acid as acidic pH modifiers (i.e. acidifiers) into the tablet formulation can bring additional benefits to retard the disproportionation of Pioglitazone HCl during the tablet manufacturing and enhance the drug solubility in the acidic dissolution medium. Tablets containing basic excipients such as lactose monohydrate and magnesium stearate showed salt disproportionation to the free base during dissolution. The ability of basic excipients, such as magnesium stearate to induce salt disproportionation, has been reported previously in non- acidic buffered environment. However, this is the first time an excipient-induced salt disproportionation during dissolution has been reported of a salt of a weakly basic drug formulated with a basic excipient in an acidic dissolution environment. These results are indicating the main role of the microenvironment pH and the vital role of excipients in changing it. At basic pH, Pioglitazone HCl salt from converted to the free base form in all tablets as the pH of the base was well above the pH_{max} of the drug. The Raman mapping

of the cross-sectioned tablets reveals the formation of a shell consisting of the free base around the edge of the tablet. This shell decreased the rate of penetration of the dissolution medium into the tablet significantly. This structural change had implications on the release of the API into the surrounding solution shown by the UV-Vis drug release data.

Ibuprofen sodium tablets demonstrated salt disproportionation during dissolution in acidic pH medium. In contrast, high drug release of the sodium salt into the basic medium was observed, and the Raman spectroscopy detected no chemical changes. The addition of the basic pH modifiers to the ibuprofen sodium formulation did not significantly improve the salt stability in the acidic environment. Lower solubility and stronger basic excipients can be used instead to protect the salt from disproportionation during dissolution in acidic medium.

For all the Raman maps generated, the excellent peak to peak correlation between loadings and reference spectra supports the utility of MCR as a statistical method to analyse spatial-temporal Raman data. The CLS method confirmed the MCR data, showing the validity of both methods to study similar systems.

Finally, utilisation of Raman ultraviolet-visible flow cell System has proven to be a useful technique for the investigation of problematic multicomponent pharmaceutical formulations where disproportionation of the API salt occurs. The data collected from this flow cell system can enhance our understanding of the role of different factors, such as excipient properties, in inducing salt chemical changes during dissolution. Ultimately, these discoveries can help mitigate the disproportionation of API salt in tablets during dissolution, which allows pharmaceutical scientists to develop more reliable products with improved drug stability.

Chapter6: Conclusions and Future Works

6.1. Summary:

The work of this thesis aimed to employ simple, fast and *in-situ* analytical techniques to investigate the effect of moisture, pH and formulation excipients on salt disproportionation in multicomponent solid dosage forms during storage and dissolution. The experimental work in this research was split into three main sections:

- 1- Chapter 3: exploring the capabilities and limitations of advanced analytical techniques in a complex model system.
- 2- Chapter 4: investigating salt disproportionation in the presence of excipients at high relative humidity using *in-situ* optical screening technique.
- 3- Chapter 5: the application of real-time Raman spectroscopy to study salt disproportionation in multicomponent tablet during dissolution.

In Chapter 3, a wide range of state-of-the-art advanced analytical techniques (TEM, SEM, EDX, Raman spectroscopy, ToF-SIMS and super-resolution fluorescence microscopy) were explored using silica nanoparticle in PVC electrospun fibre hybrids as a challenging, complex multicomponent model system. The geometrical, chemical and surface properties of fabricated particle-fibre hybrids were characterised using scanning electron microscopy (SEM), transmission electron microscopy (TEM), energy-dispersive X-ray (EDX) spectroscopy, Raman Spectroscopy and time of flight secondary ion mass spectrometry (ToF-SIMS). Having characterised the particle-fibre hybrids, the potential application of using immobilised fluorescent silica nanoparticles in electrospun fibres as a calibration tool for instrument performance testing in super-resolution fluorescence microscopy was investigated.

Size-tunable silica particles were produced, with diameters ranging from 20 to 650 nm, by optimising the amount of each reactant and catalyst required for particle synthesis. Fabrication of different particle-fibre hybrid morphologies was achieved by changing the silica particle size and concentration in the electrospun fibres. TEM was found to be a particularly efficient method to investigate the particle-fibre hybrid's morphology and image the encapsulated particles in electrospun fibres. EDX was able to identify the main elements of particle-fibre hybrids, while Raman spectroscopy provided the chemical composition of the blackberry-like hybrid structures. ToF-SIMS analysis of the hybrids indicated the complete surface coverage of the polyvinyl chloride (PVC) polymer indicating that the silica nanoparticles were completely encapsulated within the polymer fibres.

The feasibility of using fluorescent particle-fibre hybrids as a new tool for validating and testing super-resolution fluorescence microscopy was investigated. The results suggested that fluorescent particle-fibre hybrids served as a convenient and effective calibration tool by incorporating fluorescent nanoparticles into a confined geometry. The versatility and flexibility in the design of particle-fibre hybrids microscopy standards make them suitable for the broad variety of emerging super-resolution microscopy methods compared to the existing calibration methods.

In Chapters 4 and 5, salt disproportionation of two salt model systems, Pioglitazone HCl (weak base - $pK_a=5.2$) and Ibuprofen sodium (weak acid - $pK_a=4.4$) was investigated as a function of different formulation excipients during storage and dissolution.

The aim of Chapter 4 was to investigate the effect of excipients on salt disproportionation in binary mixtures at high humidity as part of a drug-excipient compatibility study using a simple, fast and online analytical technique. *In-situ* optical screening equipped with controlled humidity

chamber was used for monitoring salt disproportionation by tracking the changes in the salt crystal morphology mixed with specific excipients at high relative humidity.

Salt conversion to the undesirable free form of the drug was tracked by monitoring the change in the crystal shape from plate-like structures to the needle-like structures using *in-situ* optical microscopy. Raman spectroscopy analysis obtained from the needle crystals confirmed the formation of the free form. Alkaline excipients such as lactose monohydrate, calcium phosphate dibasic, magnesium stearate, sodium phosphate dibasic and sodium stearyl fumarate elevated the microenvironment pH above the pH_{max} of the salt investigated. This increase in the microenvironment pH led to the conversion of Pioglitazone HCl to the free base, whereas the opposite effect (salt stabilisation) was seen in the Ibuprofen sodium salt. Acidic excipients such as citric acid and ascorbic acid both showed the ability to lower the microenvironment pH below the pH_{max} of the salts. Such decreases in the microenvironment pH led to the conversion of Ibuprofen sodium to the free acid, whereas salt stabilisation was seen in the Pioglitazone HCl case study.

In addition, the optical microscopy imaging method successfully showed the behaviour of some excipients such as disintegrant (swelling due to water absorption), controlled release polymer (HPMC precipitation inhibitor) and lubricant (hydrophobic nature) and their effect on salt stability and the onset of the salt disproportionation. The onset and extent of the salt disproportionation were found to be highly dependent on the salt pH_{max} , and excipient measured pH, while other excipient physical properties such as solubility, hydrophobicity and hygroscopicity also played a role. The *in-situ* optical microscopy technique can provide both fast results and good predictions of drug salt-excipients compatibility at an early stage of drug development, which can be a highly valuable tool to be used as part of the accelerated stability studies. The information

obtained from the *in-situ* optical microscopy set-up can play a critical role in providing a comprehensive understanding of drug stability and possible drug-excipient interactions necessary for product approval and enable rational control strategies to assure final product stability.

In Chapter 5, the disproportionation of drug salt occurring during dissolution was investigated *in-situ* using Raman microscopy combined with an ultraviolet-visible flow cell system. The effect of dissolution medium pH and various excipients on the stability and drug release of tablets containing a formulation of the drug salt and a specific excipient were studied. Here, Raman spectroscopic mapping in conjunction with a custom designed flow-dissolution set-up was used as the primary analytical technique to assess the behaviour of the salt during dissolution experiments. In-line ultraviolet-visible (UV-Vis) spectroscopy was used in parallel with Raman spectroscopy as a complementary analytical technique that allows the changes in drug release from the tablet (monitored by UV-Vis) to be directly related to physicochemical changes that occur in the tablet matrix.

For Pioglitazone HCl tablets, complete conversion of the salt form to the free base form was observed in the Raman imaging data for all the formulations when an alkaline dissolution medium (pH=6.8) was used. However, in acidic medium (pH=1.2), the Raman imaging data demonstrated insignificant salt conversion to the free base for tablets of pure drug salt and formulations containing citric acid. Tablets containing basic excipients such as lactose monohydrate and magnesium stearate showed salt disproportionation to the free base during dissolution in the acidic medium due to the role of those excipients in elevating the microenvironment pH above the pH_{max} of Pioglitazone HCl. The Raman mapping of tablets cross-sections revealed the formation of a shell of the free base around the edge of the tablet when the dissolution medium pH was alkaline or formulated with magnesium stearate. The free base

layer slowed the dissolution medium ingress into the tablet significantly, which had negative implications for the release of the API into the surrounding solution shown by the UV-Vis. In Ibuprofen sodium tablets, salt disproportionation was detected during dissolution in acidic pH medium. In contrast, fast drug release of the sodium salt was observed in the basic medium, and no chemical changes were detected using Raman spectroscopy.

The results showed the vital role of dissolution medium pH and the microenvironment pH (controlled by the formulation excipients) in inducing or preventing salt disproportionation. This is the first time, to the best of our knowledge, that *in-situ* analytical technique such as Raman imaging has been used to study the effect of excipient in inducing or preventing salt disproportionation during dissolution. The chemical specificity and drug release profiles collected using Raman-UV vis flow cell system can enhance the understanding of salt disproportionation and dynamic dissolution behaviour of the drug salt formulated with different excipients. This ultimately will result in the mitigation of disproportionation during tablet dissolution and the production of more reliable products.

In summary, a number of advanced analytical techniques were assessed and explored in this thesis to investigate different pharmaceutical formulations. Analytical techniques such as optical screening and Raman spectroscopy, which can be applied *in situ*, in-line and in an automated manner, were successfully utilised to reveal valuable information about the behaviour of API salts at high humidity and during dissolution. From the data generated it was possible to postulate some potential explanations regarding the effects of drug properties such as pH_{max} , excipient properties (microenvironment pH, solubility, hydrophobicity) and the environment condition (ex; humidity and dissolution medium pH) on the stability and dissolution performance of drug salts.

6.2. Future Work

It is hoped that this work can be a useful platform for the application of advanced analytical technologies to assess pharmaceutical systems in the future. Investigations of salt formulations in real-time can aid formulators in predicting the instability of the drug salt and identifying formulation strategies to mitigate salt disproportionation at early stages of drug development, which can establish the methods investigated in this work as reliable techniques for industrial applications.

Potential continuations of the work presented in this thesis for future investigations are summarised in the following points:

1. In Chapter 3, the potential application of the particle-fibre hybrids as a new technology for calibrating super-resolution fluorescence microscopy can be explored further. The physicochemical properties and photostability can be investigated to assess the performance and stability of the particle-fibre hybrids containing fluorescent nanoparticles. In addition, benchmarking against other competing assays such as fluorescent nanobeads (hiq-nano™) [343], fluorescent polystyrene microsphere (FocalCheck™) [344] and DNA origami nanoruler (Gattaquant™) [345], can be studied to further develop the particle-fibre hybrid technology in term of ease of preparation and use, shelf-life and measurement precision.
2. In Chapter 4, the *in-situ* optical microscopy imaging system equipped with a controlled humidity chamber has proven to be a simple and efficient technique for drug-excipient compatibility studies. A possible future strategy is to integrate additional analytical techniques, such as Raman spectroscopy, with the optical

microscopy imaging system in order to probe chemical information of the drug-excipient mixture and chemically track any salt transformation to the free form. In addition, the effect of changing the other environmental conditions such as temperature on salt stability can be investigated using the optical imaging system.

3. In Chapter 5, pH modifier excipients such as citric acid and sodium phosphate dibasic were investigated as effective formulation approaches to minimise the salt disproportionation during manufacturing and dissolution. The rapid solubility of both pH modifiers used in this study failed to control the microenvironment pH and stabilise the salt. Therefore, replacing the citric acid with lower solubility excipients such as fumaric acid may prevent rapid depletion of pH modifiers from the hydrated tablet matrix and maintain the desired microenvironment pH during the tablet dissolution [320], [346]. Similarly, replacing sodium phosphate dibasic with high basic strength pH modifiers such as sodium carbonate or poorly water-soluble salts of strong bases such as magnesium oxide (MgO) would be expected to control the microenvironment pH effectively. Bases with low water solubility remain in the tablet matrix during drug release and therefore increase the microenvironment pH within the tablet over the entire dissolution time [340], [347]–[349]. The flow-through cell is ideal for changing the dissolution medium during the dissolution test, which can be easily accomplished by changing the input from a different source. The salt formulation tablets can be investigated in a condition that mimics the gastrointestinal tract so that in vitro-in vivo correlations can be established. This can be performed by initially introducing acidic dissolution medium to mimic the stomach conditions followed by a switch during the test to

basic pH to simulate the post-stomach conditions, to probe the effect of changing the environmental pH on the tablet dissolution and apparent salt solubility.

4. In situ advanced analytical techniques such as Raman spectroscopy and optical screening provided valuable information about the drug excipient compatibility and the mechanism of salt disproportionation at different conditions. Therefore, these techniques can be employed to investigate the reversibility of the salt disproportionation reaction in solid dosage forms when changing the storage or dissolution conditions. The ability to understand the condition at which the free form may convert back to the salt form in the presence of the suitable counterions is highly important in stability studies and drug development.
5. In this thesis, the pH of the microenvironment showed to play an important role in controlling whether the salt disproportionation is thermodynamically favoured or not. Several techniques have been proposed for the measurement of the microenvironmental pH such as a slurry method [320]. However, the indirect and the bulk measurement of pH by the slurry method can be a poor surrogate for the exact microenvironmental pH conditions at a solid surface, especially for the less soluble or less hygroscopic excipients [266], [269], [350], [351]. Therefore, pH-sensitive fluorescent nanosensors like the one developed in Chapter 3 (Section 3.4.2) can be employed to measure the microenvironment pH at the microscopic level using confocal microscopy. This strategy will provide a spatial distribution of the pH within the solid system rather than the average pH value estimated by the slurry method.

References

- [1] M. V Chaubal, "Application of formulation technologies in lead candidate selection and optimization," *Drug Discov. Today*, vol. 9, no. 14, pp. 603–609, 2004.
- [2] R. Mullin, "Tufts Study Finds Big Rise In Cost Of Drug Development," *American Chemical Society*, 2018.
- [3] J. A. DiMasi, R. W. Hansen, and H. G. Grabowski, "The price of innovation: new estimates of drug development costs," *J. Health Econ.*, vol. 22, no. 2, pp. 151–185, 2003.
- [4] S. J. F. Macdonald and P. W. Smith, "Lead optimization in 12 months? True confessions of a chemistry team," *Drug Discov. Today*, vol. 6, no. 18, pp. 947–953, 2001.
- [5] R. . Lipper, "How can we optimize selection of drug development candidates from many compounds at the discovery stage?," *Mod. Drug Discov.*, vol. 2, pp. 55–60, 1999.
- [6] J. W. Scannell, A. Blanckley, H. Boldon, and B. Warrington, "Diagnosing the decline in pharmaceutical R&D efficiency," *Nat. Rev. Drug Discov.*, vol. 11, p. 191, Mar. 2012.
- [7] F. Pammolli, L. Magazzini, and M. Riccaboni, "The productivity crisis in pharmaceutical R&D," *Nat. Rev. Drug Discov.*, vol. 10, p. 428, Jun. 2011.
- [8] N. Dimitri, "An assessment of R&D productivity in the pharmaceutical industry," *Trends Pharmacol. Sci.*, vol. 32, no. 12, pp. 683–685, 2011.
- [9] B. Munos, "Lessons from 60 years of pharmaceutical innovation," *Nat. Rev. Drug Discov.*, vol. 8, p. 959, Dec. 2009.
- [10] S. M. Paul, D. S. Mytelka, C. T. Dunwiddie, C. C. Persinger, B. H. Munos, S. R. Lindborg, and A. L. Schacht, "How to improve R&D productivity: the pharmaceutical industry's grand challenge," *Nat. Rev. Drug Discov.*, vol. 9, p. 203, Feb. 2010.
- [11] P. K. Owens, E. Raddad, J. W. Miller, J. R. Stille, K. G. Olovich, N. V Smith, R. S. Jones, and J. C. Scherer, "A decade of innovation in pharmaceutical R&D: the Chorus model," *Nat. Rev. Drug Discov.*, vol. 14, p. 17, Dec. 2014.
- [12] E. L. Andrade, A. F. Bento, J. Cavalli, S. K. Oliveira, R. C. Schwanke, J. M. Siqueira, C. S. Freitas, R. Marcon, and J. B. Calixto, "Non-clinical studies in the process of new drug development - Part II: Good laboratory practice, metabolism, pharmacokinetics, safety and dose translation to clinical studies," *Brazilian J. Med. Biol. Res.*, vol. 49, no. 12, p. e5646, Dec. 2016.
- [13] A. Jekunen, "Decision-making in product portfolios of pharmaceutical research and development – managing streams of innovation in highly regulated markets," *Drug Des. Devel. Ther.*, vol. 8, pp. 2009–2016, Oct. 2014.
- [14] C. Chuang-Stein, S. Kirby, J. French, K. Kowalski, S. Marshall, M. K. Smith, P. Bycott, and M. Beltangady, *A Quantitative Approach for Making Go/No-Go Decisions in Drug Development*, vol. 45. 2011.
- [15] C. R. Gardner, C. T. Walsh, and Ö. Almarsson, "Drugs as materials: valuing physical form in drug discovery," *Nat. Rev. Drug Discov.*, vol. 3, p. 926, Nov. 2004.
- [16] E. Tobin and B. Hirshcler, "Raising the quality and cost bar for drug makers," *Reuters Company News*, 2002.
- [17] L. Abboud and S. Hensley, "New Prescription For Drug Makers: Update the Plants," *Wall Street Journal*, 2003.
- [18] A. Mathews and S. Hensley, "FDA explores obstacles to new drugs," *Wall Street Journal*, 2004.

- [19] S. Datta and D. J. W. Grant, "Crystal structures of drugs: advances in determination, prediction and engineering," *Nat. Rev. Drug Discov.*, vol. 3, p. 42, Jan. 2004.
- [20] J. H. Lin, "Role of pharmacokinetics in the discovery and development of indinavir," *Adv. Drug Deliv. Rev.*, vol. 39, no. 1, pp. 33–49, 1999.
- [21] Abbott Laboratories, "Abbott announces difficulty manufacturing Norvir® (Ritonavir) capsules," 1998.
- [22] S. Bajaj, N. Sakhuja, D. Singla, and S. Bajaj Principal, "Stability Testing of Pharmaceutical Products," *J. Appl. Pharm. Sci.*, vol. 02, no. 2012, pp. 129–138, 2012.
- [23] S. Singh and M. Bakshi, "Guidance on Conduct of Stress Tests to Determine Inherent Stability of Drugs," *Pharm. Technol. On-line*, vol. 24, pp. 1–14, Jan. 2000.
- [24] A. S. Narang, D. Desai, and S. Badawy, "Impact of Excipient Interactions on Solid Dosage Form Stability," *Pharm. Res.*, vol. 29, no. 10, pp. 2660–2683, 2012.
- [25] J. T. Carstensen, *Drug Stability: Principles and Practices*. Dekker, 1995.
- [26] G. Zografi, "States of Water Associated with Solids," *Drug Dev. Ind. Pharm.*, vol. 14, no. 14, pp. 1905–1926, Jan. 1988.
- [27] D. Zhou and Yihong Qiu, "Understanding Drug Properties in Formulation and Process Design of Solid Oral Products," *Valid. Technol.*, pp. 74–84, 2010.
- [28] A. Heinz, C. J. Strachan, K. C. Gordon, and T. Rades, "Analysis of solid-state transformations of pharmaceutical compounds using vibrational spectroscopy," *J. Pharm. Pharmacol.*, vol. 61, no. 8, pp. 971–988, Jan. 2010.
- [29] N. K. Thakral and R. C. Kelly, "Salt disproportionation: A material science perspective," *Int. J. Pharm.*, vol. 520, no. 1–2, pp. 228–240, 2017.
- [30] J. M. Merritt, S. K. Viswanath, and G. A. Stephenson, "Implementing Quality by Design in Pharmaceutical Salt Selection : A Modeling Approach to Understanding Disproportionation," *Pharm. Res.*, vol. 30, no. 1, pp. 203–217, 2013.
- [31] B. R. Rohrs, T. J. Thamann, P. Gao, D. J. Stelzer, R. S. Chao, and et al., "Tablet dissolution affected by a moisture mediated solid state interaction between drug and disintegrant," *Pharm. Res.*, 1999.
- [32] E. A. Zannou, Q. Ji, Y. M. Joshi, and A. T. M. Serajuddin, "Stabilization of the maleate salt of a basic drug by adjustment of microenvironmental pH in solid dosage form," *Int. J. Pharm.*, vol. 337, no. 1–2, pp. 210–218, 2007.
- [33] E. F. Unger, "Weighing Benefits and Risks — The FDA's Review of Prasugrel," *N. Engl. J. Med.*, vol. 361, no. 10, pp. 942–945, Sep. 2009.
- [34] M. R. Siddiqui, Z. A. AlOthman, and N. Rahman, "Analytical techniques in pharmaceutical analysis: A review," *Arab. J. Chem.*, vol. 10, pp. S1409–S1421, 2017.
- [35] R. A. Storey and I. Ymén, *Solid State Characterization of Pharmaceuticals*. Wiley, 2011.
- [36] H. G. Brittain, *Physical Characterization of Pharmaceutical Solids*. Taylor & Francis, 1995.
- [37] T. Lipiäinen, "Stability and analysis of solid-state forms in pharmaceutical powders," University of Helsinki, 2018.
- [38] C. I. C. Crucho and M. T. Barros, "Polymeric nanoparticles: A study on the preparation variables and characterization methods," *Mater. Sci. Eng. C*, vol. 80, pp. 771–784, 2017.
- [39] N. Chieng, T. Rades, and J. Aaltonen, "An overview of recent studies on the analysis of pharmaceutical polymorphs," *J. Pharm. Biomed. Anal.*, vol. 55, no. 4, pp. 618–644, 2011.

- [40] B. O'Sullivan, P. Barrett, G. Hsiao, A. Carr, and B. Glennon, "In Situ Monitoring of Polymorphic Transitions," *Org. Process Res. Dev.*, vol. 7, no. 6, pp. 977–982, Nov. 2003.
- [41] C. R. Gardner, O. Almarsson, H. Chen, S. Morissette, M. Peterson, Z. Zhang, S. Wang, A. Lemmo, J. Gonzalez-Zugasti, J. Monagle, J. Marchionna, S. Ellis, C. McNulty, A. Johnson, D. Levinson, and M. Cima, "Application of high throughput technologies to drug substance and drug product development," *Comput. Chem. Eng.*, vol. 28, no. 6, pp. 943–953, 2004.
- [42] P. Barrett, "In-situ Monitoring of Crystallization Processes," University College Dublin, 2002.
- [43] P. T. Cardew and R. J. Davey, "The kinetics of solvent-mediated phase transformations," *Proc. R. Soc. London A Math. Phys. Eng. Sci.*, vol. 398, no. 1815, pp. 415–428, 1985.
- [44] Malvern Instruments Ltd, "Zetasizer Nano Series User Manual." p. 270, 2014.
- [45] C. M. Hoo, N. Starostin, P. West, and M. Mecartney, "A comparison of atomic force microscopy (AFM) and dynamic light scattering (DLS) methods to characterize nanoparticle size distribution," *J. Nanoparticle Res.*, vol. 10, pp. 89–96, 2008.
- [46] A. Einstein, "Zur Theorie der Brownschen Bewegung," *Ann. Phys.*, vol. 324, no. 2, pp. 371–381, Sep. 1906.
- [47] A. Willemse, "Optical measuring techniques for particulate systems at the fringes of concentration - paints and aerosols," TU Delf, 1998.
- [48] D. N. Leonard, G. W. Chandler, and S. Seraphin, "Scanning Electron Microscopy," *Characterization of Materials*. 12-Oct-2012.
- [49] L. Reimer and H. Kohl, *Transmission Electron Microscopy: Physics of Image Formation*. Springer New York, 2008.
- [50] P. D. Nellist, "Scanning Transmission Electron Microscopy BT - Science of Microscopy," P. W. Hawkes and J. C. H. Spence, Eds. New York, NY: Springer New York, 2007, pp. 65–132.
- [51] A. J. Garratt-Reed, D. C. Bell, and P. Nicholson, *Energy-dispersive X-ray analysis in the electron microscope.*, vol. 25, no. 3. Wiley-Blackwell, 2006.
- [52] M. Scimeca, S. Bischetti, H. K. Lamsira, R. Bonfiglio, and E. Bonanno, "Energy Dispersive X-ray (EDX) microanalysis: A powerful tool in biomedical research and diagnosis," *Eur. J. Histochem.*, vol. 62, no. 1, p. 2841, Jan. 2018.
- [53] J. Grams, *New Trends and Potentialities of ToF-SIMS in Surface Studies*. Nova Science Publishers, 2007.
- [54] J. C. Vickerman and D. Briggs, *ToF-SIMS: Materials Analysis by Mass Spectrometry*, 2nd Editio. IM Publications, 2013.
- [55] M. S. Algahtani, D. J. Scurr, A. L. Hook, D. G. Anderson, R. S. Langer, J. C. Burley, M. R. Alexander, and M. C. Davies, "High throughput screening for biomaterials discovery," *J. Control. Release*, vol. 190, pp. 115–126, 2014.
- [56] T. J. Barnes, I. M. Kempson, and C. A. Prestidge, "Surface analysis for compositional, chemical and structural imaging in pharmaceuticals with mass spectrometry: A ToF-SIMS perspective," *Int. J. Pharm.*, vol. 417, no. 1, pp. 61–69, 2011.
- [57] J. R. Lakowicz, *Principles of Fluorescence Spectroscopy*. Springer US, 2007.
- [58] M. Sauer, J. Hofkens, and J. Enderlein, *Handbook of Fluorescence Spectroscopy and Imaging: From Ensemble to Single Molecules*. Wiley, 2010.
- [59] B. Valeur, J. C. Brochon, and O. Wolfbeis, *New Trends in Fluorescence Spectroscopy: Applications to Chemical and Life Sciences*. Springer Science & Business Media, 2001.

- [60] M. Kasha, "Characterization of electronic transitions in complex molecules," *Discuss. Faraday Soc.*, vol. 9, no. 0, pp. 14–19, 1950.
- [61] B. Valeur and M. N. Berberan-Santos, *Molecular Fluorescence: Principles and Applications*. Wiley, 2012.
- [62] R. Han, Z. Li, Y. Fan, and Y. Jiang, "Recent Advances in Super-Resolution Fluorescence Imaging and Its Applications in Biology," *J. Genet. Genomics*, vol. 40, no. 12, pp. 583–595, 2013.
- [63] M. J. Rust, M. Bates, and X. Zhuang, "Stochastic optical reconstruction microscopy (STORM) provides sub-diffraction-limit image resolution," *Nat. Methods*, vol. 3, no. 10, pp. 793–795, Oct. 2006.
- [64] B. Huang, W. Wang, M. Bates, and X. Zhuang, "Three-Dimensional Super-Resolution Imaging by Stochastic Optical Reconstruction Microscopy," *Science (80-.)*, vol. 319, no. 5864, p. 810 LP-813, Feb. 2008.
- [65] C. V. Raman and K. S. Krishnan, "A New Type of Secondary Radiation," *Nature*, vol. 121, no. 3048, pp. 501–502, 1928.
- [66] T. De Beer, a. Burggraeve, M. Fonteyne, L. Saerens, J. P. Remon, and C. Vervaet, "Near infrared and Raman spectroscopy for the in-process monitoring of pharmaceutical production processes," *Int. J. Pharm.*, vol. 417, no. 1–2, pp. 32–47, 2011.
- [67] C. Gendrin, Y. Roggo, and C. Collet, "Pharmaceutical applications of vibrational chemical imaging and chemometrics: A review," *J. Pharm. Biomed. Anal.*, vol. 48, no. 3, pp. 533–553, 2008.
- [68] P. Larkin, *Infrared and Raman Spectroscopy: Principles and Spectral Interpretation*. Elsevier Science, 2011.
- [69] G. P. S. Smith, C. M. McGoverin, S. J. Fraser, and K. C. Gordon, "Raman imaging of drug delivery systems," *Adv. Drug Deliv. Rev.*, vol. 89, pp. 21–41, 2015.
- [70] W. Sinclair, M. Leane, G. Clarke, A. Dennis, M. Tobyn, and P. Timmins, "Physical Stability and Recrystallization Kinetics of Amorphous Ibipinabant Drug Product by Fourier Transform Raman Spectroscopy," *J. Pharm. Sci.*, vol. 100, no. 11, pp. 4687–4699, Nov. 2011.
- [71] R. Smith, K. L. Wright, and L. Ashton, "Raman spectroscopy: an evolving technique for live cell studies," *Analyst*, vol. 141, no. 12, pp. 3590–3600, 2016.
- [72] G. Reich, "Near-infrared spectroscopy and imaging: Basic principles and pharmaceutical applications," *Adv. Drug Deliv. Rev.*, vol. 57, no. 8, pp. 1109–1143, 2005.
- [73] a. a. Gowen, C. P. O'Donnell, P. J. Cullen, and S. E. J. Bell, "Recent applications of Chemical Imaging to pharmaceutical process monitoring and quality control," *Eur. J. Pharm. Biopharm.*, vol. 69, no. 1, pp. 10–22, 2008.
- [74] F. Koehler and E. Lee, "Near infrared spectroscopy: the practical chemical imaging solution," *Near Spectrosc.*, vol. 3, pp. 12–16, 2002.
- [75] S. Sasic and S. Ekins, *Pharmaceutical Applications of Raman Spectroscopy*. Wiley, 2008.
- [76] J. M. Amigo, C. Ravn, N. B. Gallagher, and R. Bro, "A comparison of a common approach to partial least squares-discriminant analysis and classical least squares in hyperspectral imaging," *Int. J. Pharm.*, vol. 373, no. 1, pp. 179–182, 2009.
- [77] L. Zhang, M. J. Henson, and S. S. Sekulic, "Multivariate data analysis for Raman imaging of a model pharmaceutical tablet," *Anal. Chim. Acta*, vol. 545, no. 2, pp. 262–278, 2005.
- [78] B. Vajna, H. Pataki, Z. Nagy, I. Farkas, and G. Marosi, "Characterization of melt extruded and conventional Isoptin formulations using Raman chemical imaging and chemometrics," *Int. J. Pharm.*, vol. 419, no. 1, pp. 107–113, 2011.
- [79] F. Krier, J. Mantanus, P.-Y. Sacré, P.-F. Chavez, J. Thiry, A. Pestieau, E. Rozet, E. Ziemons, P. Hubert, and B. Evrard, "PAT tools for the control of co-extrusion implants manufacturing process," *Int. J. Pharm.*, vol. 458,

- no. 1, pp. 15–24, 2013.
- [80] J. B. Nanubolu and J. C. Burley, “Investigating the Recrystallization Behavior of Amorphous Paracetamol by Variable Temperature Raman Studies and Surface Raman Mapping,” *Mol. Pharm.*, vol. 9, no. 6, pp. 1544–1558, Jun. 2012.
- [81] B. Vajna, G. Patyi, Z. Nagy, A. Bódis, A. Farkas, and G. Marosi, “Comparison of chemometric methods in the analysis of pharmaceuticals with hyperspectral Raman imaging,” *J. Raman Spectrosc.*, vol. 42, no. 11, pp. 1977–1986, Apr. 2011.
- [82] S. Rutan, A. de Juan, and R. Tauler, “Introduction to Multivariate Curve Resolution,” in *Comprehensive Chemometrics*, Elsevier: Oxford, 2009, pp. 249–259.
- [83] A. de Juan, S. Rutan, and R. Tauler, “Two-Way Data Analysis: Multivariate Curve Resolution - Iterative Resolution Methods,” in *Comprehensive Chemometrics*, Elsevier: Oxford, 2009, pp. 325–344.
- [84] A. de Juan, J. Jaumot, and R. Tauler, “Multivariate Curve Resolution (MCR). Solving the mixture analysis problem,” *Anal. Methods*, vol. 6, no. 14, pp. 4964–4976, 2014.
- [85] A. Malik and R. Tauler, “Chapter 4 - Ambiguities in Multivariate Curve Resolution,” in *Resolving Spectral Mixtures*, vol. 30, C. Ruckebusch, Ed. Elsevier, 2016, pp. 101–133.
- [86] R. Sengupta, S. Chakraborty, S. Bandyopadhyay, S. Dasgupta, R. Mukhopadhyay, K. Auddy, and a S. Deuri, “Impact of Electrospinning Process Parameters on the Measured Current and Fiber Diameter,” *Engineering*, vol. 47, pp. 21–25, 2007.
- [87] A. Formhals, “Process and apparatus for preparing artificial threads,” 1,975,504, 1934.
- [88] P. K. Baumgarten, “Electrostatic spinning of acrylic microfibers,” *J. Colloid Interface Sci.*, vol. 36, no. 1, pp. 71–79, 1971.
- [89] G. Taylor, “Disintegration of Water Drops in an Electric Field,” *Proc. R. Soc. London A Math. Phys. Eng. Sci.*, vol. 280, no. 1382, pp. 383–397, 1964.
- [90] D. H. Reneker, A. L. Yarin, H. Fong, and S. Koombhongse, “Bending instability of electrically charged liquid jets of polymer solutions in electrospinning,” *J. Appl. Phys.*, vol. 87, no. 9, pp. 4531–4547, 2000.
- [91] G. C. Rutledge and S. V. Fridrikh, “Formation of fibers by electrospinning,” *Adv. Drug Deliv. Rev.*, vol. 59, no. 14, pp. 1384–1391, 2007.
- [92] N. Bhardwaj and S. C. Kundu, “Electrospinning: A fascinating fiber fabrication technique,” *Biotechnol. Adv.*, vol. 28, no. 3, pp. 325–347, 2010.
- [93] J. Doshi and D. H. Reneker, “Electrospinning process and applications of electrospun fibers,” *J. Electrostat.*, vol. 35, no. 2, pp. 151–160, 1995.
- [94] H. Fong, I. Chun, and D. H. Reneker, “Beaded nanofibers formed during electrospinning,” *Polymer (Guildf.)*, vol. 40, no. 16, pp. 4585–4592, 1999.
- [95] D. H. R. and I. Chun, “Nanometre diameter fibres of polymer, produced by electrospinning,” *Nanotechnology*, vol. 7, no. 3, p. 216, 1996.
- [96] D. H. Reneker, A. L. Yarin, H. Fong, and S. Koombhongse, “Bending instability of electrically charged liquid jets of polymer solutions in electrospinning,” *J. Appl. Phys.*, vol. 87, no. 9, pp. 4531–4547, Apr. 2000.
- [97] J. D. Stitzel, K. J. Pawlowski, G. E. Wnek, D. G. Simpson, and G. L. Bowlin, “Arterial Smooth Muscle Cell Proliferation on a Novel Biomimicking, Biodegradable Vascular Graft Scaffold,” *J. Biomater. Appl.*, vol. 16, no. 1, pp. 22–33, Jul. 2001.
- [98] G. K. Owens, *The Vascular Smooth Muscle Cell*. 1995.

- [99] C. Buchko, L. C. Chen, Y. Shen, and D. C. Martin, "Processing and microstructural characterization of porous biocompatible protein polymer thin films," *Polymer (Guildf)*, 1999.
- [100] F. Buket Basmanav, G. T. Kose, and V. Hasirci, "Sequential growth factor delivery from complexed microspheres for bone tissue engineering," *Biomaterials*, 2008.
- [101] Y. Zhou, Q. Dong, H. Yang, X. Liu, X. Yin, Y. Tao, Z. Bai, and W. Xu, "Photocrosslinked maleilated chitosan/methacrylated poly (vinyl alcohol) bicomponent nanofibrous scaffolds for use as potential wound dressings," *Carbohydr. Polym.*, 2017.
- [102] Y. Zhou, H. Yang, X. Liu, J. Mao, S. Gu, and W. Xu, "Electrospinning of carboxyethyl chitosan/poly(vinyl alcohol)/silk fibroin nanoparticles for wound dressings," *Int. J. Biol. Macromol.*, 2013.
- [103] Y. Zhou, D. Yang, X. Chen, Q. Xu, F. Lu, and J. Nie, "Electrospun water-soluble carboxyethyl chitosan/poly(vinyl alcohol) nanofibrous membrane as potential wound dressing for skin regeneration," *Biomacromolecules*, 2008.
- [104] S. Maretschek, A. Greiner, and T. Kissel, "Electrospun biodegradable nanofiber nonwovens for controlled release of proteins," *J. Control. Release*, 2008.
- [105] S. Y. Chew, J. Wen, E. K. F. Yim, and K. W. Leong, "Sustained release of proteins from electrospun biodegradable fibers," *Biomacromolecules*, 2005.
- [106] E. H. Sanders, R. Kloefkorn, G. L. Bowlin, D. G. Simpson, and G. E. Wnek, "Two-phase electrospinning from a single electrified jet: Microencapsulation of aqueous reservoirs in poly(ethylene-co-vinyl acetate) fibers," *Macromolecules*, 2003.
- [107] J. Zeng, X. Xu, X. Chen, Q. Liang, X. Bian, L. Yang, and X. Jing, "Biodegradable electrospun fibers for drug delivery," *J. Control. Release*, 2003.
- [108] J. M. Harris, "Introduction to Biotechnical and Biomedical Applications of Poly(Ethylene Glycol)," in *Poly(Ethylene Glycol) Chemistry*, 1992.
- [109] A. Senthamizhan, B. Balusamy, and T. Uyar, "Glucose sensors based on electrospun nanofibers: a review," *Anal. Bioanal. Chem.*, 2015.
- [110] M. Afzali, A. Mostafavi, and T. Shamspur, "Electrospun composite nanofibers of poly vinyl pyrrolidone and zinc oxide nanoparticles modified carbon paste electrode for electrochemical detection of curcumin," *Mater. Sci. Eng. C*, 2016.
- [111] M. Zhang, X. Zhao, G. Zhang, G. Wei, and Z. Su, "Electrospinning design of functional nanostructures for biosensor applications," *J. Mater. Chem. B*, 2017.
- [112] N. Shehata, E. Samir, S. Gaballah, A. Hamed, and A. Elrasheedy, "Embedded ceria nanoparticles in crosslinked PVA electrospun nanofibers as optical sensors for radicals," *Sensors (Switzerland)*, 2016.
- [113] K. Faulds, R. E. Littleford, D. Graham, G. Dent, and W. E. Smith, "Comparison of Surface-Enhanced Resonance Raman Scattering from Unaggregated and Aggregated Nanoparticles," *Anal. Chem.*, vol. 76, no. 3, pp. 592–598, 2004.
- [114] F. Bensebaa, *Nanoparticle Technologies: From Lab to Market*. Elsevier Science, 2012.
- [115] L. P. Singh, S. K. Bhattacharyya, R. Kumar, G. Mishra, U. Sharma, G. Singh, and S. Ahalawat, "Sol-Gel processing of silica nanoparticles and their applications," *Adv. Colloid Interface Sci.*, vol. 214, 2014.
- [116] A. Liberman, N. Mendez, W. C. Trogler, and A. C. Kummel, "Synthesis and surface functionalization of silica nanoparticles for nanomedicine," *Surface Science Reports*, vol. 69, no. 2–3, 2014.
- [117] A. Burns, P. Sengupta, T. Zedayko, B. Baird, and U. Wiesner, "Core/Shell Fluorescent Silica Nanoparticles for Chemical Sensing: Towards Single-Particle Laboratories," *Small*, vol. 2, no. 6, pp. 723–726, Apr. 2006.

- [118] Y. Zhang, B. Y. W. Hsu, C. Ren, X. Li, and J. Wang, "Silica-based nanocapsules: synthesis, structure control and biomedical applications," *Chem. Soc. Rev.*, vol. 44, no. 1, pp. 315–335, 2015.
- [119] S.-A. Yang, S. Choi, S. M. Jeon, and J. Yu, "Silica nanoparticle stability in biological media revisited," *Sci. Rep.*, vol. 8, no. 1, p. 185, 2018.
- [120] B. I. Tamba, A. Dondas, M. Leon, A. N. Neagu, G. Dodi, C. Stefanescu, and A. Tijani, "Silica nanoparticles: Preparation, characterization and in vitro/in vivo biodistribution studies," *Eur. J. Pharm. Sci.*, vol. 71, pp. 46–55, 2015.
- [121] W. Stöber, A. Fink, and E. Bohn, "Controlled growth of monodisperse silica spheres in the micron size range," *J. Colloid Interface Sci.*, vol. 26, no. 1, pp. 62–69, 1968.
- [122] A. K. Van Helden, J. W. Jansen, and A. Vrij, "Preparation and characterization of spherical monodisperse silica dispersions in nonaqueous solvents," *J. Colloid Interface Sci.*, vol. 81, no. 2, pp. 354–368, Jun. 1981.
- [123] G. H. Bogush, M. A. Tracy, and C. F. Zukoski, "Preparation of monodisperse silica particles: Control of size and mass fraction," *J. Non. Cryst. Solids*, vol. 104, no. 1, pp. 95–106, Aug. 1988.
- [124] G. . Bogush and C. . Zukoski, "Uniform silica particle precipitation: An aggregative growth model," *J. Colloid Interface Sci.*, vol. 142, no. 1, pp. 19–34, Mar. 1991.
- [125] A. van Blaaderen and A. Vrij, "Synthesis and Characterization of Monodisperse Colloidal Organo-silica Spheres," *J. Colloid Interface Sci.*, vol. 156, no. 1, pp. 1–18, Mar. 1993.
- [126] S. K. Park, K. D. Kim, and H. T. Kim, "Preparation of silica nanoparticles: determination of the optimal synthesis conditions for small and uniform particles," *Colloids Surfaces A*, vol. 197, pp. 7–17, 2002.
- [127] D. L. Green, J. S. Lin, Y. F. Lam, M. Z. C. Hu, D. W. Schaefer, and M. T. Harris, "Size, volume fraction, and nucleation of Stober silica nanoparticles," *J. Colloid Interface Sci.*, vol. 266, no. 2, pp. 346–358, 2003.
- [128] K. S. Rao, K. El-Hami, T. Kodaki, K. Matsushige, and K. Makino, "A novel method for synthesis of silica nanoparticles," *J. Colloid Interface Sci.*, vol. 289, no. 1, pp. 125–131, 2005.
- [129] S. Hu, L. Sun, M. Liu, H. Zhu, H. Guo, H. Sun, and H. Sun, "A highly dispersible silica pH nanosensor with expanded measurement ranges," *New J. Chem.*, vol. 39, no. 6, pp. 4568–4574, 2015.
- [130] J. Xu, J. Liang, J. Li, and W. Yang, "Multicolor Dye-Doped Silica Nanoparticles Independent of FRET," *Langmuir*, vol. 26, no. 20, pp. 15722–15725, Oct. 2010.
- [131] G. Schmidt and M. M. Malwitz, "Properties of polymer–nanoparticle composites," *Curr. Opin. Colloid Interface Sci.*, vol. 8, no. 1, pp. 103–108, 2003.
- [132] B. Dong, M. E. Smith, and G. E. Wnek, "Encapsulation of multiple biological compounds within a single electrospun fiber," *Small*, vol. 5, no. 13, pp. 1508–1512, 2009.
- [133] H. Jiang, D. Fang, B. Hsiao, B. Chu, and W. Chen, "Preparation and characterization of ibuprofen-loaded poly(lactide-co-glycolide)/poly(ethylene glycol)-g-chitosan electrospun membranes," *J. Biomater. Sci. Polym. Ed.*, 2004.
- [134] E. R. Kenawy, G. L. Bowlin, K. Mansfield, J. Layman, D. G. Simpson, E. H. Sanders, and G. E. Wnek, "Release of tetracycline hydrochloride from electrospun poly(ethylene-co-vinylacetate), poly(lactic acid), and a blend," *J. Control. Release*, 2002.
- [135] Y. Wang, W. Qiao, B. Wang, Y. Zhang, P. Shao, and T. Yin, "Electrospun composite nanofibers containing nanoparticles for the programmable release of dual drugs," *Polym. J.*, 2011.
- [136] Y. Wang, B. Wang, W. Qiao, and T. Yin, "A novel controlled release drug delivery system for multiple drugs based on electrospun nanofibers containing nanoparticles," *J. Pharm. Sci.*, 2010.
- [137] Y. J. Son and H. S. Yoo, "Dexamethasone-incorporated nanofibrous meshes for antiproliferation of smooth

muscle cells: Thermally induced drug-loading strategy," *J. Biomed. Mater. Res. - Part A*, 2012.

- [138] L. C. Ionescu, G. C. Lee, B. J. Sennett, J. A. Burdick, and R. L. Mauck, "An anisotropic nanofiber/microsphere composite with controlled release of biomolecules for fibrous tissue engineering," *Biomaterials*, 2010.
- [139] L. Ji, C. Saquing, S. A. Khan, and X. Zhang, "Preparation and characterization of silica nanoparticulate-polyacrylonitrile composite and porous nanofibers," *Nanotechnology*, 2008.
- [140] C.-L. Zhang and S.-H. Yu, "Nanoparticles meet electrospinning: recent advances and future prospects.," *Chem. Soc. Rev.*, vol. 43, no. 13, pp. 4423-48, 2014.
- [141] J. Lin, Y. Cai, X. Wang, B. Ding, J. Yu, and M. Wang, "Fabrication of biomimetic superhydrophobic surfaces inspired by lotus leaf and silver ragwort leaf," *Nanoscale*, vol. 3, no. 3, pp. 1258-1262, 2011.
- [142] Y. D., L. B., Z. Y., and J. X., "Fabrication of Aligned Fibrous Arrays by Magnetic Electrospinning," *Adv. Mater.*, vol. 19, no. 21, pp. 3702-3706, Nov. 2007.
- [143] S. Wu, F. Li, H. Wang, L. Fu, B. Zhang, and G. Li, "Effects of poly (vinyl alcohol) (PVA) content on preparation of novel thiol-functionalized mesoporous PVA/SiO₂ composite nanofiber membranes and their application for adsorption of heavy metal ions from aqueous solution," *Polymer (Guildf.)*, vol. 51, no. 26, pp. 6203-6211, 2010.
- [144] D. Crespy, K. Friedemann, and A. M. Popa, "Colloid-electrospinning: Fabrication of multicompartment nanofibers by the electrospinning of organic or/and inorganic dispersions and emulsions," *Macromol. Rapid Commun.*, vol. 33, no. 23, pp. 1978-1995, 2012.
- [145] Y. J. Son, W. J. Kim, and H. S. Yoo, "Therapeutic applications of electrospun nanofibers for drug delivery systems," *Arch. Pharm. Res.*, vol. 37, no. 1, pp. 69-78, 2014.
- [146] C. Herrmann, A. Turshatov, and D. Crespy, "Fabrication of Polymer Ellipsoids by the Electrospinning of Swollen Nanoparticles," *ACS Macro Lett.*, vol. 1, no. 7, pp. 907-909, Jul. 2012.
- [147] B. K. Brettmann, S. Tsang, K. M. Forward, G. C. Rutledge, A. S. Myerson, and B. L. Trout, "Free Surface Electrospinning of Fibers Containing Microparticles," *Langmuir*, vol. 28, no. 25, pp. 9714-9721, Jun. 2012.
- [148] F. Kathrin, C. Tomas, K. Michael, L. Katharina, and C. Daniel, "Facile and Large-Scale Fabrication of Anisometric Particles from Fibers Synthesized by Colloid-Electrospinning," *Small*, vol. 8, no. 1, pp. 144-153, Nov. 2011.
- [149] K. Friedemann, A. Turshatov, K. Landfester, and D. Crespy, "Characterization via Two-Color STED Microscopy of Nanostructured Materials Synthesized by Colloid Electrospinning," *Langmuir*, vol. 27, no. 11, pp. 7132-7139, Jun. 2011.
- [150] A. Stoiljkovic, R. Venkatesh, E. Klimov, V. Raman, J. H. Wendorff, and A. Greiner, "Poly(styrene-co-n-butyl acrylate) Nanofibers with Excellent Stability against Water by Electrospinning from Aqueous Colloidal Dispersions," *Macromolecules*, vol. 42, no. 16, pp. 6147-6151, Aug. 2009.
- [151] A. Stoiljkovic, M. Ishaque, U. Justus, L. Hamel, E. Klimov, W. Heckmann, B. Eckhardt, J. H. Wendorff, and A. Greiner, "Preparation of water-stable submicron fibers from aqueous latex dispersion of water-insoluble polymers by electrospinning," *Polymer (Guildf.)*, vol. 48, no. 14, pp. 3974-3981, 2007.
- [152] J. Eunmin, L. Seongwon, K. K. Tae, W. Y. Sun, K. Hee-Soo, C. E. Chul, and J. Unyong, "Core-Sheath Nanofibers Containing Colloidal Arrays in the Core for Programmable Multi-Agent Delivery," *Adv. Mater.*, vol. 21, no. 9, pp. 968-972, Dec. 2008.
- [153] M. K. and B. D. and S. Shiratori, "Nanoporous ultra-high specific surface inorganic fibres," *Nanotechnology*, vol. 18, no. 31, p. 315602, 2007.
- [154] J.-M. Lim, G.-R. Yi, J. H. Moon, C.-J. Heo, and S.-M. Yang, "Superhydrophobic Films of Electrospun Fibers with Multiple-Scale Surface Morphology," *Langmuir*, vol. 23, no. 15, pp. 7981-7989, Jul. 2007.

- [155] J. M. Lim, J. H. Moon, G. R. Yi, C. J. Heo, and S. M. Yang, "Fabrication of one-dimensional colloidal assemblies from electrospun nanofibers," *Langmuir*, vol. 22, no. 8, pp. 3445–3449, 2006.
- [156] Y. Jin, D. Yang, D. Kang, and X. Xiang, "Fabrication of necklace-like structures via electrospinning," *Langmuir*, vol. 26, no. 2, pp. 1186–1190, 2010.
- [157] H. Deschout, F. C. Zanacchi, M. Mlodzianoski, A. Diaspro, J. Bewersdorf, S. T. Hess, and K. Braeckmans, "Precisely and accurately localizing single emitters in fluorescence microscopy," *Nat. Methods*, vol. 11, p. 253, Feb. 2014.
- [158] E. Abbe, "Beiträge zur Theorie des Mikroskops und der mikroskopischen Wahrnehmung," *Arch. für mikroskopische Anat.*, vol. 9, no. 1, pp. 413–418, 1873.
- [159] Rayleigh, "XV. On the theory of optical images, with special reference to the microscope," *London, Edinburgh, Dublin Philos. Mag. J. Sci.*, vol. 42, no. 255, pp. 167–195, Aug. 1896.
- [160] B. Huang, M. Bates, and X. Zhuang, "Super resolution fluorescence microscopy," *Annu. Rev. Biochem.*, vol. 78, pp. 993–1016, 2009.
- [161] D. Choquet, "The 2014 Nobel Prize in Chemistry: A Large-Scale Prize for Achievements on the Nanoscale," *Neuron*, vol. 84, no. 6, pp. 1116–1119, 2014.
- [162] M. J. Rust, M. Bates, and X. Zhuang, "Sub-diffraction-limit imaging by stochastic optical reconstruction microscopy (STORM)," *Nat. Methods*, vol. 3, p. 793, Aug. 2006.
- [163] G. T. Dempsey, J. C. Vaughan, K. H. Chen, M. Bates, and X. Zhuang, "Evaluation of fluorophores for optimal performance in localization-based super-resolution imaging," *Nat. Methods*, vol. 8, p. 1027, Nov. 2011.
- [164] M. Heilemann, E. Margeat, R. Kasper, M. Sauer, and P. Tinnefeld, "Carbocyanine Dyes as Efficient Reversible Single-Molecule Optical Switch," *J. Am. Chem. Soc.*, vol. 127, no. 11, pp. 3801–3806, Mar. 2005.
- [165] G. T. Dempsey, M. Bates, W. E. Kowtoniuk, D. R. Liu, R. Y. Tsien, and X. Zhuang, "Photoswitching Mechanism of Cyanine Dyes," *J. Am. Chem. Soc.*, vol. 131, no. 51, pp. 18192–18193, Dec. 2009.
- [166] T. J. Chozinski, L. A. Gagnon, and J. C. Vaughan, "Twinkle, twinkle little star: Photoswitchable fluorophores for super-resolution imaging," *FEBS Lett.*, vol. 588, no. 19, pp. 3603–3612, 2014.
- [167] S. Ram, E. S. Ward, and R. J. Ober, "Beyond Rayleigh's criterion: A resolution measure with application to single-molecule microscopy," *Proc. Natl. Acad. Sci.*, vol. 103, no. 12, pp. 4457–4462, 2006.
- [168] D. J. Metcalf, R. Edwards, N. Kumarswami, and A. E. Knight, "Test Samples for Optimizing STORM Super-Resolution Microscopy," *J. Vis. Exp.*, no. 79, pp. 1–17, 2013.
- [169] P. C. B. T.-M. in C. B. Goodwin, "Evaluating Optical Aberration Using Fluorescent Microspheres: Methods, Analysis, and Corrective Actions," in *Digital Microscopy, 3rd Edition*, vol. 81, Academic Press, 2007, pp. 397–413.
- [170] X. D. Wang, Z. X. Shen, T. Sang, X. B. Cheng, M. F. Li, L. Y. Chen, and Z. S. Wang, "Preparation of spherical silica particles by Stober process with high concentration of tetra-ethyl-orthosilicate," *J. Colloid Interface Sci.*, vol. 341, no. 1, pp. 23–29, 2010.
- [171] J. Lim, S. Ha, and J. Lee, "Precise Size-control of Silica Nanoparticles via Alkoxy Exchange Equilibrium of Tetraethyl Orthosilicate (TEOS) in the Mixed Alcohol Solution †," vol. 33, no. 3, pp. 1067–1070, 2012.
- [172] M. Mishra and Y. Yagci, *Handbook of Vinyl Polymers: Radical Polymerization, Process, and Technology, Second Edition*. Taylor & Francis, 2008.
- [173] X. Chen, M.-C. Estevez, Z. Zhu, Y.-F. Huang, Y. Chen, L. Wang, and W. Tan, "Using Aptamer-Conjugated Fluorescence Resonance Energy Transfer Nanoparticles for Multiplexed Cancer Cell Monitoring," vol. 81, no. 16, pp. 7009–7014, 2009.

- [174] M. Instruments, "Zetasizer Nano Series User Manual." 2004.
- [175] Y. Zhu, Y. Fang, L. Borchardt, and S. Kaskel, "PEGylated hollow mesoporous silica nanoparticles as potential drug delivery vehicles," *Microporous Mesoporous Mater.*, vol. 141, no. 1–3, pp. 199–206, May 2011.
- [176] K. Nozawa, H. Gailhanou, L. Raison, P. Panizza, H. Ushiki, E. Sellier, J. P. Delville, and M. H. Delville, "Smart Control of Monodisperse Stöber Silica Particles: Effect of Reactant Addition Rate on Growth Process," *Langmuir*, vol. 21, no. 4, pp. 1516–1523, 2005.
- [177] P. P. von Weimarn, "The Precipitation Laws," *Chem. Rev.*, vol. 2, no. 2, pp. 217–242, 1925.
- [178] V. M. Chauhan, G. R. Burnett, and J. W. Aylott, "Dual-fluorophore ratiometric pH nanosensor with tuneable pKa and extended dynamic range," *Analyst*, vol. 136, no. 9, pp. 1799–1801, 2011.
- [179] V. M. Chauhan, G. Orsi, A. Brown, D. I. Pritchard, and J. W. Aylott, "Mapping the Pharyngeal and Intestinal pH of *Caenorhabditis elegans* and Real-Time Luminal pH Oscillations Using Extended Dynamic Range pH-Sensitive Nanosensors," *ACS Nano*, vol. 7, no. 6, pp. 5577–5587, 2013.
- [180] R. V. Benjaminsen, H. Sun, J. R. Henriksen, N. M. Christensen, K. Almdal, and T. L. Andresen, "Evaluating Nanoparticle Sensor Design for Intracellular pH Measurements," *ACS Nano*, vol. 5, no. 7, pp. 5864–5873, 2011.
- [181] M. Es-saheb, A. A. Elzatahry, E. S. M. Sherif, A. S. Alkaraki, and E. R. Kenawy, "A novel electrospinning application for polyvinyl chloride nanofiber coating deposition as a corrosion inhibitor for aluminum, steel, and brass in chloride solutions," *Int. J. Electrochem. Sci.*, vol. 7, no. 7, pp. 5962–5976, 2012.
- [182] Z. Zhong, Q. Cao, B. Jing, X. Wang, X. Li, and H. Deng, "Electrospun PVdF-PVC nanofibrous polymer electrolytes for polymer lithium-ion batteries," *Mater. Sci. Eng. B Solid-State Mater. Adv. Technol.*, vol. 177, no. 1, pp. 86–91, 2012.
- [183] K. Phatcharasit, W. Taweepreda, K. Boonkerd, and J. K. Kim, "Electrospun conditions of poly(vinyl chloride) nanofibrous membrane plasticized with polyurethane," *J. Teknol. (Sciences Eng.)*, vol. 68, no. 5, pp. 59–62, 2014.
- [184] L. Spallino, L. Vaccaro, L. Sciortino, S. Agnello, G. Buscarino, M. Cannas, and F. M. Gelardi, "Visible-ultraviolet vibronic emission of silica nanoparticles," *Phys. Chem. Chem. Phys.*, vol. 16, no. 40, pp. 22028–22034, 2014.
- [185] K. A. Prokhorov, D. A. Aleksandrova, E. A. Sagitova, G. Y. Nikolaeva, T. V. Vlasova, P. P. Pashinin, C. A. Jones, and S. J. Shilton, "Raman Spectroscopy Evaluation of Polyvinylchloride Structure," *J. Phys. Conf. Ser.*, vol. 691, no. 1, p. 12001, 2016.
- [186] J. L. S. Lee, I. S. Gilmore, I. W. Fletcher, and M. P. Seah, "Topography and field effects in the quantitative analysis of conductive surfaces using ToF-SIMS," *Appl. Surf. Sci.*, vol. 255, no. 4, pp. 1560–1563, 2008.
- [187] B. J. Tyler, G. Rayal, and D. G. Castner, "Multivariate analysis strategies for processing ToF-SIMS images of biomaterials," *Biomaterials*, vol. 28, no. 15, pp. 2412–2423, May 2007.
- [188] L. Yang, N. Shirahata, G. Saini, F. Zhang, L. Pei, M. C. Asplund, D. G. Kurth, K. Ariga, K. Sautter, T. Nakanishi, V. Smentkowski, and M. R. Linford, "Effect of Surface Free Energy on PDMS Transfer in Microcontact Printing and Its Application to ToF-SIMS to Probe Surface Energies," *Langmuir*, vol. 25, no. 10, pp. 5674–5683, May 2009.
- [189] A. Benninghoven, "Chemical Analysis of Inorganic and Organic Surfaces and Thin Films by Static Time-of-Flight Secondary Ion Mass Spectrometry (ToF-SIMS)," *Angew. Chemie Int. Ed. English*, vol. 33, no. 10, pp. 1023–1043, Sep. 2018.
- [190] N. Olivier, D. Keller, V. S. Rajan, P. Gönczy, and S. Manley, "Simple buffers for 3D STORM microscopy," *Biomed. Opt. Express*, vol. 4, no. 6, pp. 885–899, May 2013.

- [191] W. Yuan and K. Q. Zhang, "Structural evolution of electrospun composite fibers from the blend of polyvinyl alcohol and polymer nanoparticles," *Langmuir*, vol. 28, no. 43, pp. 15418–15424, 2012.
- [192] C. Chen, Y.-F. Li, Y. Qu, Z. Chai, and Y. Zhao, "Advanced nuclear analytical and related techniques for the growing challenges in nanotoxicology," *Chem. Soc. Rev.*, vol. 42, no. 21, pp. 8266–8303, 2013.
- [193] H. Cui, W. Zhao, Y. Wang, Y. Fan, L. Qiu, and K. Zhu, "Improving spatial resolution of confocal Raman microscopy by super-resolution image restoration," *Opt. Express*, vol. 24, no. 10, pp. 10767–10776, 2016.
- [194] N. R. Council, "Imaging Techniques: State of the Art and Future Potential," in *Visualizing Chemistry: The Progress and Promise of Advanced Chemical Imaging*, Washington, DC: The National Academies Press, 2006.
- [195] J. Xu, H. Ma, and Y. Liu, "Stochastic Optical Reconstruction Microscopy (STORM)," *Curr. Protoc. Cytom.*, vol. 81, p. 12.46.1-12.46.27, Jul. 2017.
- [196] A. T. Florence and D. Attwood, *Physicochemical Principles of Pharmacy*. Pharmaceutical Press, 2006.
- [197] C. Lipinski, *Poor aqueous solubility - An industry wide problem in drug discovery*, vol. 5. 2002.
- [198] C. A. Lipinski, "Drug-like properties and the causes of poor solubility and poor permeability," *J. Pharmacol. Toxicol. Methods*, vol. 44, no. 1, pp. 235–249, 2000.
- [199] P. Gribbon and S. Andreas, "High-throughput drug discovery: What can we expect from HTS?," *Drug Discov. Today*, vol. 10, no. 1, pp. 17–22, 2005.
- [200] R. H. Müller and C. Keck, *Second generation of drug nanocrystals for delivery of poorly soluble drugs: SmartCrystal technology*, vol. 34. 2008.
- [201] C. T. John, W. Xu, L. K. Lupton, and P. A. Harmon, "Formulating Weakly Basic HCl Salts : Relative Ability of Common Excipients to Induce Disproportionation and the Unique Deleterious Effects of Magnesium Stearate," pp. 1628–1641, 2013.
- [202] M. Crew, "Bioavailability Enhancement – A New Year for Solubility Enhancement," *Drug Dev. Deliv.*, vol. 14, no. 1, p. 22, 2014.
- [203] D. T. Friesen, R. Shanker, M. Crew, D. T. Smithey, W. J. Curatolo, and J. A. S. Nightingale, "Hydroxypropyl Methylcellulose Acetate Succinate-Based Spray-Dried Dispersions: An Overview," *Mol. Pharm.*, vol. 5, no. 6, pp. 1003–1019, Dec. 2008.
- [204] D. L. Pole, "Physical and biological considerations for the use of nonaqueous solvents in oral bioavailability enhancement," *J. Pharm. Sci.*, vol. 97, no. 3, pp. 1071–1088, 2008.
- [205] P. Gao and W. Morozowich, "Development of supersaturatable self-emulsifying drug delivery system formulations for improving the oral absorption of poorly soluble drugs," *Expert Opin. Drug Deliv.*, vol. 3, no. 1, pp. 97–110, Jan. 2006.
- [206] C. J. H. Porter, K. M. Wasan, and P. Constantinides, "Lipid-based systems for the enhanced delivery of poorly water soluble drugs," *Adv. Drug Deliv. Rev.*, vol. 60, no. 6, pp. 615–616, 2008.
- [207] M. J. Hageman, "Solubility, Solubilization and Dissolution in Drug Delivery During Lead Optimization BT - Optimizing the 'Drug-Like' Properties of Leads in Drug Discovery," R. T. Borchardt, E. H. Kerns, M. J. Hageman, D. R. Thakker, and J. L. Stevens, Eds. New York, NY: Springer New York, 2006, pp. 99–130.
- [208] A. Fahr and X. Liu, "Drug delivery strategies for poorly water-soluble drugs," *Expert Opin. Drug Deliv.*, vol. 4, no. 4, pp. 403–416, Jul. 2007.
- [209] C. Timpe, *Strategies for formulation development of poorly water-soluble drug candidates - A recent perspective*, vol. 10. 2007.
- [210] V. J. Stella and K. W. Nti-Addae, "Prodrug strategies to overcome poor water solubility," *Adv. Drug Deliv.*

- Rev., vol. 59, no. 7, pp. 677–694, 2007.
- [211] W. Kuei-Meng, *A New Classification of Prodrugs: Regulatory Perspectives*, vol. 2. 2009.
- [212] E. Nelson, "Solution Rate of Theophylline Salts and Effects from Oral Administration," *J. Am. Pharm. Assoc. (Scientific ed.)*, vol. 46, no. 10, pp. 607–614, 1957.
- [213] E. Nelson, "Comparative Dissolution Rates of Weak Acids and Their Sodium Salts," *J. Am. Pharm. Assoc. (Scientific ed.)*, vol. 47, no. 4, pp. 297–299, 1958.
- [214] A. T. M. Serajuddin, "Salt formation to improve drug solubility," *Adv. Drug Deliv. Rev.*, vol. 59, no. 7, pp. 603–616, 2007.
- [215] J. D. Dunitz, "Crystal and co-crystal: a second opinion," *CrystEngComm*, vol. 5, no. 91, p. 506, 2003.
- [216] G. R. Desiraju, "Crystal and co-crystal," *CrystEngComm*, vol. 5, no. 82, pp. 466–467, 2003.
- [217] C. Leuner and J. Dressman, "Improving drug solubility for oral delivery using solid dispersions," *Eur. J. Pharm. Biopharm.*, vol. 50, no. 1, pp. 47–60, 2000.
- [218] P. H. Stahl, C. G. Wermuth, I. U. of Pure, and A. Chemistry, "Chapter1: The Physicochemical Background: Fundamentals of Ionic Equilibria," in *Handbook of Pharmaceutical Salts Properties, Selection, and Use*, Wiley, 2008.
- [219] P. Guerrieri and L. S. Taylor, "Role of Salt and Excipient Properties on Disproportionation in the Solid-State," vol. 26, no. 8, 2009.
- [220] G. A. Stephenson, A. Aburub, and T. A. Woods, "Physical Stability of Salts of Weak Bases in the Solid-State," *J. Pharm. Sci.*, vol. 100, no. 5, pp. 1607–1617, 2011.
- [221] J. Wells, *Pharmaceutical Preformulation: The Physicochemical Properties of Drug Substances*. Taylor & Francis, 1999.
- [222] J. N. Brønsted, "Neuere Gesichtspunkte für die Säure-Basen-Funktion," *Angew. Chemie*, vol. 43, no. 11, pp. 229–233.
- [223] P. H. Stahl, *Handbook of Pharmaceutical Salts Properties, Selection, and Use*. Wiley, 2008.
- [224] Y. Qiu, Y. Chen, G. G. Z. Zhang, L. Yu, and R. V Mantri, *Developing Solid Oral Dosage Forms: Pharmaceutical Theory and Practice*. Elsevier Science, 2016.
- [225] N. Peter, A. Christensen, J. Rantanen, C. Cornett, and L. S. Taylor, "Disproportionation of the calcium salt of atorvastatin in the presence of acidic excipients," *Eur. J. Pharm. Biopharm.*, vol. 82, no. 2, pp. 410–416, 2012.
- [226] H. Nie, W. Xu, J. Ren, L. S. Taylor, P. J. Marsac, C. T. John, and S. R. Byrn, "Impact of Metallic Stearates on Disproportionation of Hydrochloride Salts of Weak Bases in Solid-State Formulations," *Mol. Pharm.*, vol. 13, p. 3541–3552, 2016.
- [227] J. B. Bogardus and R. K. Blackwood, "Solubility of Doxycycline in Aqueous Solution," *J. Pharm. Sci.*, vol. 68, no. 2, pp. 188–194, 1979.
- [228] M. Pudipeddi, A. T. M. Serajuddin, D. J. W. Grant, and P. H. Stahl, "Chapter2: Solubility and dissolution of weak acids, bases, and salts," in *Pharmaceutical Salts: Properties, Selection and Use*, Wiley, 2002.
- [229] H. Nie, Z. Liu, B. C. Marks, L. S. Taylor, S. R. Byrn, and P. J. Marsac, "Analytical approaches to investigate salt disproportionation in tablet matrices by Raman spectroscopy and Raman mapping," *J. Pharm. Biomed. Anal.*, vol. 118, pp. 328–337, 2016.
- [230] Y. Hsieh, W. Yu, Y. Xiang, W. Pan, K. C. Waterman, E. Y. Shalaev, S. L. Shamblin, and L. S. Taylor, "Impact of sertraline salt form on the oxidative stability in powder blends," *Int. J. Pharm.*, vol. 461, no. 1–2, pp. 322–

330, 2014.

- [231] N. R. Mathias, Y. Xu, D. Patel, M. Grass, B. Caldwell, C. Jager, J. Mullin, L. Hansen, J. Crison, A. Saari, C. Gesenberg, J. Morrison, B. Vig, and K. Raghavan, "Assessing the risk of pH-dependent absorption for new molecular entities: A novel in vitro dissolution test, physicochemical analysis, and risk assessment strategy," *Mol. Pharm.*, vol. 10, no. 11, pp. 4063–4073, 2013.
- [232] P. J. Skrdla and D. Zhang, "Disproportionation of a crystalline citrate salt of a developmental pharmaceutical compound : Characterization of the kinetics using pH monitoring and online Raman spectroscopy plus quantitation of the cry," *J. Pharm. Biomed. Anal.*, vol. 90, pp. 186–191, 2014.
- [233] H. Nie, W. Xu, L. S. Taylor, P. J. Marsac, and S. R. Byrn, "Crystalline solid dispersion—a strategy to slowdown salt disproportionation in solid state formulations during storage and wet granulation," *Int. J. Pharm.*, vol. 517, no. 1–2, pp. 203–215, 2017.
- [234] N. K. Thakral, R. J. Behme, A. Aburub, J. A. Peterson, T. A. Woods, B. A. Diserod, R. Suryanarayanan, and G. A. Stephenson, "Salt Disproportionation in the Solid State: Role of Solubility and Counterion Volatility," *Mol. Pharm.*, vol. 13, no. 12, pp. 4141–4151, 2016.
- [235] C. T. Rhodes and J. T. Carstensen, *Drug Stability: Principles and Practices*. Marcel Dekker, 2000.
- [236] Z. T. Chowhan, "pH–Solubility Profiles of Organic Carboxylic Acids and Their Salts," *J. Pharm. Sci.*, vol. 67, no. 9, pp. 1257–1260, 1978.
- [237] W. I. Higuchi, "Diffusional Models Useful in Biopharmaceutics: Drug Release Rate Processes," *J. Pharm. Sci.*, vol. 56, no. 3, pp. 315–324, 1967.
- [238] S. Chandran, C. Gesenberg, J. Levons, M. Hubert, and K. Raghavan, "A high-throughput spectrophotometric approach for evaluation of precipitation resistance," *J. Pharm. Biomed. Anal.*, vol. 56, no. 4, pp. 698–704, 2011.
- [239] C. D. Bevan and R. S. Lloyd, "A High-Throughput Screening Method for the Determination of Aqueous Drug Solubility Using Laser Nephelometry in Microtiter Plates," *Anal. Chem.*, vol. 72, no. 8, pp. 1781–1787, Apr. 2000.
- [240] K. Punčochová, A. V Ewing, M. Gajdošová, N. Sarvašová, S. G. Kazarian, J. Beránek, and F. Štěpánek, "Identifying the mechanisms of drug release from amorphous solid dispersions using MRI and ATR-FTIR spectroscopic imaging," *Int. J. Pharm.*, vol. 483, no. 1, pp. 256–267, 2015.
- [241] S. G. Kazarian and K. L. A. Chan, "'Chemical Photography' of Drug Release," *Macromolecules*, vol. 36, no. 26, pp. 9866–9872, Dec. 2003.
- [242] K. Wang and F. P. Guengerich, "Bioactivation of Fluorinated 2-Aryl-benzothiazole Antitumor Molecules by Human Cytochrome P450s 1A1 and 2W1 and Deactivation by Cytochrome P450 2S1," no. Gw 610, 2012.
- [243] P. Guerrieri, K. Jarring, and L. S Taylor, *Impact of Counterion on the Chemical Stability of Crystalline Salts of Procaine*, vol. 99. 2009.
- [244] R. C. Rowe, P. J. Sheskey, S. C. Owen, and A. P. Association, *Handbook of Pharmaceutical Excipients*. Pharmaceutical Press, 2006.
- [245] J. Walsh, A. Cram, K. Woertz, J. Breikreutz, G. Winzenburg, R. Turner, and C. Tuleu, "Playing hide and seek with poorly tasting paediatric medicines: Do not forget the excipients," *Adv. Drug Deliv. Rev.*, vol. 73, pp. 14–33, 2014.
- [246] R. Gao, Y. Jin, Q.-Y. Yang, B.-W. Sun, and J. Lin, "Study of stability and drug-excipient compatibility of estradiol and pharmaceutical excipients," *J. Therm. Anal. Calorim.*, vol. 120, no. 1, pp. 839–845, 2015.
- [247] R. Chadha and S. Bhandari, "Drug–excipient compatibility screening—Role of thermoanalytical and spectroscopic techniques," *J. Pharm. Biomed. Anal.*, vol. 87, pp. 82–97, 2014.

- [248] Y. Hsieh and L. S. Taylor, "Salt Stability - Effect of Particle Size , Relative Humidity , Temperature and Composition on Salt to Free Base Conversion," pp. 549–561, 2015.
- [249] S. W. Baertschi, K. M. Alsante, and R. A. Reed, *Pharmaceutical Stress Testing: Predicting Drug Degradation*, 2nd Editio. CRC Press, 2016.
- [250] D. Monkhouse and A. Maderich, "Excipient compatibility possibilities and limitations in stability prediction.," in *Stability Testing in the EC, Japan and the USA*, 1993, pp. 67–74.
- [251] S. Stodghill, "Thermal Analysis – A Review of Techniques and Applications in the Pharmaceutical Sciences," *Am. Pharm. Rev.*, vol. 13, no. 2, 2010.
- [252] F. Monajjemzadeh and F. Ghaderi, "Thermal methods of analysis in solid dosage technology," *J Mol Pharm Org Process Res*, vol. 3, no. 1, 2015.
- [253] A. V Ewing, P. S. Wray, G. S. Clarke, and S. G. Kazarian, "Evaluating drug delivery with salt formation Drug disproportionation studied in situ by ATR-FTIR imaging and Raman mapping," *J. Pharm. Biomed. Anal.*, vol. 111, pp. 248–256, 2015.
- [254] P. S. Wray, W. E. Sinclair, J. W. Jones, G. S. Clarke, and D. Both, "The use of in situ near infrared imaging and Raman mapping to study the disproportionation of a drug HCl salt during dissolution," *Int. J. Pharm.*, vol. 493, no. 1–2, pp. 198–207, 2015.
- [255] G. Bruni, V. Berbenni, C. Milanese, A. Girella, and A. Marini, "Drug-excipient compatibility studies in binary and ternary mixtures by physico-chemical techniques," *J. Therm. Anal. Calorim.*, vol. 102, no. 1, pp. 193–201, 2010.
- [256] M. L. Cotton, D. W. Wu, and E. B. Vadas, "Drug-excipient interaction study of enalapril maleate using thermal analysis and scanning electron microscopy," *Int. J. Pharm.*, vol. 40, no. 1, pp. 129–142, 1987.
- [257] F. Balestrieri, A. D. Magri, A. L. Magri, D. Marini, and A. Sacchini, "Application of differential scanning calorimetry to the study of drug-excipient compatibility," *Thermochim. Acta*, vol. 285, no. 2, pp. 337–345, 1996.
- [258] J. L. Sims, J. A. Carreira, D. J. Carrier, S. R. Crabtree, L. Easton, S. A. Hancock, and C. E. Simcox, "A New Approach to Accelerated Drug-Excipient Compatibility Testing," *Pharm. Dev. Technol.*, vol. 8, no. 2, pp. 119–126, Jan. 2003.
- [259] J. De Calderon Anda, X. Z. Wang, X. Lai, K. J. Roberts, K. H. Jennings, M. J. Wilkinson, D. Watson, and D. Roberts, "Real-time product morphology monitoring in crystallization using imaging technique," *AIChE J.*, vol. 51, no. 5, pp. 1406–1414, 2005.
- [260] R. F. Li, R. Penchev, V. Ramachandran, K. J. Roberts, X. Z. Wang, R. J. Tweedie, A. Prior, J. W. Gerritsen, and F. M. Huguen, "Particle Shape Characterisation via Image Analysis: from Laboratory Studies to In-process Measurements Using an in Situ Particle Viewer System," *Org. Process Res. Dev.*, vol. 12, no. 5, pp. 837–849, Sep. 2008.
- [261] X. Z. Wang, J. Calderon De Anda, and K. J. Roberts, "Real-time measurement of the growth rates of individual crystal facets using imaging and image analysis: A feasibility study on needle-shaped crystals of L-glutamic acid," *Chem. Eng. Res. Des.*, vol. 85, no. 7 A, pp. 921–927, 2007.
- [262] J. Calderon De Anda, X. Z. Wang, X. Lai, and K. J. Roberts, "Classifying organic crystals via in-process image analysis and the use of monitoring charts to follow polymorphic and morphological changes," *J. Process Control*, vol. 15, no. 7, pp. 785–797, 2005.
- [263] J. De Calderon Anda, X. Z. Wang, and K. J. Roberts, "Multi-scale segmentation image analysis for the in-process monitoring of particle shape with batch crystallisers," *Chem. Eng. Sci.*, vol. 60, no. 4, pp. 1053–1065, 2005.
- [264] K. Vilegave, G. Vidyasagar, and P. Chandankar, *Preformulation Studies of Pharmaceutical New Drug*

Molecule & Products: An Overview, vol. 1. 2013.

- [265] A. K. El-Zhry El-Yafi and H. El-Zein, "Technical crystallization for application in pharmaceutical material engineering: Review article," *Asian J. Pharm. Sci.*, vol. 10, no. 4, pp. 283–291, 2014.
- [266] W. A. Dulin, "Degradation of Bisoprolol Fumarate in Tablets Formulated with Dicalcium Phosphate," *Drug Dev. Ind. Pharm.*, vol. 21, no. 4, pp. 393–409, Jan. 1995.
- [267] C.-A. Scheef, D. Oelkrug, and P. C. Schmidt, "Surface acidity of solid pharmaceutical excipients III. Excipients for solid dosage forms," *Eur. J. Pharm. Biopharm.*, vol. 46, no. 2, pp. 209–213, 1998.
- [268] B. W. Glombitza and P. C. Schmidt, *Surface acidity of solid pharmaceutical excipients II. Effect of the surface acidity on the decomposition rate of acetylsalicylic acid*, vol. 41. 1995.
- [269] M. Pudipeddi, E. A. Zannou, M. Vasanthavada, A. Dontabhaktuni, A. E. Royce, Y. M. Joshi, and A. T. M. Serajuddin, "Measurement of Surface pH of Pharmaceutical Solids: A Critical Evaluation of Indicator Dye-Sorption Method and its Comparison With Slurry pH Method," *J. Pharm. Sci.*, vol. 97, no. 5, pp. 1831–1842, 2008.
- [270] R. Govindarajan, M. Landis, B. Hancock, L. A. Gatlin, R. Suryanarayanan, and E. Y. Shalaev, "Surface Acidity and Solid-State Compatibility of Excipients with an Acid-Sensitive API: Case Study of Atorvastatin Calcium," *AAPS PharmSciTech*, vol. 16, no. 2, pp. 354–363, Apr. 2015.
- [271] ICH Expert Working Group, "ICH Harmonised Tripartite Guideline: Pharmaceutical Development Q8 (R2)," p. 24, 2009.
- [272] FDA, "Quality by Design for ANDAs: An Example for Immediate Release Dosage Forms," p. 107, 2014.
- [273] United States Food and Drug Administration, "Q1A(R2) Stability Testing of New Drug Substances and Product.," *Fed. Regist.*, 2003.
- [274] V. Sarveiya, J. F. Templeton, and H. A. E. Benson, "Ion-pairs of ibuprofen: increased membrane diffusion," *J. Pharm. Pharmacol.*, vol. 56, no. 6, pp. 717–724, 2004.
- [275] A. T. M. Serajuddin, A. B. Thakur, R. N. Ghoshal, M. G. Fakes, S. A. Ranadive, K. R. Morris, and S. A. Varia, "Selection of solid dosage form composition through drug–excipient compatibility testing," *J. Pharm. Sci.*, vol. 88, no. 7, pp. 696–704, Jun. 2000.
- [276] K. Stoyanova, Z. Vinarov, and S. Tcholakova, "Improving Ibuprofen solubility by surfactant-facilitated self-assembly into mixed micelles," *J. Drug Deliv. Sci. Technol.*, vol. 36, pp. 208–215, 2016.
- [277] A. K. Tiwary, "Modification of Crystal Habit and Its Role in Dosage Form Performance," *Drug Dev. Ind. Pharm.*, vol. 27, no. 7, pp. 699–709, Jan. 2001.
- [278] A. R. Sheth and D. J. W. Grant, "Relationship between the Structure and Properties of Pharmaceutical Crystals," *KONA Powder Part. J.*, vol. 23, pp. 36–48, 2005.
- [279] A. S. Myerson, "Crystallization Basics," in *Molecular Modeling Applications in Crystallization*, Cambridge University Press, 2005.
- [280] S. Kupfer, J. Guthmuller, M. Wächtler, S. Losse, S. Rau, B. Dietzek, J. Popp, and L. González, "Protonation effects on the resonance Raman properties of a novel (terpyridine)Ru(4H-imidazole) complex: an experimental and theoretical case study," *Phys. Chem. Chem. Phys.*, vol. 13, no. 34, pp. 15580–15588, 2011.
- [281] M. Barańska, K. Chruszcz, B. Boduszek, and L. M. Proniewicz, "FT-IR and FT-Raman study of selected pyridinephosphonocarboxylic acids," *Vib. Spectrosc.*, vol. 31, no. 2, pp. 295–311, 2003.
- [282] H. S. Yathirajan, B. Nagaraj, P. Nagaraja, and M. Bolte, "Pioglitazone hydrochloride," *Acta Crystallogr. Sect. E*, vol. 61, no. 1, pp. o154–o155, Jan. 2005.
- [283] S. Bonora, A. Pisi, S. Ottani, D. Cesini, A. Maris, and M. Di Foggia, "Raman and SERS study on ibuprofen

- metal complexes with biomedical interest," *Vib. Spectrosc.*, vol. 73, no. July, pp. 45–55, 2014.
- [284] A. Jubert, M. L. Legarto, N. E. Massa, L. L. Tévez, and N. B. Okulik, "Vibrational and theoretical studies of non-steroidal anti-inflammatory drugs Ibuprofen [2-(4-isobutylphenyl)propionic acid]; Naproxen [6-methoxy- α -methyl-2-naphthalene acetic acid] and Tolmetin acids [1-methyl-5-(4-methylbenzoyl)-1H-pyrrole-2-acetic acid]," *J. Mol. Struct.*, vol. 783, no. 1–3, pp. 34–51, 2006.
- [285] S. I. F. Badawy, S. Badawy, R. C. Williams, and D. L. Gilbert, "Effect of Different Acids on Solid-State Stability of an Ester Prodrug of a IIb/IIIa Glycoprotein Receptor Antagonist," *Pharm. Dev. Technol.*, vol. 4, no. 3, pp. 325–331, Jan. 1999.
- [286] B. Stanis, "The influence of pharmaceutical excipients on quinapril hydrochloride stability," *Acta Pol. Pharm. - Drug Res.*, vol. 62, no. 3, pp. 189–193, 2005.
- [287] S. Badawy, D. B Gray, F. Zhao, D. Sun, A. Schuster, and M. Hussain, *Formulation of Solid Dosage Forms to Overcome Gastric pH Interaction of the Factor Xa Inhibitor, BMS-561389*, vol. 23. 2006.
- [288] A. Streubel, J. Siepmann, A. Dashevsky, and R. Bodmeier, "pH-independent release of a weakly basic drug from water-insoluble and -soluble matrix tablets," *J. Control. Release*, vol. 67, no. 1, pp. 101–110, 2000.
- [289] K. Thoma and T. Zimmer, "Retardation of weakly basic drugs with diffusion tablets," *Int. J. Pharm.*, vol. 58, no. 3, pp. 197–202, 1990.
- [290] A. S. Tatavarti and S. W. Hoag, "Microenvironmental pH Modulation Based Release Enhancement of a Weakly Basic Drug from Hydrophilic Matrices *," *J. Pharm. Sci.*, vol. 95, no. 7, pp. 1459–1468, Jul. 2006.
- [291] A. Bendich, L. J. Machlin, O. Scandurra, G. W. Burton, and D. D. M. Wayner, "The antioxidant role of vitamin C," *Adv. Free Radic. Biol. Med.*, vol. 2, no. 2, pp. 419–444, 1986.
- [292] J. Li and Y. Wu, "Lubricants in Pharmaceutical Solid Dosage Forms," *Lubricants*, vol. 2, no. 1, pp. 21–43, 2014.
- [293] M. Çelik, "Lubricant Sensitivity," in *Pharmaceutical Powder Compaction Technology, Second Edition*, CRC Press, 2016.
- [294] J. Zhu and F. Picha, "Pioglitazone salts, such as pioglitazone sulfate, and pharmaceutical compositions and processes using the same," US 7,230,016 B2, 2007.
- [295] G. Roberts, *Langmuir-Blodgett Films*. Springer US, 2013.
- [296] I. A. Price, "Dosage form of ibuprofen," EP0881899B1, 2004.
- [297] D. Markl and J. A. Zeitler, "A Review of Disintegration Mechanisms and Measurement Techniques," *Pharm. Res.*, vol. 34, no. 5, pp. 890–917, Mar. 2017.
- [298] K. Khan and C. T Rhodes, *Disintegration properties of calcium phosphate dibasic dihydrate tablets*, vol. 64. 1975.
- [299] L. S. C. Wan and K. P. P. Prasad, "Uptake of water by excipients in tablets," *Int. J. Pharm.*, vol. 50, no. 2, pp. 147–153, 1989.
- [300] K. A. Khan and C. T. Rhodes, "Water-sorption properties of tablet disintegrants," *J. Pharm. Sci.*, vol. 64, no. 3, pp. 447–451, Aug. 2018.
- [301] M. Odaka, Hiroyuki Yamane, "Pharmaceutical composition for the treatment of diabetes," US10036208, 2011.
- [302] G. W. Skinner, W. W. Harcum, P. E. Barnum, and J.-H. Guo, "The Evaluation of Fine-Particle Hydroxypropylcellulose as a Roller Compaction Binder in Pharmaceutical Applications," *Drug Dev. Ind. Pharm.*, vol. 25, no. 10, pp. 1121–1128, Jan. 1999.

- [303] A. Z. A. Teixeira, "Hydroxypropylcellulose controlled release tablet matrix prepared by wet granulation: effect of powder properties and polymer composition," *Brazilian Arch. Biol. Technol.*, vol. 52, pp. 157–162, 2009.
- [304] D. A. Alderman, "Sustained release compositions comprising hydroxypropyl cellulose ethers," *United States Pat. No. 4,704,285*, 1987.
- [305] D.-Y. Lee and Chih-Ming Chen, "Delayed pulse release hydrogel matrix tablet," *United States Pat. No. 6,103,263*;, 2000.
- [306] S. Hong, S. A. Nowak, and C. L. Wah, "Impact of Physicochemical Properties of Cellulosic Polymers on Supersaturation Maintenance in Aqueous Drug Solutions," *AAPS PharmSciTech*, vol. 19, no. 4, pp. 1860–1868, 2018.
- [307] G. A. Ilevbare, H. Liu, K. J. Edgar, and L. S. Taylor, "Maintaining Supersaturation in Aqueous Drug Solutions: Impact of Different Polymers on Induction Times," *Cryst. Growth Des.*, vol. 13, no. 2, pp. 740–751, Feb. 2013.
- [308] A. Zimmermann, A. Millqvist-Fureby, M. R. Elema, T. Hansen, A. Müllertz, and L. Hovgaard, "Adsorption of pharmaceutical excipients onto microcrystals of siramesine hydrochloride: Effects on physicochemical properties," *Eur. J. Pharm. Biopharm.*, vol. 71, no. 1, pp. 109–116, 2009.
- [309] F. Tian, D. Saville, K. Gordon, C. Strachan, J. Zeitler, N. Sandler, and T. Rades, *The influence of various excipients on the conversion kinetics of carbamazepine polymorphs in aqueous suspension*, vol. 59. 2007.
- [310] D. A. Miller, J. C. DiNunzio, W. Yang, J. W. McGinity, and R. O. Williams, "Enhanced In Vivo Absorption of Itraconazole via Stabilization of Supersaturation Following Acidic-to-Neutral pH Transition," *Drug Dev. Ind. Pharm.*, vol. 34, no. 8, pp. 890–902, Jan. 2008.
- [311] P. Gao and Y. Shi, "Characterization of Supersaturatable Formulations for Improved Absorption of Poorly Soluble Drugs," *AAPS J.*, vol. 14, no. 4, pp. 703–713, Dec. 2012.
- [312] M. A. Khan and I. K. Reddy, "Calcium Phosphate in Pharmaceutical Product Development BT - Calcium Phosphates in Biological and Industrial Systems," Z. Amjad, Ed. Boston, MA: Springer US, 1998, pp. 303–323.
- [313] P. C. Schmidt and R. Herzog, "Calcium phosphates in pharmaceutical tableting," *Pharm. World Sci.*, vol. 15, no. 3, pp. 116–122, 1993.
- [314] O. M. Y. Koo, *Pharmaceutical Excipients: Properties, Functionality, and Applications in Research and Industry*. Wiley, 2016.
- [315] N. H. Shah, D. Stiel, M. Weiss, M. H. Infeld, and A. W. Malick, "Evaluation of Two New Tablet Lubricants - Sodium Stearyl Fumarate and Glyceryl Behenate. Measurement of Physical Parameters (Compaction, Ejection and Residual Forces) in the Tableting Process and the Effect on the Dissolution Rate," *Drug Dev. Ind. Pharm.*, vol. 12, no. 8–9, pp. 1329–1346, Jan. 1986.
- [316] G. K. Bolhuis and A. W. Holzer, *Lubrication Issues in direct compaction*. 2011.
- [317] A. A. Noyes and W. R. Whitney, "The rate of solution of solid substances in their own solutions," *J. Am. Chem. Soc.*, vol. 19, no. 12, pp. 930–934, Dec. 1897.
- [318] C. DOHERTY and P. YORK, "The In-vitro pH-Dissolution Dependence and In-vivo Bioavailability of Frusemide-PVP Solid Dispersions," *J. Pharm. Pharmacol.*, vol. 41, no. 2, pp. 73–78, Aug. 2018.
- [319] P. Bassi and G. Kaur, "pH modulation: a mechanism to obtain pH-independent drug release," *Expert Opin. Drug Deliv.*, vol. 7, no. 7, pp. 845–857, Jul. 2010.
- [320] S. Badawy and M. Hussain, *Microenvironmental pH modulation in solid dosage forms*, vol. 96. 2007.
- [321] C. Guthmann, R. Lipp, T. Wagner, and H. Kranz, "Development of a multiple unit pellet formulation for a

- weakly basic drug," *Drug Dev. Ind. Pharm.*, vol. 33, no. 3, pp. 341–349, 2007.
- [322] H. Alyami, E. Dahmash, J. Bowen, and A. R. Mohammed, "An investigation into the effects of excipient particle size, blending techniques and processing parameters on the homogeneity and content uniformity of a blend containing low-dose model drug," *PLoS One*, vol. 12, no. 6, p. e0178772, Jun. 2017.
- [323] C. G. Wilson, "The Organization of the Gut and the Oral Absorption of Drugs: Anatomical, Biological and Physiological Considerations in Oral Formulation Development BT - Controlled Release in Oral Drug Delivery," C. G. Wilson and P. J. Crowley, Eds. Boston, MA: Springer US, 2011, pp. 27–48.
- [324] "Lactose Monohydrate (SDS Sheet). Sigma-Aldrich Production GmbH, Industriestrasse 25, 9471 Buchs / Switzerland," 2012.
- [325] V. Sawale, D. Dhabarde, and D. Kar Mahapatra, "Development and Validation of UV Spectrophotometric Method for Simultaneous Estimation of Olmesartan Medoxomil and Chlorthalidone in Bulk and Tablet," *Eurasian J. Anal. Chem.*, vol. 12, no. 1, pp. 55–66, 2016.
- [326] R. S. Joshi, N. S. Pawar, S. S. Katiyar, D. B. Zope, and A. T. Shinde, "Development and validation of UV spectrophotometric methods for simultaneous estimation of Paracetamol and Ibuprofen in pure and tablet dosage form," *Pelagia Res. Libr.*, vol. 4, no. 4, pp. 68–72, 2013.
- [327] M. A. Patel, S. Luthra, S. L. Shamblin, K. Arora, J. Krzyzaniak, and L. S. Taylor, *Effect of excipient properties, water activity, and water content on the disproportionation of a pharmaceutical salt*, vol. 546. 2018.
- [328] S. Koranne, R. Govindarajan, and R. Suryanarayanan, "Investigation of spatial heterogeneity of salt disproportionation in tablets by synchrotron X-ray diffractometry," *Mol. Pharm.*, vol. 14, no. 4, pp. 1133–1144, 2017.
- [329] K. Dvořáčková, P. Doležel, E. Mašková, J. Muselík, M. Kejdušová, and D. Vetchý, "The Effect of Acid pH Modifiers on the Release Characteristics of Weakly Basic Drug from Hydrophilic–Lipophilic Matrices," *AAPS PharmSciTech*, vol. 14, no. 4, pp. 1341–1348, 2013.
- [330] C. Taniguchi, R. Inoue, Y. Kawabata, K. Yamashita, K. Wada, Y. Yamauchi, S. Yamada, and S. Onoue, "Novel formulations of dipyridamole with microenvironmental pH-modifiers for improved dissolution and bioavailability under hypochlorhydria," *Int. J. Pharm.*, vol. 434, no. 1, pp. 148–154, 2012.
- [331] W. Wolfgang, E. Michael, M. J. C. A., S. Joachim, B. Ulrich, E. Thomas, S. Jochen, L. Horst, M. Kandace, K.-R. Joan, G. Volker, and H. N. H., "A Review on Telmisartan: A Novel, Long-Acting Angiotensin II-Receptor Antagonist," *Cardiovasc. Drug Rev.*, vol. 18, no. 2, pp. 127–154.
- [332] J.-H. Guo, "Lactose in Pharmaceutical Applications," *Drug Deliv. Technol.*, vol. 4, no. 5, 2004.
- [333] H. M. Gaffour, M. Bouterfas, N. Bekhti, S. N. Derrar, and M. Sekkal Rahal, "Harmonic Dynamics of α -D-Lactose in the Crystalline State," *J. Mol. Imaging Dyn.*, vol. 01, no. 01, p. 1000102, 2011.
- [334] M. De Veij, P. Vandenabeele, T. De Beer, J. P. Remon, and L. Moens, "Reference database of Raman spectra of pharmaceutical excipients," *J. Raman Spectrosc.*, vol. 40, no. 3, pp. 297–307, 2009.
- [335] A. Ariyasu, Y. Hattori, and M. Otsuka, "Delay effect of magnesium stearate on tablet dissolution in acidic medium," *Int. J. Pharm.*, vol. 511, no. 2, pp. 757–764, 2016.
- [336] D. Cebeci-Maltaş, Derya Alam, MD ANIK Wang, PING BEN-AMOTZ and R. PINAL, "Photobleaching profile of Raman peaks and fluorescence background," *Eur. Pharm. Rev.*, no. 6, 2017.
- [337] "Ibuprofen Sodium (SDS Sheet). Sigma-Aldrich Production GmbH, Industriestrasse 25, 9471 Buchs / Switzerland," 2013.
- [338] J.-G. Chen, J.-G. (James) Chen, D. A. Markovitz, A. Y. Yang, S. R. Rabel, J. Pang, O. Dolinsky, L.-S. Wu, and M. Alasandro, "Degradation of a Fluoropyridinyl Drug in capsule Formulation: Degradant Identification, Proposed Degradation Mechanism, and Formulation Optimization," *Pharm. Dev. Technol.*, vol. 5, no. 4, pp.

561–570, Jan. 2000.

- [339] M. M. Al-Omari, M. K. Abdelah, A. A. Badwan, and A. M. Y. Jaber, "Effect of the drug-matrix on the stability of enalapril maleate in tablet formulations," *J. Pharm. Biomed. Anal.*, vol. 25, no. 5, pp. 893–902, 2001.
- [340] T. Riis, A. Bauer-Brandl, T. Wagner, and H. Kranz, "pH-independent drug release of an extremely poorly soluble weakly acidic drug from multiparticulate extended release formulations," *Eur. J. Pharm. Biopharm.*, vol. 65, no. 1, pp. 78–84, 2007.
- [341] M. Szumiło, K. Wiąder, P. Belniak, J. Wojciechowska, and E. Poleszak, "The influence of excipients on physical properties of tablets and dissolution of caffeine," *Acta Pol. Pharm. - Drug Res.*, vol. 72, no. 4, pp. 791–797, 2015.
- [342] A. Abd-Elbary, M. I. Tadros, and A. A. Alaa-Eldin, "Sucrose Stearate-Enriched Lipid Matrix Tablets of Etodolac: Modulation of Drug Release, Diffusional Modeling and Structure Elucidation Studies," *AAPS PharmSciTech*, vol. 14, no. 2, pp. 656–668, 2013.
- [343] HiQ-Nano, "Ultrastable Fluorescent Nanobeads." .
- [344] Thermo Fisher Scientific, "Fluorescent microspheres for calibrating microscopes and flow cytometers," *Thermo Fisher Scientific*. [Online]. Available: <https://www.thermofisher.com/uk/en/home/references/newsletters-and-journals/bioprobables-journal-of-cell-biology-applications/bioprobables-70/fluorescent-microspheres-for-calibration.html>.
- [345] Gatta-Quant, "GATTA-PAINT NANORULER." [Online]. Available: <http://www.gattaquant.com/products/localization-based/gatta-paint-nanoruler.html>.
- [346] P. Timmins, S. R. Pygall, and C. D. Melia, *Hydrophilic Matrix Tablets for Oral Controlled Release*. Springer New York, 2014.
- [347] Y. E.-S. Hamza and M. H. Aburahma, "Design and in vitro evaluation of novel sustained-release matrix tablets for lornoxicam based on the combination of hydrophilic matrix formers and basic pH-modifiers," *Pharm. Dev. Technol.*, vol. 15, no. 2, pp. 139–153, Apr. 2010.
- [348] P. H. L. Tran, H. T. T. Tran, and B.-J. Lee, "Modulation of microenvironmental pH and crystallinity of ionizable telmisartan using alkalizers in solid dispersions for controlled release," *J. Control. Release*, vol. 129, no. 1, pp. 59–65, 2008.
- [349] J. Huang, H. Lin, B. Peng, Q. Huang, F. Shuai, and Y. Xie, "Design and Evaluation of Hydrophilic Matrix System for pH-Independent Sustained Release of Weakly Acidic Poorly Soluble Drug," *AAPS PharmSciTech*, vol. 19, no. 5, pp. 2144–2154, 2018.
- [350] B. W. Glombitza, D. Oelkrug, and P. C. Schmidt, *Surface acidity of solid pharmaceutical excipients. I. Determination of the surface acidity*, vol. 40. 1994.
- [351] R. Govindarajan, A. Zinchuk, B. Hancock, E. Shalaev, and R. Suryanarayanan, "Ionization States in the Microenvironment of Solid Dosage Forms: Effect of Formulation Variables and Processing," *Pharm. Res.*, vol. 23, no. 10, pp. 2454–2468, 2006.

Appendix A

Chapter 4 Figures

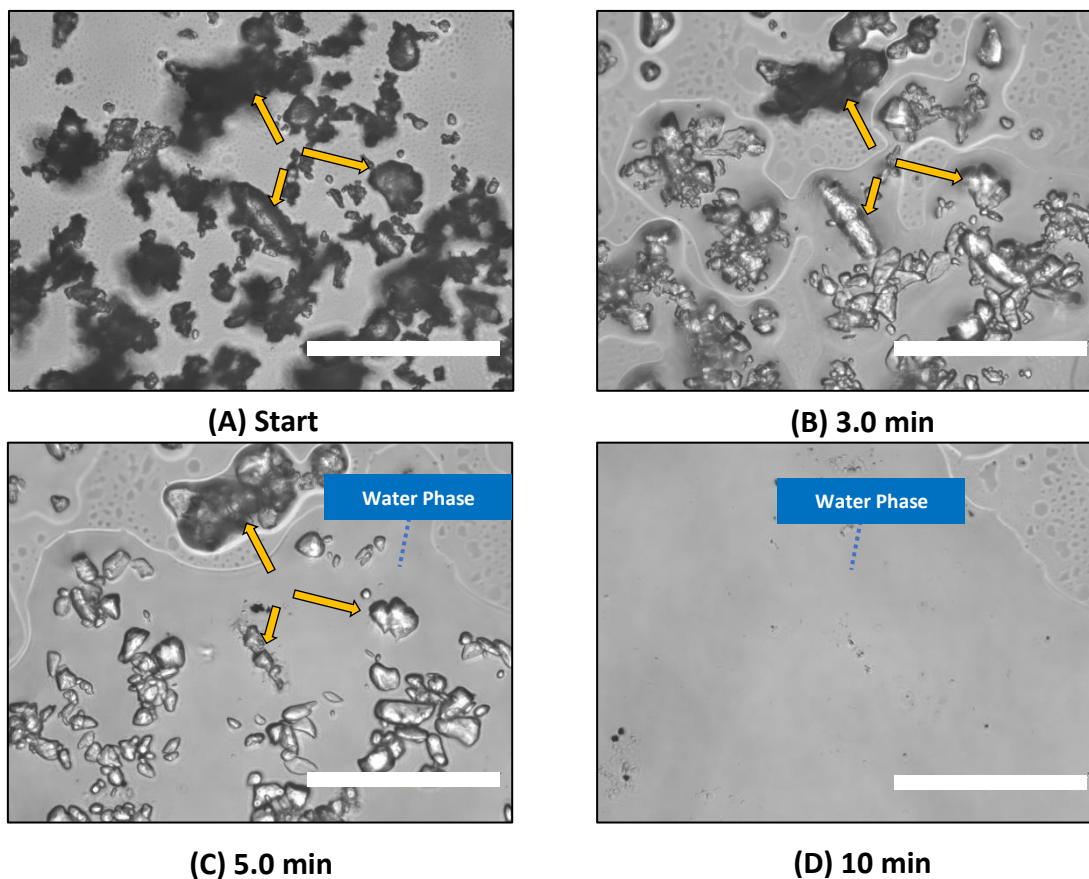


Figure A. 1: *In situ* optical microscopy images of Pioglitazone HCl multiple crystals (Orange arrows) mixed with ascorbic acid during storage at 75-90% RH: (A) Start (B) 3.0 min (C) 5.0 min (D) 10 min. Scale bar for images is 100 μ m.

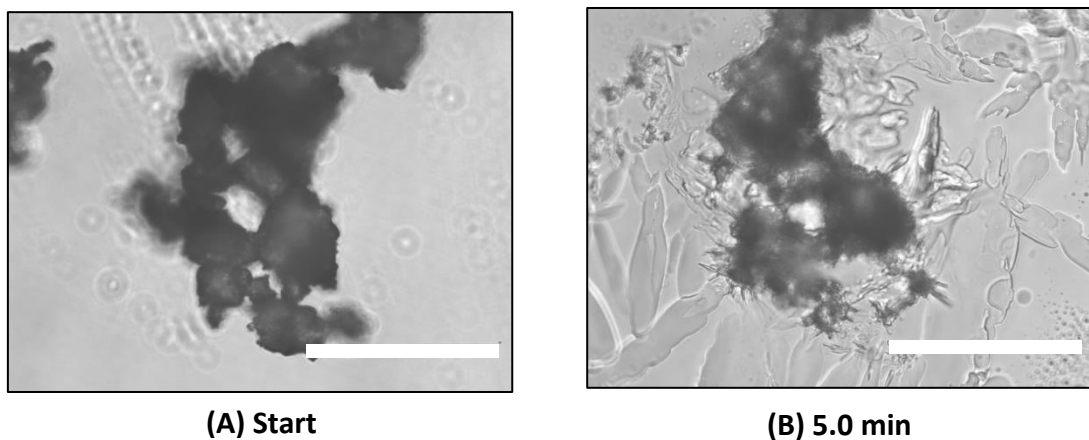


Figure A. 2: *In situ* optical microscopy images of Ibuprofen crystals mixed with ascorbic acid during storage at 75-90% RH: (A) Start (B) 5.0 min. Scale bar for images is 100 μ m

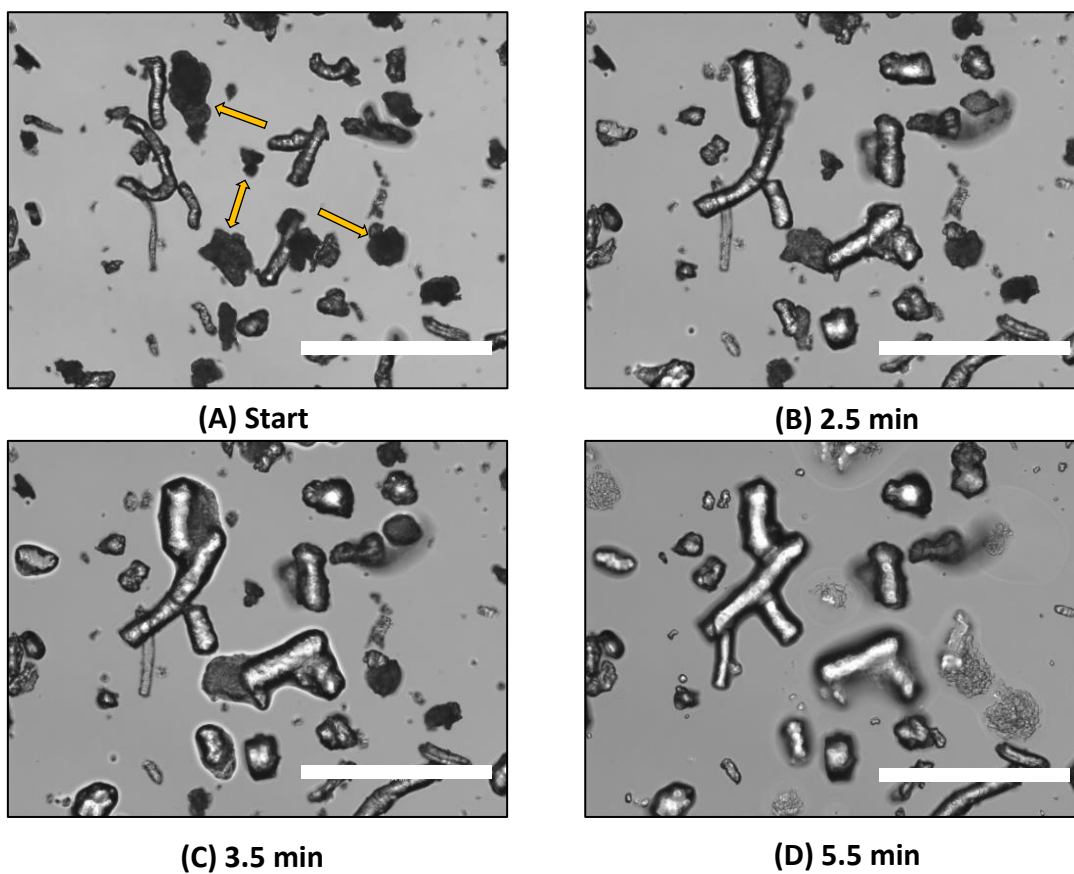


Figure A. 3: *In situ* optical microscopy images of Ibuprofen sodium crystals (Orange arrows) mixed with croscarmellose sodium during storage at 75-90% RH: (A) Start (B) 2.5 min (C) 3.5 min (D) 5.5 min. Scale bar for images is 200 μm .

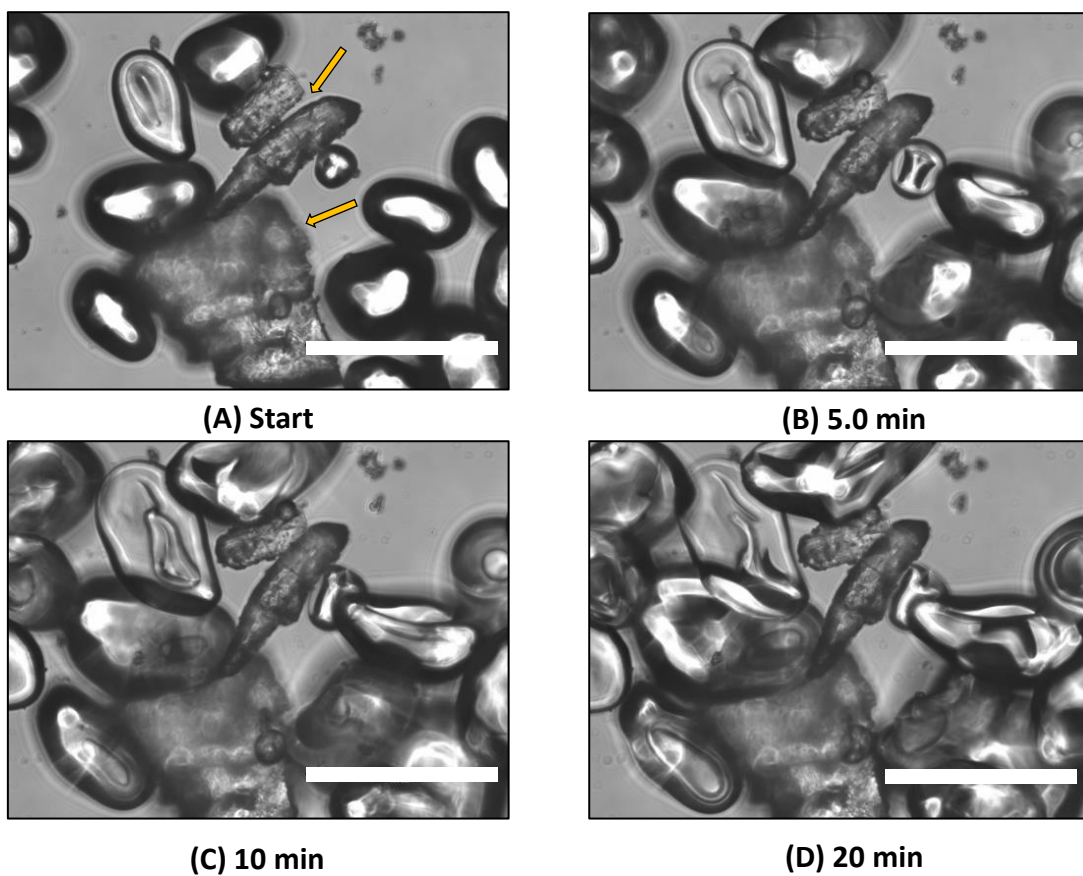


Figure A. 4: *In situ* optical microscopy images of Pioglitazone HCl crystals (Orange arrows) mixed with sodium starch glycolate during storage at 75-90% RH: (A) Start (B) 5.0 min (C) 10 min (D) 20 min. Scale bar for images is 100 μm .

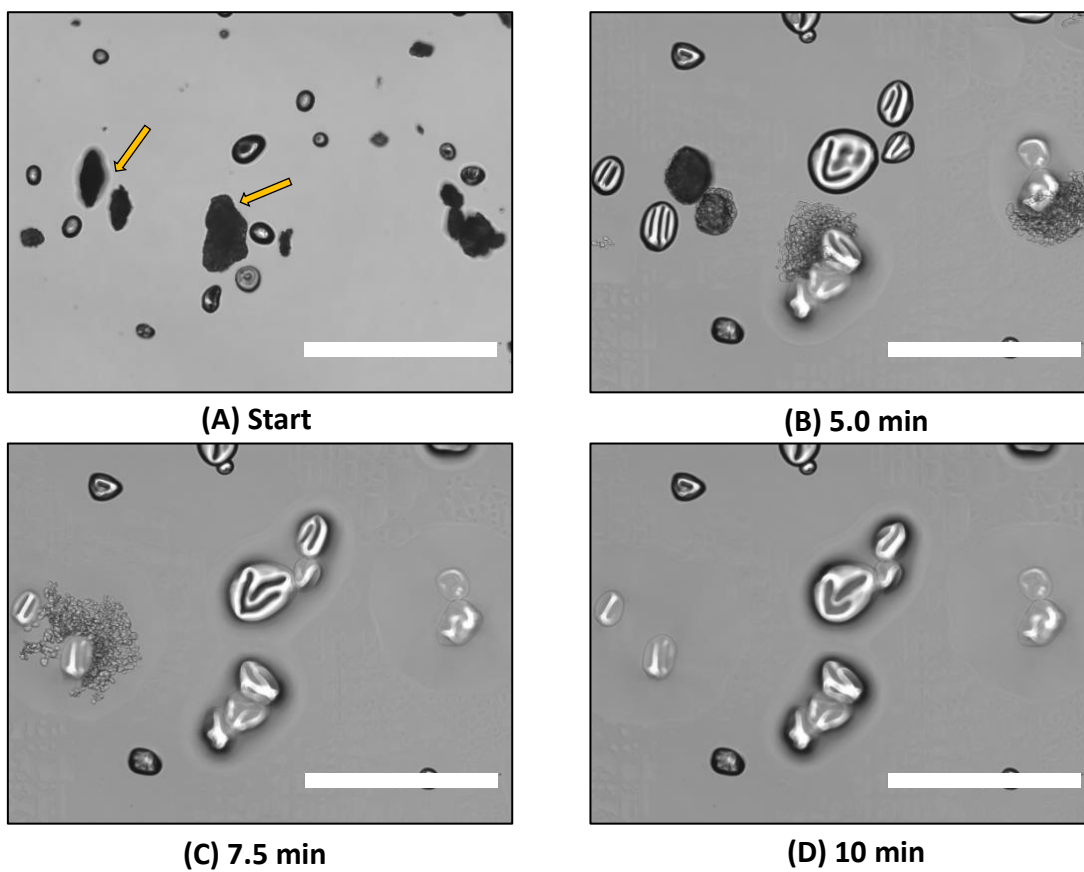


Figure A. 5: *In situ* optical microscopy images of Ibuprofen sodium crystals (Orange arrows) mixed with sodium starch glycolate during storage at 75-90% RH: (A) Start (B) 5 min (C) 7.5 min (D) 10 min. Scale bar for images is 200 μm .

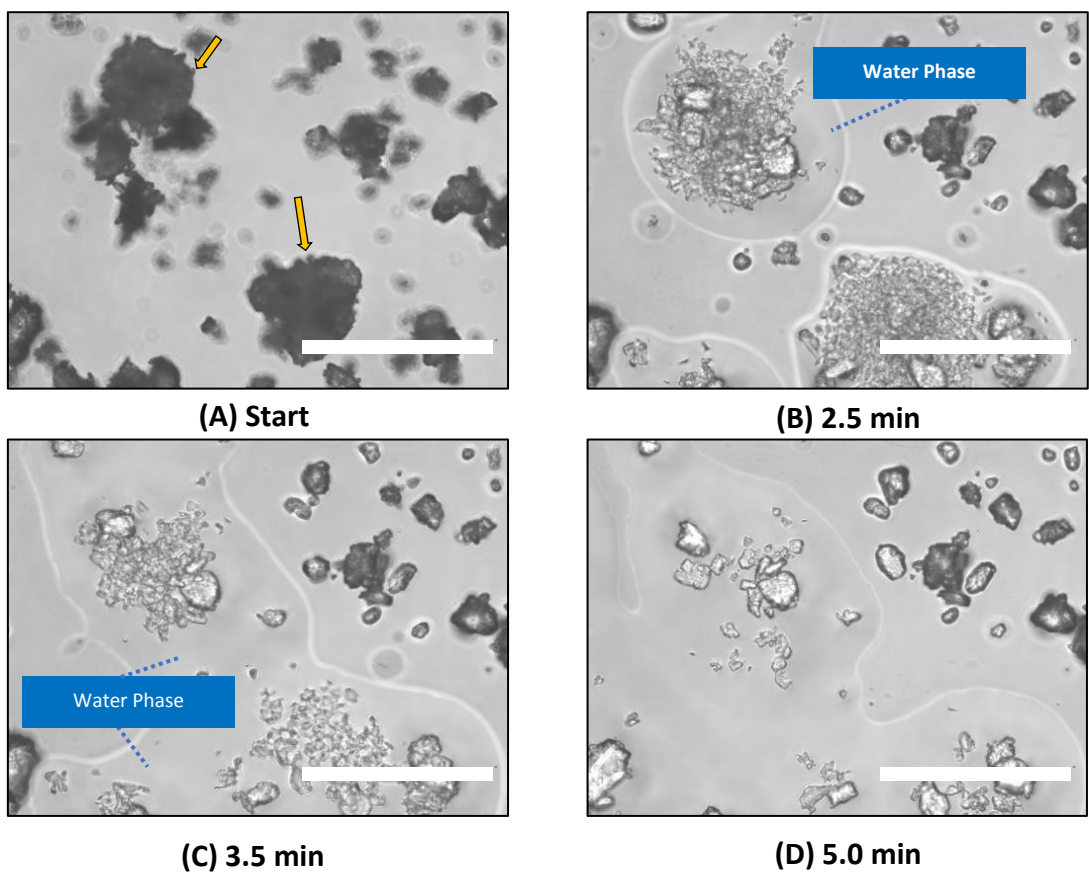


Figure A. 6: *In situ* optical microscopy images of Ibuprofen sodium crystals (Orange arrows) mixed with lactose monohydrate during storage at 75-90% RH: (A) Start (B) 2.5 min (C) 3.5 min (D) 5.0 min. Scale bar for images is 100 μm .

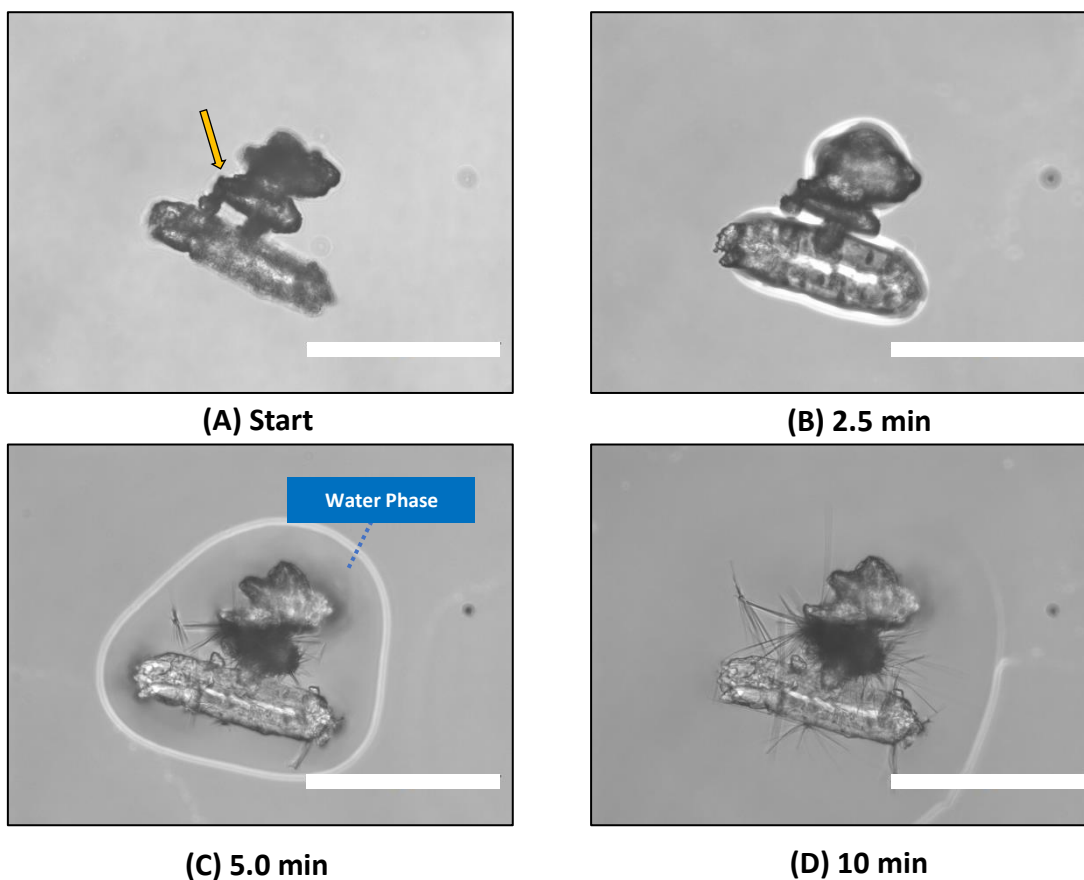


Figure A. 7: *In situ* optical microscopy images of Pioglitazone HCl crystal (Orange arrow) mixed with microcrystalline cellulose during storage at 75-90% RH: (A) Start (B) 2.5 min (C) 5.0 min (D) 10 min. Scale bar for images is 100 μm .

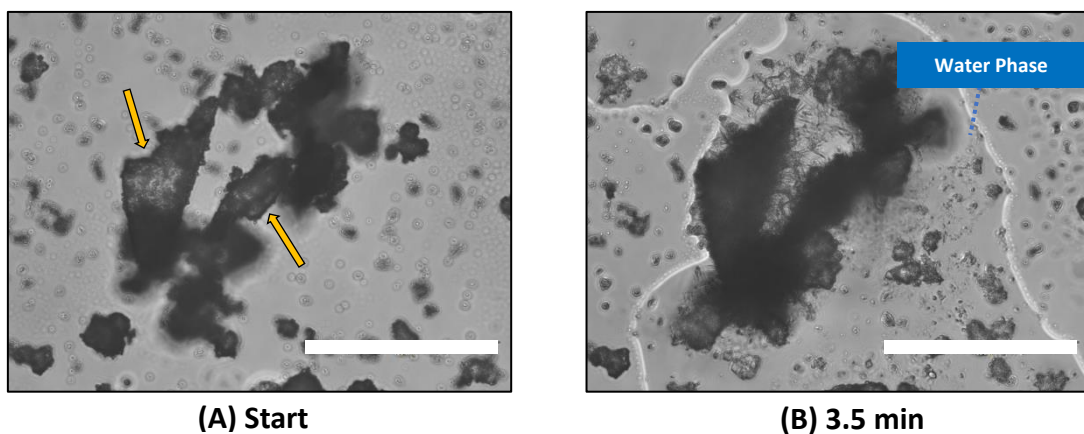
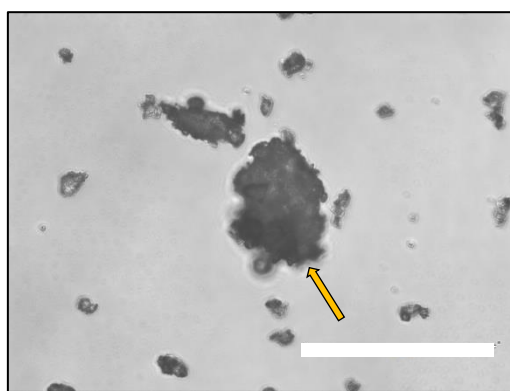
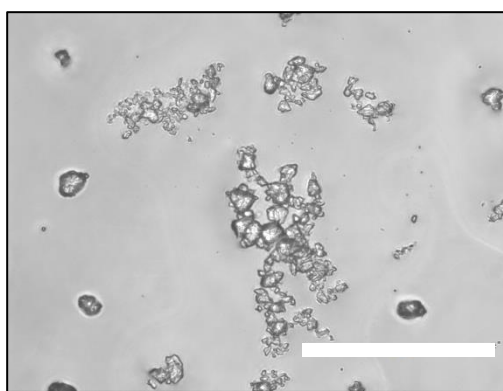


Figure A. 8: *In situ* optical microscopy images of Pioglitazone HCl crystal (Orange arrow) mixed with calcium phosphate dibasic during storage at 75-90% RH: (A) Start (B) 3.5 min. Scale bar for images is 100 μm .

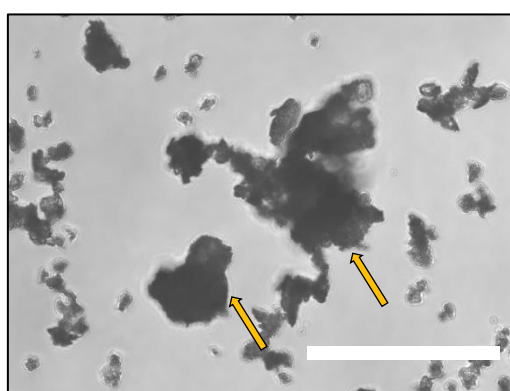


(A) Start

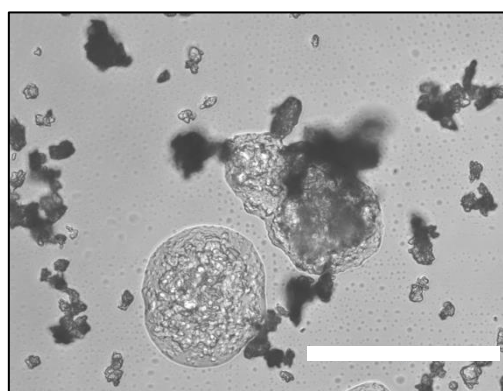


(B) 5.0 min

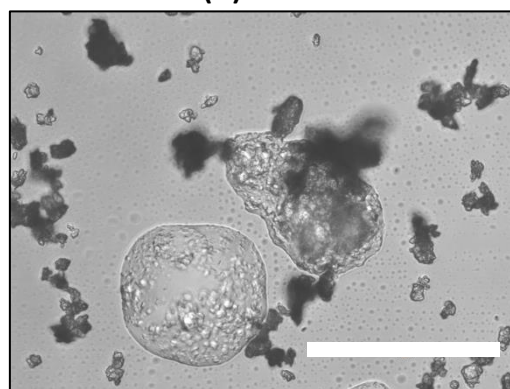
Figure A. 9: *In situ* optical microscopy images of Ibuprofen sodium crystal (Orange arrow) mixed with calcium phosphate dibasic during storage at 75-90% RH: (A) Start (B) 5.0 min. Scale bar for images is 100 μ m.



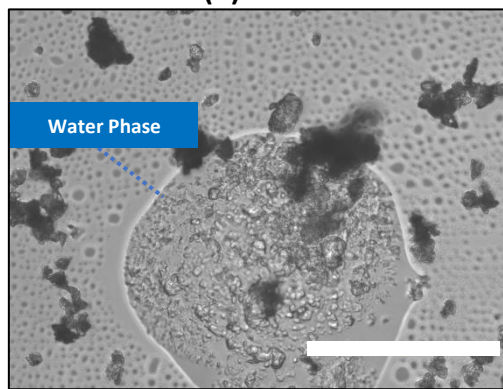
(A) Start



(B) 1.5 min



(C) 2.0 min



(D) 5.0 min

Figure A. 10: *In situ* optical microscopy images of Ibuprofen sodium crystals (Orange arrows) mixed with magnesium stearate during storage at 75-90% RH: (A) Start (B) 1.5 min (C) 2.0 min (D) 5.0 min. Scale bar for images is 100 μ m.

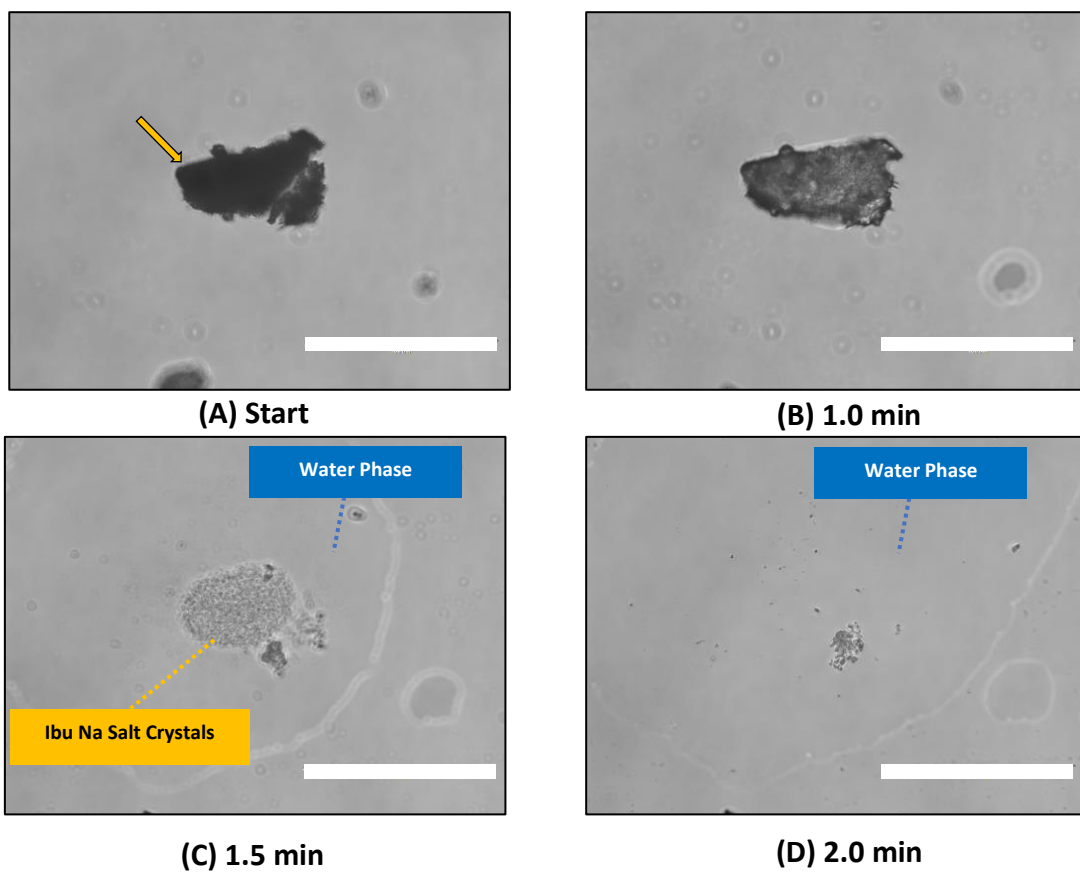


Figure A. 11: *In situ* optical microscopy images of Ibuprofen sodium crystal (Orange arrow) mixed with sodium phosphate dibasic during storage at 75-90% RH: (A) Start (B) 1.0 min (C) 1.5 min (D) 2.0 min. Scale bar for images is 100 μm .

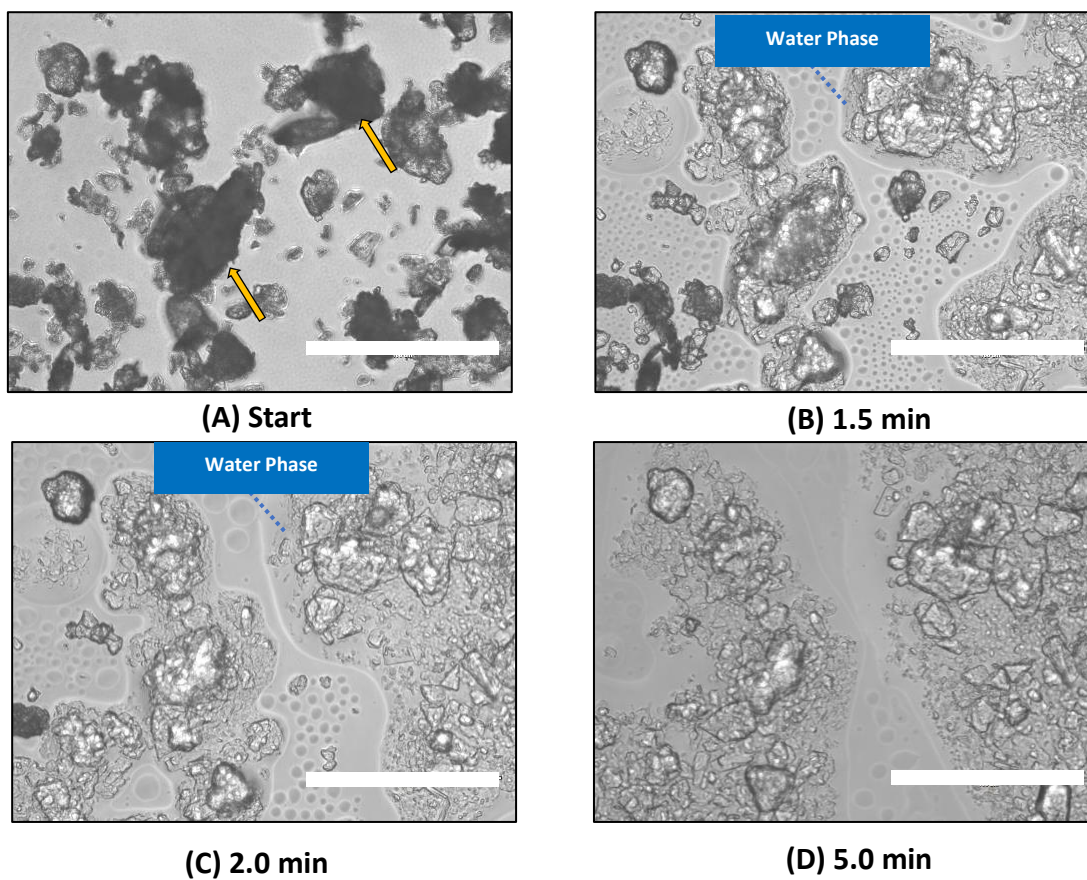


Figure A. 12: *In situ* optical microscopy images of Ibuprofen sodium crystals (Orange arrows) mixed with sodium stearyl fumarate during storage at 75-90% RH: (A) Start (B) 1.5 min (C) 2.0 min (D) 5.0 min. Scale bar for images is 100 μm .

Appendix B

Chapter 5 Figures

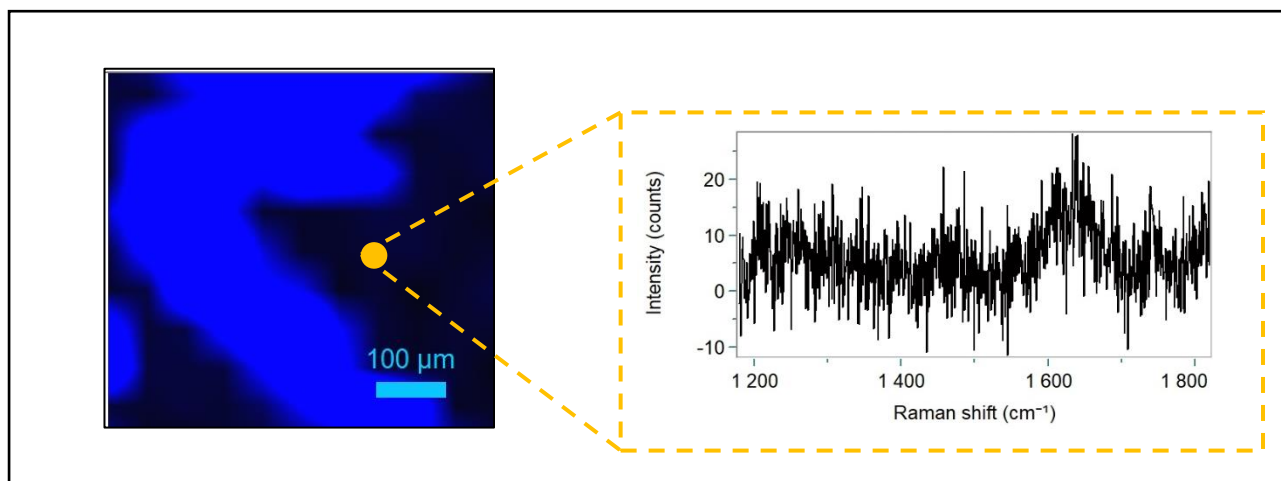


Figure B. 1: Amorphous spectra recovered from formulation A (Pio HCl: Citric Acid) tablet during dissolving in the acidic media

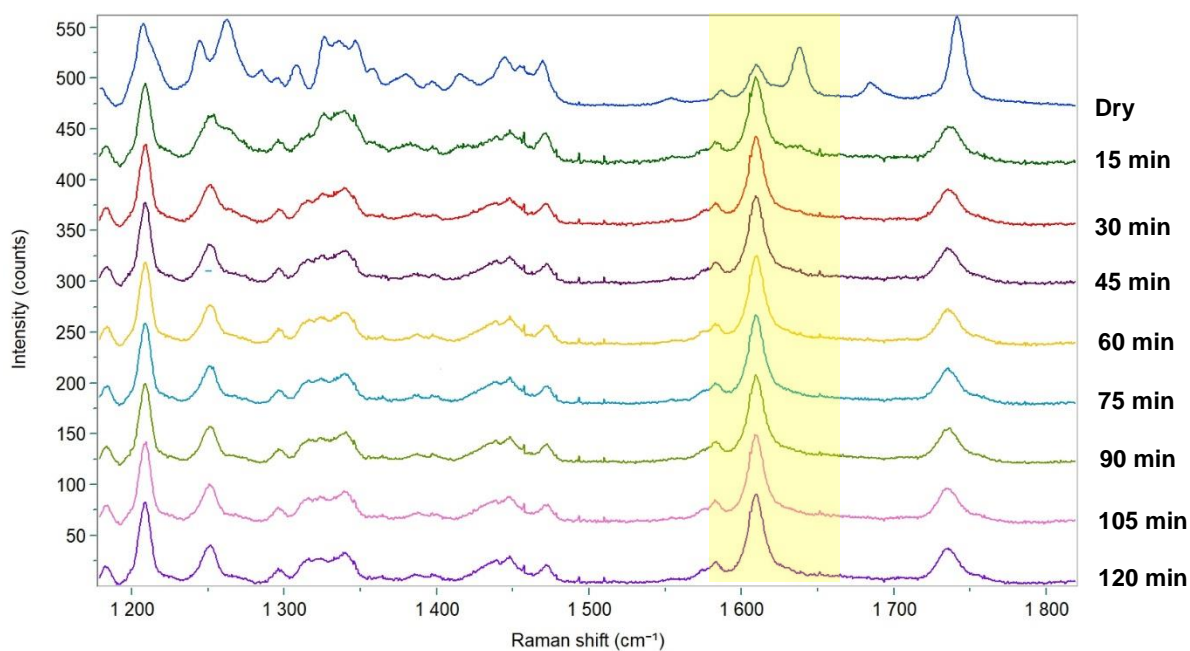


Figure B. 2: Averaged Raman spectra (1200 to 1800 cm^{-1}) of the dissolution of formulation B (Pio HCl: LM) tablet in the basic buffer. Y-axis offsets were applied for presentational purposes.

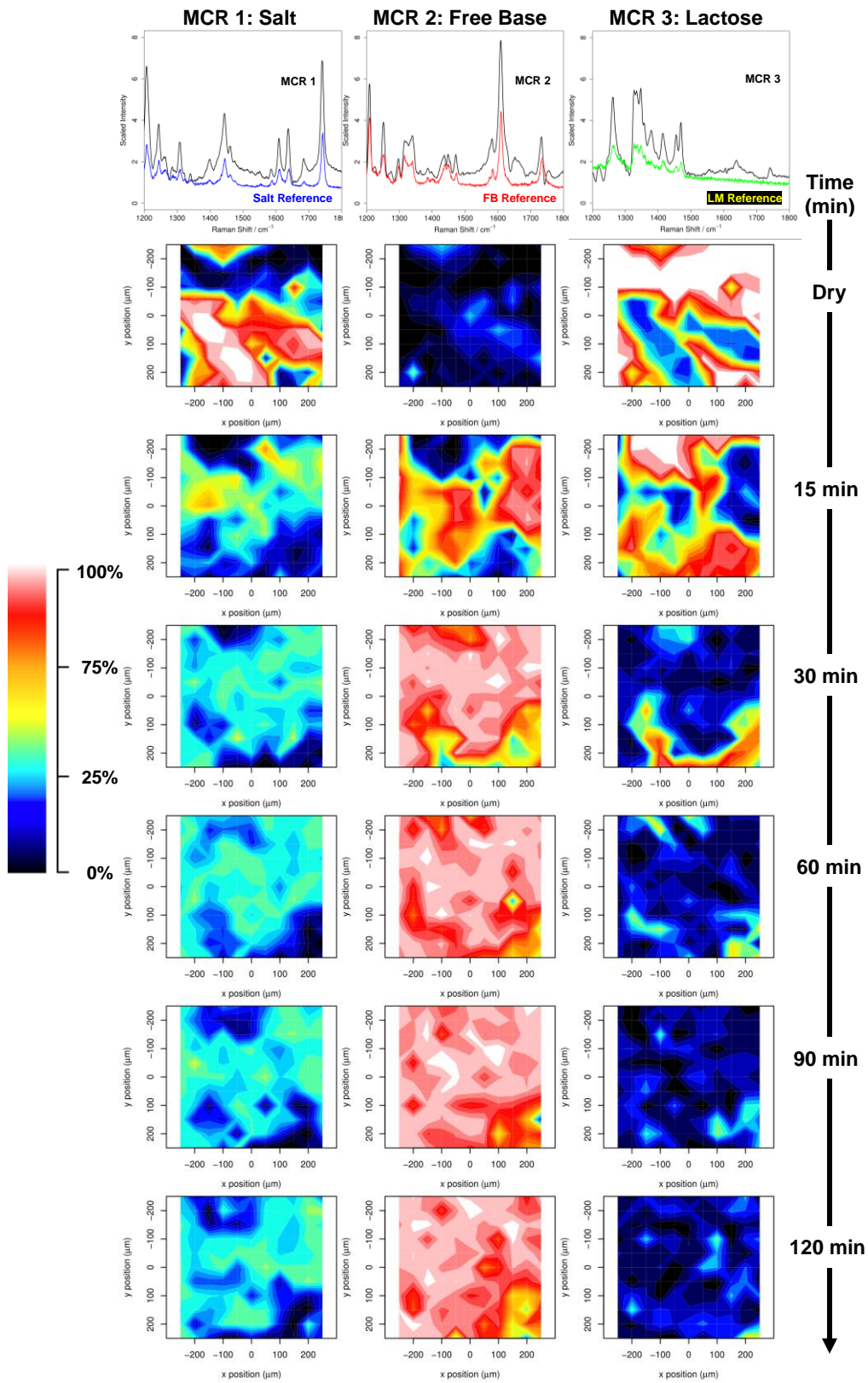


Figure B. 3: Raman maps of formulation B tablet (Pio HCl: LM) during dissolution in the basic buffer as a function of time, generated by MCR analysis

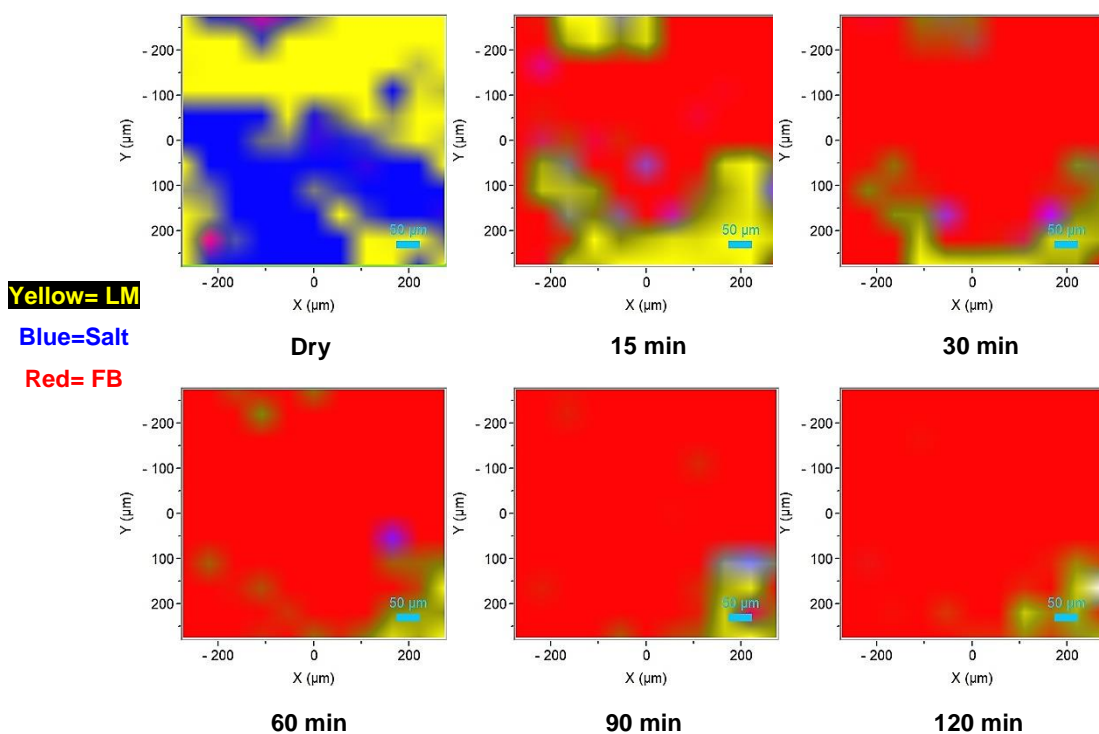


Figure B. 4: Raman maps of formulation B tablet (Pio HCl: LM) during dissolution in the basic buffer as a function of time, generated by CLS analysis

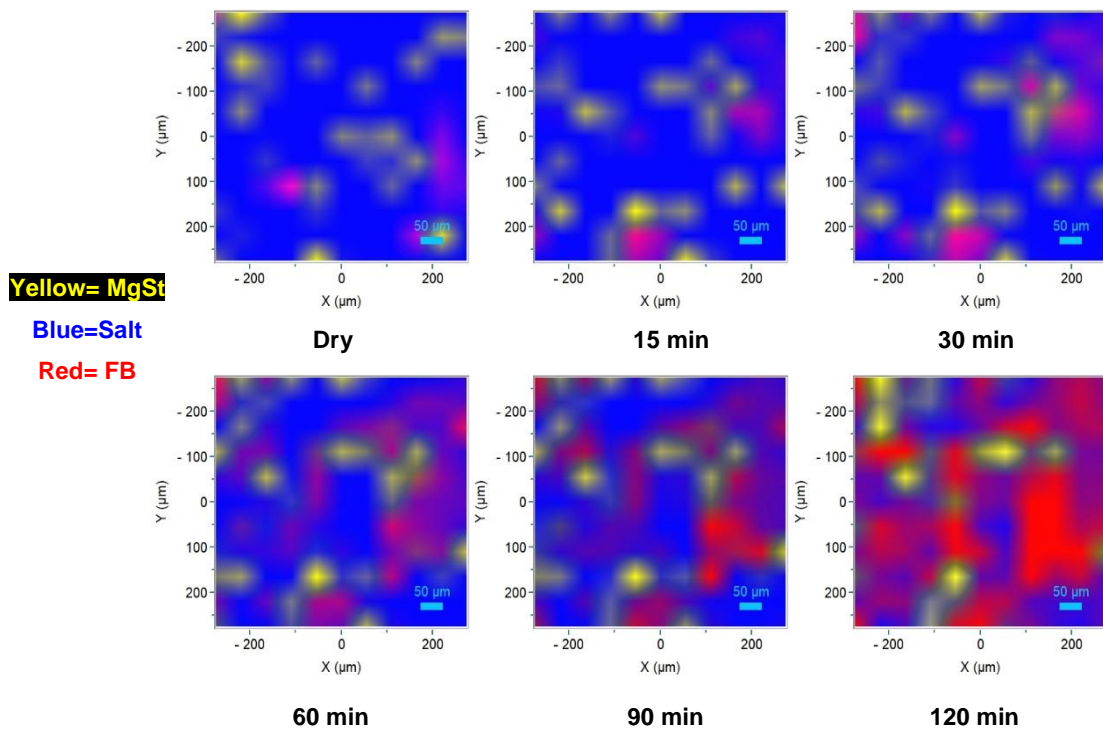


Figure B. 5: Raman maps of formulation C tablet (Pio HCl: MgSt) during dissolution in the basic buffer as a function of time, generated by CLS analysis

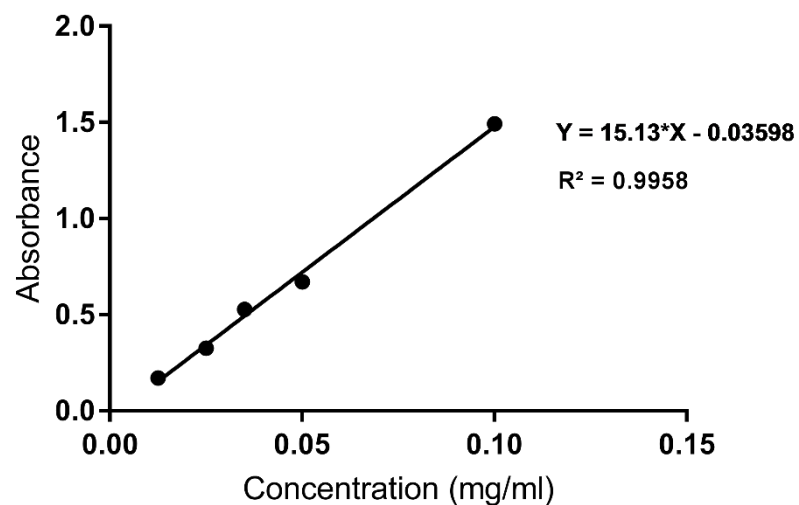


Figure B. 6: Calibration curve showing the concentration of dissolved Pioglitazone vs. absorbance at 270 nm, recorded for Pioglitazone dissolved in methanol. The calibration plot was used to quantify the release of Pioglitazone from the different formulation tablets.

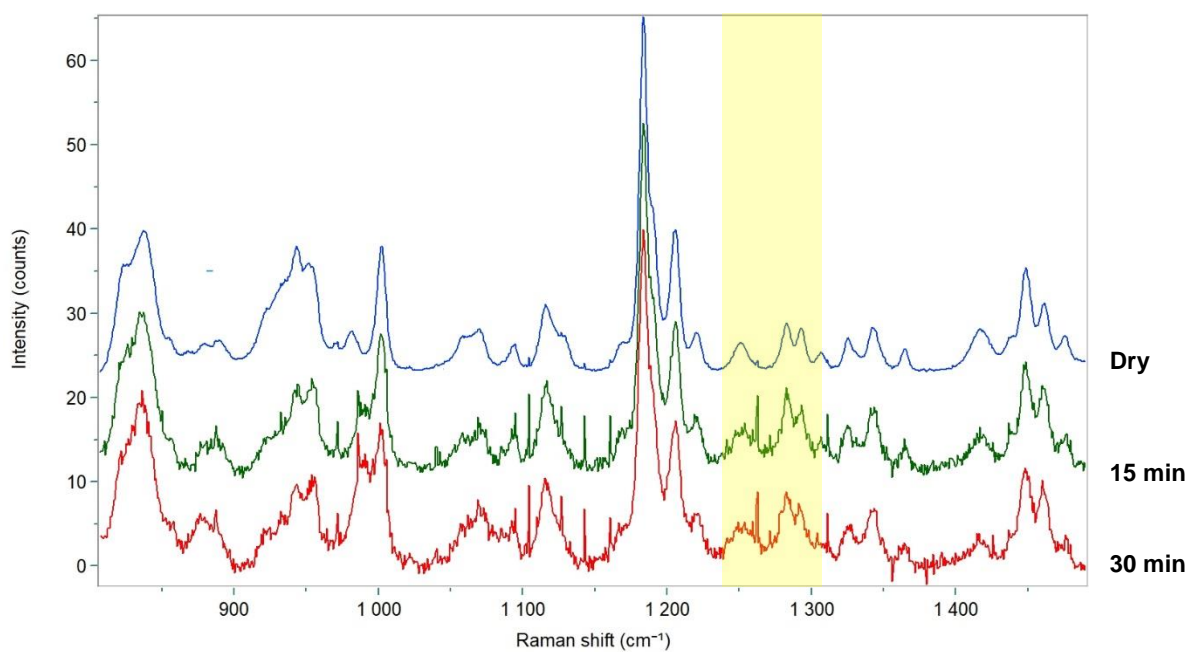


Figure B. 7: Averaged Raman spectra (800 to 1500 cm^{-1}) of the dissolution of the formulation (E) tablet in the basic buffer. Y-axis offsets were applied for presentational purposes.

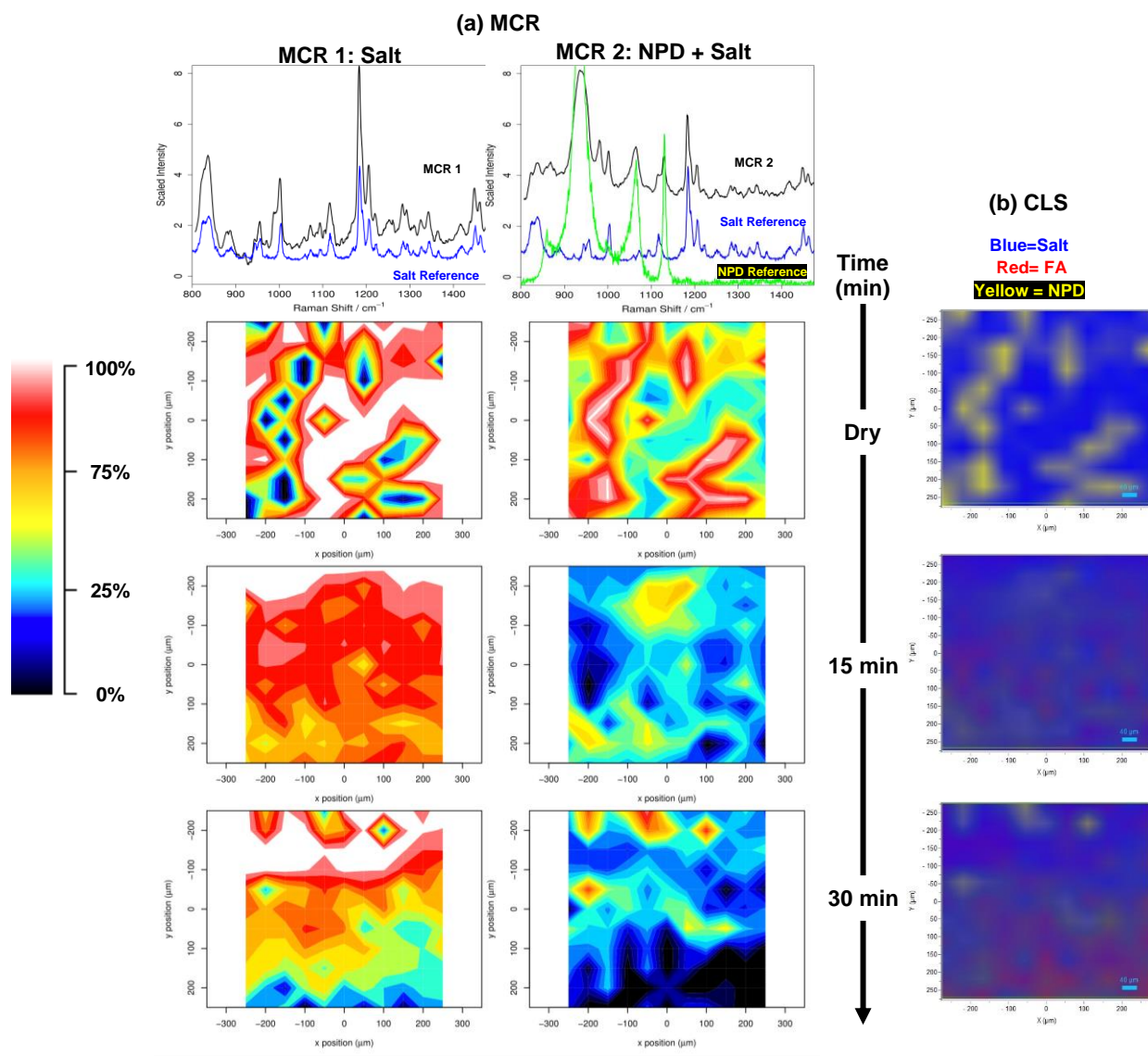


Figure B. 8: Raman maps of formulation E (Ibu Na: NPD) tablet during dissolution in the basic buffer as a function of time, generated by (a) MCR analysis (b) CLS analysis

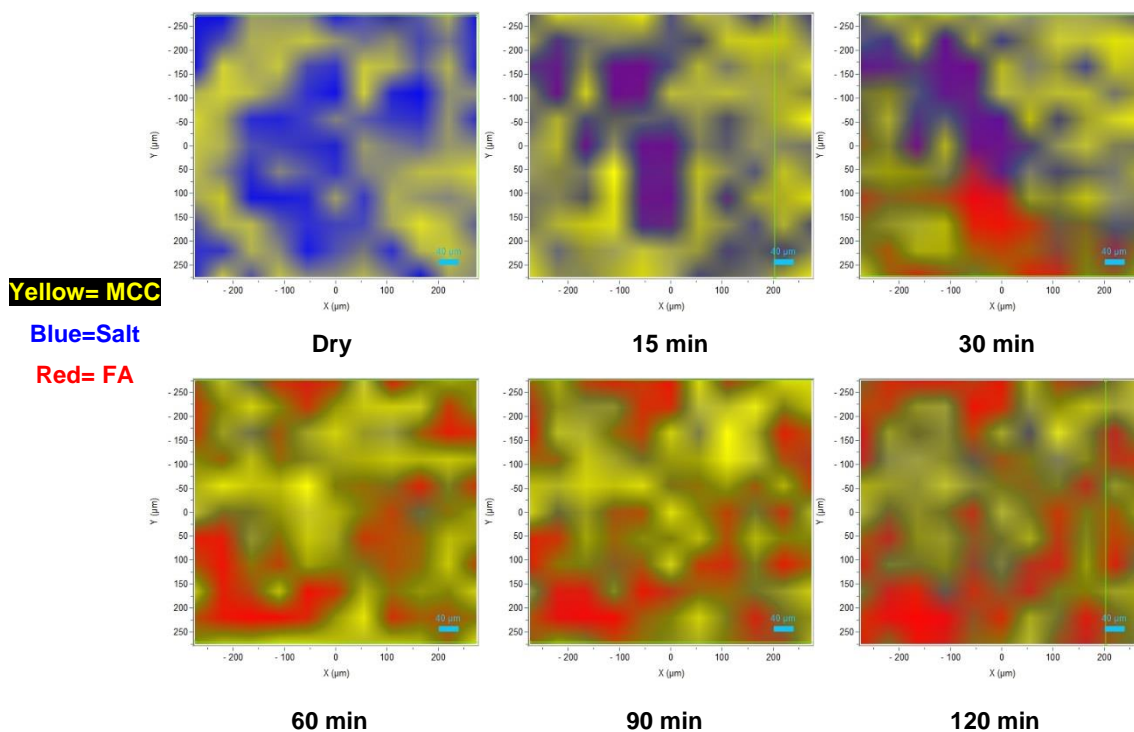


Figure B. 9: Raman maps of the formulation (G) tablet during dissolution in the acidic buffer as a function of time, generated by DCLS analysis

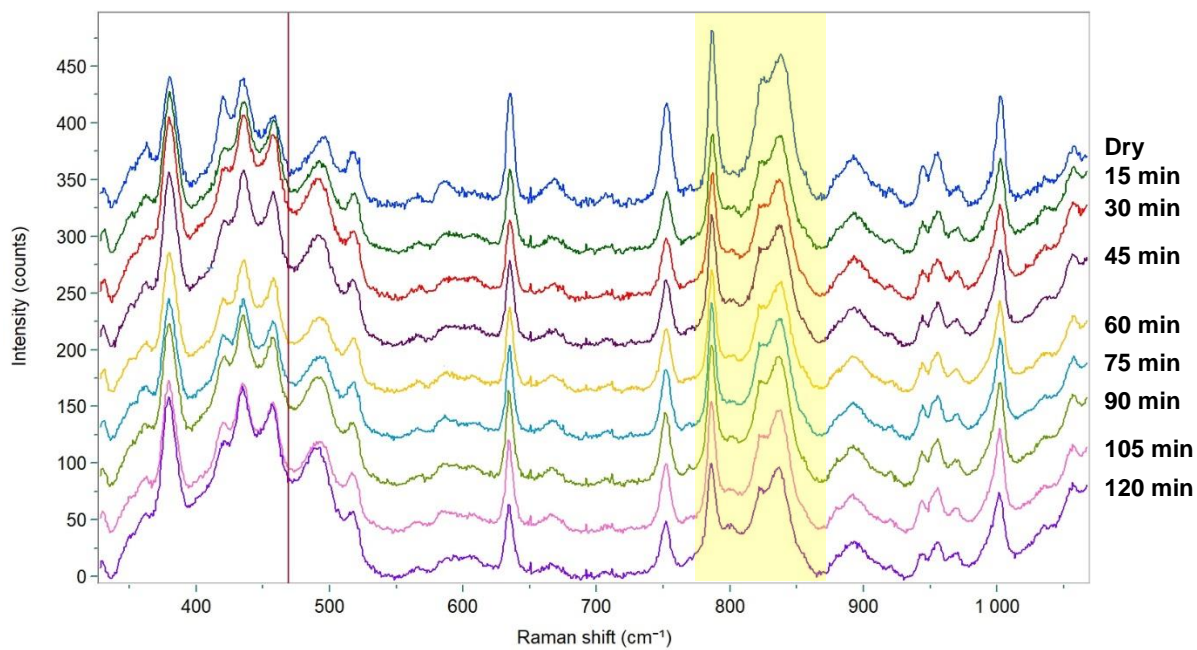


Figure B. 10: Averaged Raman spectra (400 to 1100 cm^{-1}) of the dissolution of the formulation (G) tablet in the basic buffer. Y-axis offsets were applied for presentational purposes.

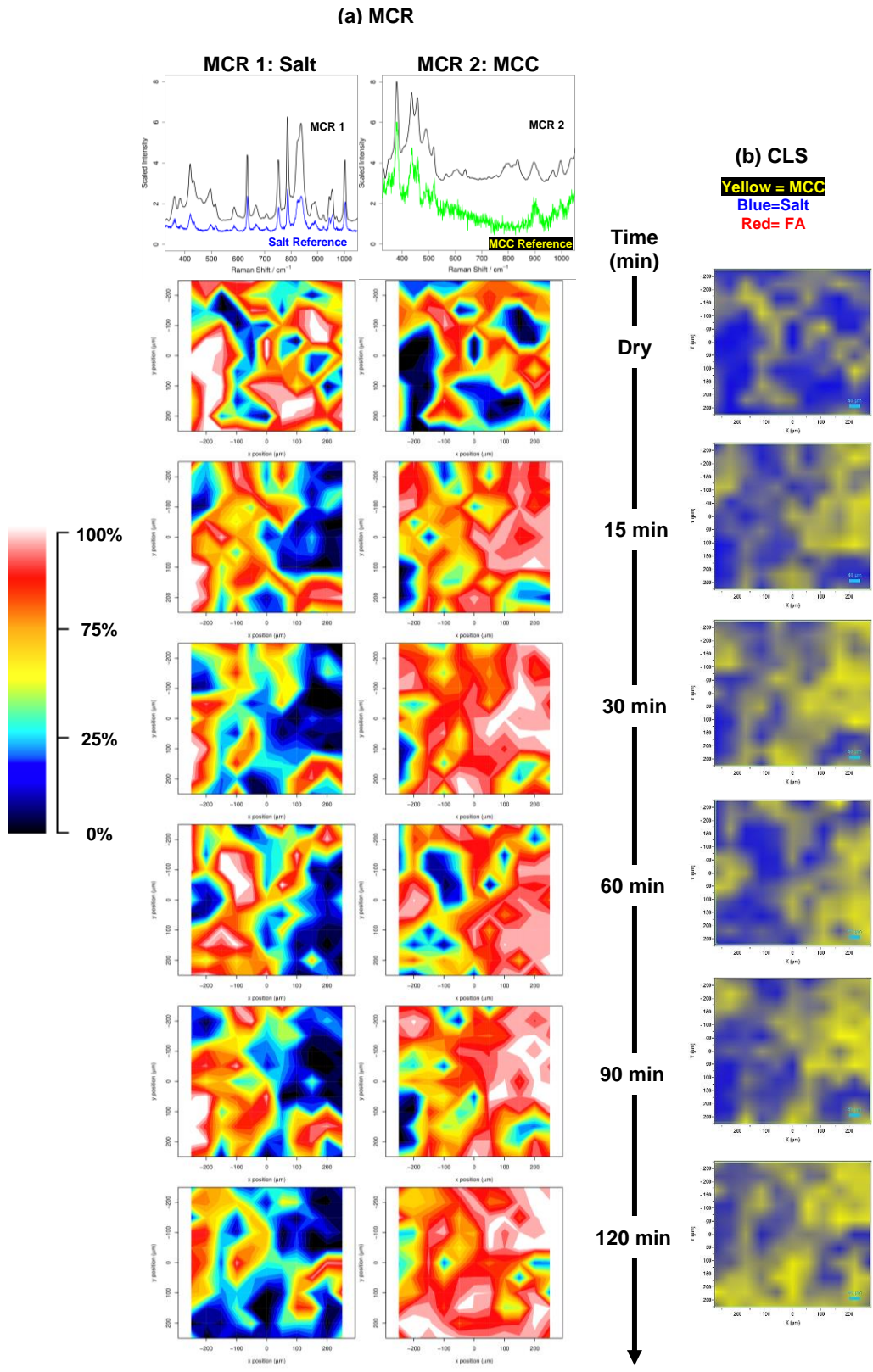


Figure B. 11: Raman maps of the formulation (G) tablet during dissolution in the basic buffer as a function of time, generated by (a) MCR analysis (b) CLS analysis

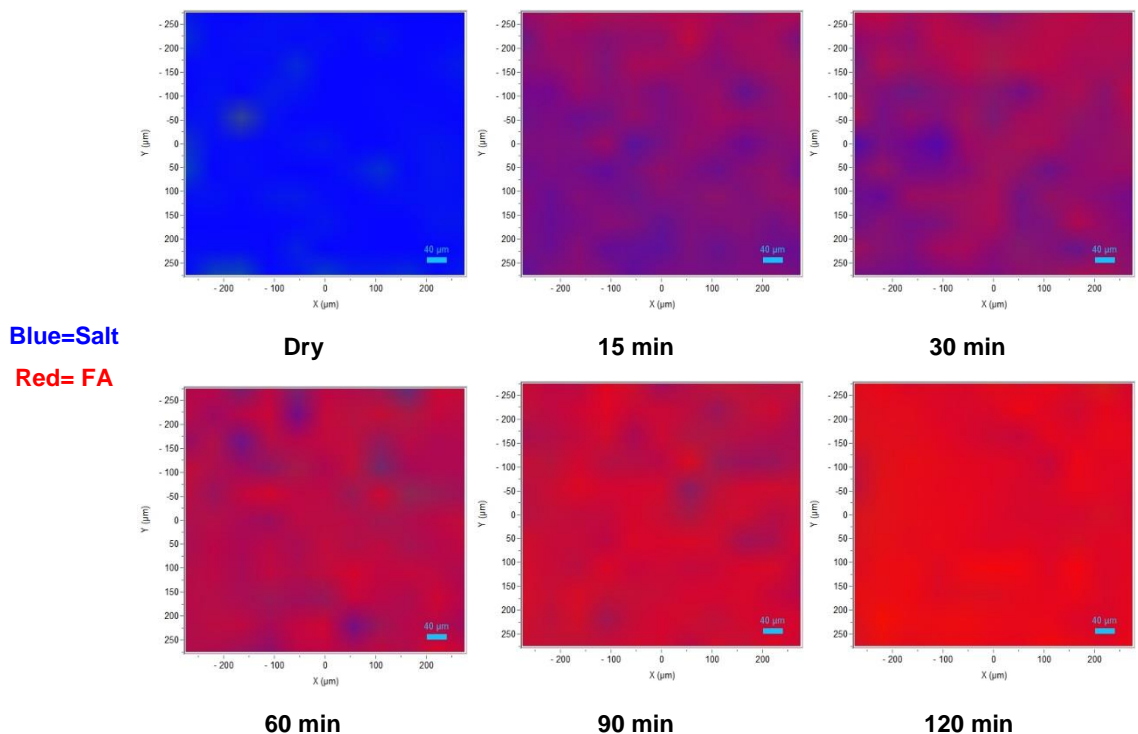


Figure B. 12: Raman maps of the formulation (H) tablet during dissolution in the the acidic buffer as a function of time, generated by CLS analysis

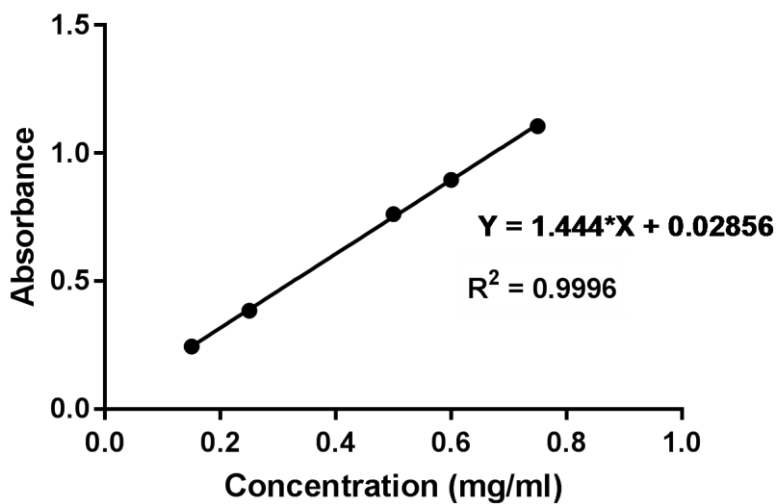


Figure B. 13: Calibration curve showing the concentration of dissolved Ibuprofen sodium vs absorbance at 270 nm, recorded for Ibuprofen dissolved in water. The calibration plot was used to quantify the release of Ibuprofen from the different formulation tablets.